Final Report for the Office of Hydrologic Development
NATIONAL OCEANIC AND ATMOSPHERIC ADMINISTRATION
NATIONAL WEATHER SERVICE

Project title:

Towards Probabilistic Quantitative Precipitation WSR-88D Algorithms: Data Analysis and Development of Ensemble Generator Model: Phase 4

NOAA Contract:
DG133W-02-CN-0089

Principal Investigators:

Witold F. Krajewski and Grzegorz J. Ciach
IIHR-Hydroscience & Engineering
The University of Iowa
Iowa City, Iowa 52242

Report Authors:

Witold F. Krajewski, Grzegorz J. Ciach, and Gabriele Villarini
IIHR-Hydroscience & Engineering
The University of Iowa

October 2005
Revised February 2006

EXECUTIVE SUMMARY

The report describes progress made towards developing a scientifically rigorous methodology for operational probabilistic quantitative precipitation estimation (PQPE) for hydrologic applications. The methodology will be based on the WSR-88D measurements complemented with rain gauge and satellite data. It is flexible enough to allow a smooth transition to the polarimetric era after the planned upgrade of the operational network of radars. The overall strategy is to demonstrate hydrologic utility of the probabilistic information of the precipitation estimates. This involves two major elements (1) developing a theoretical and operational framework for probabilistic radar-rainfall estimation; and (2) connecting the PQPE input with a hydrologic application. This report documents initial progress made in both elements.

The authors define a radar PQPE product as a set of situation-dependent parameter values in a model describing the probability distributions of the uncertainties in the radar-estimated rainfall. The distributions quantify the available probabilistic knowledge about the true spatial rainfall that is likely, given current radar measurements and other available information. The model parameter values determine unambiguously the uncertainty distributions for each operationally useful distance from the radar and spatiotemporal averaging scale. This allows generating different user-specific outputs demanded by various operational applications. Among these outputs are the uncertainty bounds and probabilities of exceedence. Generating an ensemble of the probable rainfall maps to provide the input for the ensemble forecasting schemes is also possible. The report presents early results of the model formulation.

The hydrologic utility of the PQPE methodology will be demonstrated using the flash flood forecasting problem. This part of the project is performed in close collaboration with the Hydrologic Research Center (HRC). The demonstration is limited geographically to the Oklahoma region. This report documents developments leading to PQPE application in a Flash Flood Guidance and Monitoring (FFGM) system. The authors present uncertainty analysis of the Thresh-R model which is the basis for FFGM and of the soil moisture accounting model. The early results also include effect of the uncertainty in the rainfall input via an example of ensemble PQPE simulation.

Useful Acronyms

ABRFC	Arkansas Basin River Forecast Center
CDP	conditional distribution of precipitation
CSI	Critical Success Index
DHR	Digital Hybrid Scan Reflectivity
DPA	Digital Precipitation Array
FAR	False Alarm Ratio
FFG	Flash Flood Guidance
FFMP	Flash Flood Monitoring and Prediction
HL	Hydrologic Laboratory
HRC	Hydrologic Research Center
HRAP	Hydrologic Rainfall Analysis Project
KDP	specific differential phase shift
KINX	WSR-88D in Tulsa, OK
KTLX	WSR-88D in Twin Lakes, OK
MAP	Mean Area Precipitation
MFB	Mean-field-bias
MPE	Multisensor Precipitation Estimation
NCDC	National Climatic Data Center
NSSL	National Severe Storms Laboratory
NWS	National Weather Service
PED	product-error-driven
POD	Probability of Detection
PPS	Precipitation Processing System
PQPE	Probabilistic Quantitative Precipitation Estimation
RFC	River Forecast Center
SOW	Statement of Work
WFO	Weather Forecast Office
WSR-88D	Weather Surveillance Radar - Doppler
Z	radar reflectivity
ZDR	differential reflectivity
CSSA	Convective/Stratiform Separation Algorithm
REC	Radar Echo Classifier
RCA	Range Correction Algorithm
EPPS	Enhanced PPS
HCA	Hydrometeor Classification Algorithm
EPRE	Enhanced Preprocessing

TABLE OF CONTENTS

A. BACKGROUND INFORMATION

Hydrologic forecasting and water resources services performed for the public by the National Weather Service (NWS) require decision making in presence of uncertainty due to limitation in our understanding of nature, available information, and predictability of natural phenomena. High space and time resolution precipitation estimates are the main input for many of the forecasting and decision support models and systems. These estimates are based on information from the network of weather radars WSR-88D combined with rain gauge and satellite data (e.g. Fread et al. 1995; Stallings and Wenzel 1995). The current operational NWS multi-sensor rainfall algorithms produce only deterministic fields of precipitation intensity and accumulations (e.g. Fulton et al. 1998). The operationally provided rainfall products are deterministic in the sense that, while significant errors associated with these products are widely acknowledged, no quantitative information on their magnitude associated with the products is routinely available. Users of these products would be better able to make informed decisions if they knew not only the best rainfall estimate but also the associated uncertainty and/or range that most likely includes the actual amount of rainfall that occurred.

The Office of Hydrologic Development of the NWS intends to address this shortcoming of the existing algorithms by preparing a comprehensive plan for development of a new generation of algorithms for the precipitation estimation. These algorithms are referred to as *probabilistic quantitative precipitation estimation*, or PQPE. Krajewski and Ciach (2003) developed a comprehensive plan for nation-wide development of the PQPE algorithms. Their report lays out an early formulation of the problem, identifies conceptual, methodological and technological issues, and proposes a feasible plan of action. However, because the plan calls for considerable expenditures of resources, the PQPE Advisory Team suggested preceding it with a geographically focused effort of an end-to-end demonstration of the utility of the PQPE approach. In response, Krajewski et al. (2003) formulated a plan for developing such a demonstration.

In this report we present first results of an extensive data analysis and development of an initial version of ensemble generator that could be used operationally to provide users with plausible realizations of rainfall fields. Following Krajewski et al. (2003), we describe (1) a formulation of the radar-only PQPE algorithm; (2) the corresponding extensive data analyses and identification of an appropriate model and estimation of its parameters based on actual data from Oklahoma; and (3) the ensemble generator and examples of its workings with potential operational use.

B. FORMULATION OF THE PQPE METHODOLOGY

During the project, we continued our analysis and refinement of the methodological framework for the PQPE problem that was initiated in Phase I (Krajewski and Ciach 2003). For the sake of completeness of this report, we briefly summarize the proposed methodology for the PQPE algorithm development as we understand it now.

B.1. Basic Definitions

The four fundamental notions defined below are used throughout this report:

- *True rainfall*: The amount of rain-water that has fallen on a specified area in a specified time-interval.
- *Radar-rainfall (RR)*: An approximation of the true rainfall based on radar data corresponding to the same spatio-temporal domain.
- *RR uncertainties*: All systematic and random discrepancies between RR and the corresponding true rainfall.
- *Ground reference (GR)*: Estimates of the area-averaged rainfall accumulations based on rain-gauge data that are used to evaluate RR products.

B.2. Problem Description

Progressive evolution of the operational RR products has been guided by the attempts to quantify and to reduce the uncertainties in the RR estimates. The currently existing RR maps produced operationally by the NWS (the Stage II and III products) are just arrays of numbers describing the spatial distribution of approximate rainfall accumulation values that are obtained based on the WSR-88D reflectivity measurements corrected with the available concurrent rain-gauge data. Application of the term "quantitative precipitation estimates" QPE to such products implies that the maps are completed with quantitative information about the product uncertainties. Without such information about the relation of the RR product to the corresponding true rainfall, both the notion of "quantitative" and the mathematical term "estimation" would be meaningless in this context. However, despite a wide use of this term, the operational QPE products are devoid of their uncertainty information. We believe that the development of the probabilistic quantitative precipitation estimation (PQPE) products based on sound empirical evidence will be a comprehensive solution for this pathological situation.

The probabilistic products, both in meteorology and hydrology, convey the inferred information about the unknown true value of a physical quantity in terms of its probability distribution rather than its one "best" estimate (e.g. Krzysztofowicz 2001). Thus, the radar PQPE product can be mathematically defined through the conditional probability distributions of the likely true rainfall, given the current radar measurements and other available information. These distributions can be determined by specific parameter values of a general uncertainty distribution model developed in this project. The model parameters have to determine

unambiguously the uncertainty distributions of given RR estimates in different rainfall regimes for each operationally useful distance from the radar and spatio-temporal averaging scale. From such a general PQPE product, one can directly derive any specific uncertainty characteristics (for example, the RR expectation, standard errors, probabilities of exceedence, or an ensemble of probable rainfall maps) that can be required for different operational applications.

B.3. Basic Requirements

During the discussions with the panel of experts engaged in the Phase I of this project (Krajewski and Ciach 2003), it was agreed that any method that will be applied to generate the PQPE products has to satisfy several key requirements. These requirements were further discussed, analyzed and refined in the course of the Phase II of the project. We summarize them briefly below:

1. The method has to be empirically "verifiable." Conditions have to be assured to systematically evaluate the degree of agreement between the PQPE results and the RR uncertainties estimated based on reliable GR in selected "validation sites."

2. The method has to be adjustable to different synoptic and topographical situations, and to the changing operational environment, by its model parameter calibration using available information.

3. The method has to account for the spatio-temporal dependencies in the errors process to provide the PQPE products over a broad range of spatial and temporal scales used in different hydrological applications.

4. The method has to work with the current reflectivity-only WSR-88D algorithms, the multi-parameter (MPE) algorithms using the available concurrent rain-gauge and satellite data, and the polarimetric algorithms (using differential reflectivity and differential phase-shift) available operationally after the upcoming upgrades of the WSR-88D radars.

5. The method has to provide the PQPE products in a format appropriate for their efficient usage in different hydrological applications.

B.4. Development of the PQPE Algorithm

During the previous phases of this project, it has been agreed that the product-error-driven (PED) modeling approach for the PQPE algorithm, described in our reports for the Phase1 and Phase 2, will be developed using a fully empirically-based framework. This decision acknowledges the obvious fact that building a PQPE algorithm has to be preceded by the development of a realistic and parsimonious mathematical model of RR uncertainties underlying the probabilistic nature of RR products. Only a thorough and comprehensive data analysis can result in the identification of such a realistic model suitable for the PQPE applications. We describe the data preparation, analysis, and model development in the following sections of the

report. First, we describe development of the PED modeling methodology. In Appendix A we present a methodology we propose for the problem of filtering the point vs. area process differences as they pertain to the Ground Reference problem (Habib et al. 2004). In Appendix B we address the issue of estimating small-scale rainfall correlation based on the Piconet data (Ciach and Krajewski 2005).

B.4.1. Development of the PED Modeling Methodology

There are many sources of errors in RR products and we discussed them in the Phase 1 report. The PED approach focuses on the combined effect of all the errors, its modeling, and estimation of the model parameters. This follows the fact that one cannot delineate the separate effects using the available measurable quantities. In practice, only the combined effect on the RR estimates can be measured and quantified. Our objective is to create a flexible parameterized mathematical model of the relation between the RR product values and the corresponding True Rainfall conditioned on different situations. The four conditions that we plan to quantify are the distance from the radar, space-time averaging scale, rainfall regime, and the PPS setup. In the PQPE algorithm, this model will be used to quantify the probability distributions of the probable True Rainfall, given the RR value and the other abovementioned conditions.

B.4.1.1. *General Structure of the Model*

The relationships between RR and the corresponding truth can be described by the family of the conditional bivariate frequency distributions that we call the "true verification distributions" (TVD):

$$(R_a , R_r)_{L,T,d,S} = f(R_a , R_r \mid L, T, d, S) \quad (1)$$

where R_a and R_r are the corresponding (concurrent and collocated) True Rainfall and RR values, respectively, L is the spatial averaging scale, T is the temporal scale (accumulation interval), d is the distance from the radar station, and S denotes the type of the precipitation system (rain regime). In principle, these distributions can be retrieved from the radar-gauge data samples, if additional information on the rainfall variability is available (see section B.4.3 below).

To simplify the notation, we can focus on one spatiotemporal resolution (L, T), distance (d) from the radar and rain regime (S). To model the (R_a , R_r) distribution for these specified conditions, we claim it is convenient to use the following functional-statistical representation:

$$R_a = h(R_r)\, e(R_r) \quad (2)$$

where $h(\cdot)$ is a deterministic distortion function, and e is a random variable representing the random uncertainties that we call the multiplicative random uncertainty factor. If parametric models of the deterministic function, $h(R_r)$, and the stochastic function, $e(R_r)$, are identified and its parameter estimates conditioned on a specific situation are known, this representation prescribes a way in which the ensembles of probable True Rainfall values, or only its selected statistical characteristics required by the users, can be generated for each given value of RR.

B.4.1.2. *Main Elements of the Model*

Because all systematic biases can be described by the deterministic distortion function, we can assume without any loss of generality that the mean of the random uncertainty factor is always equal to unity ($E\{e\}=1$). This allows for a rigorous definition of the $h(\cdot)$ function based on the general regression formula:

$$h(x) = E\{R_a \mid R_r=x\}, \tag{3}$$

which, in practice, can be identified and estimated using any version of the nonparametric regression apparatus (e.g. Hardle 1990; Simonoff 1996).

Although the mean of the multiplicative random uncertainty factor, $E\{e(R_r)\}$, is equal to unity for each value of R_r, its distribution can vary with R_r. The first step in identifying this dependence is to estimate the variance of $e(R_r)$ as a function of R_r. This can be done in a similar way as estimating the $h(R_r)$ function. An example of such a procedure is shown in the section B.4.1.3 below.

Next, we have to find a suitable parametric model for the $e(R_r)$ distributions. This can be achieved based on extensive data analysis by examining the shapes of the actual $e(R_r)$ distributions under different values of the conditioning factors. Since the extreme rainfall events are the most important in hydrological practice, it is essential that the selected probability distribution model describes the uncertainty distribution tails with a reasonable accuracy. Examples of the models that have distinctly different tails are the gamma, lognormal and beta distributions. Each of them can lead to different decisions based on the PQPE results. The goodness-of-fit of these and perhaps several other models will have to be tested on the large data sample before a justified choice can be made.

Once parametric models of the $h(R_r)$ function and the $e(R_r)$ variable (or the family of random variables indexed by R_r) are identified, the dependence of their parameters on the averaging scale (L, T), distance from the radar (d) and rain regime (S) can be estimated based on the family of the verification distributions (estimated bivariate distributions of RR and the corresponding True Rainfall):

$$(R_r\ ,\ R_a)_{Ln,Tn,d,S}\ ,\ \ n=1,\ 2,\ \ldots\ ,\ N_{max} \tag{4}$$

where the distributions are sampled for several spatio-temporal scales that are multiples of the original RR product scale. Spatio-temporal dependencies in the model parameters can then be modeled to reproduce the dependence of these conditional model parameter estimates on the discrete series of scales (A_n ,T_n), for each given distance from the radar (d) and precipitation regime (S).

It is still unclear to us how to stratify the data sample according to the precipitation regime (S) so that this information is meaningful for the PQPE methodology. The appropriate classification has to be based on data that are readily operationally available during the PPS processing, preferably the radar data alone. In addition, it should exhibit distinct differences in the PED model parameter values for the different regimes. One of such classification schemes by Steiner

et al. (1995) has been investigated by Ciach et al. (1997). Our results indicated that its effects on the RR estimation algorithm are practically the same as the stratification of the data sample according to different RR values. Consequently, using this specific precipitation regime classification can only complicate the PQPE algorithm unnecessarily without adding any value to it. A classification of the synoptic situation, or some other information (e.g., the zero isotherm level) based on the operational weather forecasts could perhaps be a better alternative to the schemes using the radar data only. However, the best way to use this external information remains to be investigated.

Obviously, the successful development of operationally applicable parametric models of the $h(R_r)$ function and the $e(R_r)$ variable will most likely require a number of generalizations and simplifications in the mathematical description of the abovementioned dependences. The specific formulas will be identified during the extensive analysis of large data samples described later in the report.

B.4.1.3. *Preliminary Analysis of RR Error Structure*

In the Phase 3 of this project, we performed a preliminary study of the basic elements of the RR error structure. It is an extension of our first analysis that we described in the Phase 1 report. This analysis is based on a relatively small data sample of 50 rainy days and its main purpose was to develop and test the first version of the data processing and functional estimation tools that will be applied to the large samples of the operational RR products. The radar data from the Tulsa, Oklahoma, NEXRAD station (KINX) were quality controlled and converted into hourly accumulations in polar grids over 23 surrounding rain gauge stations (Vignal and Krajewski 2001; Krajewski and Vignal 2001).

Because there are two variables (R_a , R_r), there exist two mathematically equivalent ways to represent their joint distribution in the form of a functional-statistical relationship between these variables. The first form is defined in Equation (2), whereas the second is obtained by switching the R_a and R_r variables in this Equation. Although the second representation is more suitable for characterizing the RR error structure than for building the PQPE ensemble generator, we used it in this preliminary analysis to obtain results that are formally comparable with the results that we had obtained previously. From the point of view of the estimation technique, both representations are exactly the same and the same data processing tools can be applied to both of them. However, to avoid confusion, we denote the equivalent deterministic and random components as h_1 and e_1, respectively. Additionally, we simplified the analysis by assuming the raingauge rainfall accumulations, R_g, for the approximations of the true rainfall R_a. In fact, using our area-point error filtering procedure (see section B.4.2) was impossible for this sample due to the lack of the corresponding small-scale rainfall variability data.

Using the 50-storm data sample, we estimated the deterministic error function, $h_1(\cdot)$, and the variance of the multiplicative random error, $e_1(\cdot)$, as functions of the accumulation time. At this stage, we did not consider the dependences on the spatial scale, distance from the radar, or the rain regime. The temporal dependences in the RR error process were estimated for five accumulation intervals: 1, 3, 6, 12, and 24 hours. The deterministic distortion function was estimated using the following scheme of moving-window averaging:

$$h_1(r) \approx < R_r \mid r-u \le R_g \le r+u > \qquad (5)$$

where R_g is the rain gauge rainfall accumulation and u is the averaging window size. The window size was increased with R_g to compensate for the decreasing number of data points. These functions, for the five time scales, are shown in Figure 1.

The results in Figure 1 show that the systematic distortion component is a nonlinear function of the True Rainfall. This function is a way to quantify the conditional biases in different RR products that have been qualitatively demonstrated long time ago by Austin (1987) and investigated using an idealized analytical model by Ciach et al. (2000). For the larger accumulation intervals (6, 12 and 24 hours), these conditional biases are relatively small and invariant with respect to the time-scale. The outstanding results for the 1-hour and 3-hour time-scales might be the effect of large rain gauge representativeness errors, however, they might as well indicate a distinctly different uncertainty structure at the short scales. This question requires more extensive analyses using the area-point error filtering method described in Appendix A.

The standard deviation of the random error factor as a function of the rain gauge rainfall accumulation for the same five accumulation intervals is shown in Figure 2. The $e_1(\cdot)$ variances, σ_{e1}^2, as a function of R_g were estimated in a similar way as the $h_1(\cdot)$ functions:

$$\sigma_{e1}^2(r) \approx \langle (e_1(R_g)-1)^2 \mid r-u \le R_g \le r+u \rangle \qquad (6)$$

using the same moving-averaging scheme with variable window size.

The results in Figure 2 show that, for each of the five accumulation intervals, the standard deviation of the multiplicative random uncertainty factor decreases rapidly with increasing rainfall and then stabilizes at the level of about 30%. The estimates of the random component seem to be less sensitive to the shorter time-scales than the estimates of the systematic distortion function. This invariance, if confirmed on the large data sample that we currently prepare, can be a good basis to reduce the number of parameters of the final PED model that will be used for the PQPE algorithm.

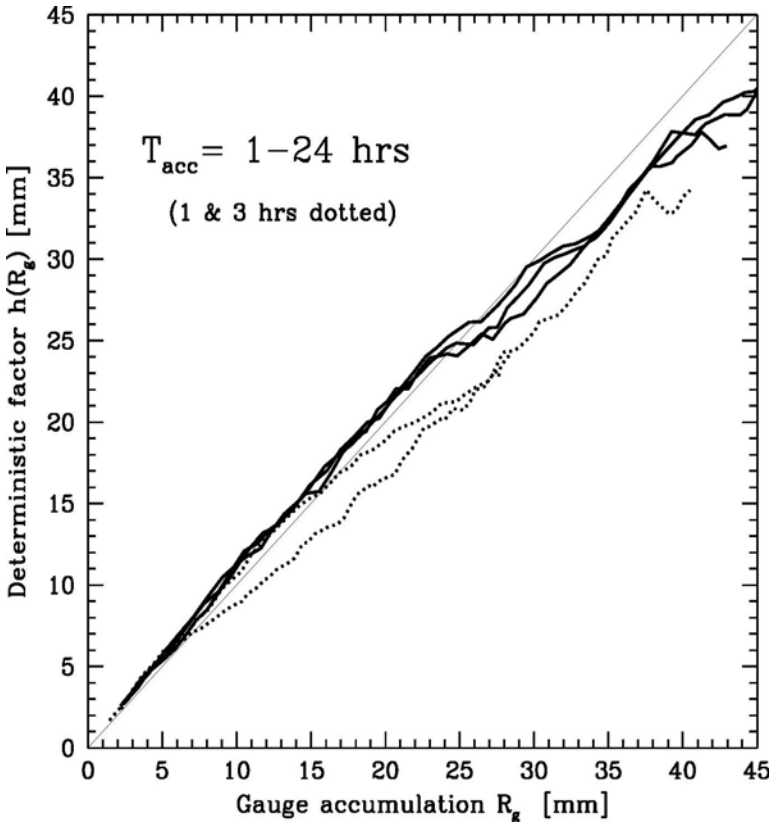

Figure 1. Systematic distortions, *h*, as functions of True Rainfall for the five accumulation intervals.

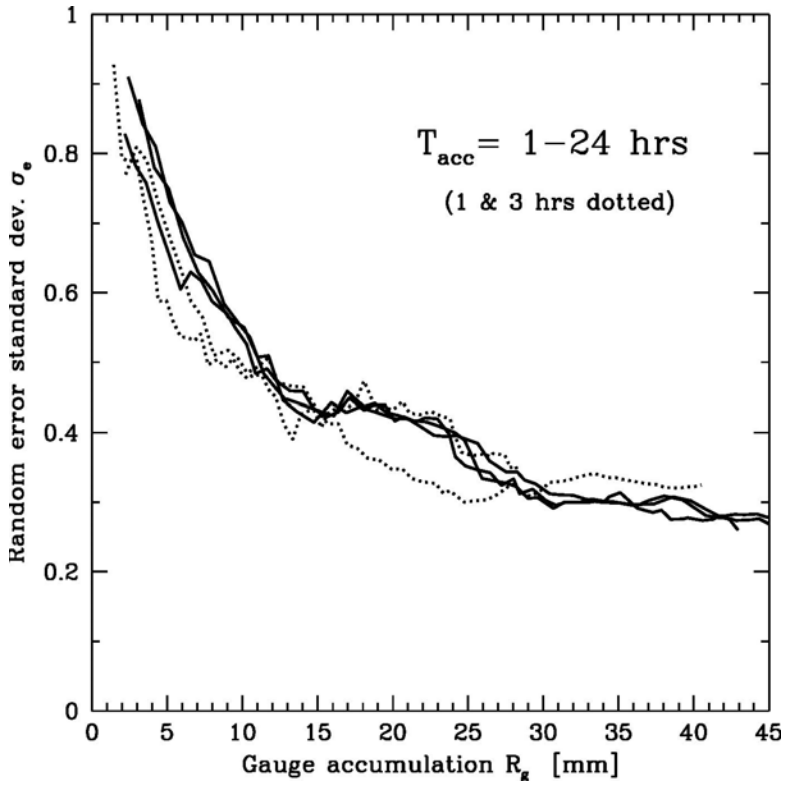

Figure 2. Standard deviations of the multiplicative random error factor, *e*, as functions of True Rainfall for the five accumulation intervals.

Note that the results shown in Figures 1 and 2 are based on a research sample that was carefully selected and quality controlled. A well tested and sample-calibrated ground clutter and AP reduction procedure based on a neural-network algorithm was applied prior to the Z-R conversion (Krajewski and Vignal 2001). The coordinate transformation errors are not present because the RR estimates are only in the polar coordinates. Additionally, a correction of the vertical profile of reflectivity (VPR) reduced the RR errors considerably at larger distances (Vignal and Krajewski 2001). Consequently, the uncertainties presented above can be significantly smaller than what we expect to obtain based on the operational PPS products. Therefore, it is essential to repeat the analysis on the large sample of the PPS products that we described in section C.1.

B.4.1.4. *Two Idealized Implementations*

One of the most difficult elements of the PQPE methodology concerns including the spatial and temporal dependences that exist in the RR uncertainty process into the probabilistic model that we create using the PED approach. In the course of developing a viable technique to treat this problem, we started with two idealized implementations of the PQPE algorithm that are based on the following simple model of the (R_a , R_r) distribution:

$$R_a = R_r \, e \tag{7}$$

where the random uncertainty factor, e, is lognormally distributed and does not depend on the RR value (a multiplicative homoscedastic model). Both algorithms are designed to simulate ensembles of the probable true rainfall conditioned on the RR values obtained from the radar data. The first algorithm includes the temporal dependences in the uncertainty process, whereas the second algorithm generates ensembles of spatially correlated uncertainty fields. These dependences in the e variable were modeled based on a meta-Gaussian model that starts with a time series (or spatial field) of the uncorrelated standard normal white noise. Next, this variable is correlated in time (or space) using weighted moving-window averaging with a specified averaging mask, and the outcomes are transformed into the positively defined random process through the exponential transformation. The parameters of this transformation are such that the resulting variable has the mean equal to unity and the specified variance.

The temporally correlated 1-D version of this simple PQPE algorithm was applied to generate the ensembles of time-series of probable true rainfall for the lumped flash flood forecasting model that we implemented and upgraded into probabilistic framework with the help of the Hydrologic Research Center. This numerical experiment is a part of the PQPE project and we described its application to a flash-flood prediction problem in Krajewski et al. (2003). The flowchart of this algorithm consists of the following steps:

1. Generate a one-dimensional array of independent standard normal deviates.
2. Apply the weighted averaging moving-window to the array.
3. Apply the exponential transformation to the smoothed array.

This procedure generates one time-series of the time-correlated meta-Gaussian uncertainty process. It is repeated to obtain the required number of the ensemble members. The weighted moving-window averaging can, in principle, be performed using any averaging mask. This allows fairly flexible adjustment of the simulated temporal uncertainty structure to the empirical estimates that we will obtain from the data analysis. At this stage, we used a simple polynomial mask for this smoothing. The parameters controlling the algorithm outcomes are:

1. The number of realizations in the ensemble.
2. The length of the simulated time-series.
3. The size and shape of the smoothing mask.
4. The standard deviation of the uncertainty factor.

The 1-D algorithm described above is fast and enables generating large ensembles consisting of 10^5, or more, realizations for the probabilistic hydrological forecasting model. However, it can only be applied to the lumped rainfall-runoff models.

The spatially correlated 2-D version of the PQPE algorithm was applied to generate the ensembles of spatial fields of probable true rainfall. It can be applied to a distributed hydrological forecasting model, or used to compute the RR uncertainty bounds for different spatial scales. The flow-chart of this algorithm consists of the following steps:

1. Generate a 2-D array of independent standard normal deviates.
2. Apply the weighted moving-window averaging to the array.
3. Apply the exponential transformation to the smoothed array.

This procedure simulates one field of the space-correlated meta-Gaussian uncertainty process and is repeated to generate the required number of the ensemble members. The weighted moving-window averaging can, in principle, be performed using any averaging mask. It can also be adjusted to the empirical estimates that we plan to obtain from the data analysis. The parameters controlling the algorithm outcomes are:

1. The number of realizations in the ensemble.
2. The size of the simulated spatial array.
3. The size and shape of the smoothing mask.
4. The standard deviation of the uncertainty factor.

The 2-D algorithm described above is computationally demanding and the largest ensembles that we generated so far consisted of up to 10^3 realizations. However, it can be used in a much broader range of applications than the 1-D algorithm. Therefore, it will be the basis for the development of the full PQPE algorithm. During its further development, we will extend the simulation procedure to include the dependences of the uncertainty factor on the RR values and the distance from the radar, and implement different probability distribution models.

C. DATA ANALYSES

Development and testing of the above described PQPE framework requires massive radar and rain gauge data sets. As we argued in Krajewski and Ciach (2003) and Krajewski et al. (2003), for the PQPE algorithm to be meaningful it must be strongly based in empirical data. Fundamentally, two data types are required for this: (1) radar-rainfall estimates and (2) rain gauge data. While the PED approach relies on radar-rainfall products, it is important to begin with basic radar volume scan data. This way the calculated products are consistent. For the rain gauge data the basic issue is data quality (e.g. Steiner et al. 1999). Below we discuss our data collection and preparation.

C.1.1. Preparation of the Large Data Sample

To facilitate our studies we compiled a large sample of Level II radar reflectivity data acquired from the National Climatic Data Center (NCDC) for the Oklahoma City NEXRAD WSR-88D site (KTLX). The current sample covers the six-year period from January 1998 to December 2003. We used the Level II data as input to Build 4 of the Open Radar Product Generator (ORPG) Precipitation Processing System (PPS) software system and generate the Digital Precipitation Array (DPA) products which represent one-hour accumulations and are given on the Hydrologic Rainfall Analysis Project grid (Reed and Maidment 1999). For rain gauge data we use observations from three networks: (1) the Oklahoma Mesonet (we acquired the data from the JOSS Office in support of another NOAA-sponsored project); (2) the USDA Agricultural Research Service (ARS) Micronet (we acquired the data through the OHD), and (3) the University of Oklahoma Environmental Verification and Analysis Center (EVAC) Piconet located at the Oklahoma City International Airport (we established and maintained the network ourselves). We described these data sets in more detail below.

C.1.1.1. *The 6-year Sample of the KTLX Data*

This sample consists of about 350,000 data files and contains radar observations collected during the years of 1998-2003. We converted the files from the standard UNIX compression format that is still used by the NCDC to the much more efficient “bzip” format that is currently used as a standard by the OHD. We decided to adapt to this standard for its speed and efficient use of disk space.

We performed a quality check of all the files which revealed occasional errors in the file structure. About 7,000 (or 2%) of the files are affected by these errors. The impact of these errors on the automatic ORPG data processing has been tested and discussed with the OHD specialists. We excluded these suspect files from further processing.

C.1.1.2. *Oklahoma CS Mesonet Data*

The Oklahoma Mesonet (Brock et al. 1995), established and maintained by the Oklahoma Climate Survey, is known as perhaps the best regional network of surface meteorological sensors

in the country. The stations are fairly uniformly distributed over the state and thus the data cover the full range of distances from the KTLX radar.

The Mesonet rainfall data are provided as cumulative values, reset at the beginning of each day. For this dataset, a flagging system is associated with the data to indicate data quality. While preprocessing the data and organizing them as 5-minute rain gauge rainfall, we found about 100 entries of negative accumulation that were erroneously flagged as good quality data. We reported these cases to the Oklahoma Mesonet's quality-assurance team and they manually flagged these cases in their database. Based on our input they investigated the causes of the bad data and decided to reprocess their entire data set.

Within the KTLX umbrella, there are about 100 rain gauges, almost uniformly distributed, covering a wide range of distances (from about 25 km to the edge of the radar umbrella). Four of the Mesonet stations are within or very close to the Micronet network. The information obtainable from the flags in these Mesonet stations is useful during the QC of the Micronet data.

C.1.1.3. *Oklahoma ARS Micronet Data*

The network has been established by the Agricultural Research Service over an experimental watershed called Little Washita. We acquired the corresponding rain gauge data through the OHD. We received the 5-minute rain gauge accumulation data for 42 stations covering the Little Washita watershed located about 90 km south-west from the KTLX WSR-88D site (see Figure 3). One limitation of the analysis based on this ground reference is that it covers only a very limited range of the distances from the radar (from about 70 km to about 105 km).

The original ARS Micronet archive is organized in a very inefficient way and consists of about 640,000 small files. In addition, the timing convention in this archive is incompatible with our radar data. To make the data usable, we preprocessed the entire archive and converted it to 72 monthly files of the 5-minute rain gauge rainfall. During this preprocessing, we detected several errors in the data. These errors were corrected, whenever possible, or flagged as missing data records.

The ARS Micronet data we were provided did not have quality control (QC) flags. At this stage, we have not yet performed extensive QC on the rain gauge data. However, while organizing the data in 5-minute rain gauge rainfall, we checked for negative accumulations and we found more than 20 of such entries. We also found a case where high rainfall was detected by only one station but no rain was collected by any other gauge for few hours before and after. We have corrected these errors, whenever possible, or flagged them as missing data records.

After organizing the dataset in a more efficient way, we have georeferenced the rain gauges to the HRAP grid, and extracted the corresponding and collocated radar values. We have then accumulated the rain gauge rainfall to hourly scale to have the same temporal resolution of the RR estimates.

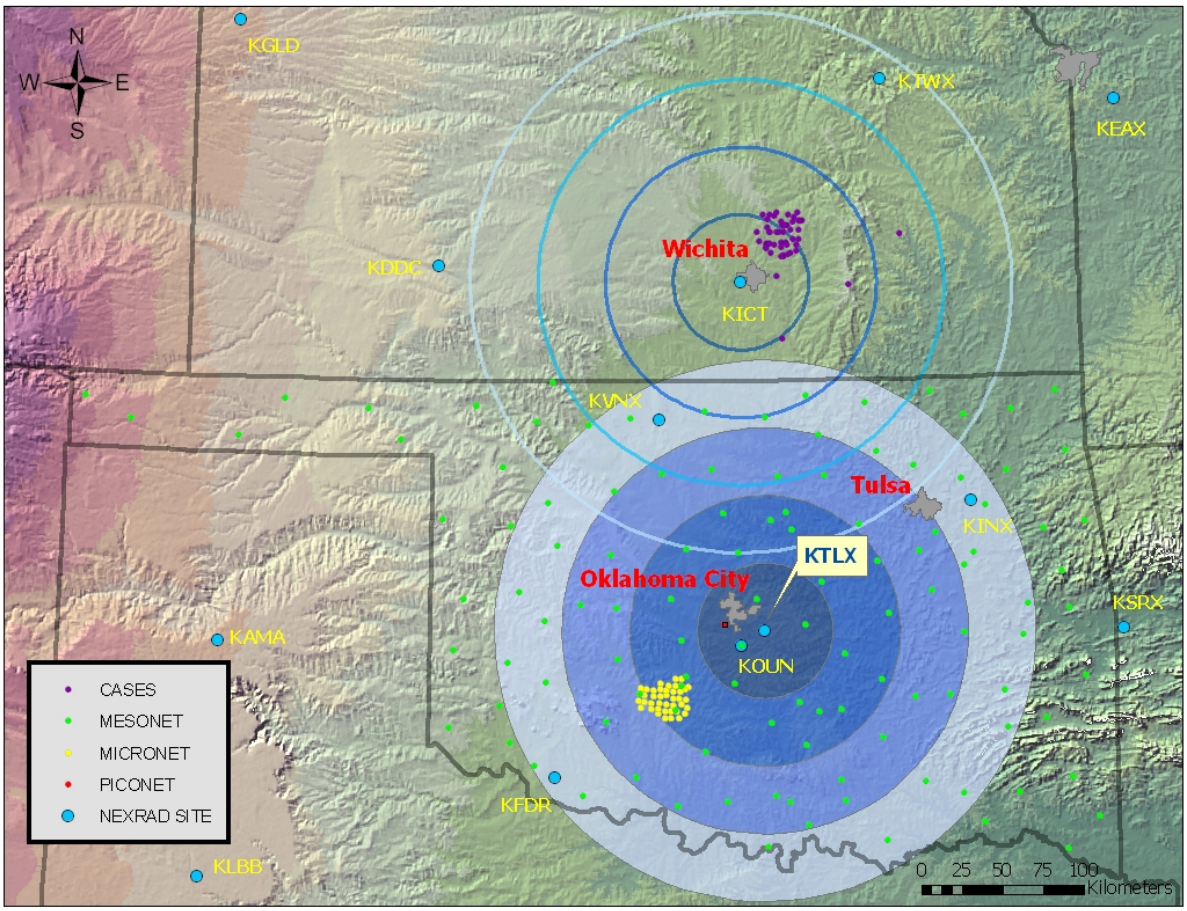

Figure 3. Schematic map of the Oklahoma/Kansas area and the relevant rain gauge networks. (We did not use data from the CASES network in this study.)

C.1.1.4. *Oklahoma EVAC Piconet Data*

The data sample that we used in this study was collected using a very dense network of raingauges designed, deployed and maintained by the Environmental Verification and Analysis Center (EVAC) at the Oklahoma University in cooperation with the hydrometeorology group of the IIHR–Hydroscience & Engineering at The University of Iowa. The EVAC PicoNet network consists of 25 stations (sites) covering an area of about 3 km by 3 km within the Will Rogers International Airport in Oklahoma City. The EVAC PicoNet was deployed in 2001 and comprises several unique features that facilitate direct measurements and comprehensive analyses of small-scale rainfall structure with an unprecedented accuracy.

The EVAC PicoNet stations are distributed over the flat and practically obstruction-free measurement area in the form of a fairly regular grid of 5 by 5 sites (Figure 4). Each station, apart from the central one, consists of two high-precision tipping-bucket rain gauges mounted about 2 m apart. An example of a typical PicoNet measurement point (Station 02) is shown in the inset of Figure 1. The central point (Station 13) consists of 5 rain gauges to reduce the local random errors so that this station can additionally serve as a test-bed to evaluate the accuracy of other rain gauge designs. The rain gauges are manufactured by MetOne Inc. and have the rainfall measurement resolution of 0.254 mm (0.01 inch) and the orifice diameter of 30.5 cm (12 inches). Static and dynamic calibrations of the gauges were performed with the help of the Oklahoma Climatological Survey using the equipment of the Oklahoma Mesonet Laboratory.

The rain gauges are equipped with individual event-counting data-loggers that record the tip-times with the resolution of 0.5 second and have the capacity of 8000 tips (HOBO loggers manufactured by Onset Computer Corporation). The loggers are mounted inside of the rain gauge tubes, which proved to be an effective way for protecting them from the elements. In our previous experiments (Ciach 2003) the loggers were exposed and, in about 15% of cases, the latch of their plastic enclosures broke after 1-2 years of field operation. This never happened during the four years of the PicoNet operation in its current setup.

The EVAC PicoNet data that are available for this study were collected during the warm months of 2001 and 2002. The 2001 data used here were collected from May 1 (the launching of the PicoNet) through October 16, whereas the 2002 data are from March 7 through November 6. The total gauge-averaged rainfall depth in this two-season sample is equal to 1252 mm (about 50 inches), from which 527 mm was collected during the 2001 season and 725 mm in the 2002 season. About 70% (857 mm) of this sample-total rainfall was produced by 32 events that yielded more than 10 mm of gauge-averaged rainfall depth.

A more informative way to describe the rainfall data sample is through use of the rainfall frequency distributions at different time-scales. The shapes of the distribution tails are especially important characteristics of the occurrence of extreme rainfall events. In the specific context of this study, the distribution tails have strong effect on the estimation of second order statistics such as the correlations considered here (Habib et al. 2001 and references therein).

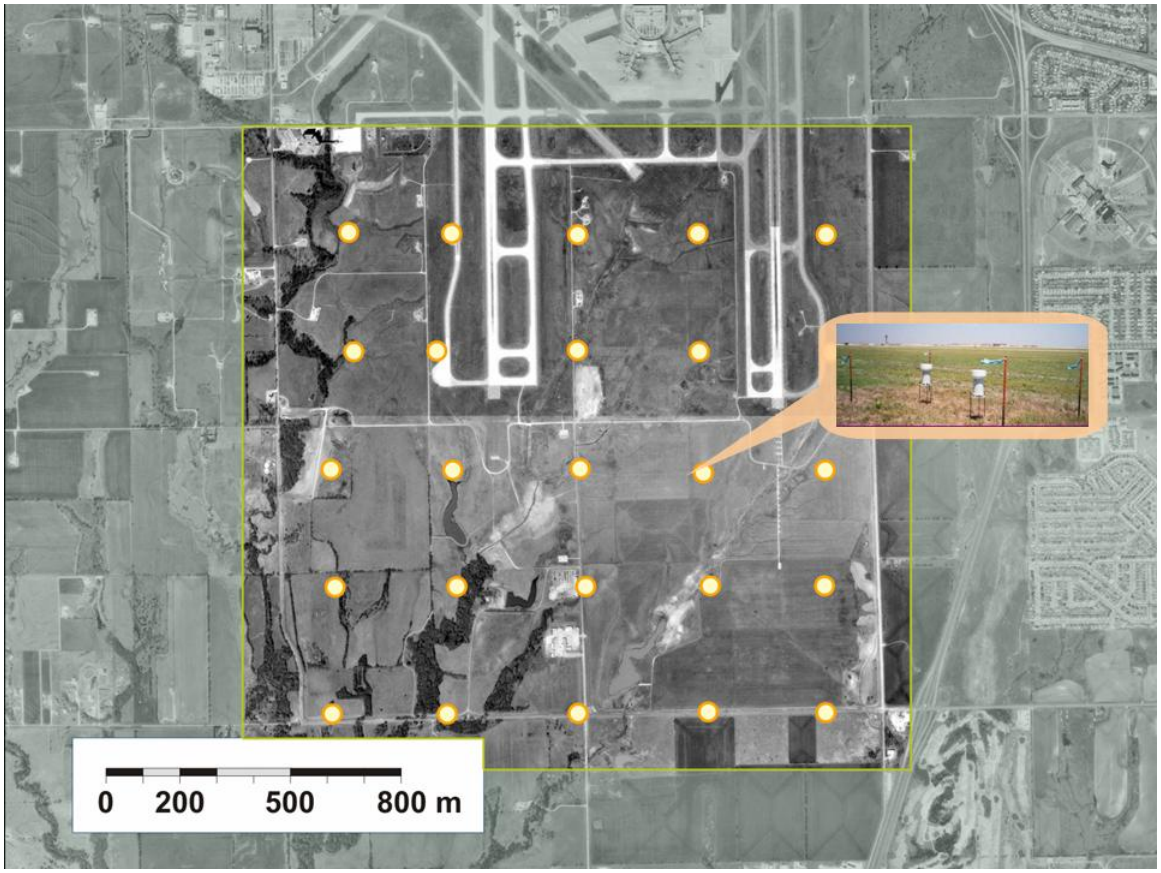

Figure 4. Schematic locations of the PicoNet rain gauges. The scale is not quite correct. The inset shows the double gauge configuration and installation.

C.1.2. Basic Data Characteristics

The results below are based mainly on the Micronet data and before data quality control.

C.1.2.1. *Seasonal Partitioning*

Since it is well known that seasonal variability strongly affect the uncertainty of radar-rainfall products, we performed a simple analysis of rain gauge data to determine a possible division of our sample into adequate periods that are more homogeneous in terms of their statistical characteristics. As an index, we used the rain-weighted temperatures (T_{rw}) for each month, defined as:

$$T_{rw} = \frac{\sum_i R_i T_i}{\sum_i R_i}, \tag{8}$$

where R_i and T_i are the rainfall and air temperature measured at the i^{th} station.

Figure 5 shows the monthly T_{rw} averaged over the six years of data. Based on this plot, we have decided to divide the dataset into three season: cold (January, February, March, November and December), where the average T_{rw} is below or around 10°C; warm (April, May and October), where the average T_{rw} is between 15 and 20°C; hot (June, July, August, September), where the average T_{rw} is above 20°C.

In Figure 6 a different characteristic distribution of the rain-weighted temperature is evident: the cold season is positively skewed, the warm season is more symmetrical, while the hot season is negatively skewed.

C.1.2.2. *General Data Features*

Figure 7 shows the time series of the monthly accumulation from gauge and radar estimates. It is possible to notice how the radar tends to have larger values than the rain gauge. This feature is more evident from Figure 8, where we show the overall bias, defined as:

$$bias = \frac{\sum_{i=1}^{n} G_i}{\sum_{i=1}^{n} R_i} \tag{9}$$

where G_i is the rain from the i^{th} gauge and R_i is the corresponding value from the radar.

In fact notice how, for most of the months, the value of the bias is smaller than 1. It seems that for some months, the value of the bias is very large. However, looking at Figure 7, we notice how these cases correspond to months with low accumulation. Overall, there is a good agreement between radar and gauge estimates, as illustrated by high correlation coefficient values (Figure 8).

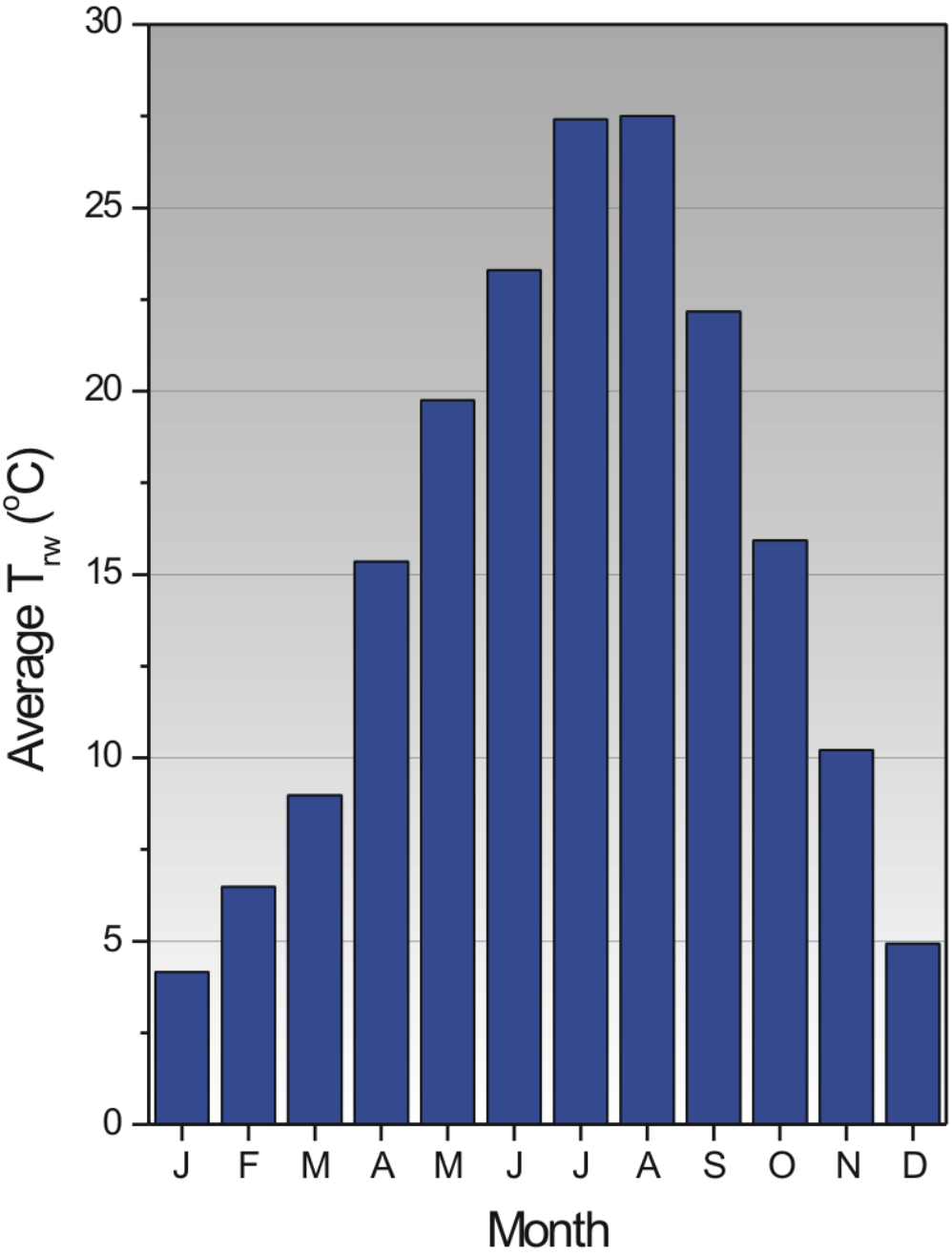

Figure 5. Histogram of the rain-weighted temperature (T_{rw}) according to month, averaged over the six-year period under study.

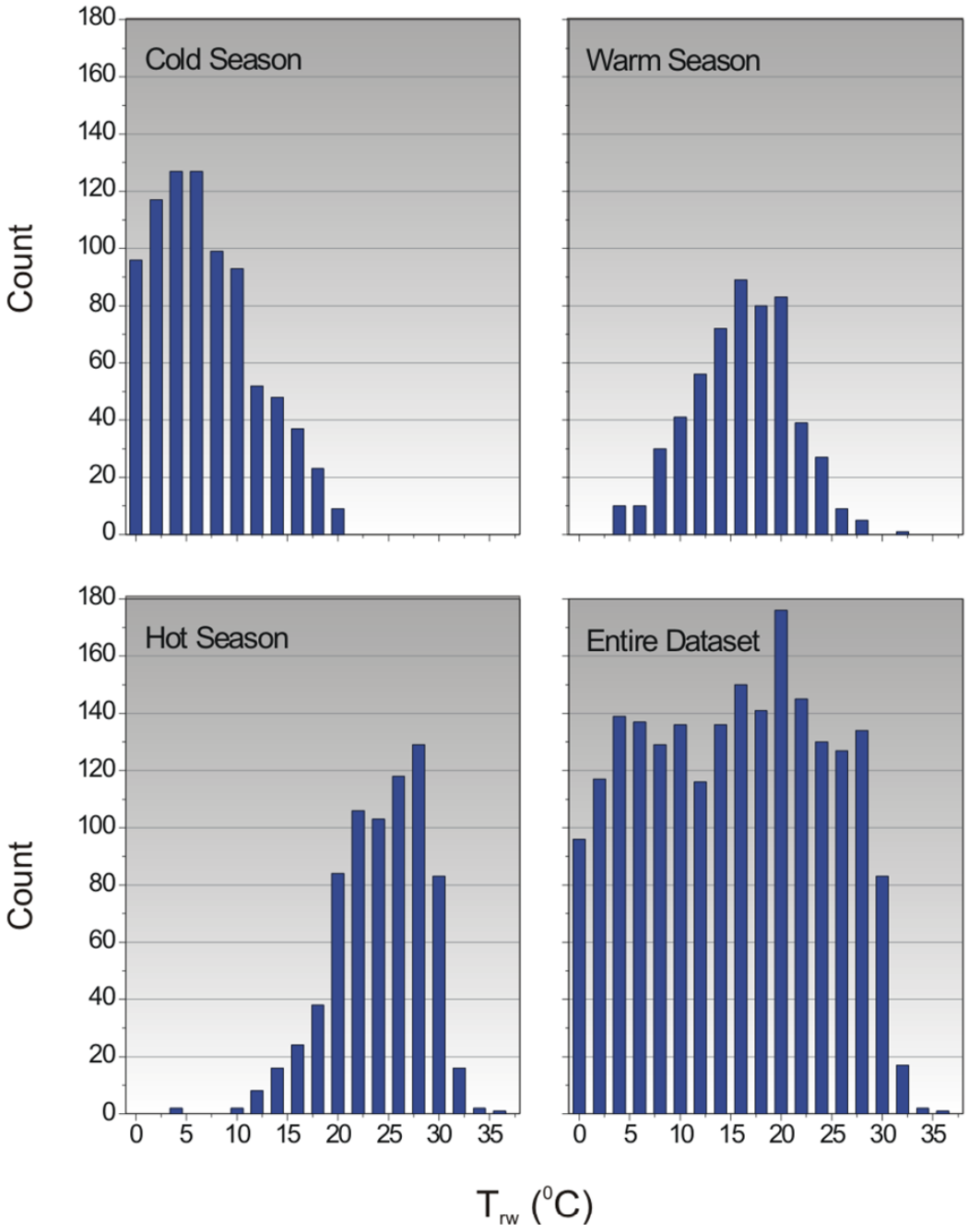

Figure 6. Histogram of the rain-weighted temperatures (T_{rw}) for the three seasons and for the entire dataset. Each of the seasons is characterized by a different behavior: the cold season is positively skewed, the warm season is more symmetrical while the hot season is negatively skewed.

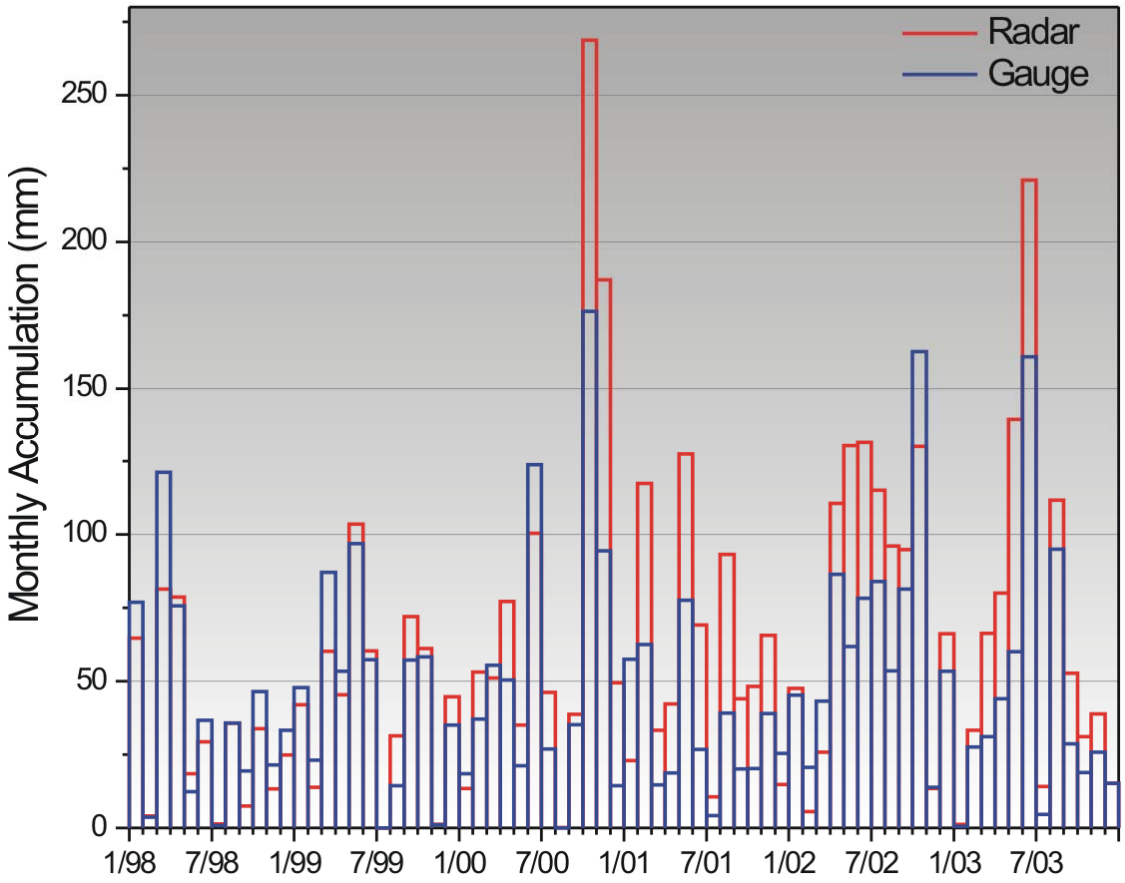

Figure 7. Time series of the monthly accumulation for the rain gauges and the radar for the six-year study period. These values have to be considered as an underestimation of the true value because of the missing data.

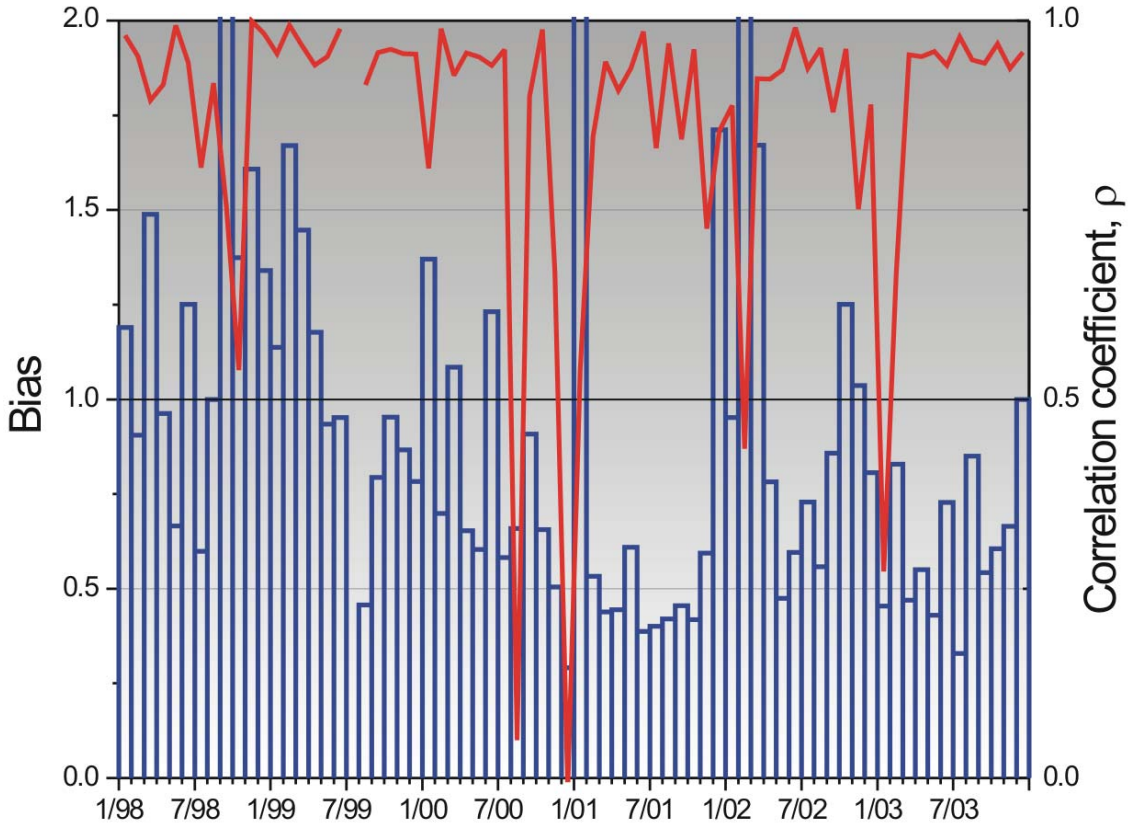

Figure 8. Time series of the bias (blue bars) and correlation coefficient (red solid line) for the six-year period under study.

To characterize the variability of rainfall in our study we calculated spatial and temporal scale correlations. Figures 9 and 10 show the correlations and the correlation function estimated from the rain gauge rainfall and the collocated RR estimated for the hourly time scale. To help quantify the variability we fit a three-parameter exponential model:

$$\rho(d) = \theta_0 \exp\left[-\left(\frac{d}{\theta_1} \right)^{\theta_2} \right] \tag{10}$$

where d is the separation distance, θ_0 is the correlation at $d = 0$, θ_1 the correlation distance and θ_2 the shape factor. We obtained the parameters using a two-step methodology. First, a global grid search of the parameter space is performed. Then, the results are used as initial values for the Levenberg-Marquardt algorithm. Notice how θ_1 is always bigger for the gauge correlation, with the exception of the hot season. These results are in agreement with those by Gebremichael and Krajewski (2004). In the same figures, we have also plotted the correlation function estimated for the EVAC Piconet network (Ciach and Krajewski 2005). We will discuss this result later.

C.1.2.3. *Overall Bias*

Before estimating the deterministic and the random components, we have removed the bias from the radar data. According to our partitioning, we have four different values, three for the three seasons and one for the entire dataset:

- Cold season: 0.90
- Warm season: 0.75
- Hot season: 0.72
- Whole dataset: 0.78

According to our definition of the bias, these preliminary results based on Micronet data prior to data quality control imply that there is an overall overestimation by the radar, more evident during the warm and hot seasons. It is difficult to ascribe it to a specific reason (e.g. radar miscalibration, the OKC radar is known as “hot”); in addition, we should point out that for the above analysis we used rain gauge data before quality control.

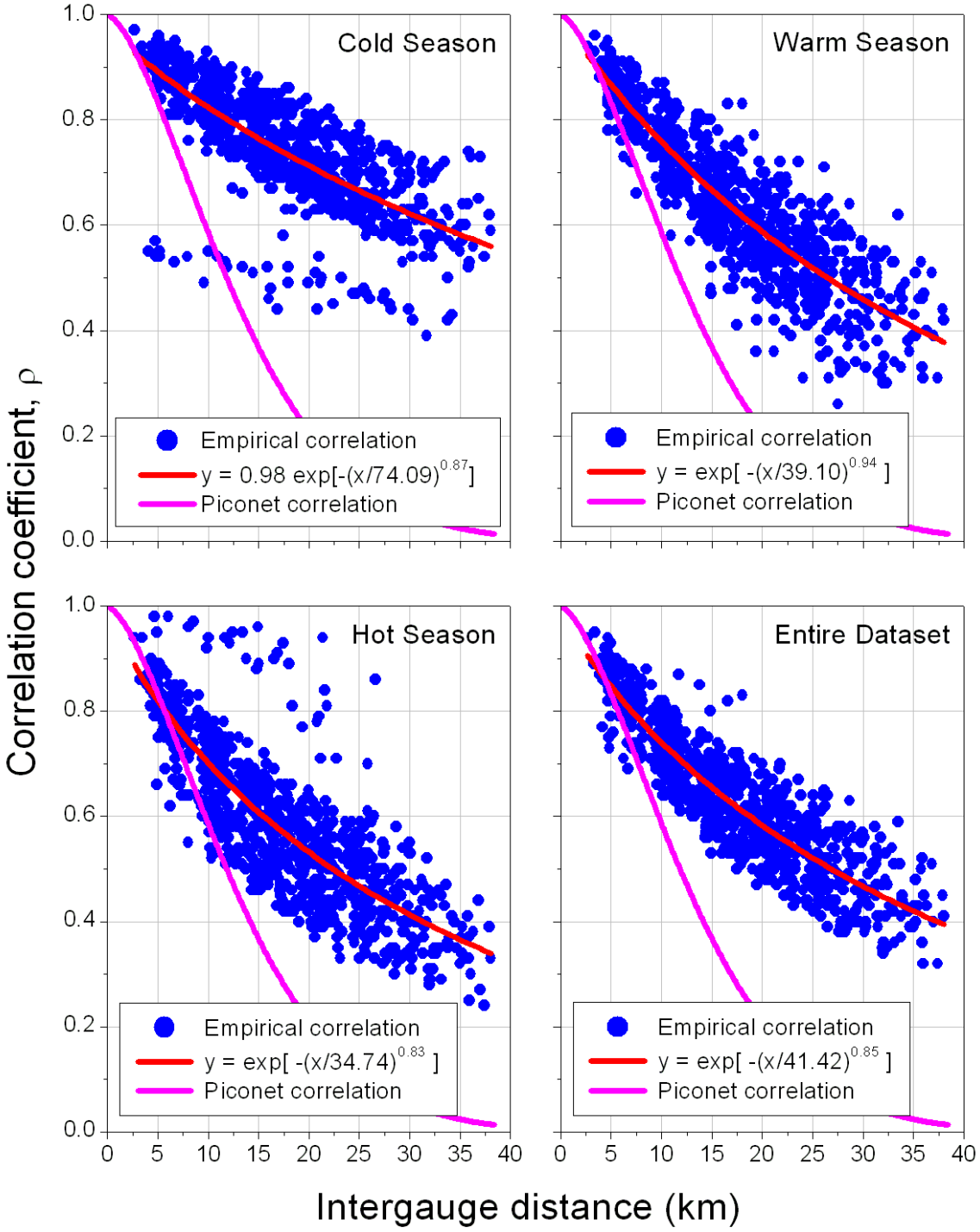

Figure 9. Spatial correlation of the Micronet rain gauges for the three seasons and the whole dataset. The solid red lines are obtained fitting the data with a three-parameter exponential function; the solid magenta line is from the spatial correlation function estimated by Ciach and Krajewski (2005) for the Piconet rain gauge network.

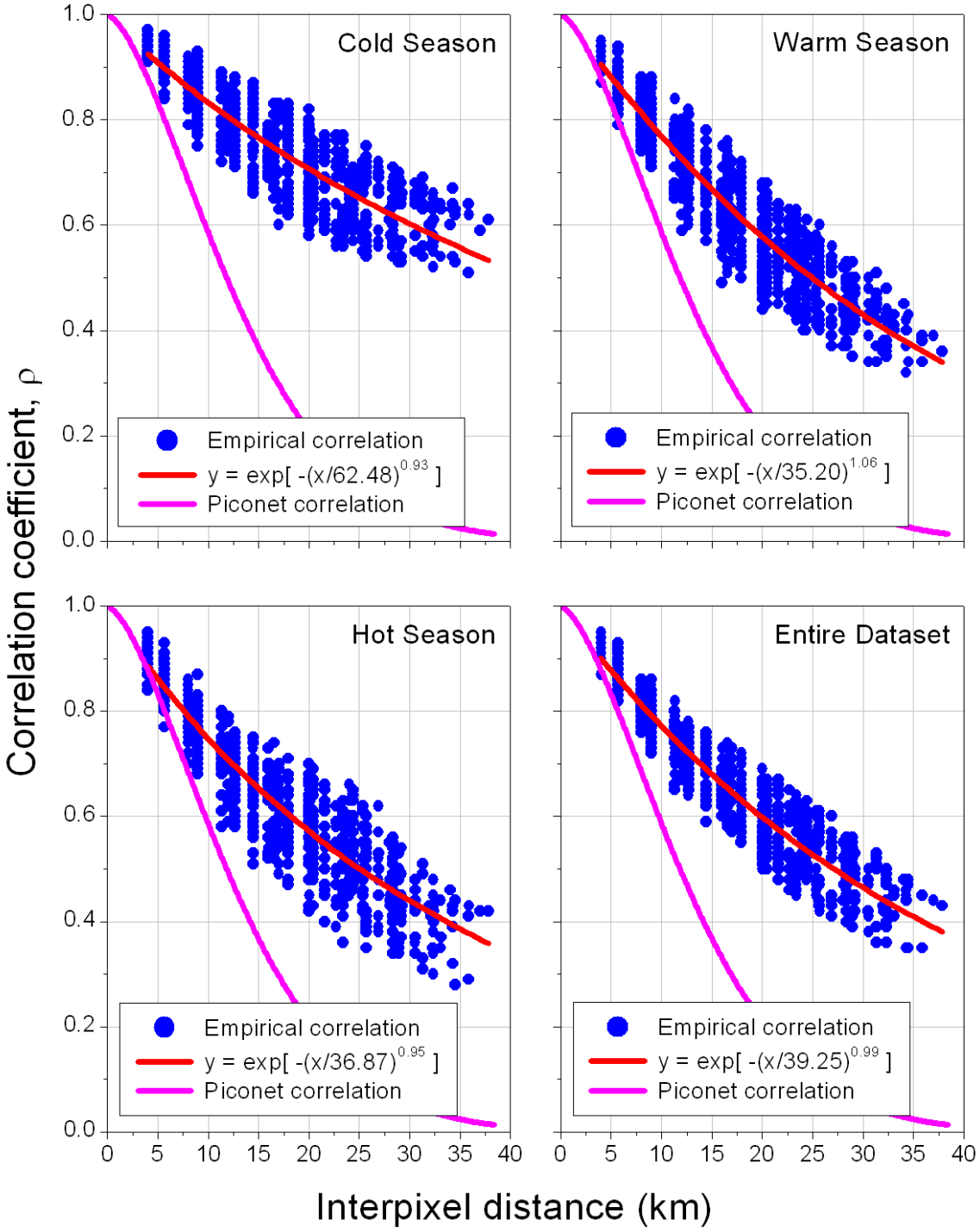

Figure 10. Spatial correlation of the radar data at the locations of the Micronet rain gauges for the three seasons and the entire dataset. The solid red lines are obtained fitting the data with a three-parameter exponential function; the solid magenta line is from the spatial correlation function estimated by Ciach and Krajewski (2005) for the EVAC Piconet rain gauge network.

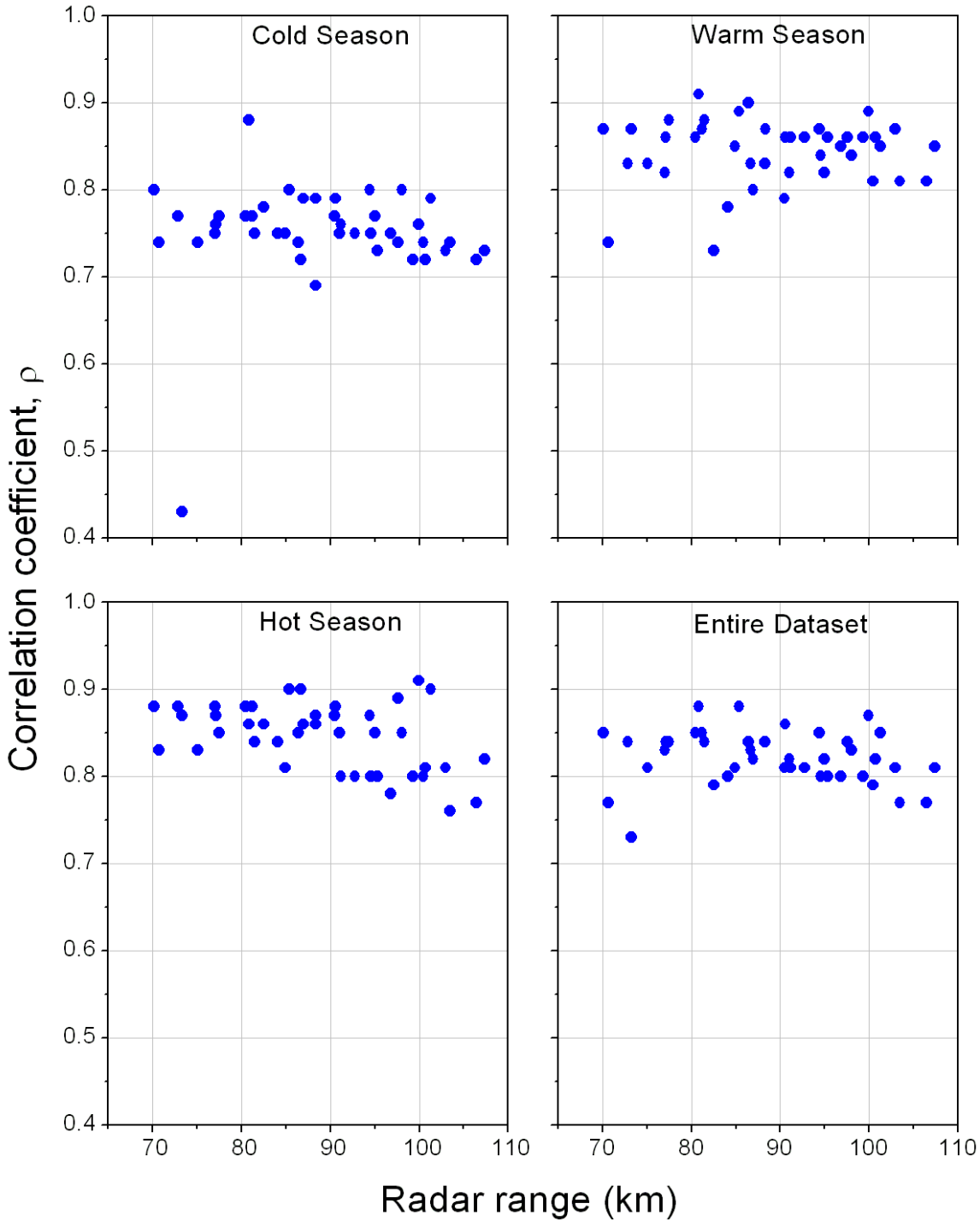

Figure 11. Correlation coefficients between rain gauge and collocated radar values estimated from the Micronet network as a function of the distance from the radar site.

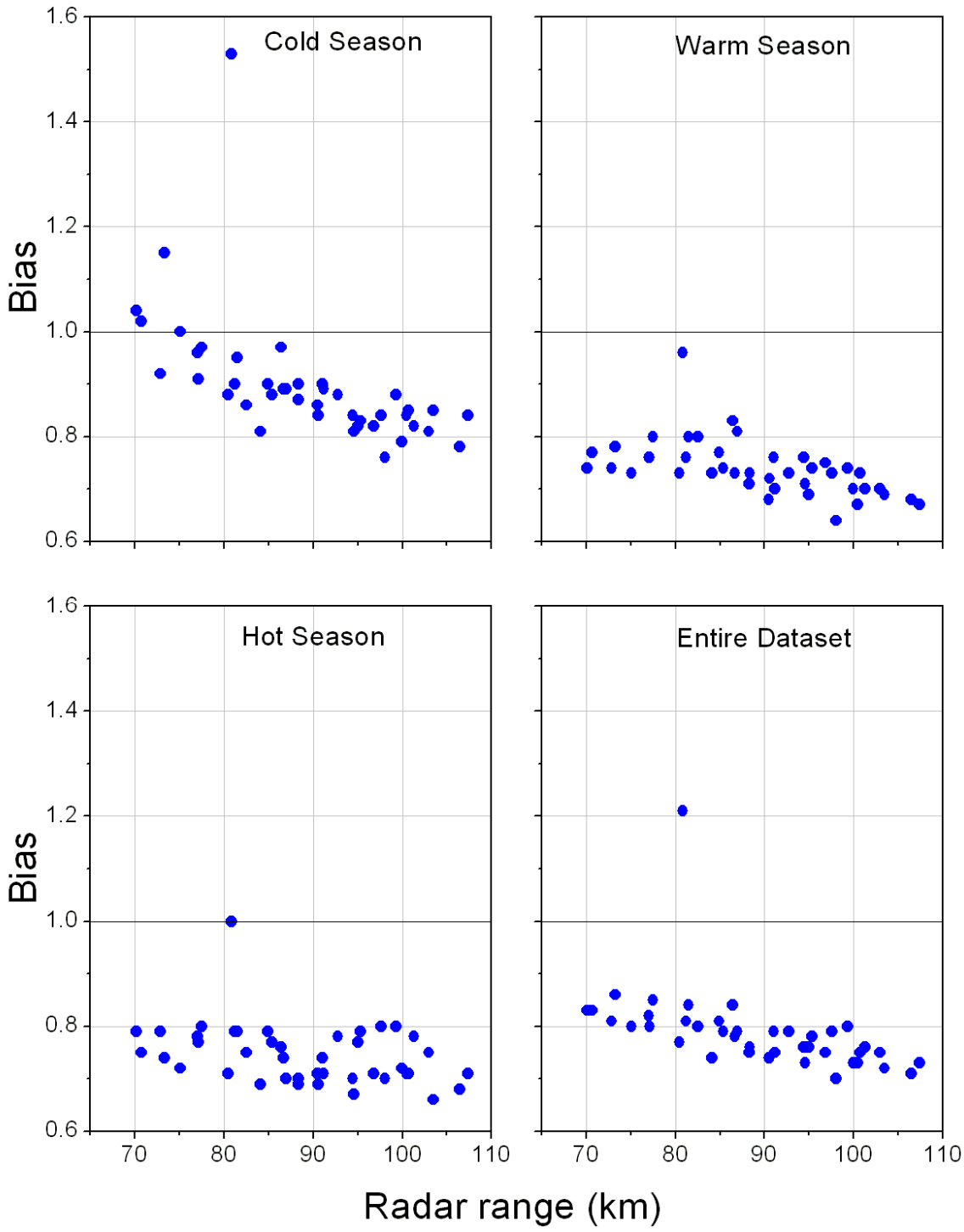

Figure 12. Bias estimated from the Micronet network as a function of the distance from the radar site.

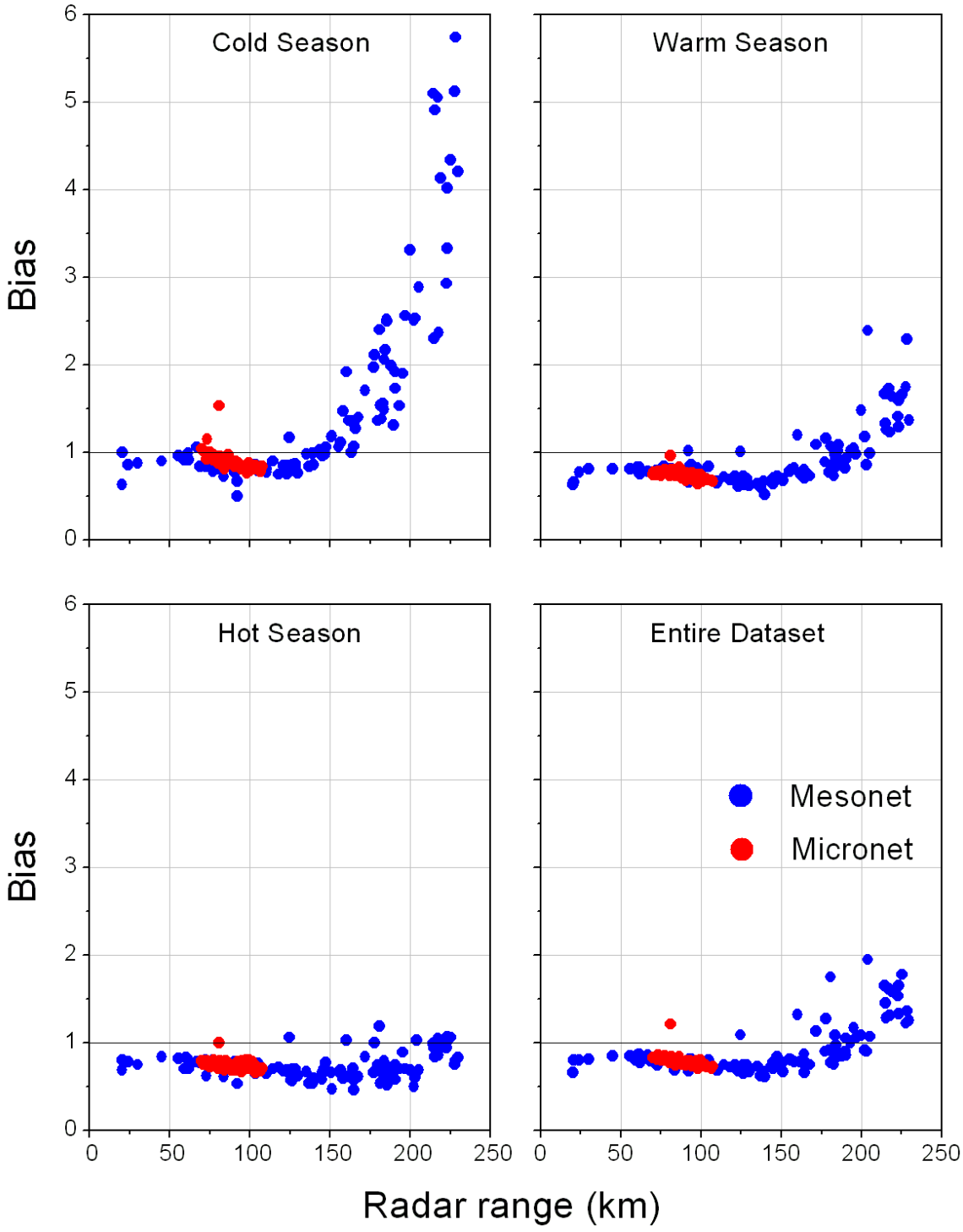

Figure 13. Bias between radar and rain gauges before QC of the Mesonet. The QC process eliminated the outlying points.

C.1.3. Summary of Rain Gauge Data QC

To quality control the rain gauge data we followed an iterative process. Preliminary data analysis, including the results presented above, identified wrong data values based on simple checks, as well as inconsistent behavior of certain rain gauges. Through tedious work we eliminated much of the bad data but almost certainly we failed to identify and eliminate them all.

Below we only highlight the major procedures and findings of our quality control.

C.1.3.1. *Mesonet Data*

Oklahoma Mesonet is perhaps the best operated surface meteorological network in the United States. Their staff constantly strives to improve their procedures for data quality control and comprehensive documentation of their entire database (Shafer et al. 2000). They developed a system of QC flags that accompany the data. Users can take advantage of these flags in their analyses.

C.1.3.2. *Micronet Data*

Although recently the Oklahoma Climatological Survey took over maintenance of the Micronet, the network historical database has not yet been incorporated into the system thus it lacks the same reliability as the Mesonet. In our investigation we easily identified and corrected obvious errors. To detect other errors we investigated statistical consistency of various simple to calculate indices. For example, we calculated conditional probabilities $Pr(G>0|R=0)$, $Pr(R>0|G=0)$, $Pr(G>0|R>0)$ and $Pr(R>0|G>0)$, for different seasons. While the "correct" values of these indices are unknown, any departure from an overall pattern seems suspicious. Consider, for example, plots in Figures 11-14. It is easy to notice a couple of gauges that need more investigation: 1) there is one station at around 80 km from the radar that constantly seem to lie outside the general pattern; 2) there is another station, at about 73 km from the radar that lies outside the general trend when considering $Pr(R>0|G>10)$. Indeed, these two stations behaved suspiciously in terms of other statistics as well. For example, in Figures 15-16 we show a simple conditional mean of RR (see Section C.1.4 for details) calculated on a gauge by gauge basis. While most gauges follow a certain pattern a couple of them seem to depart. These are the same gauges that we isolated in a previous analysis. We completed this analysis by computing similar conditional probabilities but for different values of the exceedence threshold (0.25, 1, 5, and 10 mm).

Rather than eliminating the entire record for the identified stations, we followed the above analyses with temporal analysis to zoom in on the period of trouble. The first step was to compute the same conditional probabilities for each year singularly. In this way, it was possible to considerably reduce the period under investigation. To narrow it down further, we considered each season separately and plotted the cumulative rainfall for each month. From these plots, we tried to find the time intervals that appeared suspicious with respect to the other rain gauges, then repeated the analysis. This was a recursive procedure, which lead to a much improved overall pattern in the conditional statistics.

Finally, we developed a flagging system for the data, trying to follow as close as possible the flagging system used for the Mesonet data.

C.1.3.3. *PicoNet data*

Prior to our analysis of the PicoNet rainfall measurements, we had to perform a number of the quality-control (QC) procedures to assure reliability of the results. The corrupted data detected in the QC investigation were flagged as invalid and removed from further analysis. The major part of the QC analysis was the comparison of the concurrent rainfall records in the collocated pairs of the gauges. Since the magnitude of the local random errors in the rain gauges can be estimated based on the results reported in Ciach (2003), it is fairly easy to identify the situations when one of the gauges fails, and to flag the missing or wrong data periods. Typical causes of the failures that we encountered were partial clogging of the rain gauge funnel by the debris and occasional problems with the tipping-bucket reed-switches. In addition to the basic pair-wise diagnostics, we also checked the integrity of each PicoNet station with the neighboring stations. Using this spatial consistency test, we identified two stations which, during the highest vegetation growth (May-June) in 2002, started to be clogged by the plant debris. Since the effect occurred in a similar way in both collocated gauges, their pair-wise comparison could not detect it. Therefore, in these two cases, the approximate identification of the time when the clogging started to affect the measurements was based on the comparison with neighboring stations. This example shows that the redundancy of the double-gauge network design, although very effective in many failure situations, does not solve all the possible problems with rain gauge measurements. Frequent inspection and cleaning of these instruments is still indispensable to ensure good quality of the rainfall data.

Although the time resolution of the HOBO loggers is high (0.5 second), the factory guarantee of their time measurement accuracy is only up to 1 minute per one week. According to our experience in the PicoNet, all the 53 data-loggers show systematic positive time drifts ranging from about 10 seconds per week up to about 40 seconds per week for the individual loggers. Our two-year long data sample was collected in 7 periods of variable length ranging from 10 days to 4 months. Although the logger timers were set accurately when they were launched at the start of each period, at the end of the longer data collection periods they were considerably desynchronized. For the four-month period, the time errors range from 3 to 12 minutes. We corrected these errors assuming that the time-drifts increase linearly in time with the rates characteristic for each data-logger. These individual drift-rates were computed based on the cumulative time errors that we measured at the end of each data collection period while downloading the data.

For the data analysis we converted the raw rainfall data collected in a form of tip-time series into rainfall intensities averaged over 1-minute intervals. Then, we aggregated these rain rates into accumulations, or time-averaged intensities, over several other time-scales that we consider in this study. To compute the 1-minute rain rates, we applied an inter-tip interpolation scheme described in Ciach (2003). This scheme allows retrieval of the short-time rain rates with relatively high accuracy.

C.1.3.4. *Summary*

Quality control of rain gauge data resulted in minor loss of the total number of data points. We eliminated data from those sites and or periods that clearly malfunctioned. At the end, after QC, we were left with more than 13 million pairs. In Figure 17 we present summary of data

organized according to pairs of sites separated by a certain distance. This arrangement is particularly relevant for estimation of spatial dependence of rainfall as well as the radar-rainfall errors.

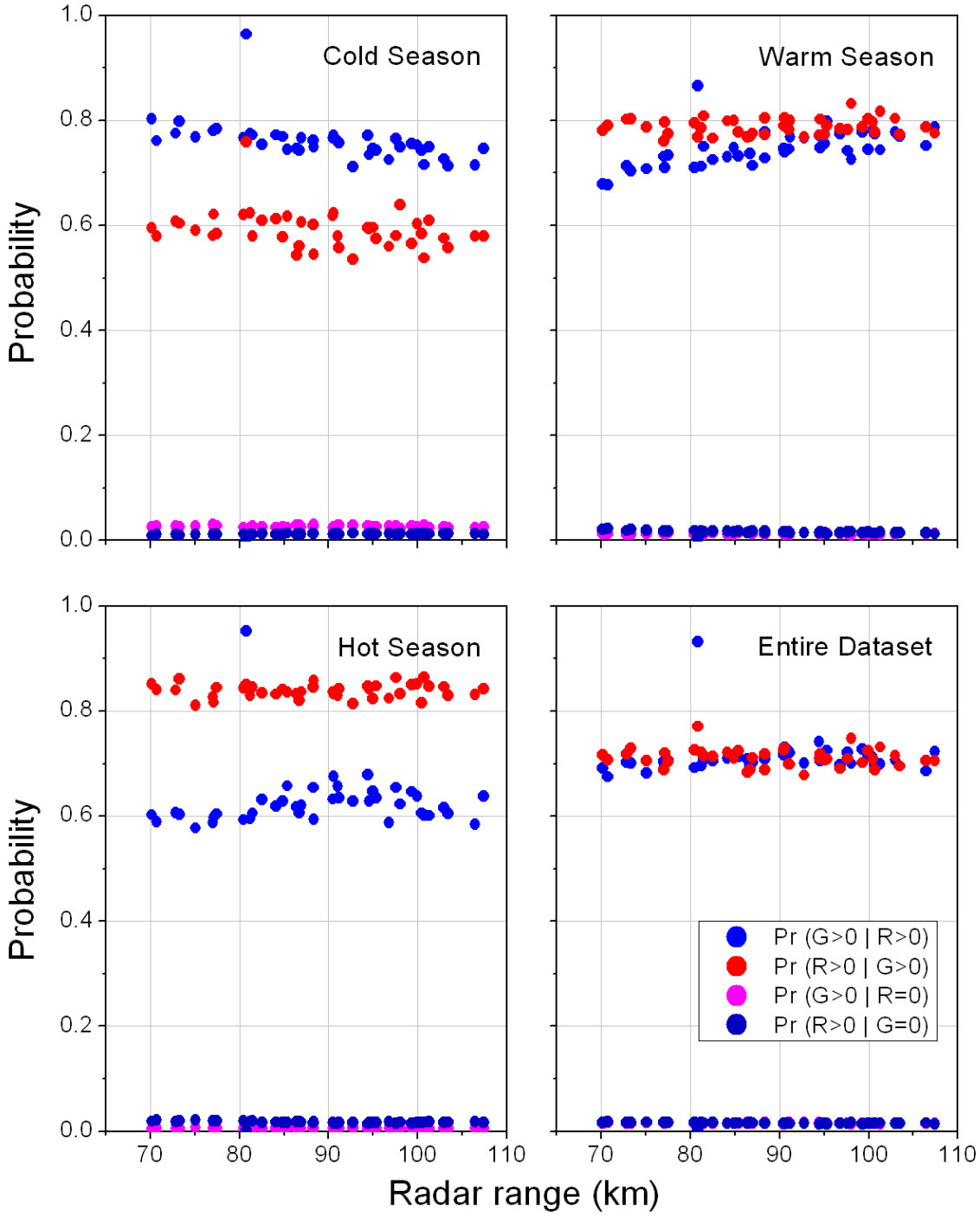

Figure 14. Conditional probability of detection within the Micronet on a gauge by gauge basis. Visual inspection of the plots served to identify potentially bad gauges.

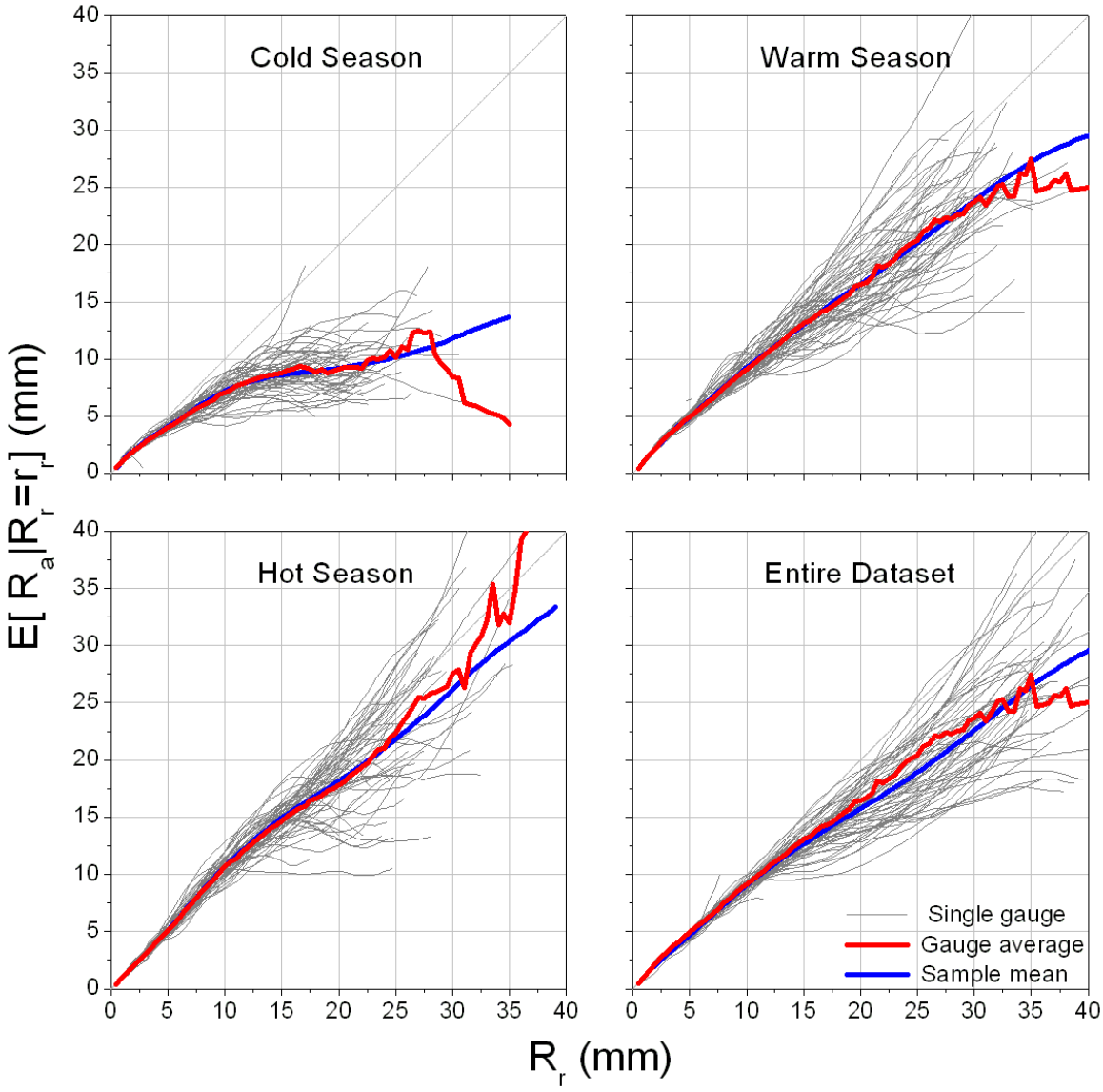

Figure 15. Rain gauge averages, conditioned on radar rainfall values, after removing the bias for the hourly scale, for the three seasons and the whole dataset. The black lines correspond to individual gauges, the red line is obtained averaging each individual trace and the blue line is the sample mean.

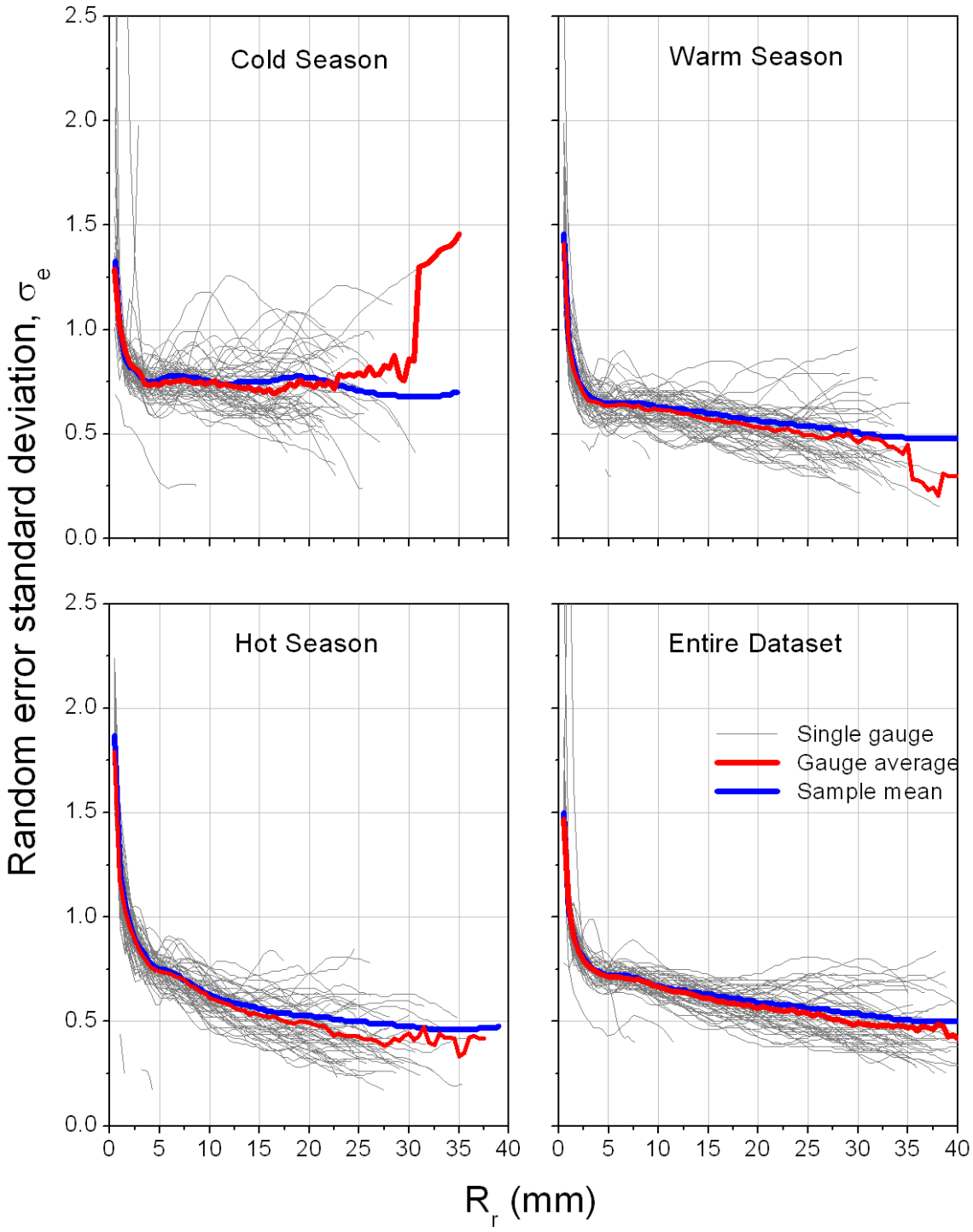

Figure 16. Standard deviation of the random component of the error model, conditioned on radar rainfall values, after removing the bias for the hourly scale, for the three seasons and the whole dataset. The black lines correspond to individual gauges, the red line is obtained averaging each individual trace and the blue line is the sample mean.

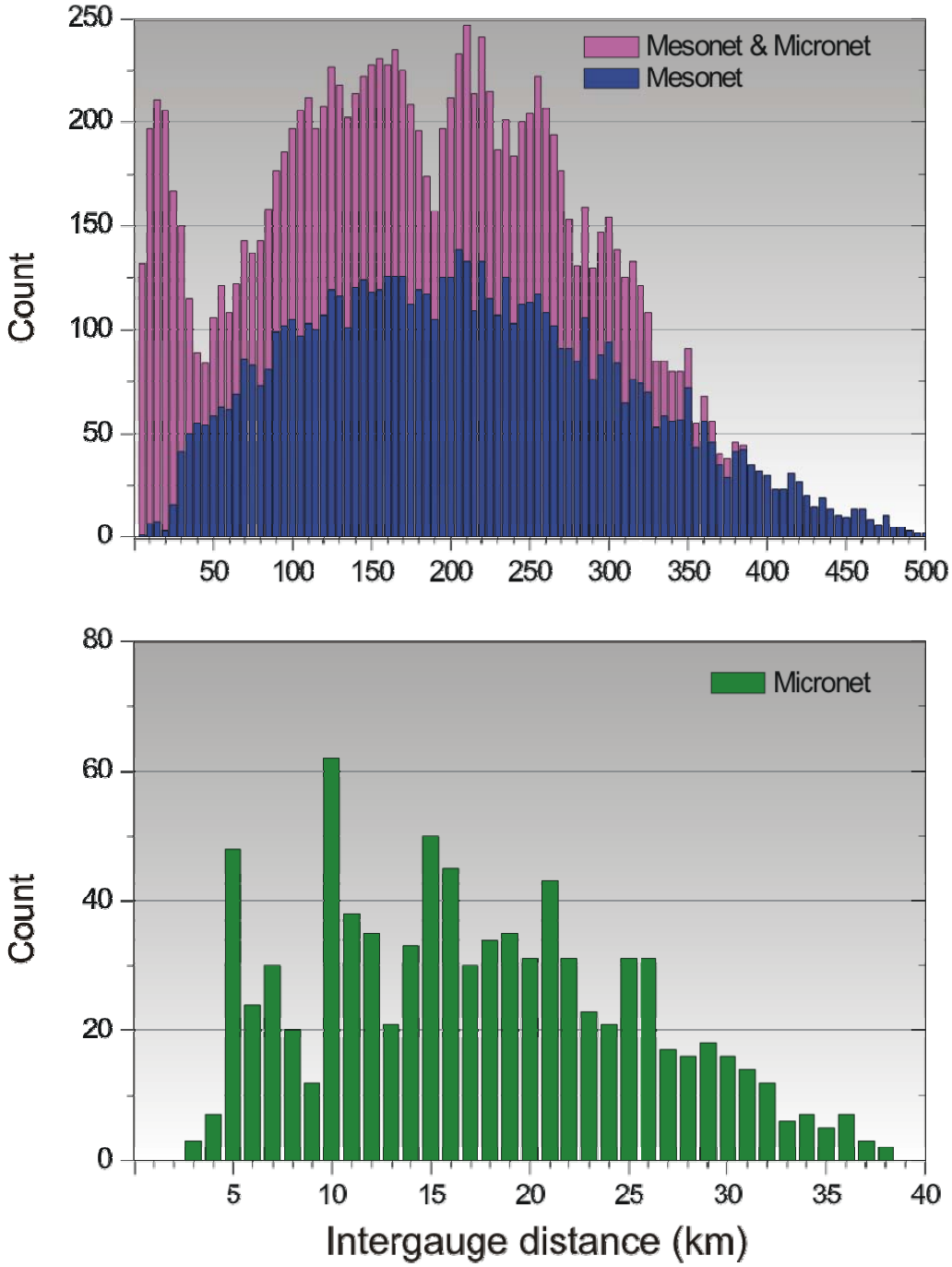

Figure 17. Histogram of the number of gauges separated by a certain distance for the Mesonet and for the Micronet. The plots are helpful in interpretation of the spatial dependence (correlation).

To facilitate analyses of range dependence we divided our data set into five zones according to the distance of the gauges from the OKC radar. Our criteria included requirement for a similar number of sites in each zone and sufficient range resolution to capture eventual range dependency behavior of various statistics. To avoid erratic behavior we allow small overlap (5 km) between different zones. We show the final choice of the zones in Figure 18. Since almost the entire Micronet is located in Zone II, the number of gauges in this zone is disproportionately large compared to other zones. It is evident that the number of gauges in Zone I is small compared to other zones. Also, the density of zone coverage by gauges is not even but most our statistics ignore inter gauge dependence. For those that explicitly reflect this dependence the density of rain gauges in zones other than Zone II is too small for meaningful analysis, as we will see later on.

Based on the zonal division and the quality controlled data we recomputed the values of the overall bias. We summarize the results in Table 1 below.

Table 1. Estimated bias for the 5 zones for different time scales (1, 3, 6, and 24 h)

1 hr	Cold season	Warm season	Hot season	Entire dataset
Zone I	0.95	0.78	0.76	0.82
Zone II	0.88	0.76	0.73	0.78
Zone III	0.87	0.68	0.65	0.72
Zone IV	1.29	0.78	0.65	0.83
Zone V	2.33	1.11	0.75	1.12

3 hr	Cold season	Warm season	Hot season	Entire dataset
Zone I	0.95	0.78	0.75	0.82
Zone II	0.89	0.76	0.73	0.78
Zone III	0.88	0.68	0.65	0.72
Zone IV	1.29	0.78	0.65	0.83
Zone V	2.36	1.11	0.75	1.13

6 hr	Cold season	Warm season	Hot season	Entire dataset
Zone I	0.94	0.78	0.75	0.81
Zone II	0.88	0.77	0.73	0.78
Zone III	0.88	0.68	0.65	0.72
Zone IV	1.28	0.78	0.65	0.83
Zone V	2.35	1.12	0.75	1.13

24 hr	Cold season	Warm season	Hot season	Entire dataset
Zone I	0.94	0.79	0.74	0.81
Zone II	0.88	0.78	0.70	0.78
Zone III	0.88	0.69	0.63	0.72
Zone IV	1.26	0.78	0.65	0.83
Zone V	2.33	1.09	0.75	1.14

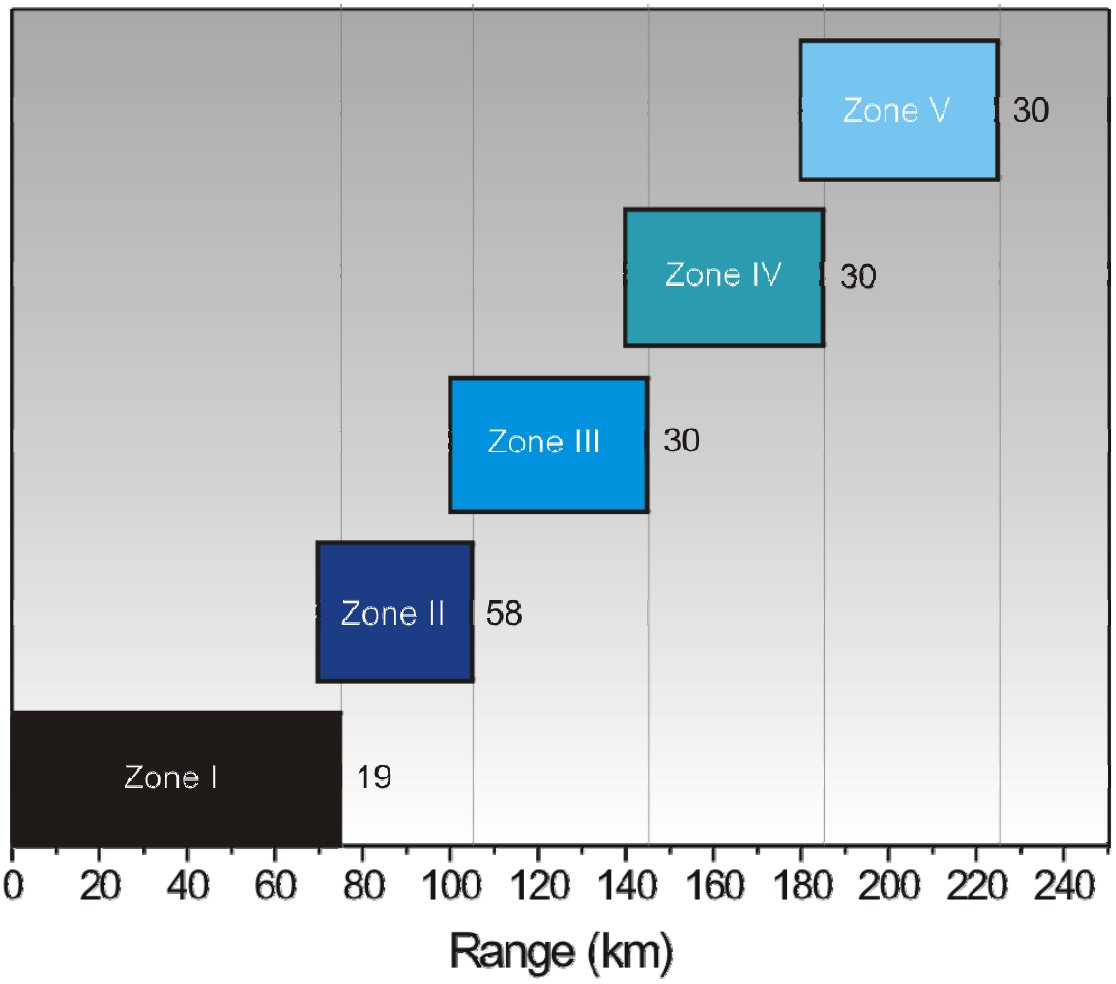

Figure 18. Selected zones with the number of included rain gauges.

C.1.4. Conditional Analyses

C.1.4.1. *Outline of the Nonparametric Procedure for Conditional Analysis*

As we mentioned earlier, to characterize the relation between radar-rainfall (RR) and the true rainfall, it is possible to consider the true rainfall (RA) as the product of a deterministic distortion function $h(\cdot)$ of the RR and of the random uncertainties $e(\cdot)$:

$$R_a = h(R_r) \cdot e(R_r) \tag{11}$$

where R_r and R_a represent the corresponding (concurrent and collocated) RR and RA. This relation has the flexibility to account for different spatio-temporal scales, distance from the radar and synoptic conditions.

To identify the model, it is necessary to estimate the deterministic function $h(\cdot)$ and the statistical distribution of the random component. We used data from both the Mesonet and the Micronet. Once removed the overall bias, we have defined the deterministic component $h(r_r)$ as the following conditional expectation:

$$h(r_r) = E[R_a \mid R_r = r_r] \tag{12}$$

The deterministic component can be approximated using a nonparametric regression method (e.g. Hardle 1990; Simonoff 1996). In this study we have used the following moving-window averaging:

$$h(r_r) = \left. \frac{\sum_i (w_i R_{a,i})}{\sum_i w_i} \right| \frac{r_r}{k} \le R_r \le r_r k \tag{13}$$

where k is a parameter that regulates the size of the moving window centered on $R_r = r_r$, and w_i is the weighting factor. The size of the windows linearly increases with r_r so that a reasonable number of data points are used for the estimation. For this study, k is set equal to 1.5. The weighting factor w_i is computed as:

$$w = 1 - \left(\frac{\log \frac{R_r}{r_r}}{\log k} \right)^2 \tag{14}$$

Accordingly, w is equal to 1 for $R_r = r_r$ and it decreases moving far from the center of the window.

Once we have estimated the deterministic component, we are able to characterize the random errors $e(R_r)$ in the multiplicative and additive forms:

$$e(R_r) = \frac{R_a}{h(R_r)} \tag{15}$$

$$e(R_r) = R_a - h(R_r) \tag{16}$$

From these formulations, notice that the conditional expected values of $e(\cdot)$ are always equal to 1 for the multiplicative form and 0 for the additive form, while the standard deviations of the random component $\sigma_e(r_r)$ depends on RR estimates:

$$\sigma_e(r_r) = \sqrt{\frac{1}{N}\sum_{i=1}^{N}\left(\frac{R_a}{h(r_r)} - 1\right)^2} \qquad \text{(multiplicative)} \tag{17}$$

$$\sigma_e(r_r) = \sqrt{\frac{1}{N}\sum_{i=1}^{N}\left[R_a - h(r_r)\right]^2} \qquad \text{(additive)} \tag{18}$$

Using the same nonparametric approach as described above, we estimated $\sigma_e(r_r)$ as:

$$\sigma_e(r_r) = \sqrt{\left|\frac{\sum_i \left[w_i\left(\frac{R_{a,i}}{h(r_r)} - 1\right)^2\right]}{\sum_i w_i}\right|} \quad \frac{r_r}{k} \le R_r \le r_r k \qquad \text{(multiplicative)} \tag{19}$$

$$\sigma_e(r_r) = \sqrt{\left|\frac{\sum_i \left\{w_i\left[R_{a,i} - h(r_r)\right]^2\right\}}{\sum_i w_i}\right|} \quad \frac{r_r}{k} \le R_r \le r_r k \qquad \text{(additive)} \tag{20}$$

C.1.4.2. *Deterministic Component of the Error*

The deterministic distortion function h(·) complements the systematic bias by accounting for dependence on RR. We estimated it using the aforementioned nonparametric framework for four different time scales (1, 3, 6, and 24 hours) for the three seasons and the whole dataset. Due to the fact that hourly RR are estimated every five minutes there is strong statistical dependence in the hourly values. On the other hand, if we took only adjacent hours that would reduce significantly our sample size. As a compromise between these two aspects of sample selection,

we have not considered all hourly data, but only those for which the initial scans were separated by at least 20% of the temporal resolution. In this way, we have more independent information included in our statistics. As RR increases the sample size decreases and the computed statistics become less significant. For our analysis we have considered a minimum weighted sample size of 100.

To avoid overwhelming the reader with numerous plots, in the text below we include and discuss results for hourly scale only. We include the results for the remaining temporal scales of three-six- and 24-hours in their respective Appendix (C, D, and E).

Figure 19 shows the results of analysis. The curves tend to be close to the 1:1 line, due to the removal of the overall bias, and then bend towards the x-axis indicating gradual overestimation of the large values except for Zone I during hot season. In the warm and hot seasons it seems that the curves follow the 1:1 line for a longer range. This can probably be attributed to the fact that there are more numerous smaller values in the cold season than in the warm and hot ones. However, this conditional on rainfall deterministic distortion function displays little, if any, range dependence during warm and hot seasons within the range of 180 km from the radar.

C.1.4.3. *Random Component of the Error*

The random component $e(\cdot)$ describes all random uncertainties. As we mentioned before, it can be formulated in two ways, multiplicative or additive. Its mean does not depend on the RR values, while the standard deviation does. In Figure 20 we show the standard deviation of the random component in the additive form, while in Figure 21 in the multiplicative form. The corresponding results for other time scales are in the Appendices. Comparing the results from the two formulations, it is easy to notice a more regular behavior of the multiplicative form. Thus, in the rest of the analysis we abandon the additive form and proceed with the modeling of the random component in the multiplicative error formulation. Also, comparing results for different temporal scales we note that the standard deviation in the multiplicative form for RR > 10 mm does not depend much on the temporal scale (with the exception of the cold season). This temporal invariance of $e(\cdot)$ in the multiplicative form will be very useful in the modeling effort.

To characterize the random component in terms of its statistical distribution, we computed the 0.9, 0.75, 0.50, 0.25, and 0.10 quantiles, focusing our attention on the multiplicative form. As mentioned before, we know that its expected value is equal to 1 and does not depend on RR, while its standard deviation does.

Looking at the results for the three seasons and the whole dataset at the four time scales (Figures 22-25 and corresponding plots in the Appendixes), it is possible to notice how the quantiles tend to be symmetrical with respect of the median. For this reason we tried to model the empirical results with two symmetrical distributions (Gaussian and logistic, the latter not shown) with mean equal to 1 and standard deviation equal to the standard deviation from the multiplicative formulation. The quantiles from these theoretical distributions fit quite well the empirical results (perhaps with the only exception of the cold season), especially for large values of RR. These results seem to support the error model proposed by Petersen-Øverleir (2005), In that paper, the author used an error model where the observed rainfall is the product between the true rainfall and a random component accounting for the total variability in measurement data.

He assumes the random component to be normal distributed and he supports his choice by the Central Limit Theorem.

As far as we are concerned, the distribution of each source of uncertainty can be different but we are interested in the total error and therefore it is plausible that it is normally distributed by the Central Limit Theorem.

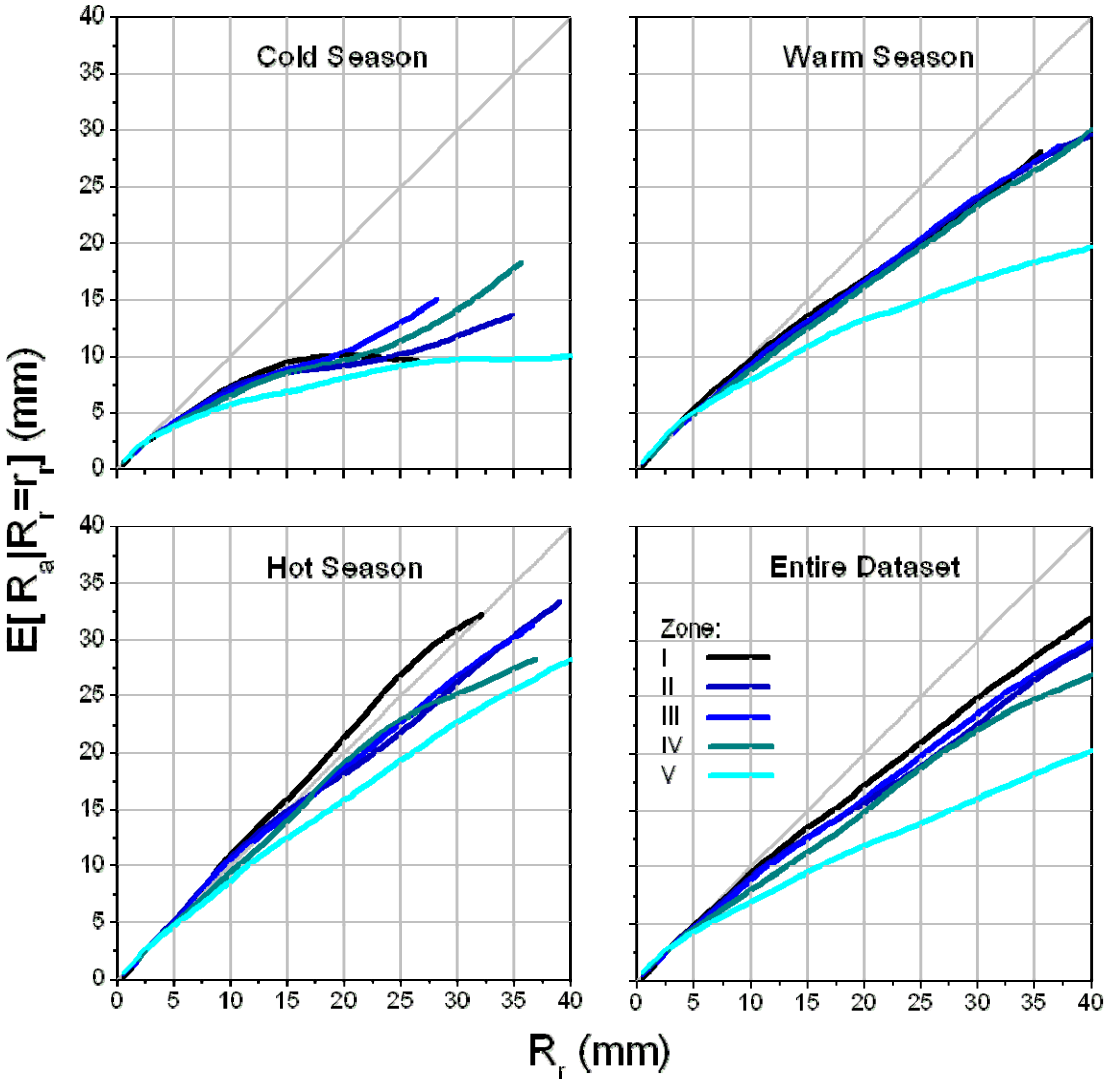

Figure 19. Rain gauge averages, conditioned on radar rainfall values, after removing the overall bias for hourly scale, for the three seasons and the whole dataset.

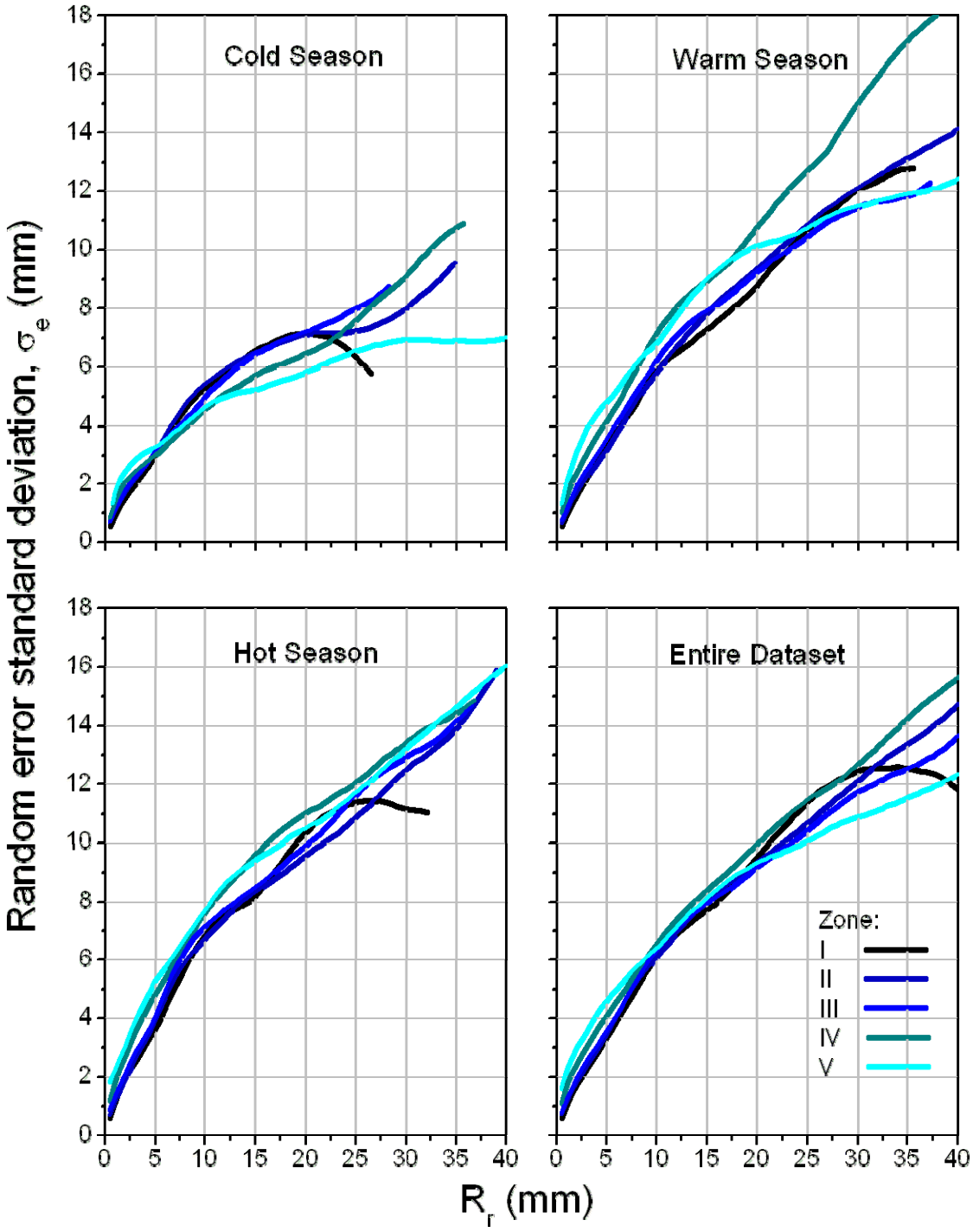

Figure 20. Standard deviations of the random component in the additive form (mm) for hourly data for the three seasons and the whole dataset.

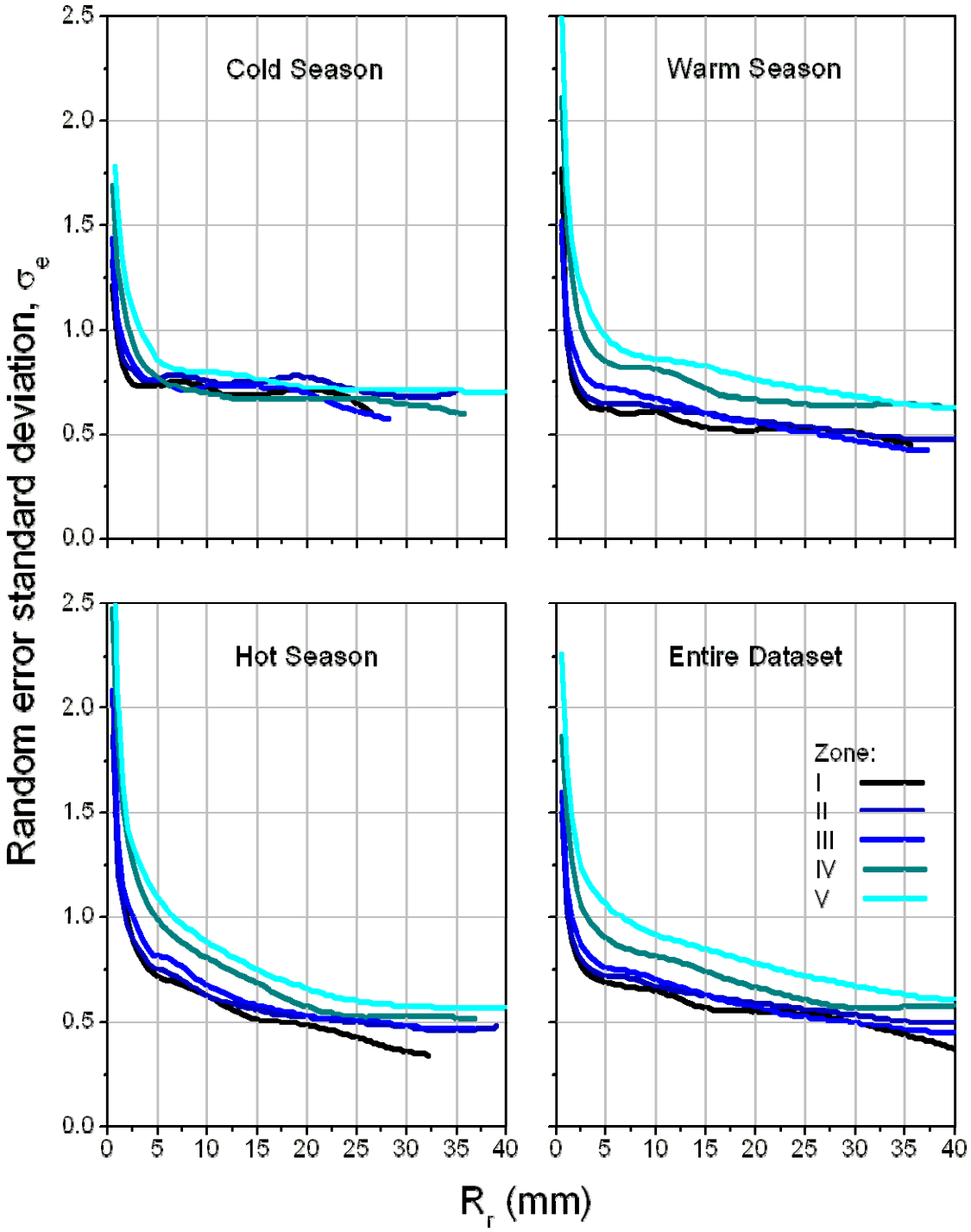

Figure 21. Standard deviations of the random component in the multiplicative form (dimensionless) for hourly data for the three seasons and the entire dataset.

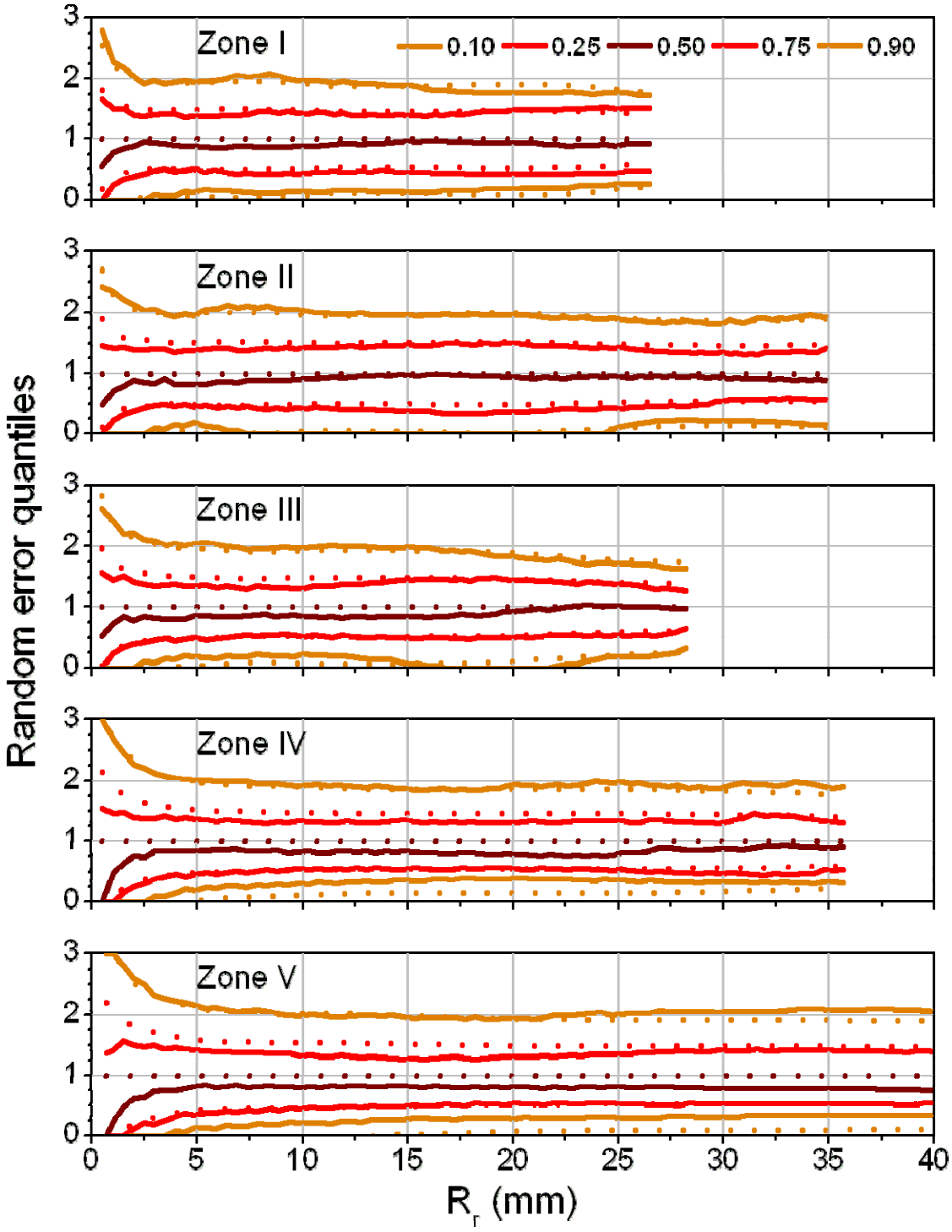

Figure 22. Comparison of the empirical and Gaussian quantiles (p=0.1, 0.25, 0.5, 0.75, 0.9). For the theoretical distribution, the mean is equal to 1 and the standard deviation is the standard deviation of the random component in the multiplicative form. Results for the cold season.

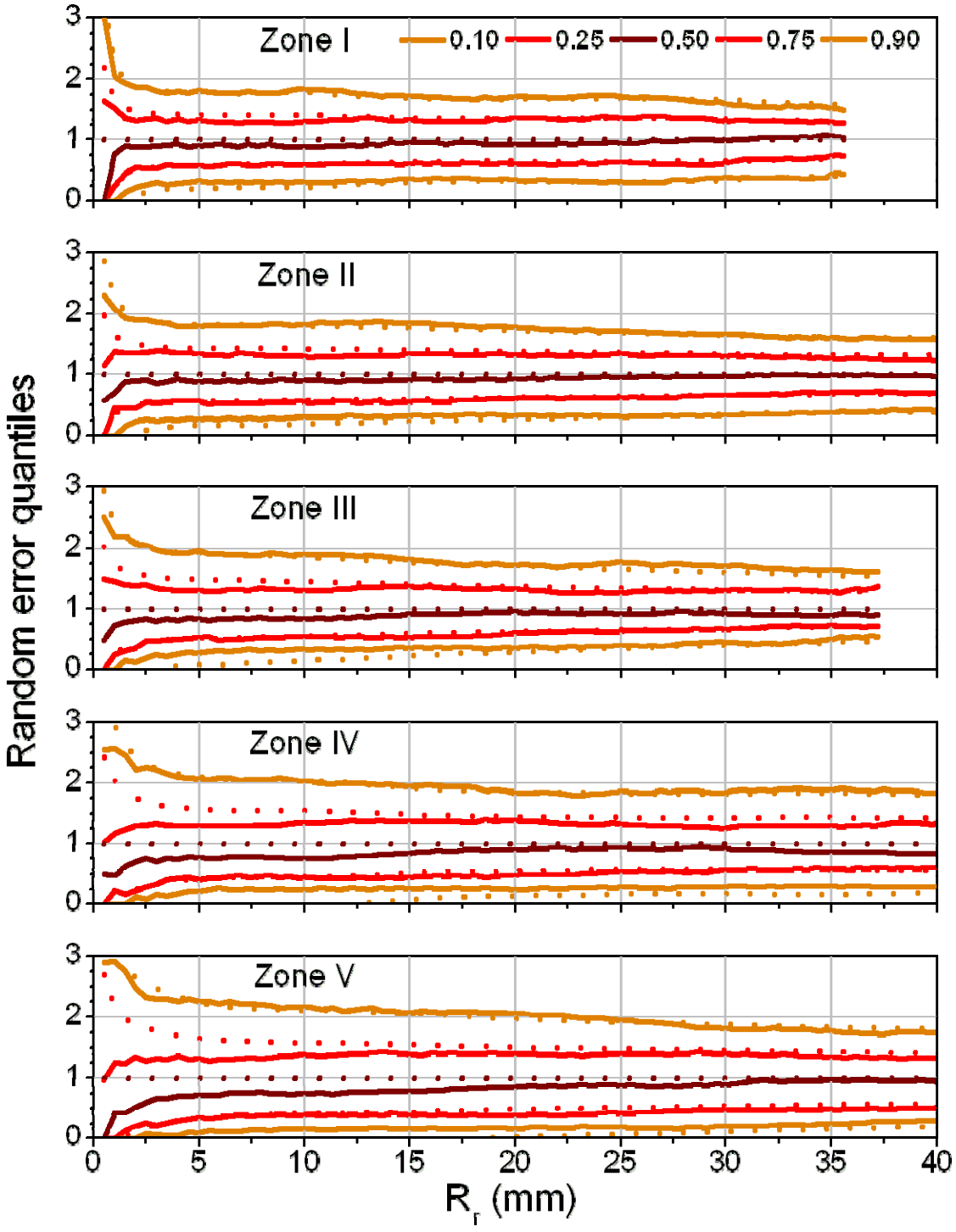

Figure 23. Comparison of the empirical and Gaussian quantiles (p=0.1, 0.25, 0.5, 0.75, 0.9). For the theoretical distribution, the mean is equal to 1 and the standard deviation is the standard deviation of the random component in the multiplicative form. Results for the warm season.

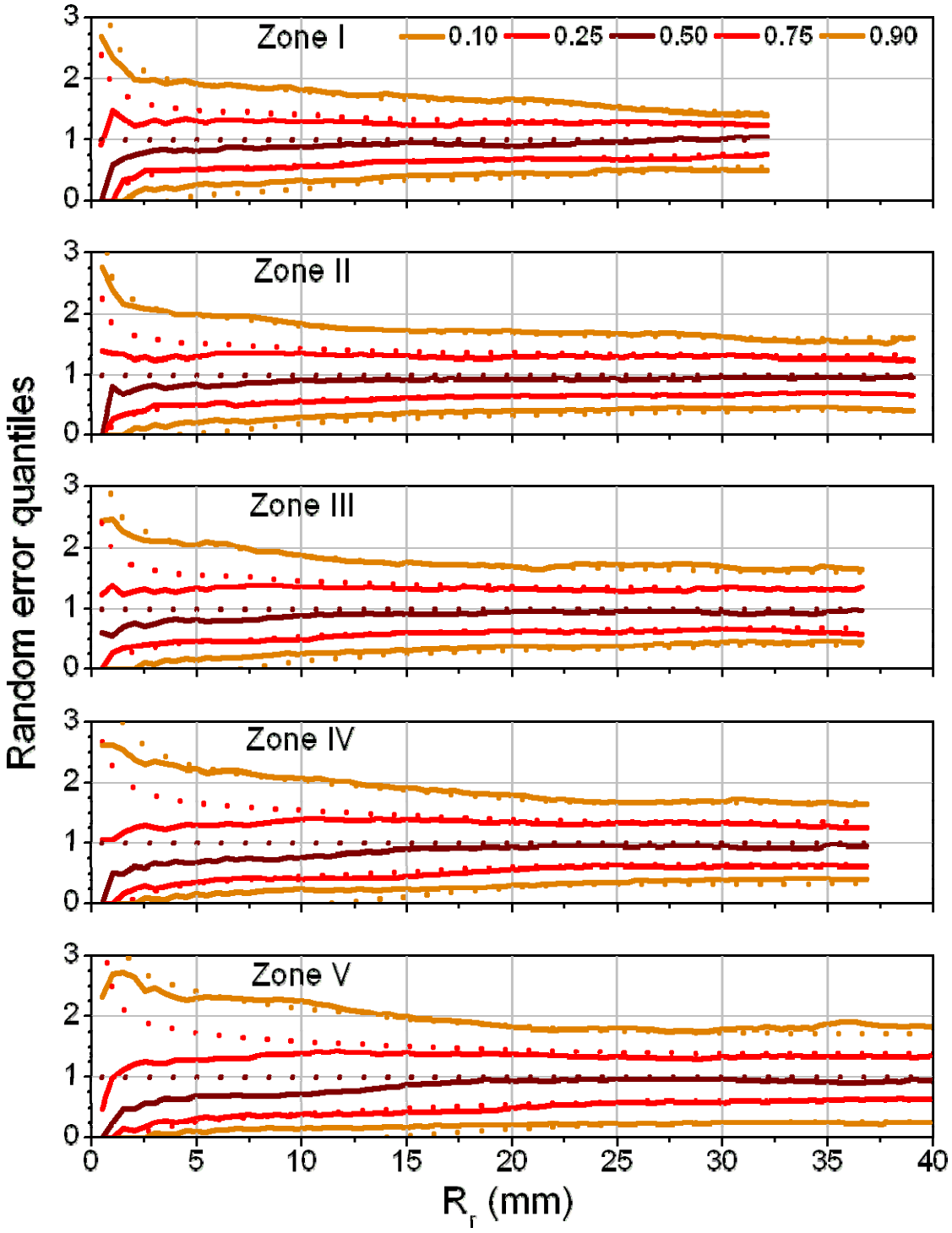

Figure 24. Comparison of the empirical and Gaussian quantiles (p=0.1, 0.25, 0.5, 0.75, 0.9). For the theoretical distribution, the mean is equal to 1 and the standard deviation is the standard deviation of the random component in the multiplicative form. Results for the hot season.

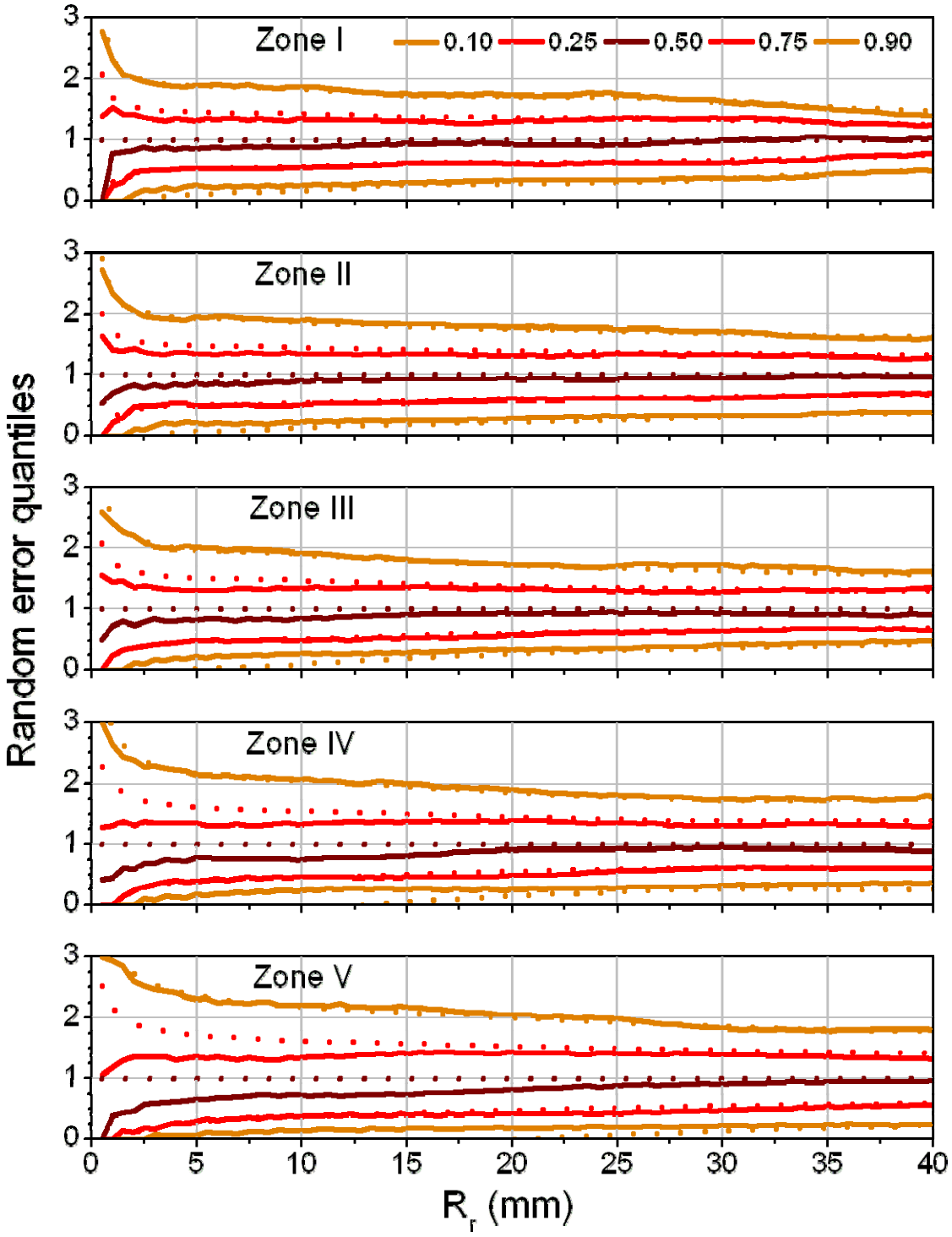

Figure 25. Comparison of the empirical and Gaussian quantiles (p=0.1, 0.25, 0.5, 0.75, 0.9). For the theoretical distribution, the mean is equal to 1 and the standard deviation is the standard deviation of the random component in the multiplicative form. Results for all seasons.

C.1.5. Error Dependence Analyses

C.1.5.1. *Temporal Correlation*

At present, the temporal correlation of the errors has not yet been characterized. Only few studies tried to take it into account (e.g., Nijssen and Lettenmaier 2004; Hossain et al. 2004).

In Figures 26-30, we plotted the temporal correlation of the random component of the error model in the multiplicative form for the hourly time resolution. We calculated it using the same nonparametric methodology as above but by keeping track of the temporal sequence of the multiplicative deviations. Notice a quick drop up to around one hour and then a subsequent slower decrease in the random component. We think that this feature can be explained by the fact that the DPA products are running 1-h rainfall accumulation and therefore, the information up to one-hour lag is not completely independent. It is also possible to notice a stronger correlation for the cold season compared to the other two.

C.1.5.2. *Spatial Correlation*

As for the temporal correlation, our current knowledge about the spatial correlation of the errors is extremely limited. Some studies have compared the possible effects in case of spatial correlation and uncorrelation, showing how the outcomes could be sensibly different (e.g., Nijssen and Lettenmaier 2004; Villarini et al. 2006).

In our study, we have found that the random component of the error in the multiplicative form is correlated in space (Figures 31-34). Compared to the spatial correlation estimated from the rain gauge data (Figure 9), the scatter is larger and the correlation is lower.

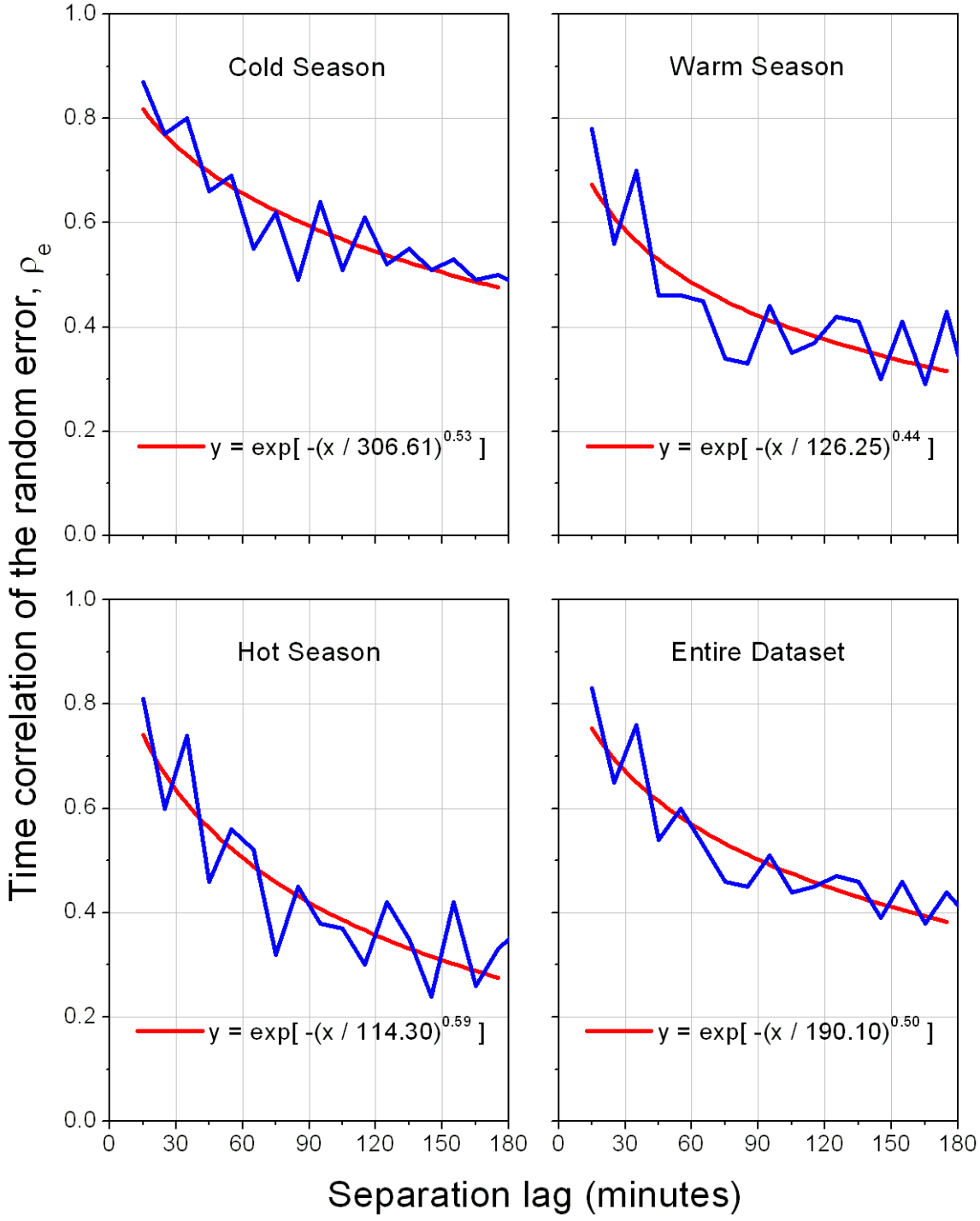

Figure 26. Empirical and model approximated temporal correlation of the random component for Zone I.

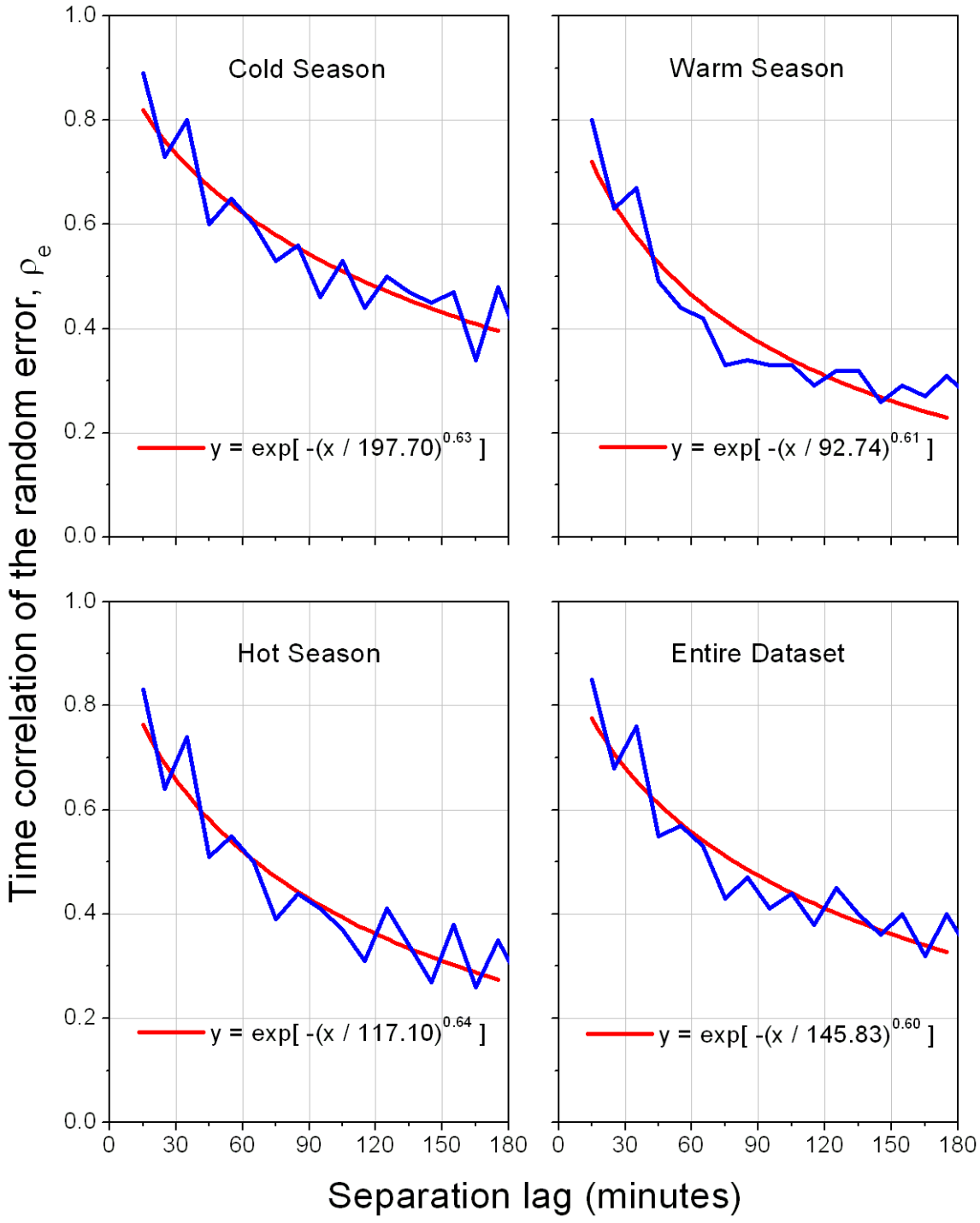

Figure 27. Empirical and model approximated temporal correlation of the random component for Zone II.

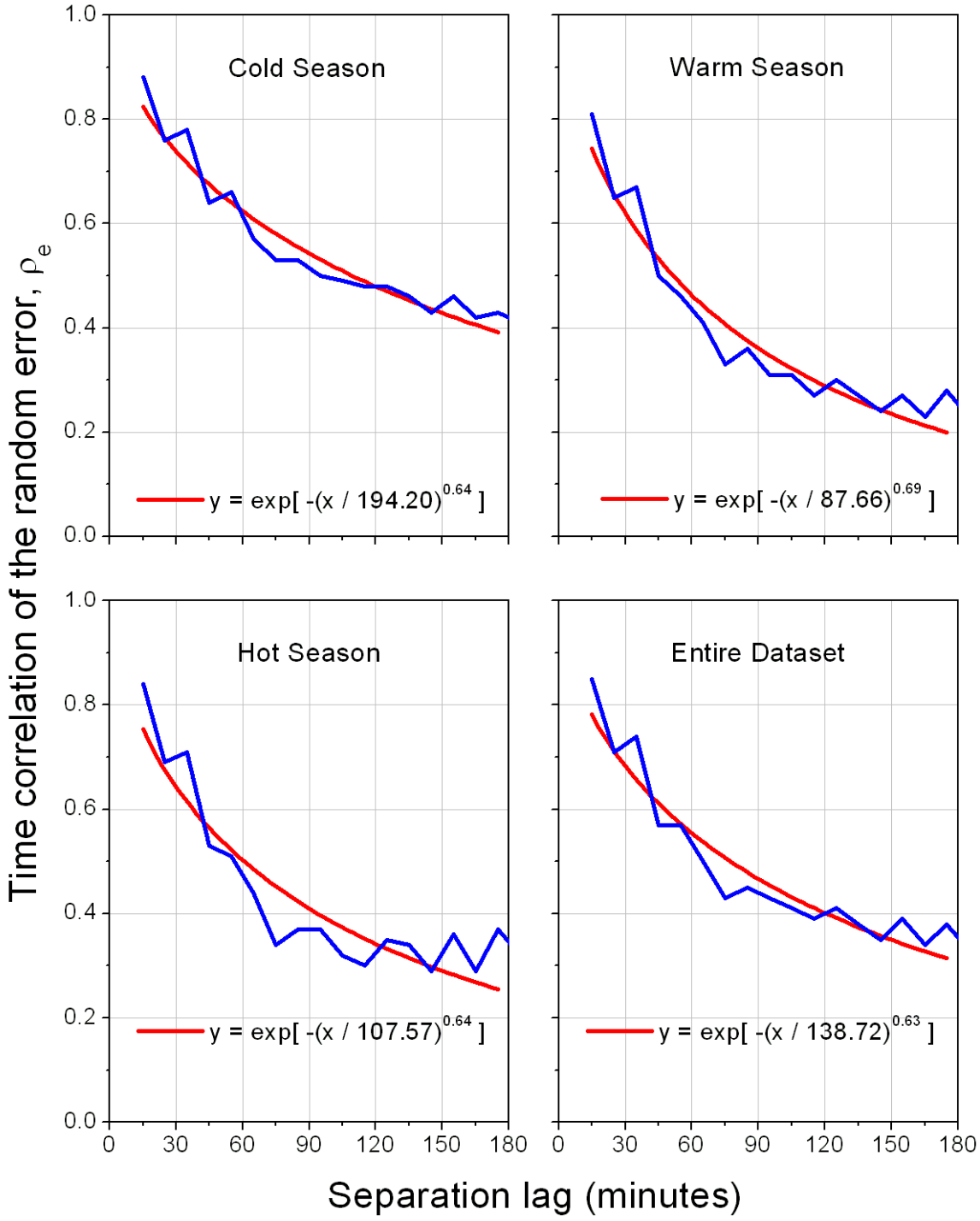

Figure 28. Empirical and model approximated temporal correlation of the random component for Zone III.

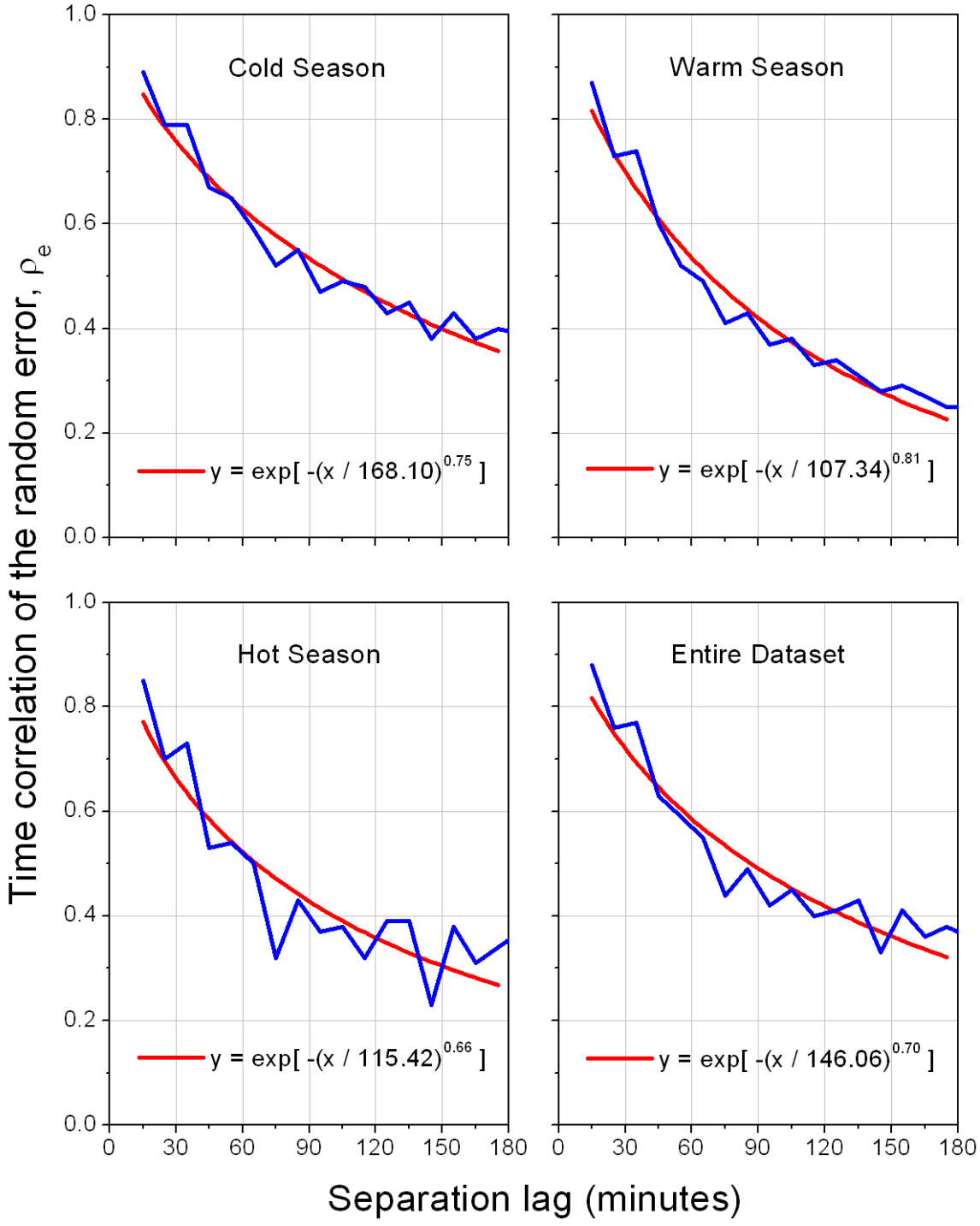

Figure 29. Empirical and model approximated temporal correlation of the random component for Zone IV.

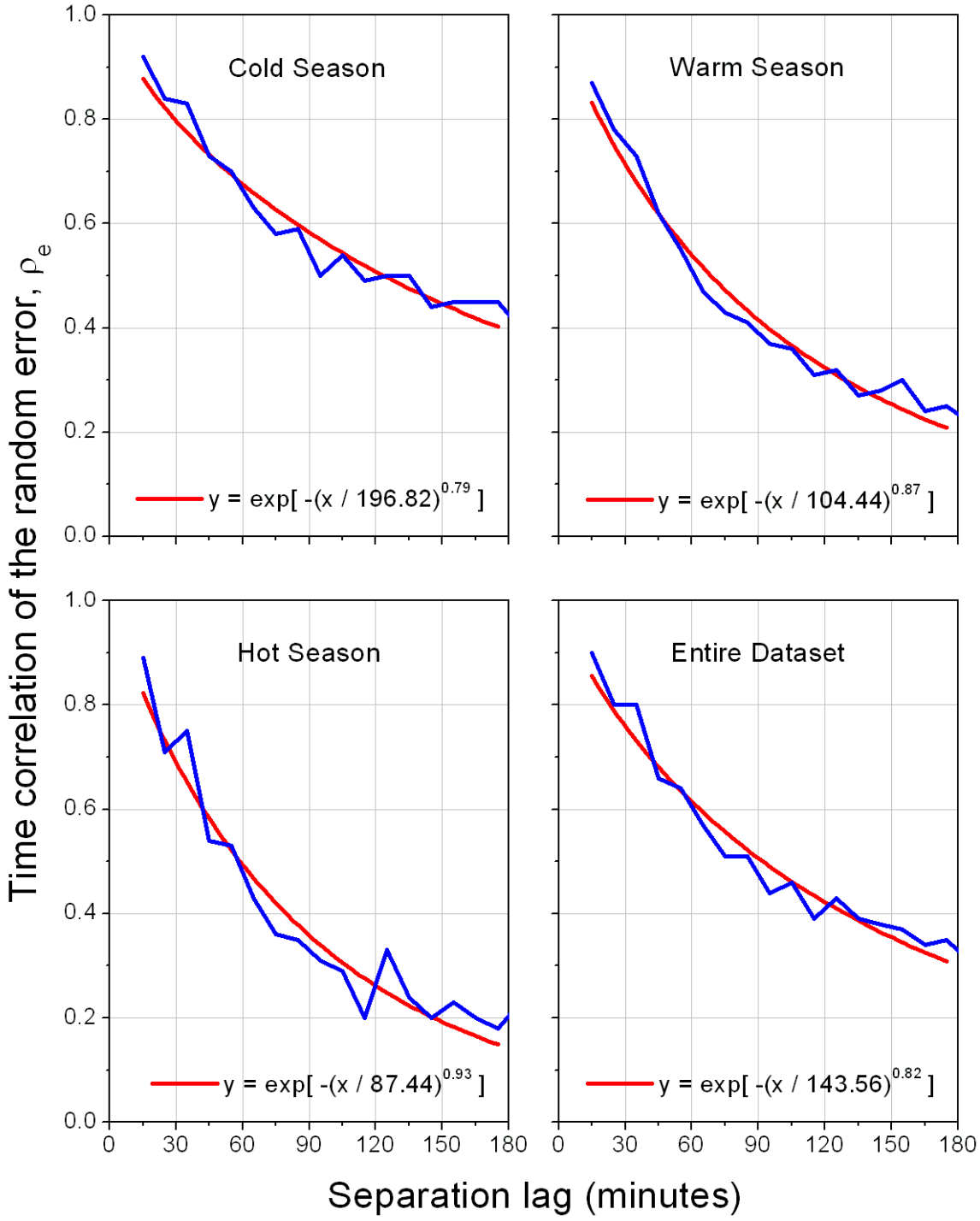

Figure 30. Empirical and model approximated temporal correlation of the random component for Zone V.

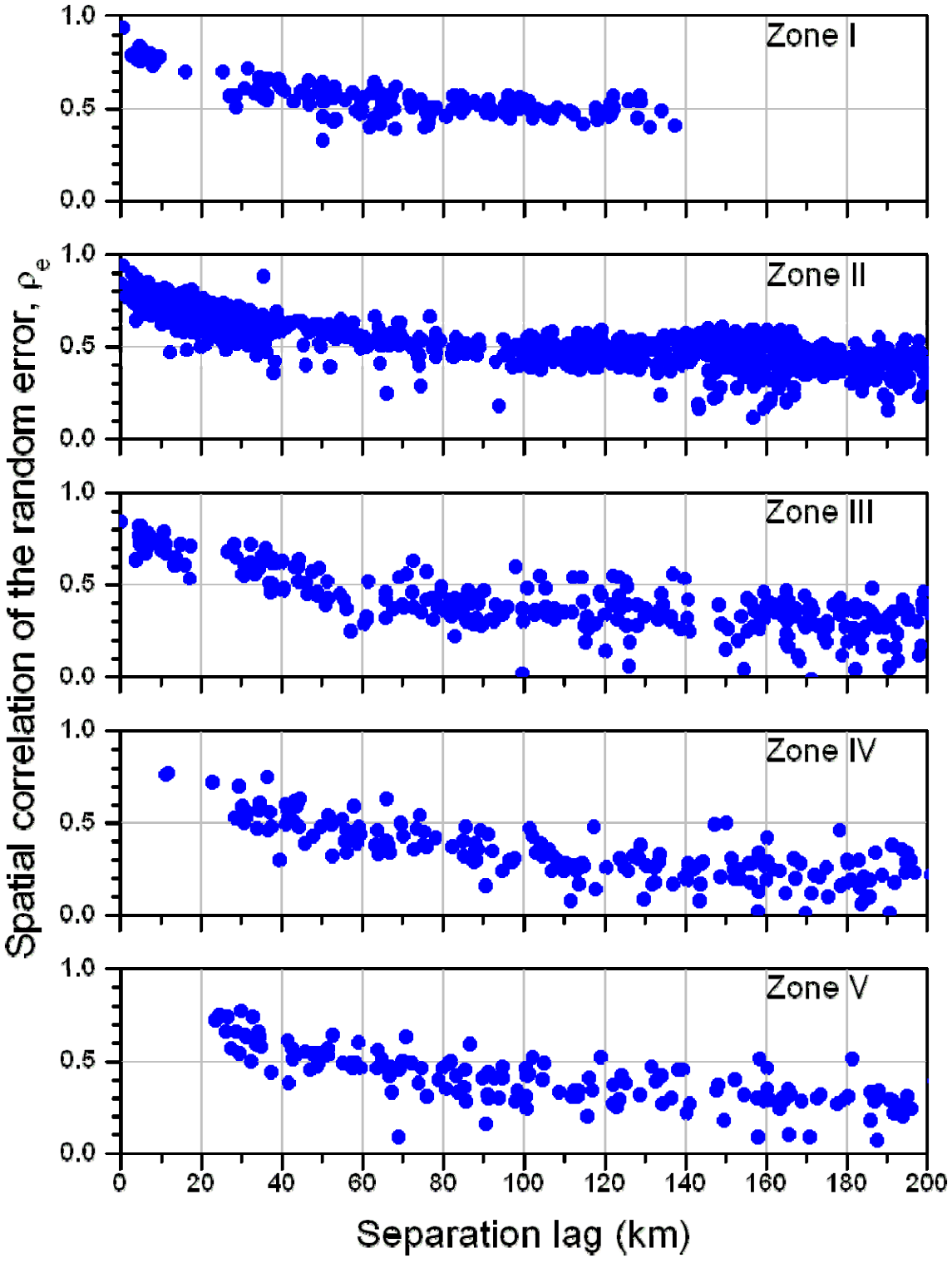

Figure 31. Intergauge spatial Pearson correlation of the random component for the cold season.

.

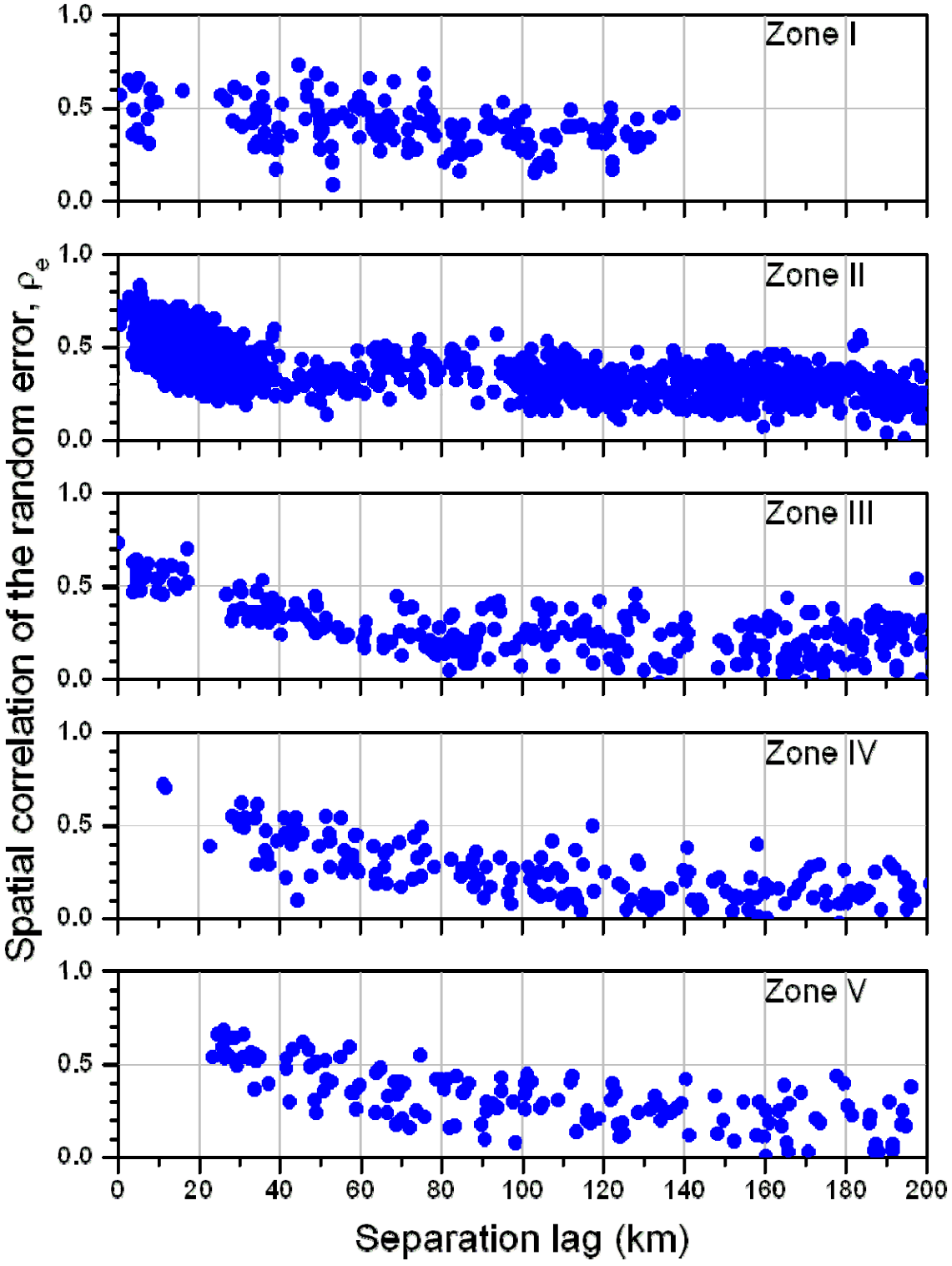

Figure 32. Intergauge spatial Pearson correlation of the random component for the warm season.

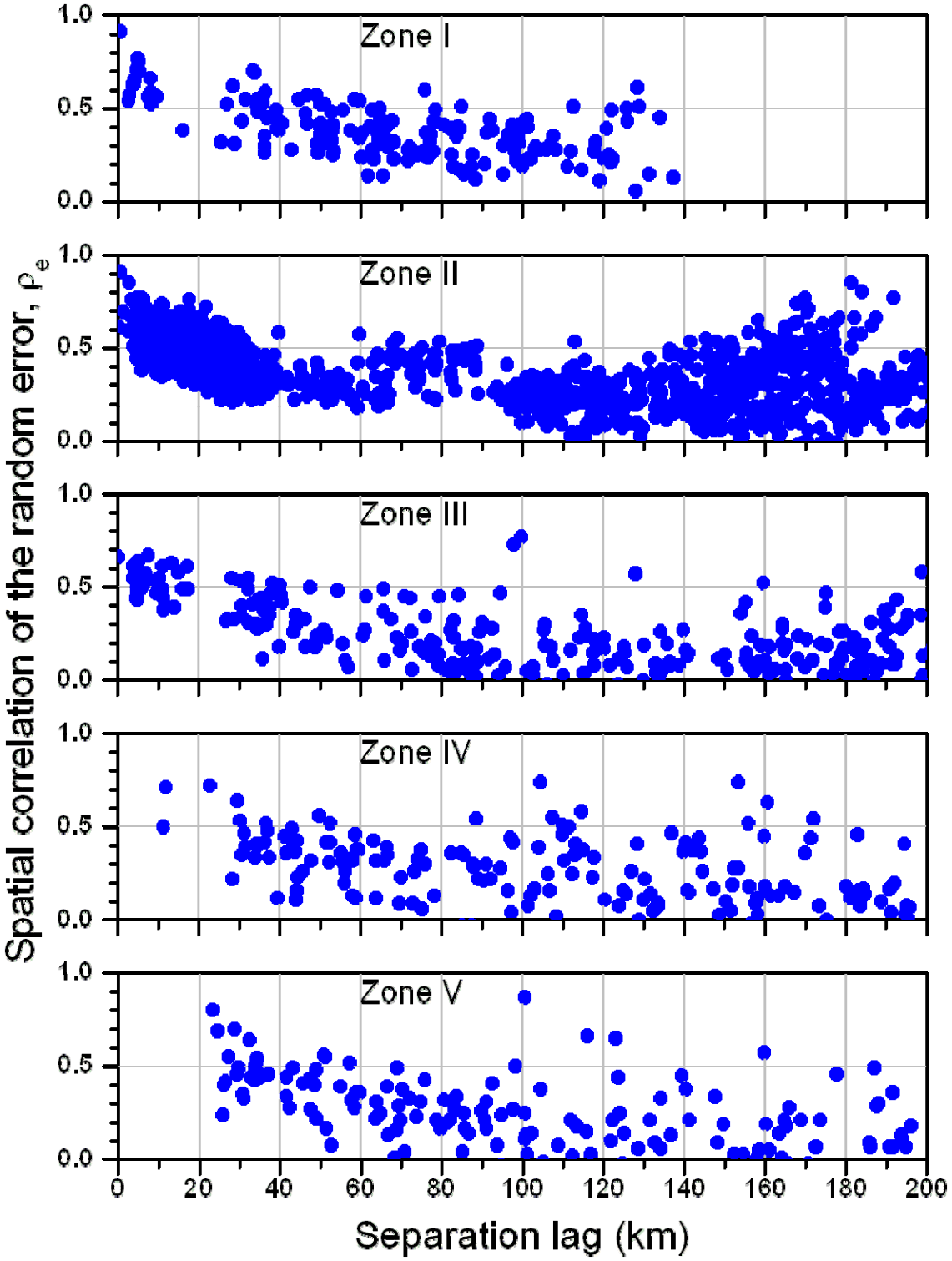

Figure 33. Intergauge spatial Pearson correlation of the random component for the hot season.

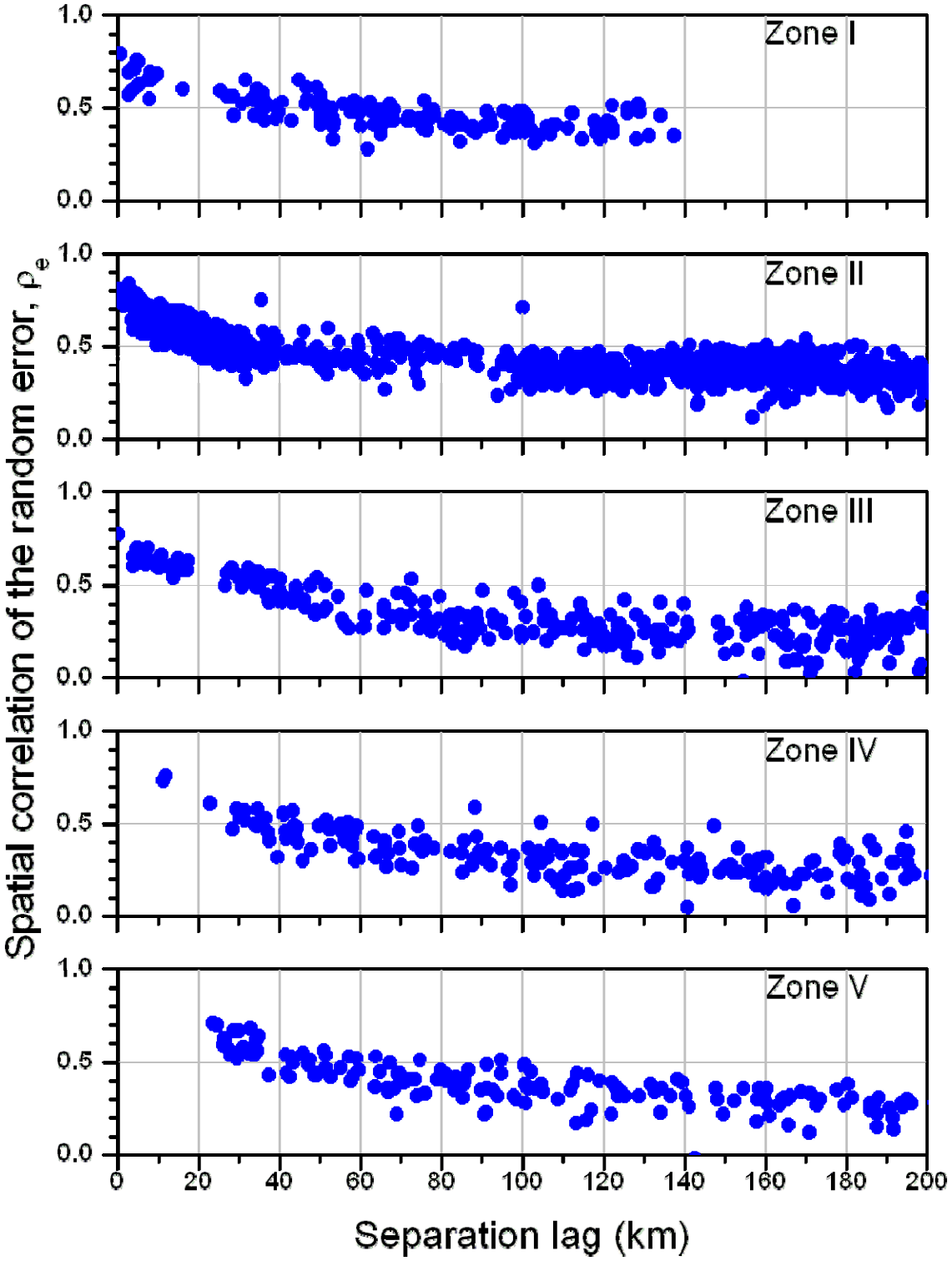

Figure 34. Intergauge spatial Pearson correlation of the random component for all seasons.

C.2. Error Modeling

C.2.1. Basic Model Structure

In this section we present results of approximating the previous analyses with simple parsimonious models. Such simple parametric models allow efficient implementation of the radar-rainfall error generator useful in ensemble based propagation of rainfall input uncertainties in hydrologic forecasting.

We already established that the probability distribution of the random component defined in the multiplicative form can be well approximated by Gaussian distribution, particularly for higher values of RR. Now we show that simple two-parameter power law type of models approximate very well the deterministic component. We used minimum least squares fitting criterion and found the optimal values of the parameters using a systematic search on a regular fine grid. Then, the results are used as initial values for the Levenberg-Marquardt algorithm.

The fit model confirms regular behavior of the deterministic component of the error model. The multiplier tends to 1 as we progress from cold to hot season and the power exponent does so too (Figures 35-39). Similarly, as we progress through temporal scales from hourly to daily, the coefficients displays regular behavior (Figures C8-C12, D8-D12, and E8-E12). We summarize the modeling of the deterministic component in Table 2.

Table 2. Two-parameter power law model coefficient values for the deterministic distortion function. The top value is the multiplier and the bottom one is the exponent.

	Time Scale											
	Hourly			**3-Hourly**			**6-Hourly**			**Daily**		
	Season			Season			Season			Season		
	Cold	Warm	Hot	Cold	Warm	Hot	Cold	Warm	Hot	Cold	Warm	Hot
Zone I	2.09 0.52	1.38 0.84	1.17 0.97	2.46 0.55	1.73 0.81	1.33 0.93	2.61 0.58	1.62 0.84	1.46 0.90	4.39 0.47	1.30 0.93	1.41 0.91
Zone II	1.84 0.55	1.34 0.84	1.35 0.87	3.24 0.43	2.03 0.74	1.38 0.89	4.02 0.42	2.18 0.73	1.53 0.86	5.94 0.36	2.84 0.68	1.36 0.91
Zone III	1.25 0.72	1.23 0.87	1.50 0.85	2.06 0.62	1.43 0.84	1.32 0.90	2.67 0.57	1.30 0.88	1.23 0.93	2.73 0.64	1.63 0.83	0.97 0.99
Zone IV	1.00 0.78	1.16 0.83	1.51 0.83	1.40 0.74	1.07 0.93	1.69 0.81	1.75 0.71	1.31 0.88	1.62 0.83	1.79 0.76	1.49 0.87	1.58 0.85
Zone V	2.03 0.45	1.95 0.63	1.25 0.85	2.79 0.46	2.07 0.67	1.80 0.76	2.51 0.55	2.22 0.68	1.80 0.77	2.13 0.66	2.14 0.72	1.40 0.86

Next we model the random component of the error model. Here too the power law model approximates the results of the data analyses well (Figures 40-44 and corresponding figures from the Appendixes). However, this time the model has three parameters. It turns out that adding an offset (or an asymptote) greatly improves the model fit. Indeed, in many cases (of time scale,

season and zone) the model and the data are indistinguishable. We summarize the modeling of the standard deviation of the random component in Table 3.

Table 3. Three-parameter power law model coefficient values for the standard deviation of the random component. The top value is the asymptote, the middle one the multiplier and the bottom one is the exponent.

	Time Scale											
	Hourly			**3-Hourly**			**6-Hourly**			**Daily**		
	Season			Season			Season			Season		
	Cold	Warm	Hot	Cold	Warm	Hot	Cold	Warm	Hot	Cold	Warm	Hot
Zone I	0.68 0.25 -1.09	0.51 0.53 -1.20	0.20 1.22 -0.52	0.71 0.34 -1.20	0.42 1.04 -0.86	0.18 1.82 -0.62	0.72 0.40 -1.21	0.38 1.37 -0.81	0.10 2.22 -0.58	0.53 0.80 -0.58	0.35 1.50 -0.67	0.00 2.76 -0.54
Zone II	0.71 0.30 -1.05	0.45 0.59 -0.62	0.34 0.97 -0.56	0.73 0.36 -1.13	0.40 0.92 -0.70	0.36 1.41 -0.73	0.72 0.40 -1.21	0.38 1.37 -0.81	0.10 2.22 -0.58	0.51 0.89 -0.59	0.32 1.51 -0.65	0.14 2.37 -0.60
Zone III	0.63 0.46 -0.77	0.15 1.00 -0.31	0.29 1.19 -0.52	0.60 0.66 -0.81	0.42 0.98 -0.72	0.31 1.60 -0.66	0.59 0.79 -0.80	0.36 1.24 -0.68	0.21 1.93 -0.59	0.36 1.12 -0.48	0.29 1.43 -0.59	0.11 2.56 -0.57
Zone IV	0.59 0.67 -0.74	0.56 0.96 -0.69	0.14 1.72 -0.44	0.34 1.17 -0.50	0.46 1.40 -0.68	0.19 2.04 -0.51	0.13 1.47 -0.38	0.40 1.59 -0.64	0.14 2.37 -0.51	0.00 1.63 -0.32	0.31 1.80 -0.57	0.00 2.85 -0.46
Zone V	0.69 0.85 -0.91	0.53 1.26 -0.62	0.38 1.85 -0.63	0.42 1.34 -0.54	0.60 1.38 -0.71	0.27 2.40 -0.58	0.22 1.61 -0.40	0.53 1.55 -0.65	0.15 2.69 -0.51	0.00 1.86 -0.29	0.26 1.82 -0.46	0.00 2.95 -0.43

C.2.2. Spatial and Temporal Dependence

Modeling spatial and temporal dependence requires an eligible covariance model. A good choice is a flexible three parameter model with exponential type decay (Figures 45-49 and corresponding figures from the Appendixes).

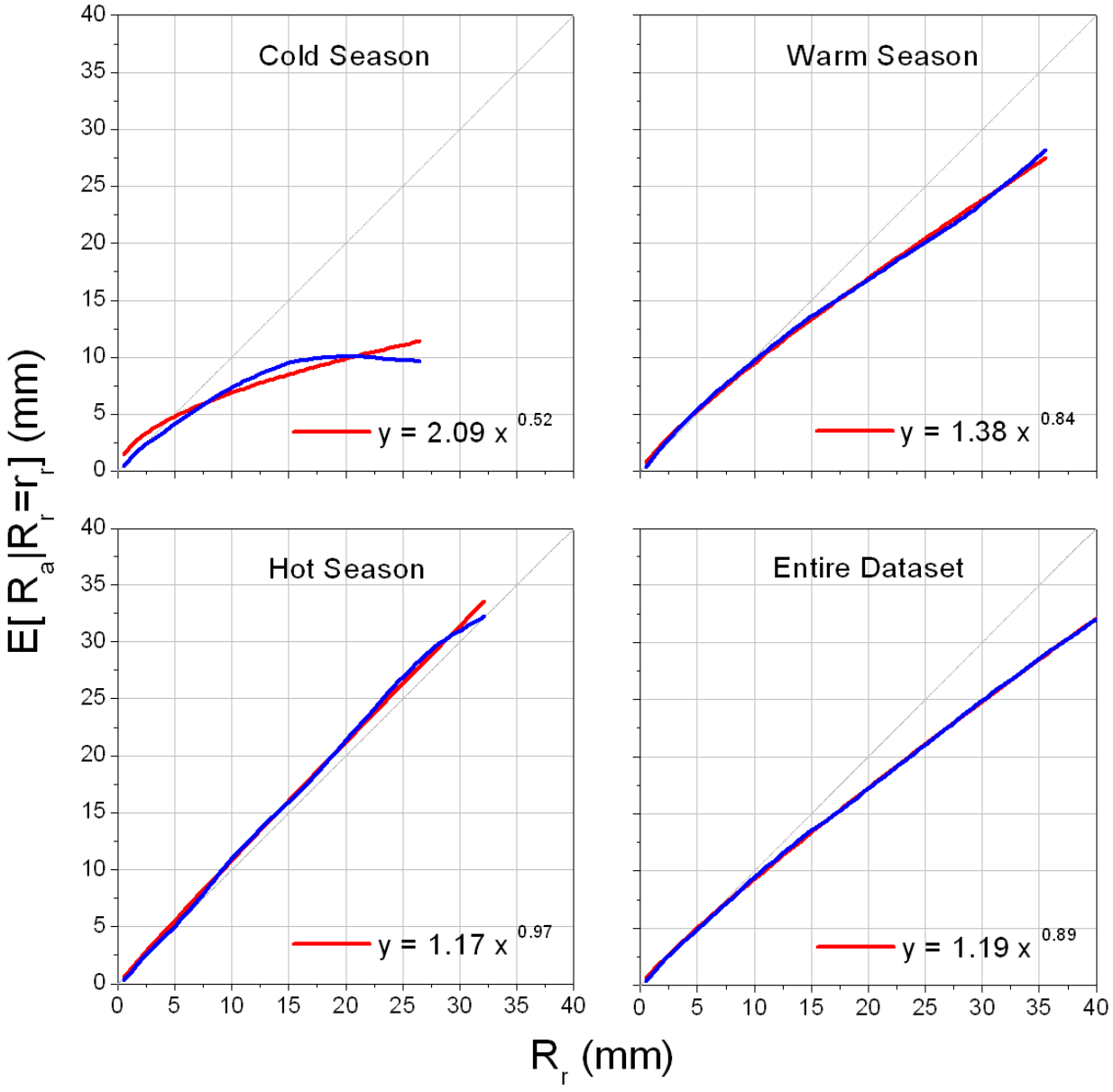

Figure 35. Modeling of the rain gauge conditional averages for Zone I. The blue lines correspond to the empirical result, the red lines are obtained from fitting the data with the indicated power law model.

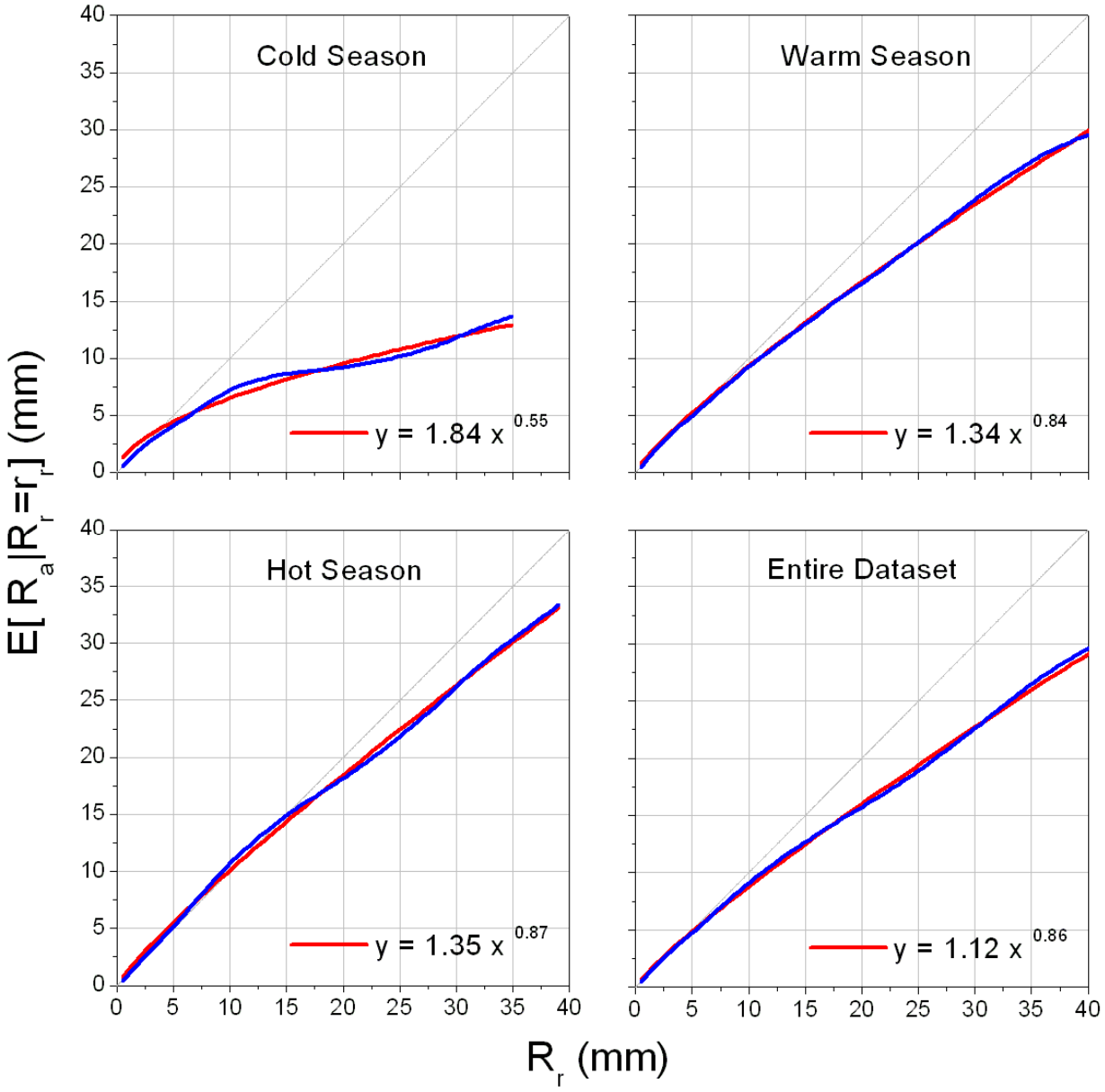

Figure 36. Modeling of the rain gauge conditional averages for Zone II. The blue lines correspond to the empirical result, the red lines are obtained from fitting the data with the indicated power law model.

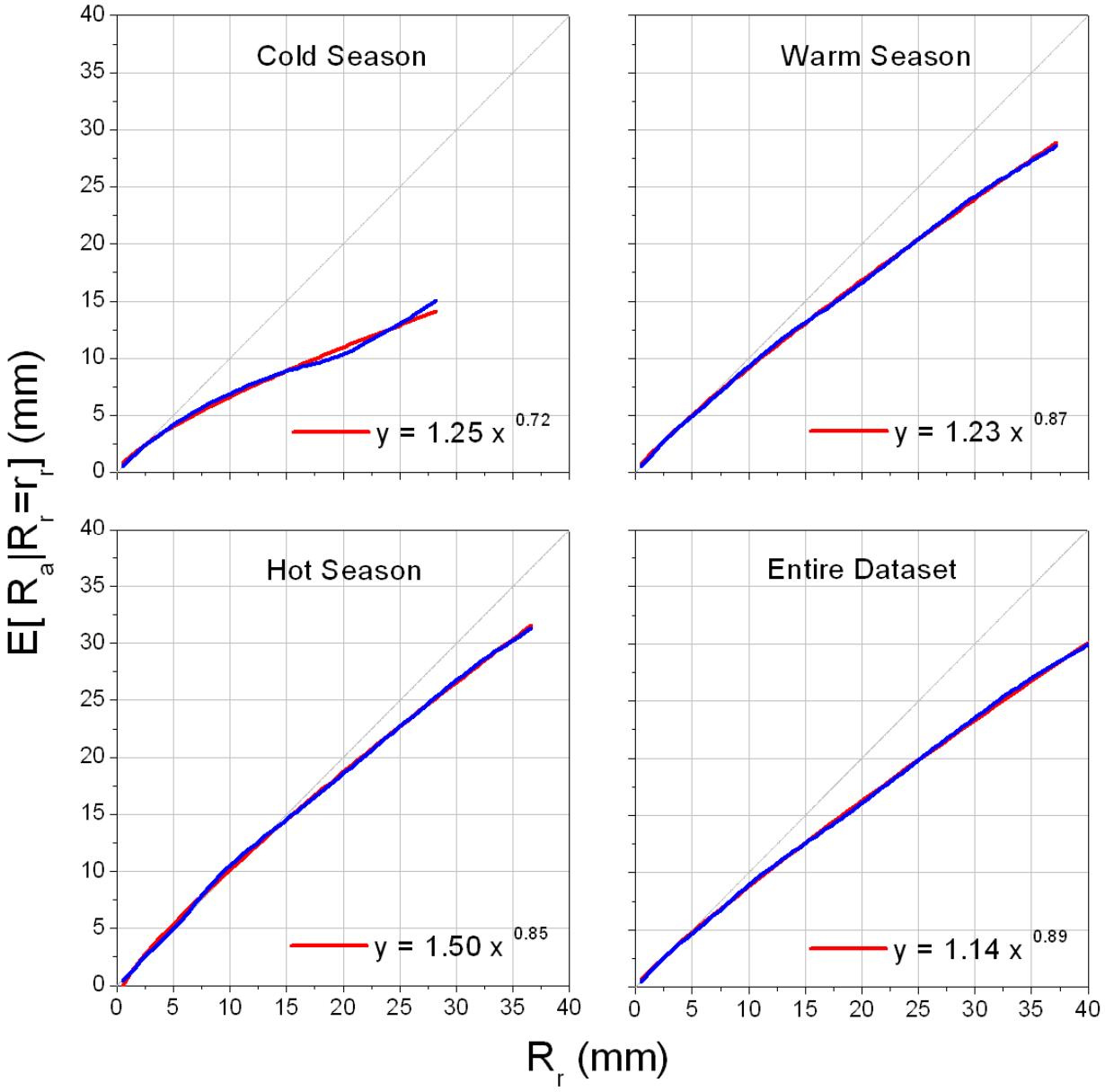

Figure 37. Modeling of the rain gauge conditional averages for Zone III. The blue lines correspond to the empirical result, the red lines are obtained from fitting the data with the indicated power law model.

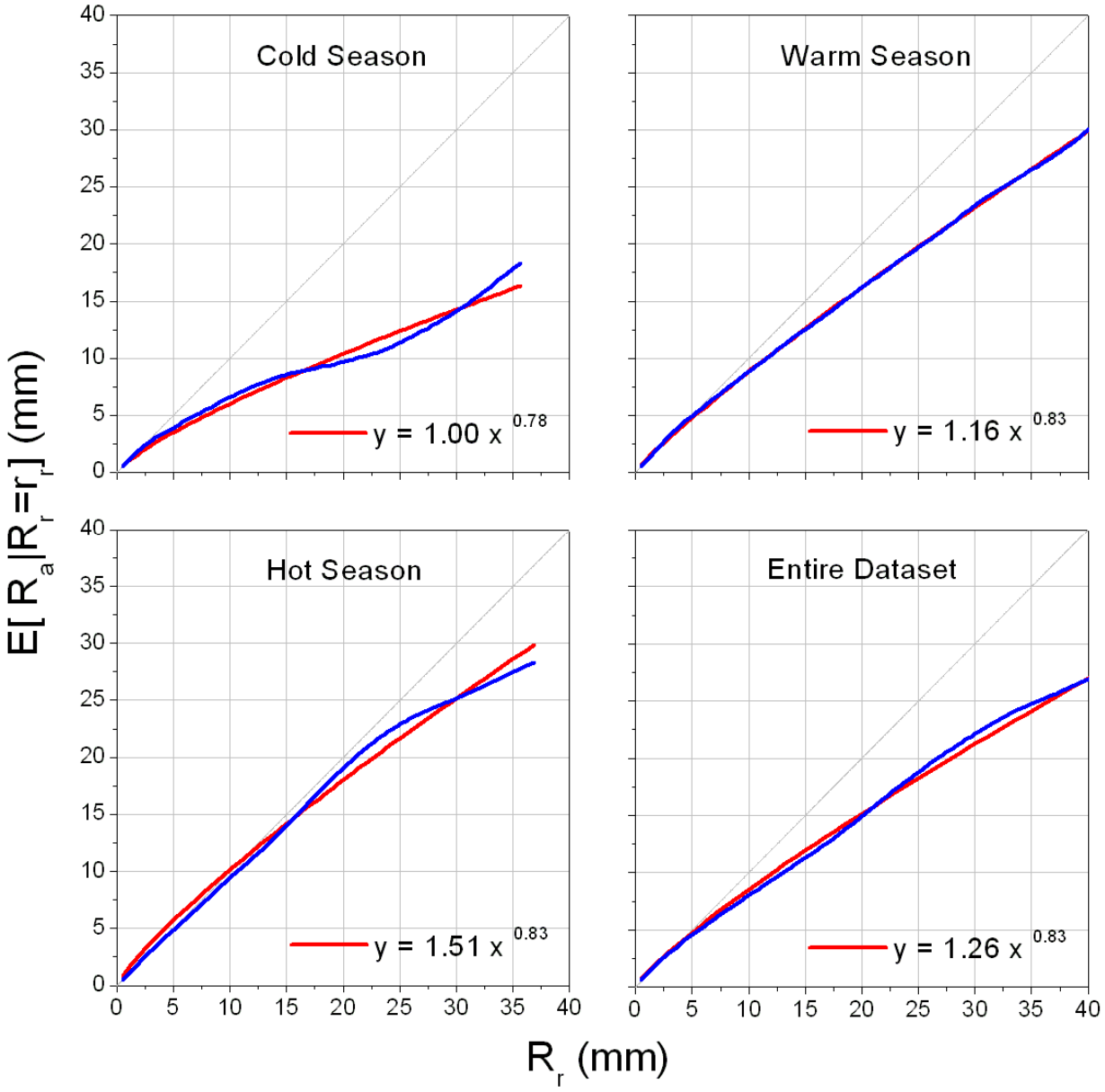

Figure 38. Modeling of the rain gauge conditional averages for Zone IV. The blue lines correspond to the empirical result, the red lines are obtained from fitting the data with the indicated power law model.

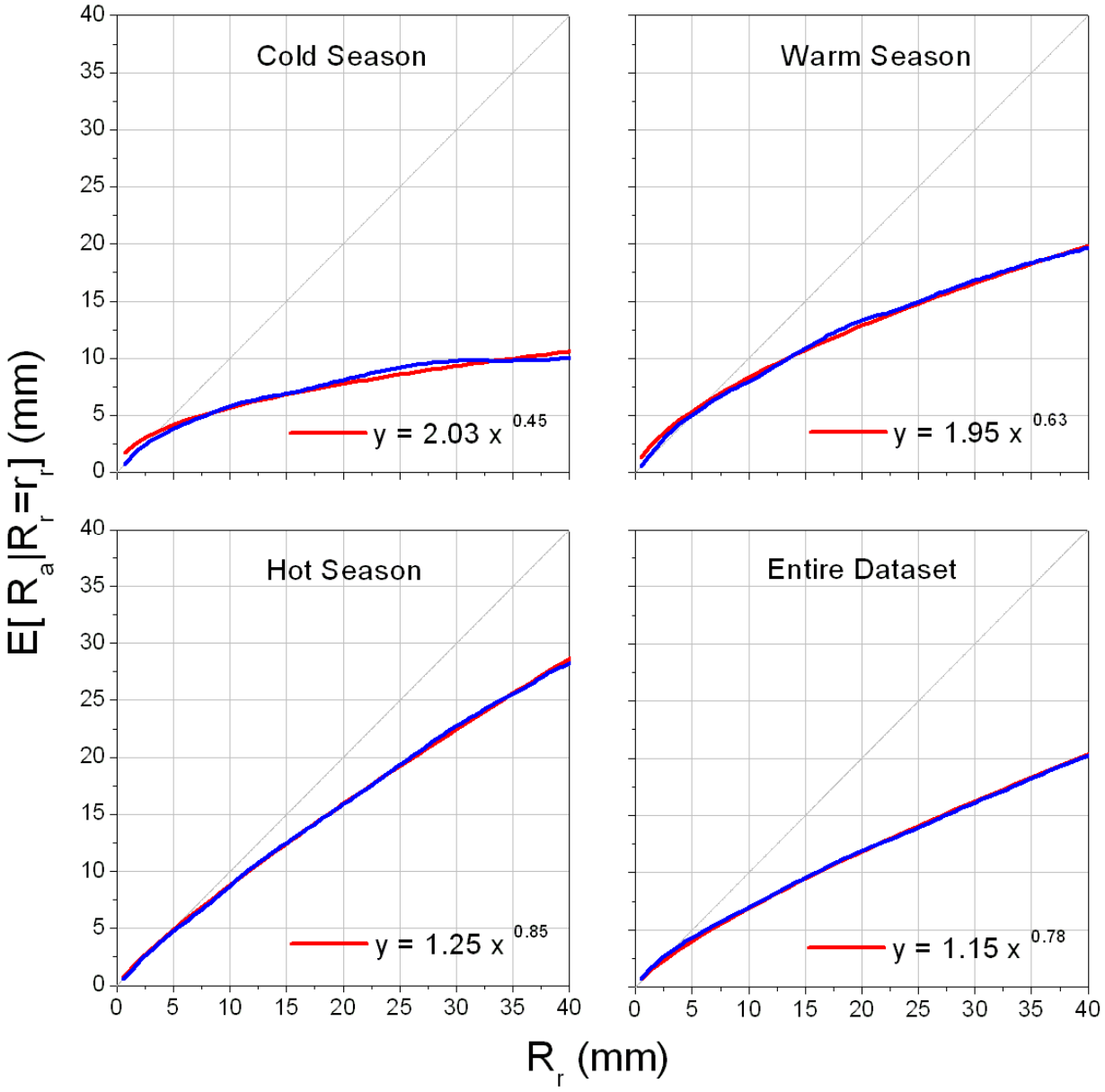

Figure 39. Modeling of the rain gauge conditional averages for Zone V. The blue lines correspond to the empirical result, the red lines are obtained from fitting the data with the indicated power law model.

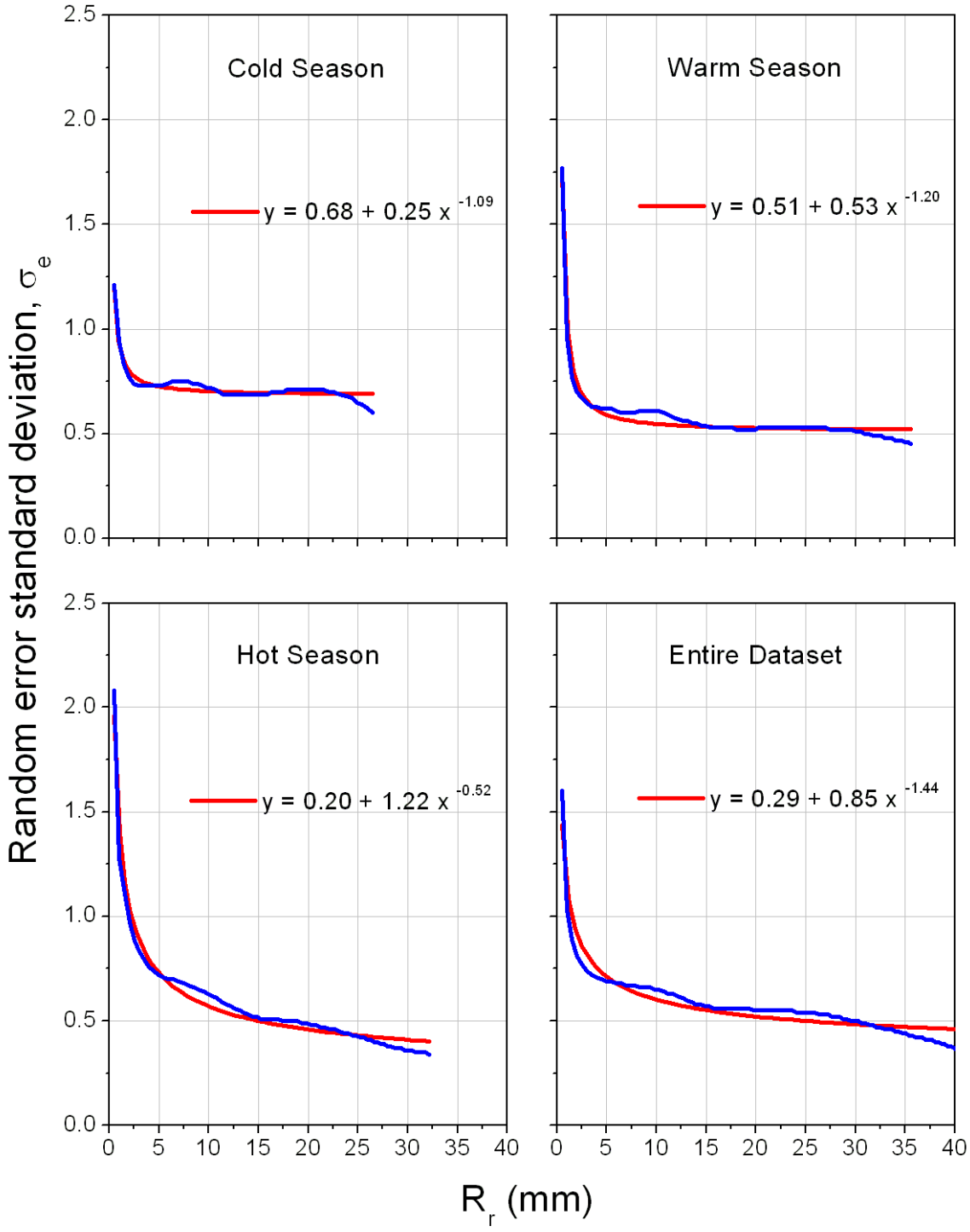

Figure 40. Modeling of the conditional random error standard deviation for Zone I. The blue lines correspond to the empirical result, the red lines are obtained from fitting the data with the indicated power law model.

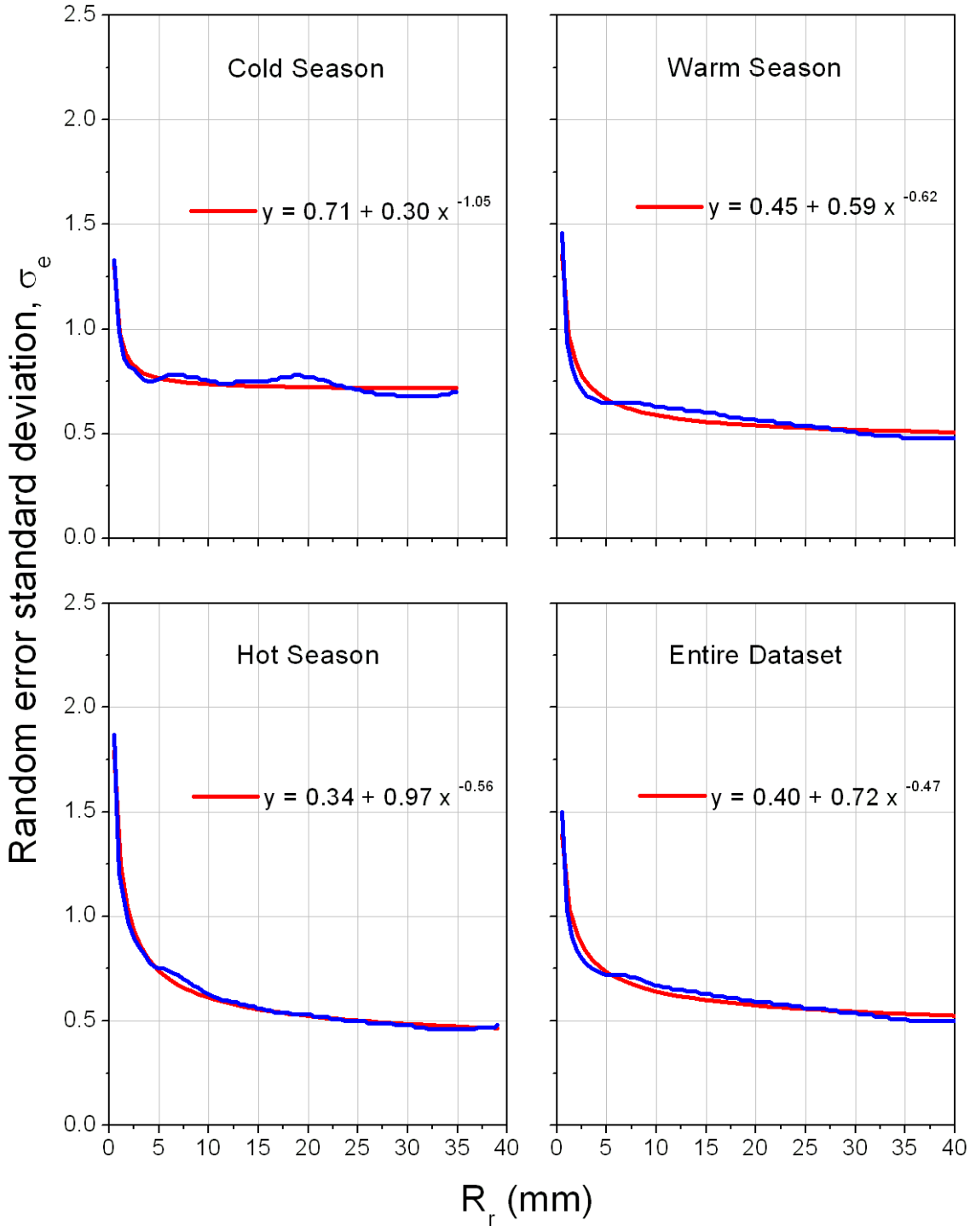

Figure 41. Modeling of the conditional random error standard deviation for Zone II. The blue lines correspond to the empirical result, the red lines are obtained from fitting the data with the indicated power law model.

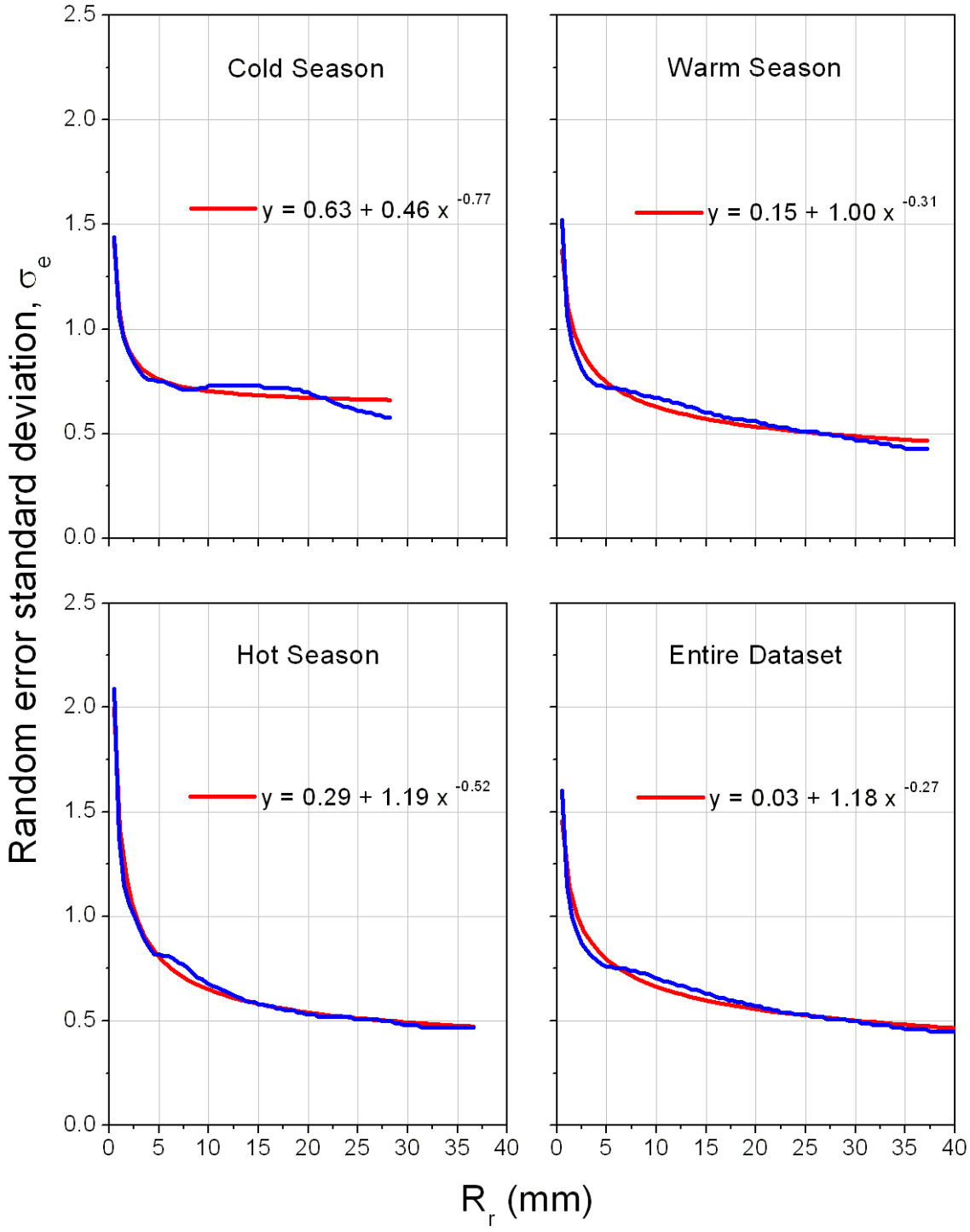

Figure 42. Modeling of the conditional random error standard deviation for Zone III. The blue lines correspond to the empirical result, the red lines are obtained from fitting the data with the indicated power law model.

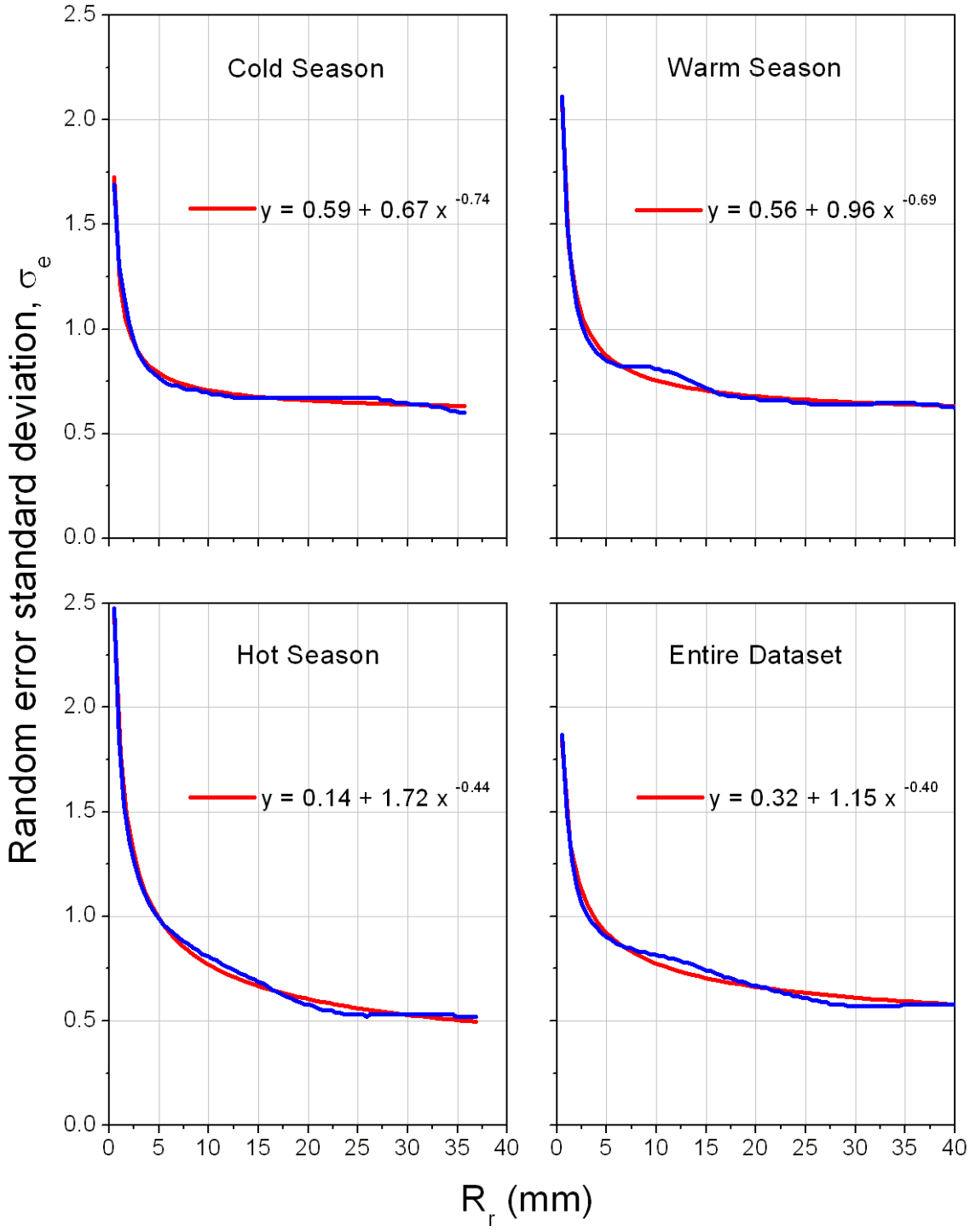

Figure 43. Modeling of the conditional random error standard deviation for Zone IV. The blue lines correspond to the empirical result, the red lines are obtained from fitting the data with the indicated power law model.

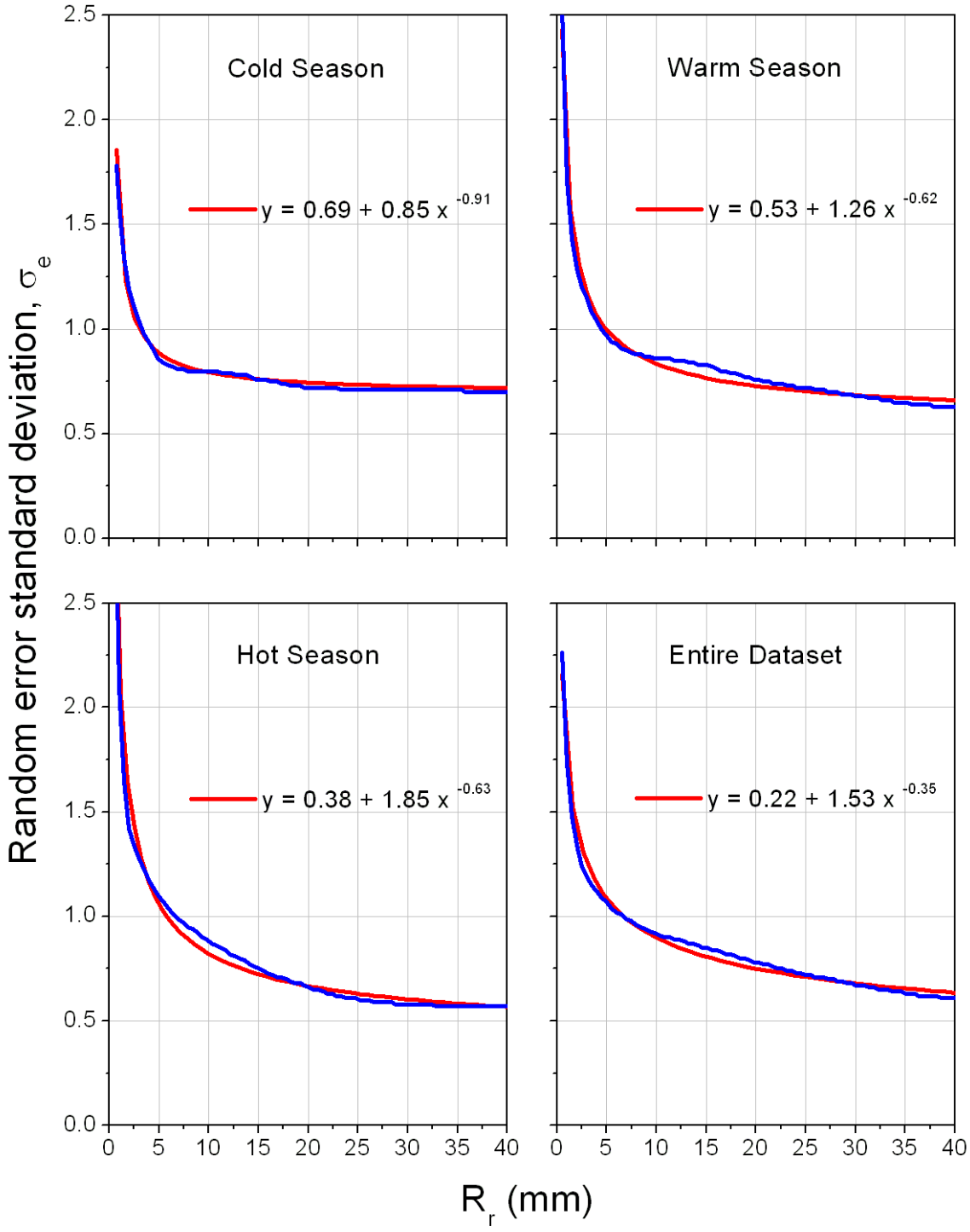

Figure 44. Modeling of the conditional random error standard deviation for Zone V. The blue lines correspond to the empirical result, the red lines are obtained from fitting the data with the indicated power law model.

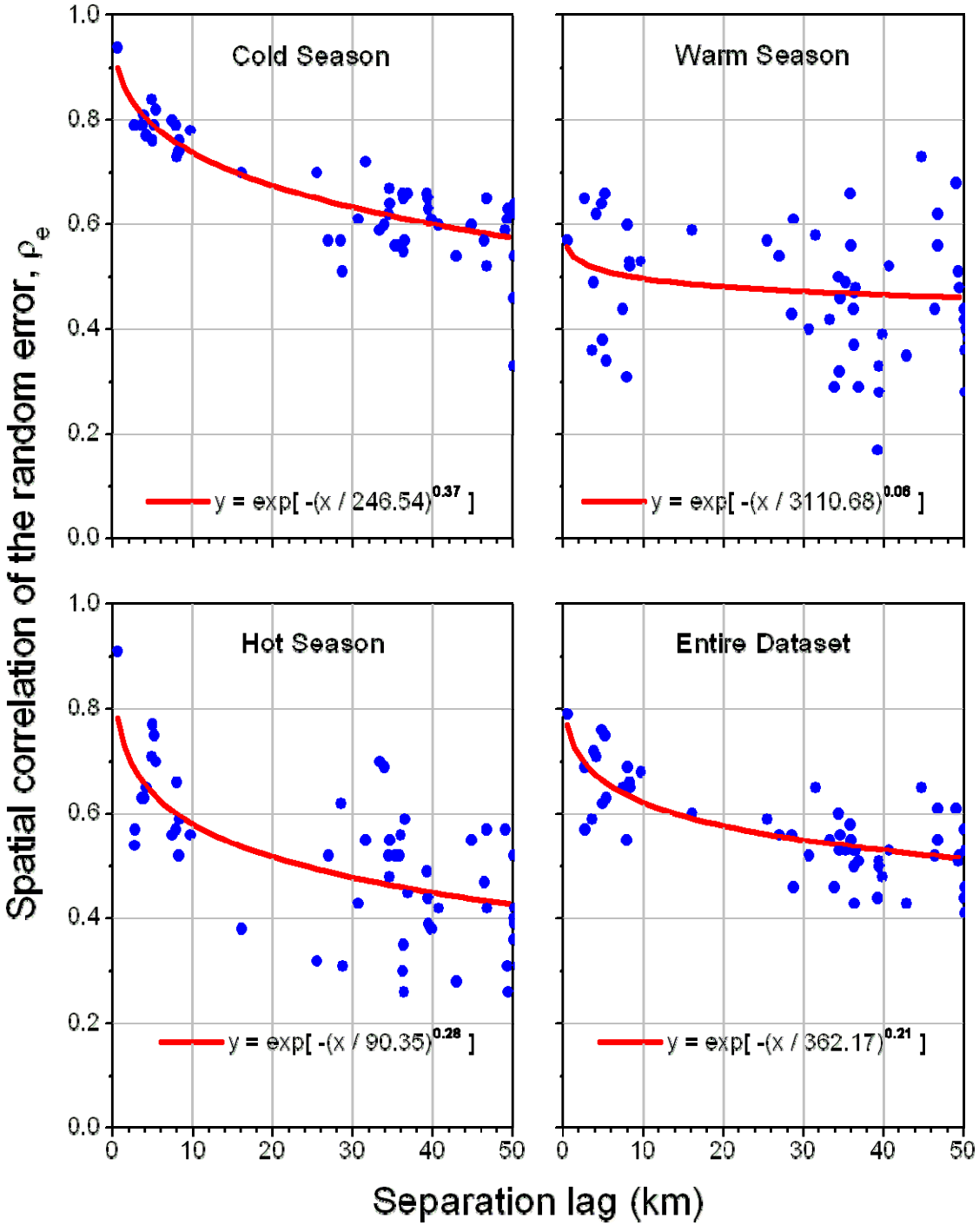

Figure 45. Empirical intergauge spatial correlation over a limited range with a three-parameter exponential model approximation for Zone I.

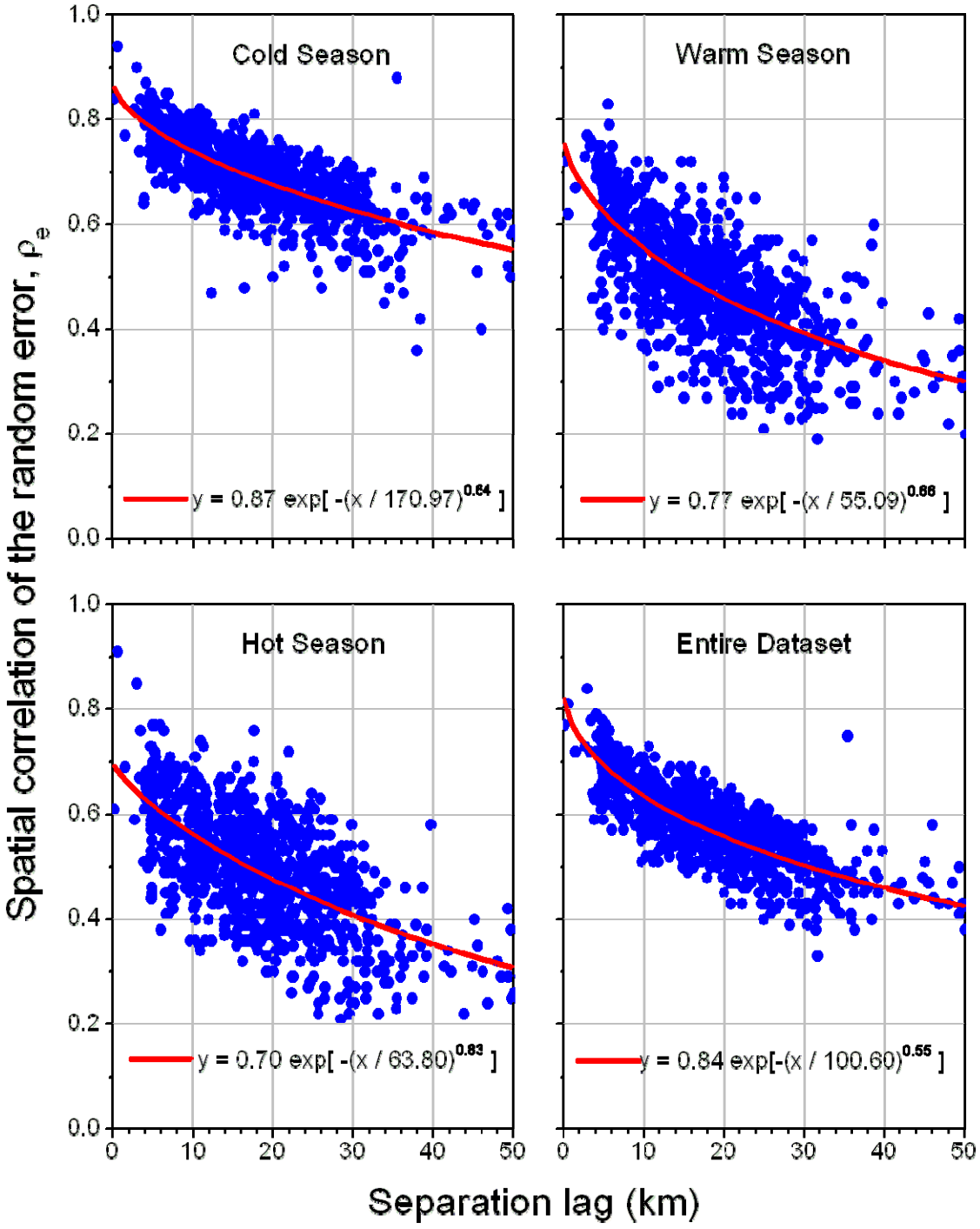

Figure 46. Empirical intergauge spatial correlation over a limited range with a three-parameter exponential model approximation for Zone II.

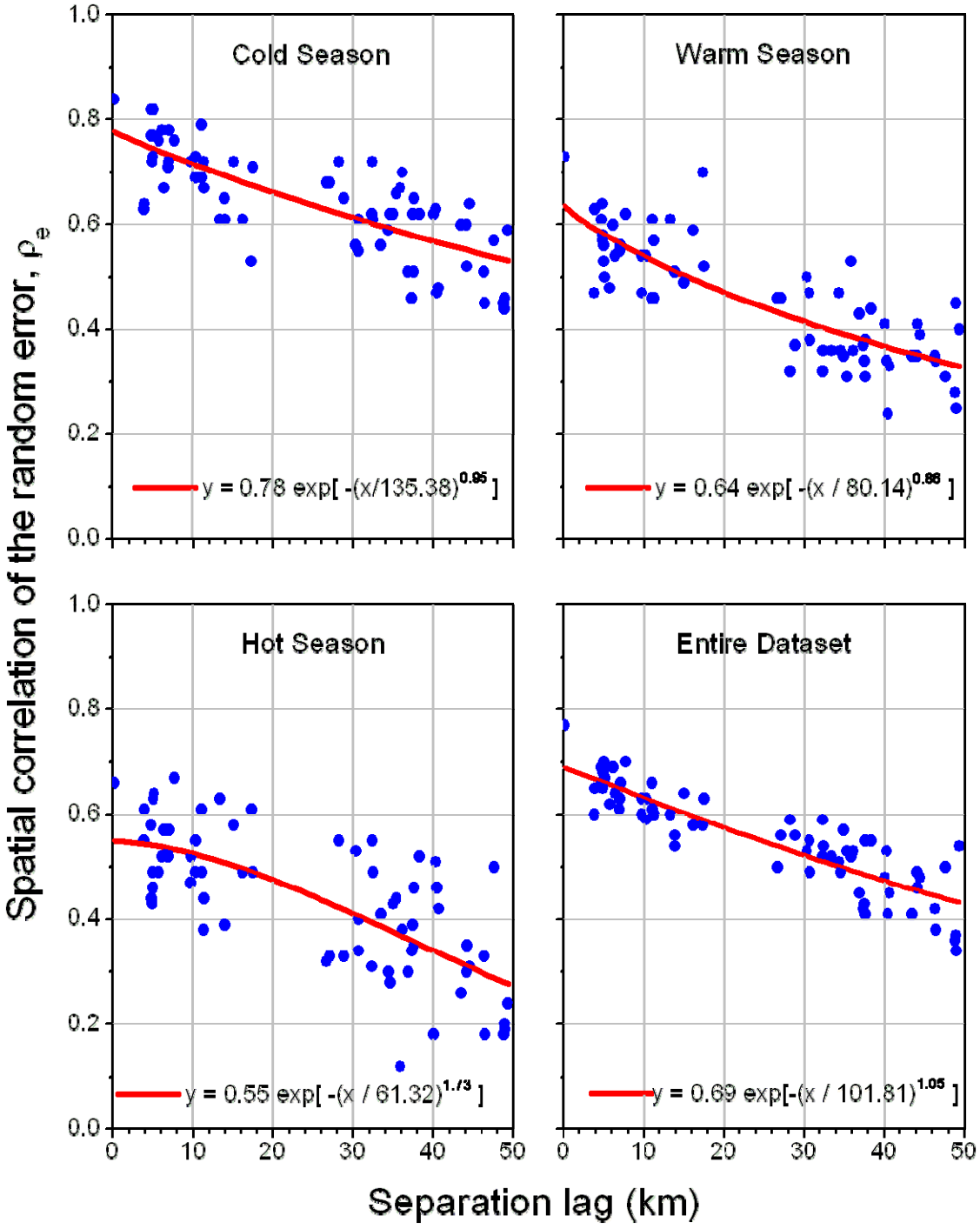

Figure 47. Empirical intergauge spatial correlation over a limited range with a three-parameter exponential model approximation for Zone III.

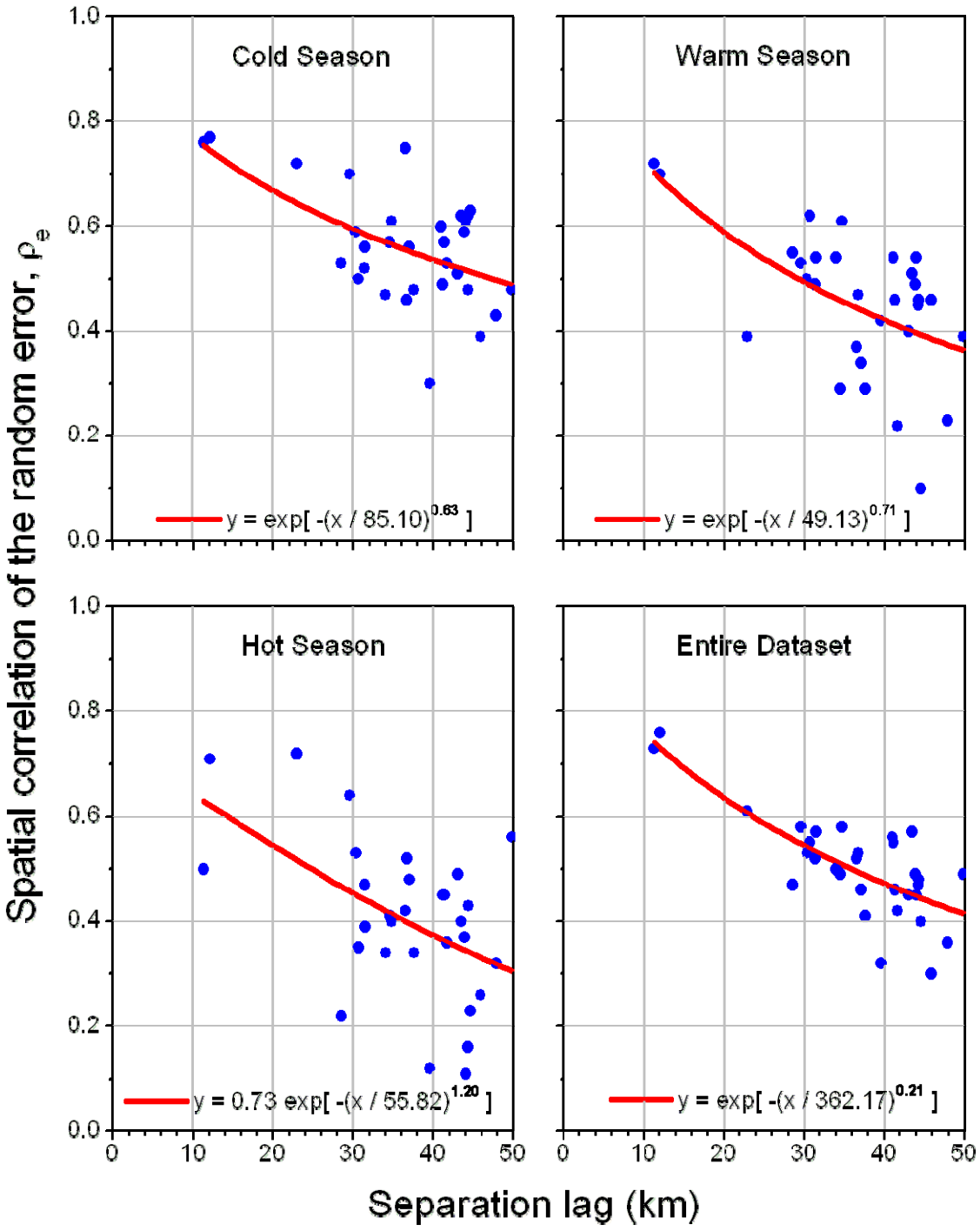

Figure 48. Empirical intergauge spatial correlation over a limited range with a three-parameter exponential model approximation for Zone IV.

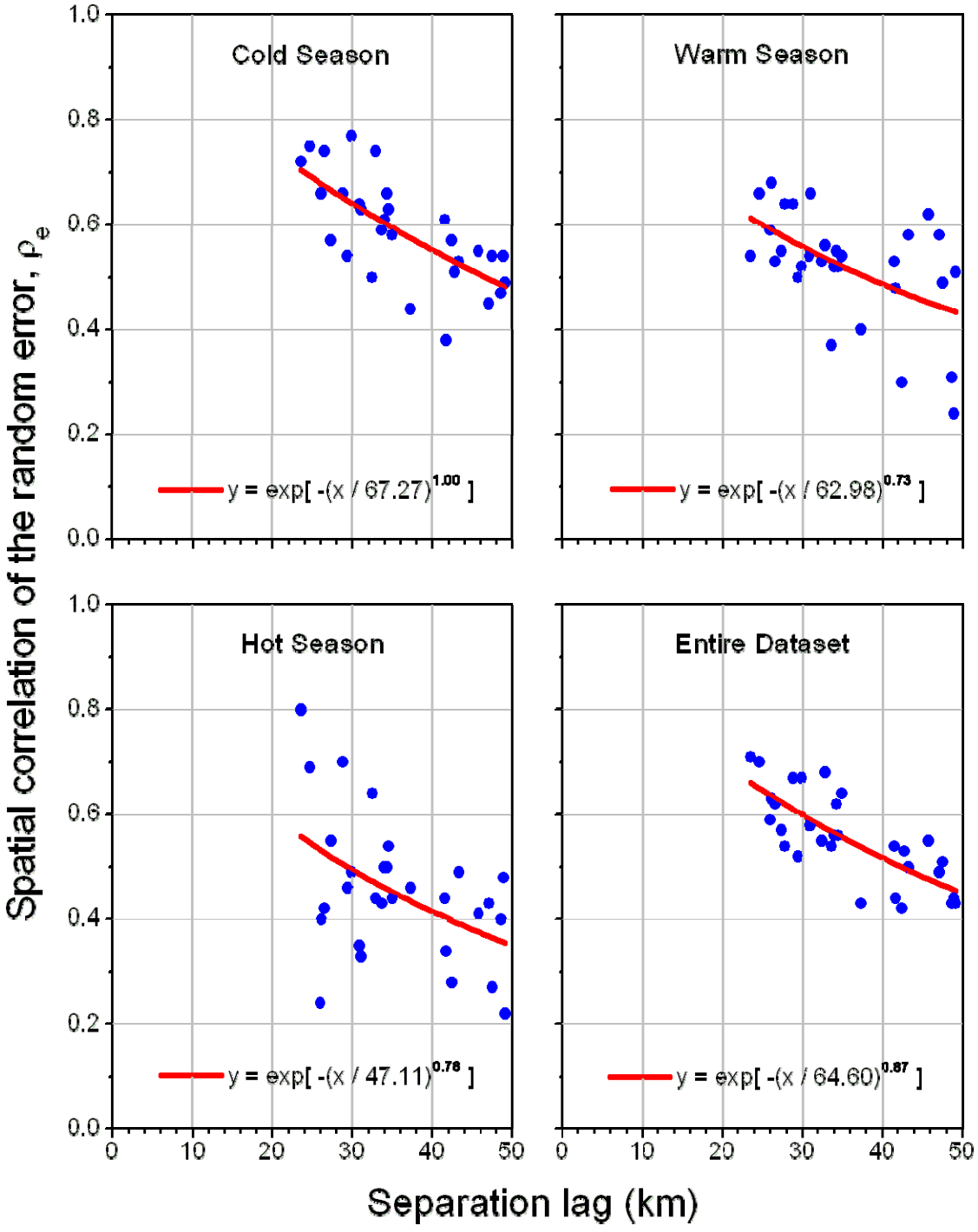

Figure 49. Empirical intergauge spatial correlation over a limited range with a three-parameter exponential model approximation for Zone V.

C.3. Probabilistic PQPE

To demonstrate the utility of our data analyses and modeling for radar based probabilistic quantitative rainfall estimation we consider two scenarios. The first one, which we refer to as static estimation, is based on a single hour of radar-estimated rainfall. The radar-rainfall field represents the DPA product. Using our error model we can estimate the corresponding probability of actual (true) rainfall exceeding some arbitrarily selected rainfall level. This rainfall level may correspond to, for example, a value determined by a component of the FFG system known as Thresh-R.

The second scenario assumes that an ensemble of a sequence of hourly rainfall fields is necessary as input to a hydrologic forecasting model. To do this a generator of different realization of RR error is necessary. The generator must preserve the statistical error structure we identified and modeled in this report. Below we briefly discuss and illustrate both scenarios.

C.3.1. Static Estimation

Consider two hourly rainfall events shown in Figure 50. The units are mm. For each of these events we can construct the corresponding probability maps: they represent the probability of exceedance a threshold value of, for example, 35 mm/h (Figure 51). To compute the maps we use the following algorithm on a pixel by pixel basis:

$$P(X \geq THRES) = 1 - \Phi(X) \tag{21}$$

where:

$$\Phi(X) = \frac{1}{2} + \frac{1}{2} erf(X) \tag{22}$$

and

$$X = \frac{x - \mu}{\sigma\sqrt{2}} = \frac{\dfrac{THRES}{DPA^*} - 1}{\sigma\sqrt{2}} = \frac{\dfrac{THRES}{a(B \cdot RR)^b} - 1}{\left[c + d(B \cdot RR)^e\right]\sqrt{2}} \tag{23}$$

where *, a* and *b* are the values of the parameters of the deterministic component model, *c, d, e* are the values of the standard deviation of the random component model for each zone, respectively, *B* is the value of the overall bias, and $B \cdot RR$ is the overall bias corrected radar-rainfall value observed at a given location in the field.

In Figure 52 we plot the maps of locations where the threshold is exceeded with probability given at six levels as follows $P(X \geq THRESH) \geq 0.10$, 0.25, 0.50. 0.75, 0.90, and 0.99. Computer code that performs this task is available upon request.

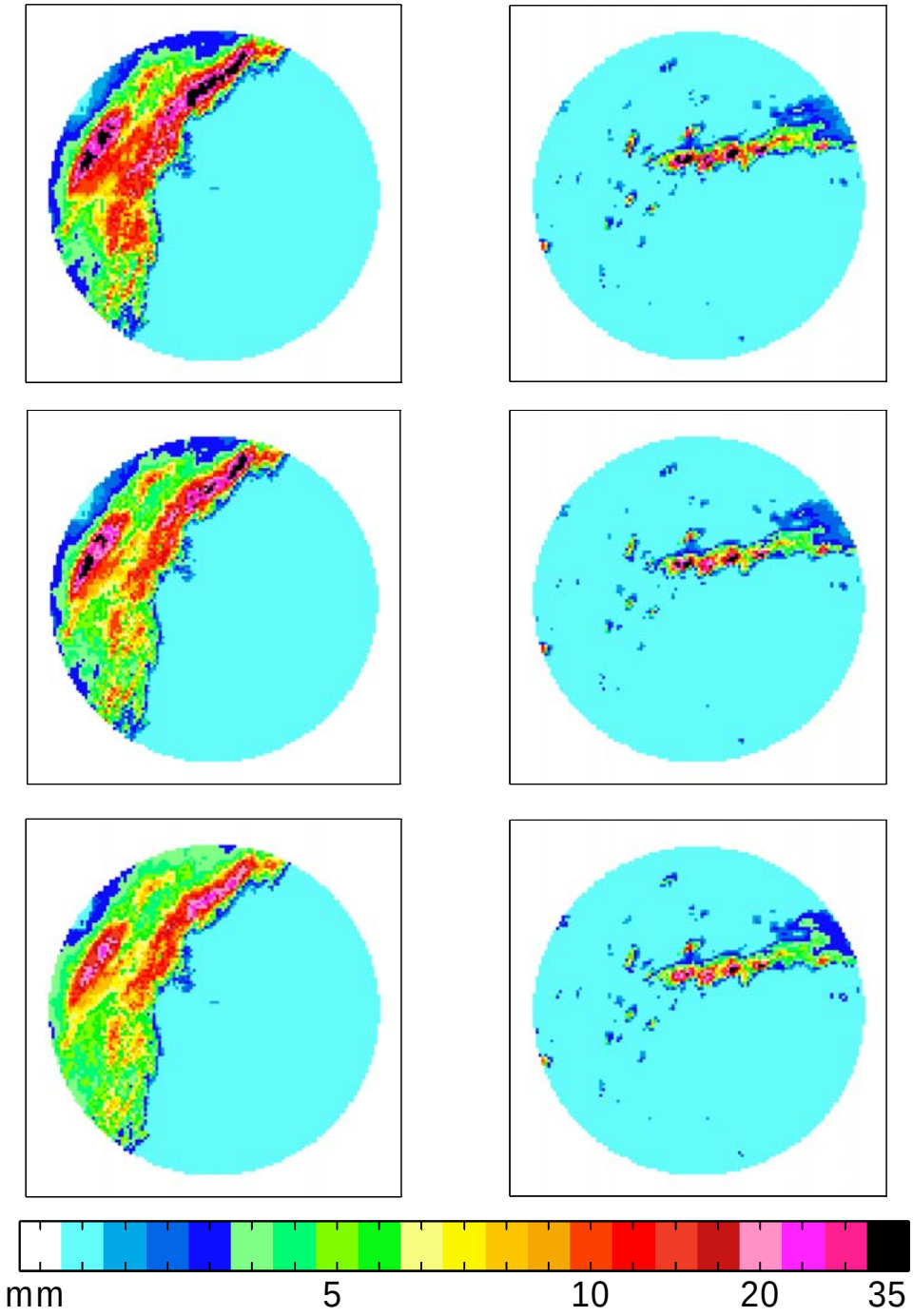

Figure 50. Two example hours with DPA maps (top panels), DPA maps after removing the overall bias (middle panels) and corresponding deterministic distortion functions (bottom panels). The corresponding maps of probability of exceedence of the threshold of 35 mm.

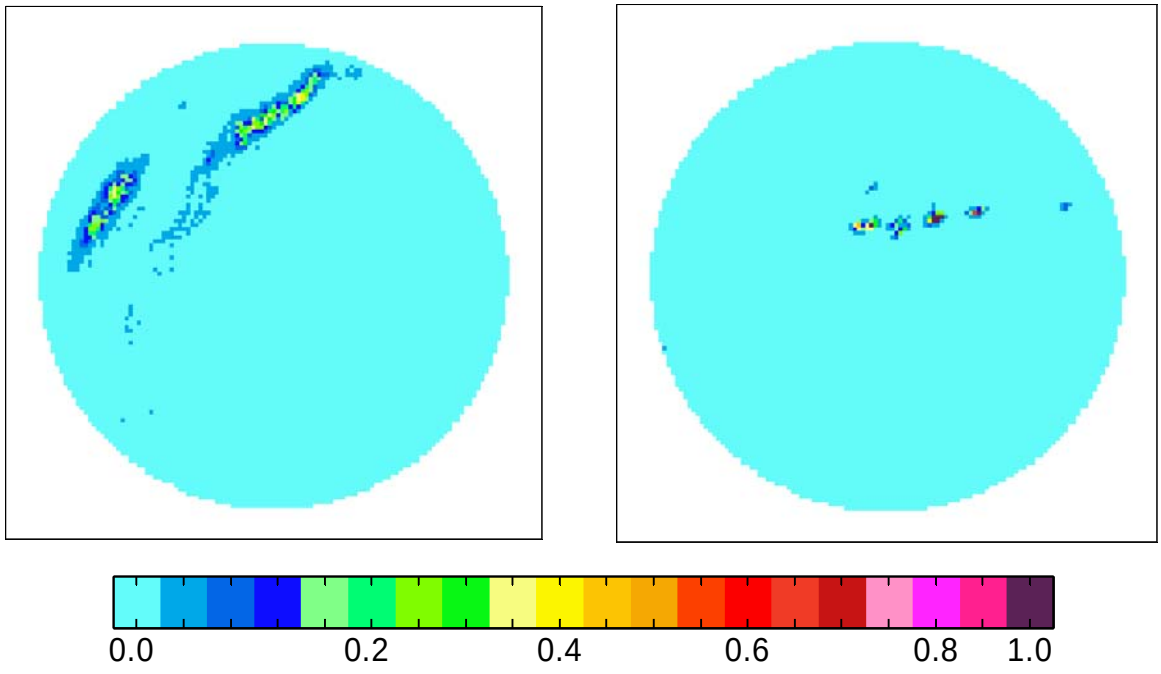

Figure 51. Maps of probability of exceedence of the threshold of 35 mm by the true rainfall for the two radar in Figure 51.

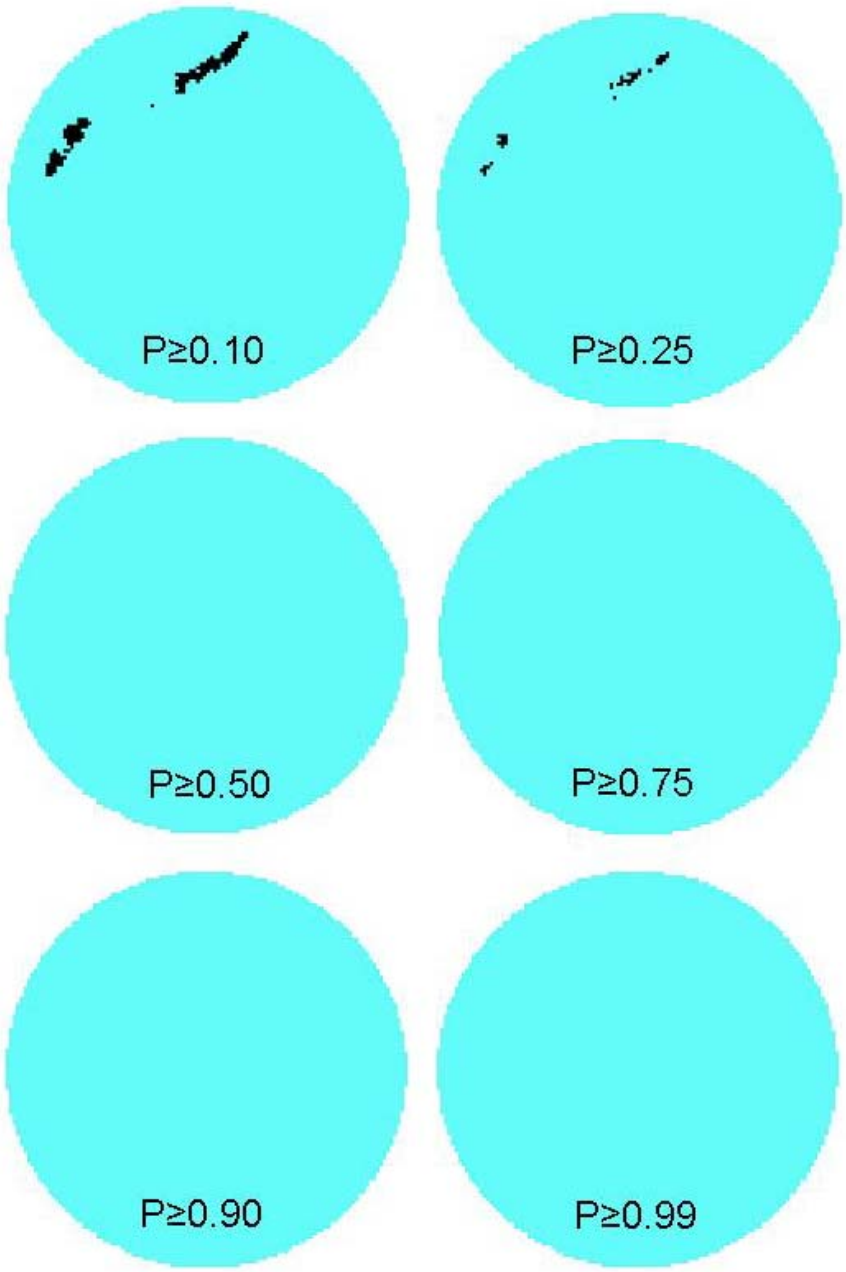

Figure 52. Maps indicating locations where the probability of exceedence is greater or equal to the indicated value.

C.3.2. Ensemble Generator

Following the notation from Krajewski and Georgakakos (1985), the synthetic radar-rainfall field *G(x, y)* can be expressed as:

$$\{G(x,y)\}_{s,t} = \{S(x,y)\cdot \varepsilon(x,y)\}_{s,t} \tag{24}$$

where $S(\cdot)$ is the deterministic distortion function, $\varepsilon(\cdot)$ is the random component, x and y are the field-point coordinates, while the subscripts s and t account for different season and time scale.

The coordinates x and y uniquely identify each zone; to provide smooth transition between adjacent zones, we compute the values for the overlapping areas as a distance-weighted combination of values of two neighboring zones. Notice that the zero-rainfall areas are preserved, due to the multiplicative nature of the generator.

Given the original DPA field *RR(x, y)*, the deterministic distortion function is given by

$$\{S(x,y)\}_{s,t} = \{a[B\cdot RR(x,y)]^b\}_{s,t} \tag{25}$$

where a and b are the deterministic distortion model parameters and B is the overall bias.

The random component $\varepsilon(x,y)$ has mean equal to 1, standard deviation $\sigma_e(RR(x,y))$, spatial correlation $\rho_s(\Delta s)$ and temporal correlation $\rho_t(\Delta t)$. The standard deviation of the random component is parameterized as:

$$\{\sigma_e(RR(x,y))\}_{s,t} = \left\{c + \frac{d}{[B\cdot RR(x,y)]^e}\right\}_{s,t} \tag{26}$$

where c, d and e are the random component parameters.

The correlation in space and time can be represented by a three-parameter exponential function as follows:

$$\{\rho_s(\Delta s)\}_{s,t} = \left\{a_0 \exp\left[-\left(\frac{\Delta s}{b_0}\right)^{c_0}\right]\right\}_{s,t} \tag{27}$$

$$\{\rho_t(\Delta t)\}_{s,t} = \left\{a_1 \exp\left[-\left(\frac{\Delta t}{b_1}\right)^{c_1}\right]\right\}_{s,t} \tag{28}$$

where a_0, b_0, and c_0 are the values of the parameters for the correlation function in space while a_1, b_1, and c_1 are the values of the parameters for the correlation function in time.

To generate random fields correlated in space and time with non-stationary variance, we use an algorithm (Cressie 1993) based on the Cholesky decomposition method. This method (e.g., Kreyszig 1999) allows writing a matrix A as the product of an upper- and lower- triangular matrices:

$$A = \begin{bmatrix} a_{11} & a_{12} & \dots & a_{1n} \\ a_{21} & a_{22} & \dots & a_{2n} \\ \dots & \dots & \dots & \dots \\ a_{n1} & a_{n2} & \dots & a_{nn} \end{bmatrix} = \begin{bmatrix} l_{11} & 0 & \dots & 0 \\ l_{21} & l_{22} & \dots & 0 \\ \dots & \dots & \dots & \dots \\ l_{n1} & l_{n2} & \dots & l_{nn} \end{bmatrix} \cdot \begin{bmatrix} l_{11} & l_{21} & \dots & l_{n1} \\ 0 & l_{22} & \dots & l_{n2} \\ \dots & \dots & \dots & \dots \\ 0 & 0 & \dots & l_{nn} \end{bmatrix} \tag{29}$$

where:

$$\begin{aligned} l_{ii} &= \sqrt{\left(a_{ii} - \sum_{k=1}^{i-1} l_{ik}^2 \right)} \\ l_{ji} &= \frac{a_{ji} - \sum_{k=1}^{i-1} \left(l_{jk} \cdot l_{ik} \right)}{l_{ii}} \end{aligned} \tag{30}$$

One condition for the use of the Cholesky decomposition is that the matrix has to be symmetric and definite positive. In this case, this condition is satisfied because the variance-covariance matrix from an exponential correlation function is symmetric and definite positive (Journel and Huijbregts 1978).

Let D be the domain over which we want to simulate the random field. In our case it is a regular grid with side n. As written above the random process $\{\boldsymbol{\varepsilon}(\mathbf{s}); \mathbf{s} \in D\}$ has the mean

$$\boldsymbol{\mu}(\mathbf{s}) \equiv 1, \qquad \mathbf{s} \in D \tag{31}$$

As far as the covariance is concerned, we assume a separable spatio-temporal model which we can write as:

$$C(\mathbf{s}_i - \mathbf{s}_j; \Delta t) = C(\mathbf{s}_i - \mathbf{s}_j) \cdot C(\Delta t) \qquad \mathbf{s}_i, \mathbf{s}_j \in D \tag{32}$$

where Δt is the time lag.

To account for non-stationarity in the variance, we can multiply the variance-covariance matrix by $\sigma_e(RR(x,y))$:

$$\Sigma = \sigma_e^2(RR(x,y)) \cdot C(\mathbf{s}_i - \mathbf{s}_j) \cdot C(\Delta t) \qquad \mathbf{s}_i, \mathbf{s}_j \in D \tag{33}$$

Therefore, the variance-covariance matrix at time t_0 can be written as:

$$\Sigma = \begin{bmatrix} \sigma_1^2 & \sigma_1\sigma_2\rho_s(|\mathbf{s}_{12}|)\rho_t(t_0) & .... & \sigma_1\sigma_{n\cdot n}\rho_s(|\mathbf{s}_{1nn}|)\rho_t(t_0) \\ \sigma_2\sigma_1\rho_s(|\mathbf{s}_{21}|)\rho_t(t_0) & \sigma_2^2 & ... & \sigma_2\sigma_{n\cdot n}\rho_s(|\mathbf{s}_{2nn}|)\rho_t(t_0) \\ ... & ... & ... & ... \\ \sigma_{n\cdot n}\sigma_1\rho_s(|\mathbf{s}_{n\cdot n1}|)\rho_t(t_0) & \sigma_{n\cdot n}\sigma_2\rho_s(|\mathbf{s}_{n\cdot n2}|)\rho_t(t_0) & ... & \sigma_{n\cdot n}^2 \end{bmatrix} \quad (34)$$

At time t_1 we have:

$$\Sigma = \begin{bmatrix} \sigma_1^2 & \sigma_1\sigma_2\rho_s(|\mathbf{s}_{12}|)\rho_t(|t_{10}|) & .... & \sigma_1\sigma_{n\cdot n}\rho_s(|\mathbf{s}_{1nn}|)\rho_t(|t_{10}|) \\ \sigma_2\sigma_1\rho_s(|\mathbf{s}_{21}|)\rho_t(|t_{10}|) & \sigma_2^2 & ... & \sigma_2\sigma_{n\cdot n}\rho_s(|\mathbf{s}_{2nn}|)\rho_t(|t_{10}|) \\ ... & ... & ... & ... \\ \sigma_{n\cdot n}\sigma_1\rho_s(|\mathbf{s}_{n\cdot n1}|)\rho_t(|t_{10}|) & \sigma_{n\cdot n}\sigma_2\rho_s(|\mathbf{s}_{n\cdot n2}|)\rho_t(|t_{10}|) & ... & \sigma_{n\cdot n}^2 \end{bmatrix} \quad (35)$$

where $s_{ij}=s_i-s_j$ *and* $t_{i0}=t_0-t_i$. Applying the Cholesky decomposition to the variance-covariance matrix, we obtain $\Sigma = LL'$.

It is possible to write

$$\boldsymbol{\varepsilon} = \boldsymbol{\mu} + \mathbf{L}\boldsymbol{\eta} \quad (36)$$

where $\boldsymbol{\eta}$ is a vector of uncorrelated random variables with mean equal to zero and variance equal to 1:

$$\boldsymbol{\eta} \equiv (\eta(\mathbf{s}_1), ..., \eta(\mathbf{s}_{n\cdot n}))' \qquad \mathbf{s}_1,...,\mathbf{s}_{n\cdot n} \in D \quad (37)$$

In this way, we can generate a field with mean equal to 1 and with the aforementioned spatio-temporal correlation and variance. Therefore, given a radar-rainfall field *RR(x, y)*, we have to generate *r* random fields $\varepsilon(x, y)$ and multiply each of them by *S(x, y)* in order to obtain *r* synthetic radar-rainfall maps.

In Figure 53 we plot the original field (upper left panel) and three simulated fields following this methodology.

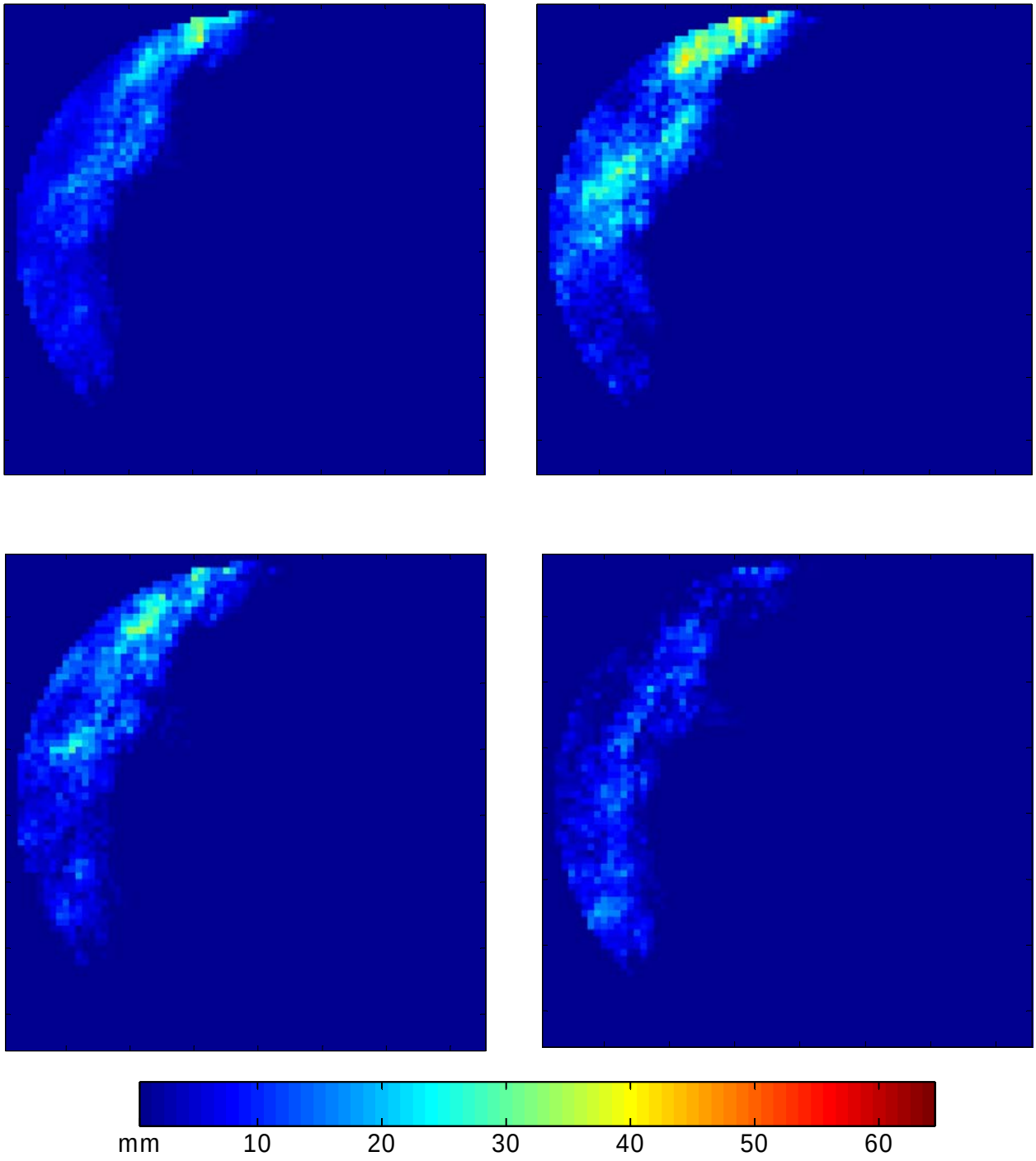

Figure 53. An example of an hourly radar-rainfall map (corrected for the overall bias; upper left panel) and three realizations that have the error structure compatible with the uncertainty model we have developed.

D. CLOSING NOTES

In this report we presented results of investigations leading towards development of probabilistic algorithms for radar-based rainfall estimation. Such algorithm may be called radar PQPE, for probabilistic quantitative precipitation estimation. We took the approach of developing a stochastic model of the combined sources of uncertainty affecting radar-rainfall estimates. The model is strongly based in empirical evidence resulting from an extensive analysis of actual data.

At this stage of development the model's validity is restricted to HRAP spatial scale of radar-rainfall products and the temporal scales (or accumulations) of 1, 3, 6, and 24 hours. The model allows quick generation of the probability maps that the true rainfall in a given location is greater then or equal to a given, user specified threshold. The model also allows generating multiple realizations of plausible "true" rainfall fields at the same resolution as the operational products. Therefore, the model can be used to generate ensembles of inputs sequences for hydrologic rainfall-runoff models.

One should keep in mind that the model is product (QPE algorithm) specific. Therefore, hourly radar-rainfall maps, even at the same spatial grid (HRAP) but produced by a different algorithm (e.g. Z-R relationship, range correction, advections correction, etc.) may have different uncertainty structure. To what extend this structure would be different from the one we estimated herein remains to be explored. Several other aspects of model development remains to be further explored. These include modeling of shorter temporal scales of rainfall accumulation, modeling smaller as well as larger spatial scales, investigation of the random component spatial and temporal correlation, the issue of ground reference representativeness, and the transferability of the results to other areas. We briefly discuss those below.

As users of radar-rainfall maps often require higher resolution than that of HRAP grid, we plan to explore spatial scales of 1×1 km^2 and 2×2 km^2 as well as the polar grid that corresponds to radar data acquisition (1 km by 1 degree). However, it is not possible to develop such products using the current version of CODE. We are planning to use our own software that will be similar to the PPS but will allow us more flexibility in generating products at different spatial scales. Investigating larger than HRAP scales is easy by aggregating the current products.

As far as shorter temporal scales are concerned, we are planning to investigate the scales of 5 minutes and 15 minutes. This brings the issue of adequacy of reference data. The representativeness of rain gauge data to study radar-rainfall uncertainty structure involves and interesting interplay of rainfall variability in space and time and the size of the investigate domain (scale). Shorter period rainfall accumulations vary significantly more than longer period accumulation (e.g. Ciach and Krajewski 2005, Appendix B). On the other hand, the smaller the size of the grid, the more representative rain gauge data are of the true area rainfall over that grid location. Thus, our studies of 1×1 km^2 and 2×2 km^2 as well as the polar grid products will be statistically more significant that the current (HRAP grid) results. At the same time, using the

same rain gauge data to study error at larger grids (e.g. 8×8 km^2, 16×16 km^2) will result in less meaningful error characterization. Also, at shorter time scale the random errors in the rain gauge data are more significant, in particular at 5 minute time scale (Ciach 2003).

To address the issue of transferability of our results, we are planning to repeat the analysis we conducted in this project using data from other networks. In particular, we plan to use data from the dense rain gauge network around Iowa City. We are also planning to use radar data from other Oklahoma WSR-88Ds in conjunction with the same rain gauge data. For example, using radar data from the Vance AFB will allow us to study the spatial correlation of the random component at far distances from the radar (Zone V) where the current scarcity of data prevents us from analyzing the important radar-rainfall error component.

Bibliography

Austin, P.M., Relation between measured radar reflectivity and surface rainfall. *Monthly Weather Review*, 115, 1053-1070, 1987.

Brock, F.V., K.C. Crawford, R.L. Elliott, G.W. Cuperus, S.J. Stadler, H.L. Johnson, and M.D. Eilts, The Oklahoma Mesonet: A technical overview, *Journal of Atmospheric and Oceanic Technology* 12(1), 5-19, 1995.

Ciach, G.J., W.F. Krajewski, E.N. Anagnostou, M.L. Baeck, J.A. Smith, J.R. McCollum, and A. Kruger, Radar rainfall estimation for ground validation studies of the Tropical Rainfall Measuring Mission. *Journal of Applied Meteorology*, 36, 735-747, 1997.

Ciach, G.J., M.L. Morrissey, and W.F. Krajewski, Conditional bias in radar rainfall estimation. *Journal of Applied Meteorology*, 39, 1941-1946, 2000.

Ciach, G.J., Local random errors in tipping-bucket raingauge measurements, *Journal of Atmospheric and Oceanic Technology*, 20, 752-759, 2003.

Ciach, G.J., and W.F. Krajewski, Analysis and modeling of spatial correlation structure in small-scale rainfall in central Oklahoma, submitted to *Advances in Water Resources*, 2005.

Cressie, N.A.C., Statistics for Spatial Data. J. Wiley & Sons, 885 pp., 1993.

Fread, D.L., R.C. Shedd, G.F. Smith, R. Farnsworth, C. Hoffeditz, L.A. Wenzel, S.M. Wiele, J.A. Smith, and G.N. Day, Modernization in the National Weather Service River and Flood Program. *Weather and Forecasting*, 10(3), 1995.

Fulton, R.A., J.P. Breidenbach, D-J. Seo, D.A. Miller, and T. O'Bannon, The WSR-88D Rainfall Algorithm. *Weather and Forecasting*, 13, 377-395, 1998.

Gebremichael, M., and W.F. Krajewski, Assessment of the statistical characterization of small-scale rainfall variability from radar: analysis of TRMM ground validation dataset, *Journal of Applied Meteorology*, 43, 1180-1199, 2004.

Habib, E., W.F. Krajewski, and A. Kruger, Sampling errors of fine resolution tipping-bucket rain gauge measurements, *Journal of Hydrologic Engineering*, 6(2), 159-166, 2001.

Habib, E., Ciach, G.J., and W.F. Krajewski, A method for filtering out raingauge representativeness errors from the verification distributions of radar and raingauge rainfall. *Advances in Water Resources*, 27(10), 967–980, 2004.

Hardle, W., *Applied Nonparametric Regression*. Cambridge University Press, 333 pp., 1990.

Hossain, F., E.N. Anagnostou, and T. Dinku, Sensitivity analyses of satellite rainfall retrieval and sampling error on flood prediction uncertainties, *IEEE Transactions on Geoscience and Remote Sensing*, 42(1), 130-139, 2004.

Journel, A.G., and CH. J. Huijbregts, *Mining Geostatistics*, Academic Press, 590 pp., 1978.

Krajewski, W.F., and K.P. Georgakakos, Synthesis of radar-rainfall data, *Water Resources Research*, 21(5), 764-768, 1985.

Krajewski, W.F., and B. Vignal, Evaluation of anomalous propagation echo detection in WSR-88D data: a large sample case study, *Journal of Atmospheric and Oceanic Technology*, 18(5), 807-814, 2001.

Krajewski, W.F., and G.J. Ciach, Towards probabilistic quantitative precipitation WSR-88D algorithms: Preliminary studies and problem formulation, *Final Report for the NWS Office of Hydrologic Development*, Silver Spring, Maryland, pp. 59, 2003.

Krajewski, W.F., G.J. Ciach, and E. Habib, An analysis of small-scale rainfall variability in different climatological regimes, *Hydrologic Sciences Journal*, 48(2), 151-162, 2003.

Kreyszig, E., Advanced Engineering Mathematics. J. Wiley & Sons, 1156 pp., 1999.

Krzysztofowicz, R., The case for probabilistic forecasting in hydrology, *Journal of Hydrology*, 249, 2-9, 2001.

Nijssen, B., and D.P. Lettenmaier, Effect of precipitation sampling error on simulated hydrological fluxes and states: anticipating the Global Precipitation Measurement satellites, *Journal of Geophysical Research*, 109, D02103, doi:10.1029/2003JD003497, 2004.

Petersen-Øverleir, A., Misspecification of extreme rainfall population and frequency inference due to measurement bias and variability, *Atmospheric Research*, 75, 283-300, 2005.

Reed, S.M., and D.R. Maidment, Coordinate transformation for using NEXRAD data in GIS-based hydrologic modeling, *Journal of Hydraulic Engineering*, 174-182, 1999.

Shafer, M.A., C.A. Fiebrich, D.S. Arndt, S.E. Fredrickson, and T.W. Hughes, Quality assurance procedures in the Oklahoma Mesonetwork, *Journal of Atmospheric and Oceanic Technology*, 17, 474-494, 2000.

Simonoff, J.S., *Smoothing Methods in Statistics*. Springer-Verlag, 338 pp., 1996.

Stallings, E.A., and L.A. Wenzel, Organization of the River and Flood Program in the National Weather Service, *Weather and Forecasting*, 10 (3), 457-464, 1995.

Steiner, M., R.A. Houze Jr., and S.E. Yuter, Climatological characterization of three-dimensional storm structure from operational radar and rain gage data. *Journal of Applied Meteorology*, 34, 1978-2007, 1995.

Steiner, M., J.A. Smith, S.J. Burges, C.V. Alonso, and R.W. Darden, Effect of bias adjustment and rain gauge data quality control on radar rainfall estimation, *Water Resources Research*, 35(8), 2487-2503, 1999.

Vignal, B., and W.F. Krajewski, Large sample evaluation of two methods to correct range-dependent error for WSR-88D rainfall estimates, *Journal of Hydrometeorology*, 2(5), 490-504, 2001.

Villarini, G., G.J. Ciach, W.K. Krajewski, K. Nordstrom, and V.J. Gupta, Impact of systematic and random errors in scaling properties of radar rainfall, to be submitted to *Journal of Geophysical Research*, 2006.

Appendix A

Ground Reference Error Filtering

GR Error Filtering

We developed a conditional distribution transformation (CDT) method for improving RR uncertainty analyses that use sparse rain gauge networks as the ground reference. The objective of the CDT method is perform a conditional point-area rainfall distribution transformation in order to filter out the rain gauge representativeness errors from radar-rain gauge samples. The application of the rain gauge error filtering is essential for the estimation of the spatial dependences in the PQPE model because large differences between the sampling areas of radar and rain gauge measurements can render the results of direct comparisons meaningless. We tested the validity and evaluated the accuracy of the CDT method. The tests were based on the data from the USDA Agricultural Research Service Micronet. A detailed description of the CDT method and its tests has been documented in Habib at al. [1]. Below, we present only an outline of this effort and its results.

Point-Area Distribution Transformation Method

Our implementation of the point-area transformation scheme follows in principle the methodology presented in Morrissey [3]. Let R_p represent point (single rain gauge) rainfall with mean $E\{R_p\}$ and variance $Var\{R_p\}$, and R_a represent the rainfall averaged over an area A with mean $E\{R_a\}$ and variance $Var\{R_a\}$. The means of the two corresponding processes are equal, i.e. $E\{R_a\}=E\{R_p\}$, and the variances can be related to each other based on the spatial correlation in the rainfall field in the following way:

$$Var\{R_a\} = \frac{Var\{R_p\}}{A^2} \int_A \int_A \rho(x, y) dx^2 dy^2 \qquad \text{(A.1)}$$

Now, given the probability distribution of R_p, we want to estimate the distribution of R_a that has the same mean as R_p, but different and known variance. As an approximate solution for this problem, we adopted a nonparametric distribution transformation method proposed by Journel and Huijbregts [2].

The probability distribution of rain gauge measurements R_p can always be represented using a transformation that expresses R_p as a function of the standard normal random variable $R_p=\phi_{Rp}(u)$, where u is the standard Gaussian variable and the equality is in the sense of the same probability distributions ([2]). This function is approximated using a decomposition (expansion) based on Hermite polynomials:

$$\phi_{R_p}(u) \approx \sum_{i=0}^{n} \frac{\psi_i}{i!} H_i(u), \qquad \text{(A.2)}$$

where $H_i(\cdot)$ are Hermite polynomials of the order i and ψ_i are their expansion coefficients, and the first four Hermite polynomials are shown as an example. The decomposition coefficients are fitted to the empirical frequency distribution of R_p using an iterative procedure described in

Journel and Huijbregts [2]. The coefficients ψ_i are related to the mean and variance of the point rainfall as follows:

$$\psi_o = E\{R_p\}, \tag{A.3}$$

$$\sum_{i=1}^{n} \frac{\psi_i^2}{i!} = Var\{R_p\}. \tag{A.4}$$

The main assumption of the point-area transformation scheme proposed by Journel and Huijbregts [2] is that the function ϕ_{Ra}, expressing the areal rainfall as a function of the standard normal random variable (just as ϕ_{Rp} represents the point rainfall), has the same Hermite expansion as ϕ_{Rp}, but its decomposition coefficients are modified by a single scaling factor, a, in the following way:

$$\phi_{R_a}(u) \approx \sum_{i=0}^{n} \frac{\psi_i a^i}{i!} H_i(u), \tag{A.5}$$

where the coefficients ψ_i are the same as in the point rainfall decomposition. Note that this distribution transformation preserves the distribution mean since $a^0=1$. On the other hand, the variance of the transformed distribution of the areal rainfall can now be expressed as:

$$Var\{R_a\} = \sum_{i=1}^{n} \frac{\psi_i^2 a^{2i}}{i!}, \tag{A.6}$$

and thus, it depends on the known decomposition coefficients ψ_i of the rain gauge rainfall and the scaling factor, a, only. This equation is a monotone function of a. Thus, if the variance of R_a is known, the scaling factor can be determined, using any iterative or graphical method, so that this equality is fulfilled.

Given the estimates of the coefficients, ψ_i, and the scaling factor, a, the computer generated standard normal deviates can be substituted into the Hermite expansion to simulate the distribution of the area-averaged rainfall. This point-area transformation procedure is general. It can be applied to the whole data sample, as well as to its sub-samples selected (conditioned) in any specific way. Since our focus in this study is on quantification of RR uncertainties, the distributions and their transformation have to be conditioned on the radar estimates, R_r.

The scheme of this conditional distribution transformation (CDT) can be summarized as follows. First, the rain gauge rainfall values in the data sample are grouped into sub-samples that are conditioned on a number of ranges of the RR values, $(R_p|R_r=r)$, each range centered on a RR value, r. The number of the sub-samples and their sizes depend on the amount of available data.

Then, the correlation function of the point rainfall conditioned on the radar estimate value, ($\rho|R_r=r$), is estimated. This enables the estimation of the conditional variances of areal rainfall, $Var\{R_a|R_r=r\}$. For each of the sub-samples ($R_p|R_r=r$), the conditional coefficients, ($\psi_i|R_r=r$), of the Hermite polynomial decomposition and the conditional scaling factors, ($a|R_r=r$), are estimated. Finally, the conditional distribution transformation functions ($\phi_{Ra}|R_r=r$) are computed and used to generate values that correspond to the areal rainfall ($R_a|R_r=r$). These generated values can then be used to provide the desired estimates of the conditional distributions of the true area-averaged rainfall, $f(R_a|R_r)$, conditioned on RR. They can be applied to reconstruct the bivariate distribution of RR and the corresponding true areal rainfall based on the following formula:

$$f(R_a , R_r) = f(R_a|R_r)\, f(R_r) , \qquad \text{(A.7)}$$

which can then be used to identify the PQPE model at different spatiotemporal scales as outlined in the previous Section of this report.

Tests of the CDT Method

The goal of the point-area transformation scheme is to obtain the estimates of conditional probability distributions of the true areal rainfall, conditioned on RR values, based on the conditional distributions of rain gauge rainfall and information on the conditional spatial correlation in the rain-field.

To evaluate the performance of the CDT method we used the data sample of point rainfall, areal rainfall and the corresponding RR estimates over three testing boxes within the USDA Agricultural Research Service Micronet that are indicated in Figure A.1.

Only one time scale of 15 minutes was considered at this stage. We stratified the sample into sub-samples of four intervals of the 15-minute RR values, R_r. For each sub-sample separately, we carried out the following procedure:

1. Construct the sample of concurrent point and areal rainfall for a specified spatiotemporal scale. The R_a values are approximated by averaging the rain gauge observations within the area of interest, whereas the R_p values come from all the individual gauges.

2. Estimate the sample variances of the point and areal rainfall values. Estimate the Hermite expansion coefficients for the point rainfall and the value of the scaling coefficient.

3. Perform the distribution transformation procedure described in section 2 to retrieve the areal rainfall distribution.

4. Compare the retrieved areal rainfall distribution against the observed one.

The estimates of the scaling coefficient, a, assumed values of about 0.6, for each of the sub-samples. The conditional quantile-quantile plots resulting from these tests are shown in Figure A.2.

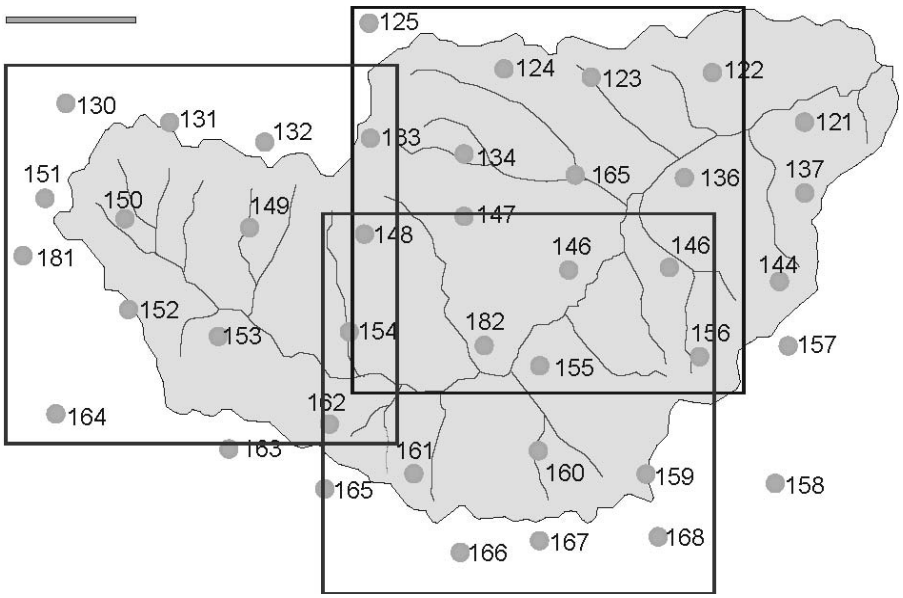

Figure A.1. A layout of the Little Washita Micronet with the three rectangular areas of about 19 km by 18 km that are used for testing the CDT method. Rain gauges within each area provide approximations of the true areal rainfall.

The solid dots in the plots show the comparisons of the quantiles corresponding to the same probability of exceedence for the transformation-based rainfall distributions as a function of the gauge-averaged (approximating the true areal) rainfall distributions. The open circles in the plots show the comparisons of the corresponding quantiles for the single-gauge rainfall distributions as a function of the gauge-averaged rainfall distributions. The transformation-based distributions are in a good agreement with the observed conditional distributions of areal rainfall and the degree of improvement of the radar rain gauge comparison can be seen from the comparison with the single rain gauge rainfall distributions. The tests confirm that the CDT method is able to retrieve the conditional distributions of the areal rainfall with quite good degree of accuracy.

Discussion

The conditional scaling factors in the CDT method and their dependence on the spatial averaging scale are determined only by the distributions and the spatial correlation functions of the radar-conditioned rain gauge rainfall. These quantities are, in principle, measurable and no other fundamental assumptions are necessary to use the CDT in practical applications. However, successful application of the CDT method requires sufficiently accurate information on the rainfall spatial correlation structure conditioned on the radar estimates over the spatial scales below the resolution of the RR product. This information is available in many situations where dense rain gauge clusters exist within the sparse networks (e.g., in Oklahoma, or Iowa). Of course, the estimates of spatial correlation are bound to be uncertain. The effects of these uncertainties on the CDT scheme are complex and their quantification remains to be investigated. However, one thing that we can be sure of is that, whatever are the uncertainties in the conditional correlations, the CDT always reduces the RR uncertainty bounds in comparison with what we could obtain if we treated the single-gauge data as the corresponding truth. By its

mathematical nature, the CDT just cannot increase the estimated RR uncertainty bounds. Of course, these RR uncertainty estimates are also not perfectly accurate, but this gauge-error filtering method always corrects them in the right direction. The effectiveness of this correction is clearly demonstrated in Figure A.2 by comparison of its results and the single-gauge performance. As one can see, the departures from the one-to-one line for the CDT transformed and the true area-average rainfall distributions are about ten times smaller than the discrepancies between the single-gauge and true area-average rainfall distributions. Error reduction by an order of magnitude is a very good performance for a relatively simple statistical method.

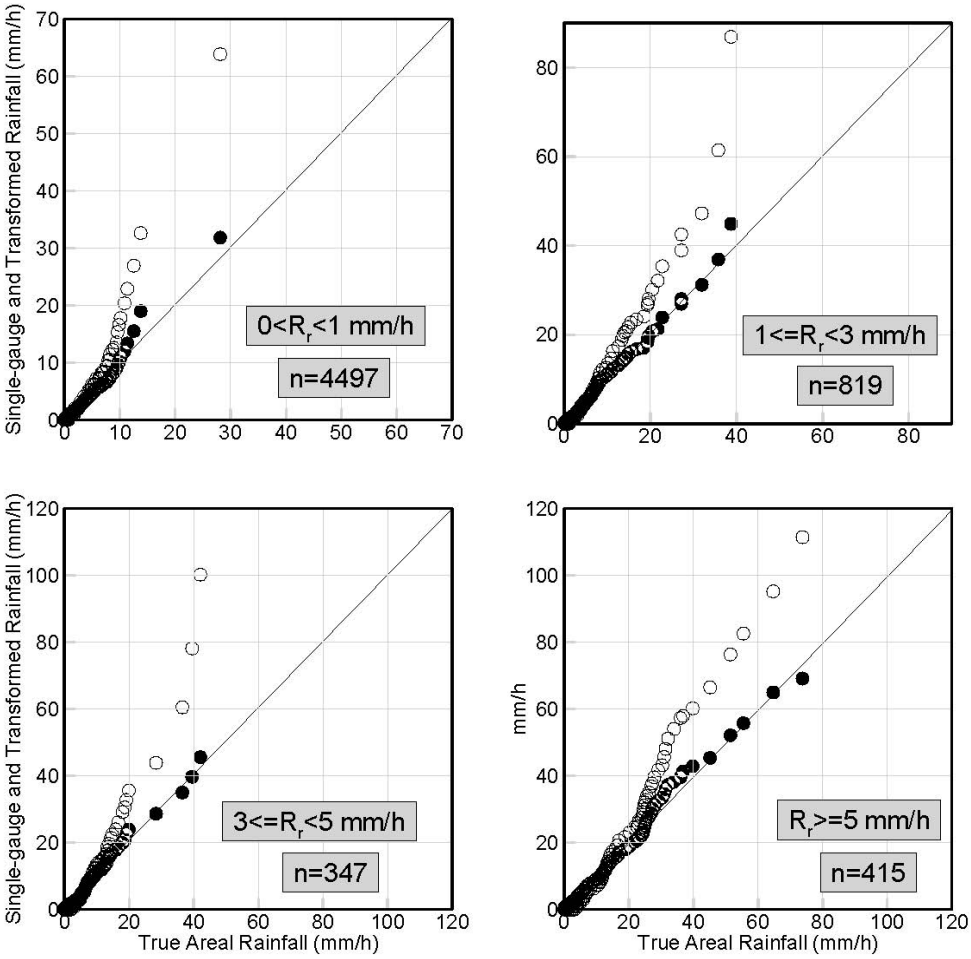

Figure A.2. A quantile-quantile plot of the cumulative rainfall distributions conditioned on the radar rainfall. Filled circles correspond to the transformation-based versus the true areal rainfall distributions. Open circles correspond to the point (single-gauge) versus the true areal rainfall distributions. The sample was stratified into four ranges of RR estimates. In the plots, n refers to the sample size in each range.

References

[1]. Habib, E., G.J. Ciach and W.F. Krajewski, 2004: A method for filtering out raingauge representativeness errors from the verification distributions of radar and raingauge rainfall, *Advances in Water Resources*, 27, 967-980.

[2]. Journel, A.G., and C.H.J. Huijbregts, 1978: *Mining Geostatistics*. Academic Press, 598 pp.

[3]. Morrissey, M.L., 1991: Using sparse raingages to test satellite-based rainfall algorithms, *Journal of Geophysical Research*, 96, 18561-18571.

Appendix B

Subgrid Scale Rainfall Variability: PicoNet Data Analysis

1. Introduction

The text that follows is almost entirely based on Ciach and Krajewski (2005) currently in review in *Advances in Water Resources*. The spatial variability of rainfall in the range of small scales between the size of a single raingauge (of the order of 0.1 m) and a few kilometers is of interest both from the practical and scientific points of view. Design of communication systems and urban storm water routing structures require high spatial and temporal resolution data ([3], [9], [25]). High variability of rainfall is a source of fundamental difficulties in conclusive verification of radar rainfall estimates (e.g. Austin [1], Kitchen and Blackall [18], Ciach and Krajewski [6], Chumchean et al. [4], Habib et al. [15]). Small-scale rainfall variability is also important for the precipitation frequency analyses across different averaging scales required in various hydrological applications (e.g. Bras and Rodriguez-Iturbe [2], De Michele at el. [11]). Mathematical models of rainfall morphology have the capability to describe a broad span of spatiotemporal scales (e.g. Foufoula-Georgiou and Krajewski [12], Lovejoy and Schertzer [22], Seed et al. [26], Kundu and Bell [21]). However, their development and validation requires adequate empirical evidence. Most of the experimental studies on spatial rainfall structure are based on the weather radar observations that are inherently spatially averaged over the domains of about 1-10 km^2, or larger, and cannot provide information on finer scales. Furthermore, radar rainfall estimates are only poor approximations of the true rainfall and the radar-based rainfall characteristics can be considerably distorted (Krajewski et al. [19], Harris et al. [17], Gebremichael and Krajewski [13]). On the other hand, direct rainfall measurements with raingauges cannot provide the continuous coverage of the observation areas. Most of the relatively dense experimental raingauge networks have the inter-gauge distances of 2-3 km, or more, whereas the station spacing in the common operational networks is about an order of magnitude larger. Therefore, spatial rainfall variability at the scales below a few kilometers is still a poorly explored research area (Krajewski et al. [20]).

In this study, we present an extensive analysis of the small-scale variability in rainfall fields that is focused on their spatial correlation structure at the distances below 3-4 km. The correlation functions are well established, normalized and commonly used measures of spatial dependences that are required by many applications (Bras and Rodriguez-Iturbe [2], Ciach and Krajewski [6], Habib and Krajewski [14]). Furthermore, in contrast to the more comprehensive spatial multi-fractal measures (Lovejoy and Schertzer [22]), they can be estimated based on a network of point rainfall measurements, provided that the network covers the required range of distances. The correlation estimates presented here are based on a large data sample from a unique local cluster of 53 well maintained tipping-bucket raingauges, called the "EVAC PicoNet." This network (described in more detail in the next section) has the inter-station distances of about 0.6 km, uses double-gauge setups in the measurement points, and covers an area of about 9 km^2 located in central Oklahoma.

Our present analysis is a continuation of the study by Krajewski et al. [20] that was based on small data samples from several locations around the world. In this case we have used data collected from May 1 to October 16 2001 and from March 7 to November 6 2002. This work is also directly relevant to our quest for quantifying uncertainty in radar and satellite remote sensing of rainfall. Our earlier work, e.g. [6], [7], [8], [14], [15], and [20], as well as the current study, all provide building blocks for a comprehensive framework addressing the problem. Relatively large size of the sample used here allowed us to look at the rainfield correlations from three different perspectives. First, we examined the dependences of the spatial correlation function on

the time-scale for the averaging interval spanning the range from 1 minute to 1 day. Second, we present and analyze the differences between the correlation estimates in the individual rainfall events. Finally, we demonstrate and discuss ambiguities associated with the conditioning of the correlation estimates on rainfall intensities.

2. Analysis and modeling method

Our objective is to describe the inter-gauge correlation coefficient in rainfall accumulations as a continuous function of the separation distance for different averaging intervals and precipitation regimes. In this study, we used a two-step procedure to quantify these characteristics. The first step consists of estimating the Pearson's product-moment correlation coefficients for each pair of the raingauges based on the time-series of rainfall accumulation obtained from the data sample. We used the standard formula for estimating these inter-gauge correlations:

$$\rho_{ij} = \frac{\overline{R_i R_j} - \overline{R}_i \overline{R}_j}{\sqrt{(\overline{R_i^2} - \overline{R}_i^2)(\overline{R_j^2} - \overline{R}_j^2)}}, \qquad \text{(B.1)}$$

where R_i and R_j are concurrent rainfall values in two raingauges, i and j are the indexes of the raingauges, and the bar denotes averaging over the sample time-series.

For small data samples with highly skewed distributions of the rainfall values, the estimates obtained using Eq. (B.1) can be biased (Habib et al. [16]). To reduce this sample bias, Habib et al. [16] proposed an estimation scheme based on logarithmic transformation of the rainfall values. However, this procedure is only applicable to the situations where rainfall values in raingauge pairs are distributed according to the bivariate mixed lognormal law (Shimizu [27]). As we demonstrated (Figure B.1) lognormal distribution model does not apply to the PicoNet rainfall sample and the tails of the rainfall amounts in Central Oklahoma are much shorter than those of lognormal distribution. In fact, they are even shorter than in the exponential distribution, especially for larger time scales. Furthermore, our sample is much larger that the sample sizes considered by Habib et al. [16] and thus the sample biases are much smaller. Therefore, in this study, we directly use the standard estimator (B.1) to compute the inter-gauge correlation coefficients.

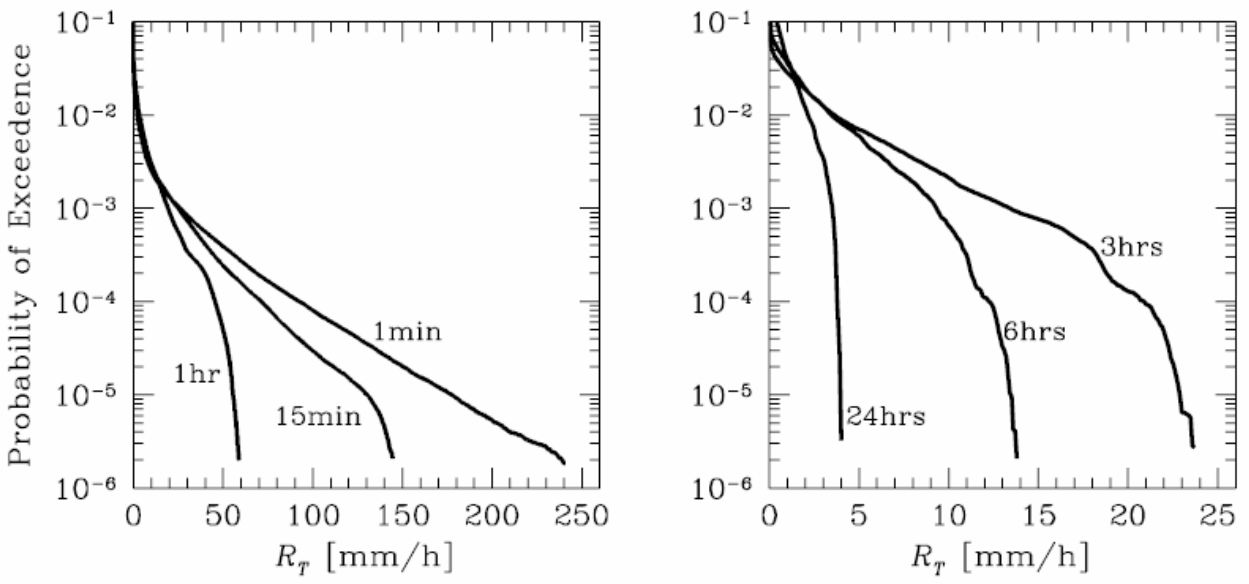

Figure B.1. Figure 3: Probabilities of exceedence of raingauge rainfall in the PicoNet for six averaging time-scales.

The second step of our analysis consists of fitting a parametric model to each set of the inter-gauge correlation coefficients obtained in the first step. We chose the following modified-exponential formula for this modeling:

$$\rho_g(d) = c_0 \exp\left[-\left(\frac{d}{d_0}\right)^{s_0}\right], \qquad \text{(B.2)}$$

where d is the separation distance between two points, c_0 is the correlation value for the near-zero distances (much smaller than the network grid, but not zero) that we call the "nugget parameter," d_0 is the correlation distance (or the spatial decorrelation scale) and we call it the "scale parameter," and s_0 is the correlogram "shape parameter." We use the term "nugget" for the c_0 parameter following the geostatistical literature (e.g., Cressie [10]). Note that (1-c_0) is the "instant decorrelation" due to the local random errors in the raingauge measurements [5]. The shape parameter s_0 controls the behavior of the functional model (2) near the origin (i.e. small separation distance); e.g. for s_0=1 we have exponential drop of the correlation while for s_0=2 the curve is flat like near the top of the bell (Gaussian) curve.

We estimated the values of the three parameters in Eq. (B.2) using the following scheme. First, we estimated the parameter c_0 as an average of the sample correlation coefficients obtained based on Eq. (B.1) for all pairs of collocated raingauges. If all the gauges work properly, there are 34 of such collocated pairs in the PicoNet (10 pairs in the central station and 24 in the other stations). With known c_0, the remaining two parameters, d_0 and s_0, were estimated by minimizing the root-mean-square (RMS) error between the model values and all the inter-gauge sample

correlation coefficients in the pairs of non-collocated raingauges. We performed this minimization using the simple "exhaustive search" of the two-parameter space with the resolution of 0.01 km for d_0 and 0.005 for s_0. This most straightforward scheme of model fitting is sufficiently fast for all our purposes. We applied this two-step procedure described to every time-scale (rainfall averaging interval) considered in this study and each sub-sample selected according to different conditions described in the next sections.

As an alternative parametric model, we also tested the second order polynomial that is also described by a three-parameter expression. The results showed that this polynomial model does not provide a better fit to the inter-gauge correlation coefficients in terms of the minimized RMS error values. Therefore, we chose the modified-exponential parameterization defined by Eq. (B.2) as the basis for the analyses in this study. In addition to the optimality of the selected model, its parameters have a convenient interpretation in terms of the local random errors in raingauges, correlation distance and correlogram shape. Note that the scale parameter, d_0, in the modified-exponential function (2) has exactly the same "e-folding distance" meaning (that is, $\rho_g(d_0)=\rho_g(0)/e$) as in the simple exponential model obtained from (2) when $s_0=1$.

Note, that in the selected parameterization of spatial rainfall correlogram, the local random errors in raingauge measurements affect only the c_0 parameter. Therefore, we can obtain spatial correlogram estimates of the true rainfall, $\rho_r(d)$, by removing this coefficient from the inter-gauge correlogram estimates:

$$\rho_r(d)=\frac{\rho_g(d)}{c_0}=\exp\left[-\left(\frac{d}{d_0}\right)^{s_0}\right]. \qquad \text{(B.3)}$$

Adding this simple "raingauge error filtering" to the rainfall analyses is especially beneficial at the short time-scales where the random errors in raingauges are large [5].

3. Dependence on time-scale

We now apply the modeling technique described in the previous section to the entire data sample and over a broad range of time-scales (averaging intervals). In Figure B.2, we show four examples of the estimation results with the inter-gauge correlation coefficients and the parametric fits as functions of the separation distance for the time-scales of 5, 15, 60 and 180 minutes. The convex shape of the correlograms and their flattening at the small distances are clearly visible and supports our selection of the three-parameter analytical approximation including the shape parameter s_0. The necessity to account for the correlogram shape, which cannot be described with the commonly used simple exponential model, has already been postulated by Krajewski et al. [20] based on several small data samples from different regions. The present study confirms that the modified-exponential function defined by Eq. (B.2) is a good choice that can be applied over a broad range of time-scales.

An interesting feature of the results in Figure B.2 is that, despite the large sample size used here, there is still a considerable scatter of the inter-gauge correlation coefficients obtained from the individual pairs of raingauges. Note that the PicoNet cluster covers a relatively small and homogenous area, and all the stations have basically the same statistical characteristics.

Therefore, the scatter is most likely the manifestation of large estimation uncertainties of second-order statistics in rainfall. These uncertainties are typical for skewed random variables as discussed in Habib et al. [16]. However, the overall RMS error of our parametric approximation is only about 1-2% for all four time-scales indicating that the large numbers of raingauge pairs in the PicoNet is essential for obtaining stable spatial correlogram estimates in rainfall.

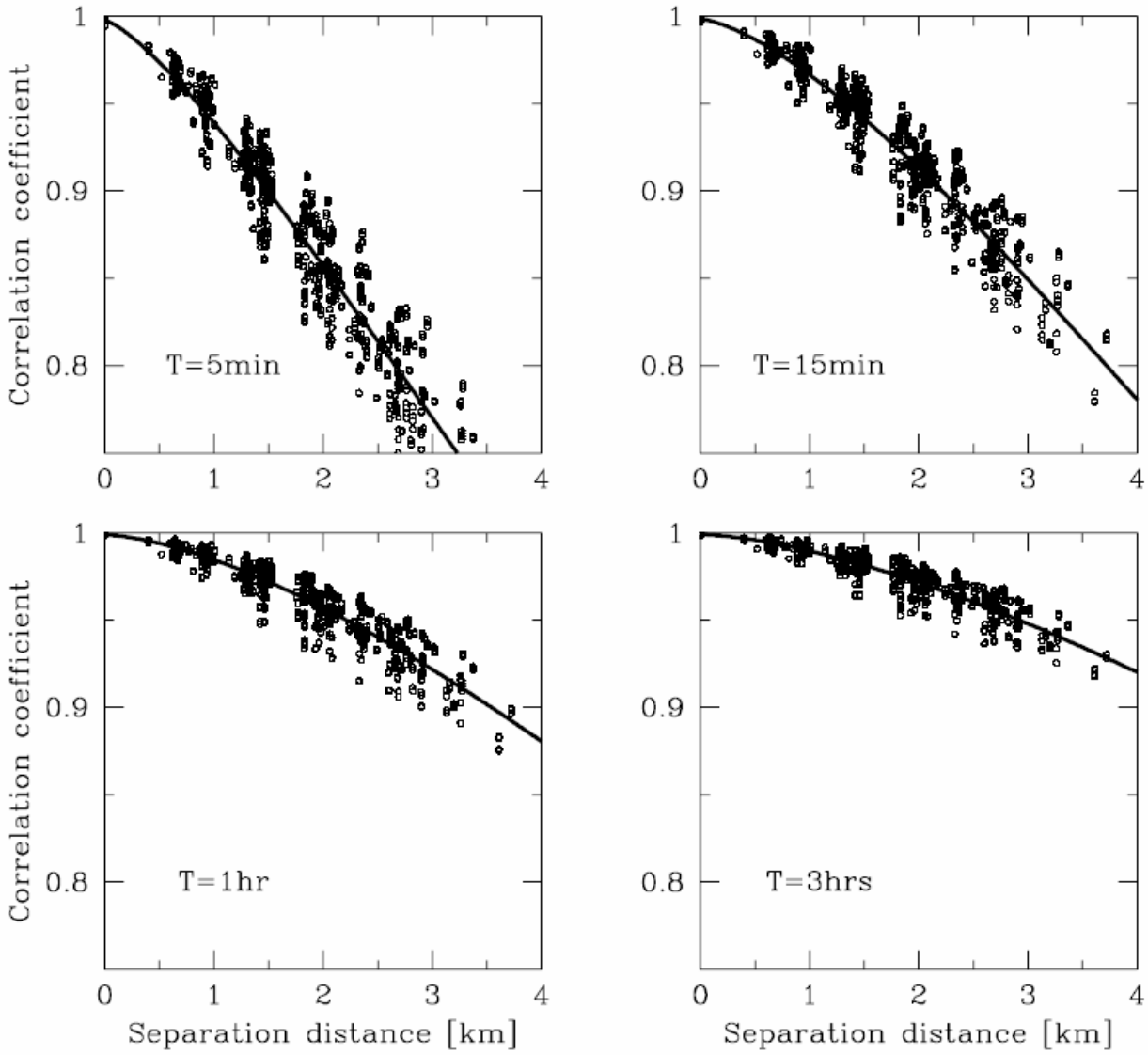

Figure B.2. Examples of the inter-gauge correlation coefficients and the corresponding estimates of the parametric correlogram model at four averaging time-scales.

In Figure B.3, we summarize these modeling results by presenting the estimated parameters as functions of the averaging time-scale ranging from 1 minute to 24 hours. In addition, the minimized RMS errors are shown to provide an assessment of the goodness-of-fit of the analytical approximation (B.2) over the broad range of time-scales. The near-zero-distance correlations as expressed by the parameter c_0 in Eq. (B.2) are presented in the panel (a) of this

figure. It increases smoothly with the averaging interval, however, its rate of growth drops quickly suggesting that, even for much longer time-scales, some residual local random errors in the raingauge measurements can still persist. This behavior is consistent with the results obtained by Ciach [5] using an experimental setup that was specifically focused on these local effects. The scale parameter, d_0, plotted in panel (b) grows very slowly for the short time-scales up to about 10 minutes, starting from the correlation distance of about 7.7 km. Then it assumes a regular shape close to the logarithmic curve (straight lines in these log-linear plots). For the averaging intervals above 1 hour, d_0 increases by about 2.5 km when the averaging interval doubles. The qualitative behavior of the shape parameter, s_0, shown in panel (c) is exactly the opposite of the correlation distance behavior. It increases approximately logarithmically for the time-scales below about 10 minutes, and then gradually slows down and stabilizes at the level of about 1.57 that remains almost constant in the region from 2 through 24 hours.

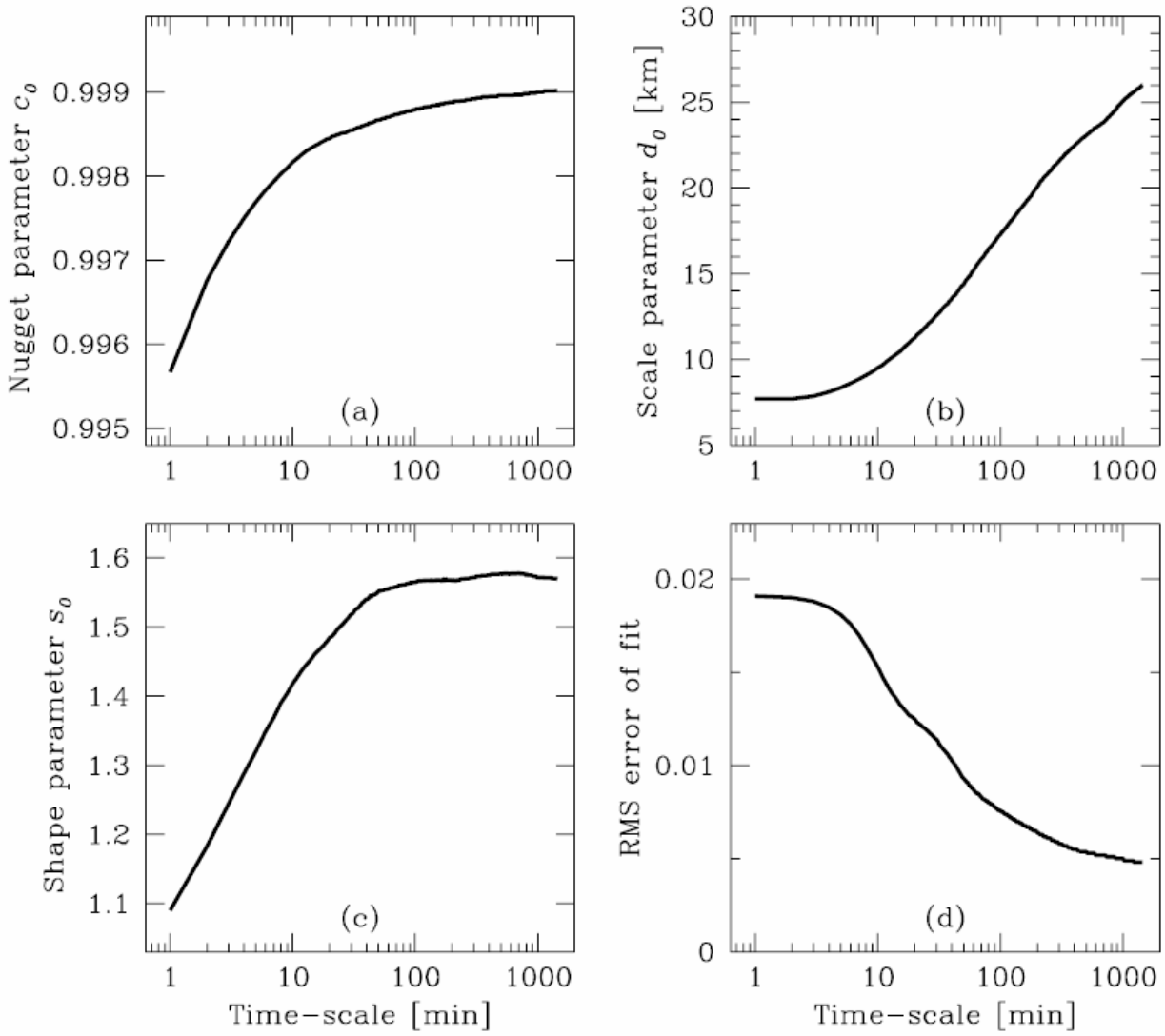

Figure B.3. Dependence of the estimated correlation function parameters and the fitting errors on the averaging time-scale ranging from 1 minute to 1 day.

The time-scale dependences exhibited in panels (b) and (c) of Figure B.3 indicate that, for the short averaging intervals, mainly the shape of the spatial correlogram is affected by the temporal averaging. On the other hand, for larger time-scales, the shape remains approximately constant and only the correlation distance changes. Furthermore, the value of s_0 becomes close to 1.0 for the shortest averaging interval suggesting that, at least on the average, the spatial correlation structure in the instantaneous rainfall intensity fields is close to exponential. Note, however, that this characteristic of spatial rainrates was obtained based on the entire sample including all storm cases in the two-season observation period. As we will see in the next section, the properties of individual storms can depart considerably from this average behavior.

From the dependence of the parameters in Eq. (B.2) on the time-scale, one can compute the rainfield decorrelation, $1-\rho_r(d_x)$, for a fixed separation distance, d_x, as a function of the time scale. This representation provides another perspective of the spatiotemporal dependences in rainfall that are observable based on a network of point rainfall measurements. The results for the distances of 0.5, 1, 2 and 4 km are shown in Figure B.4 in a log-log scale. The four curves are similar in their sigmoid shape and they gradually diverge from each other with the increasing averaging interval. In the region of time-scales between about 5 and 50 minutes, they seem to follow the allometric scaling law and gradually depart from it outside of this region. No simple formula to generalize these features into a concise mathematical model is obvious to us at present. However, the regular behavior of the fixed-distance decorrelations as functions of time-scale is an interesting feature and we will study it further in our future investigations.

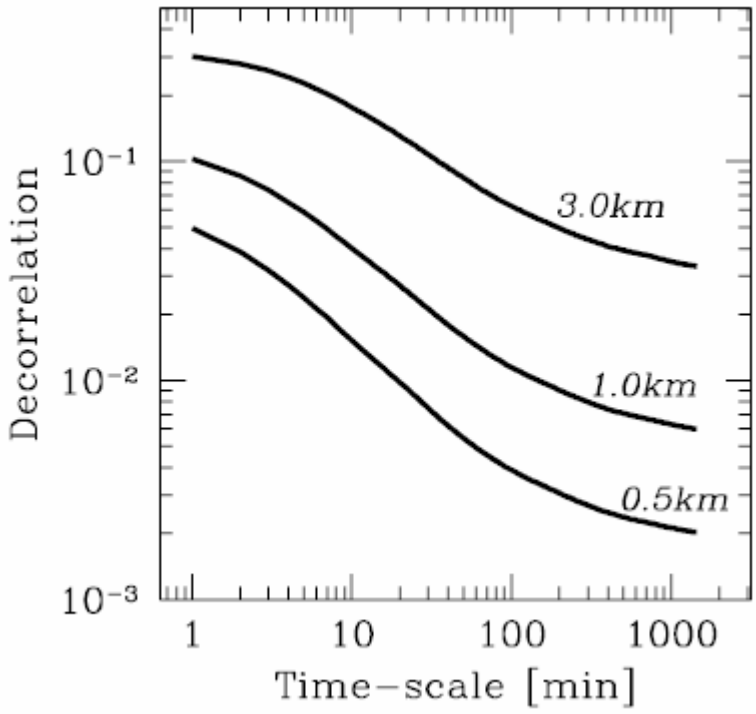

Figure B.4. Dependence of the decorrelations on the averaging time-scale at three separation distances.

4. Storm-by-storm analysis

The time-scale dependences discussed in the previous section provide only a much generalized characterization of small-scale spatial correlation structure in rainfall because they are based on the whole data sample. The spatial characteristics of individual storms can be vastly different than this "average behavior." In this section, we focus on these differences. We selected 32 events that produced above 10 mm rainfall depth as averaged over all raingauges in the PicoNet. One prominent feature of this set is the huge variability of the basic characteristics of these storms. Their durations range from 40 minutes up to 18 hours, total accumulations from 11 mm to 77 mm, average rainfall intensities (accumulation divided by duration) from about 1.8 mm/h to 26 mm/h, and the peak 3-minute rainrates from 6 mm/h up to 223 mm/h. For each of the storms, we estimated the parameters in Eq. (B.2) at 3-minute averaging time-scale. As expected, there are large differences between the estimates of the spatial correlation parameters for the individual storms. Their decorrelation scale, d_0, ranges from 2.6 km up to about 35 km, whereas the shape parameter, s_0, ranges from 0.68 to 1.82. The scatter of these two estimated parameters is presented in Figure B.5.

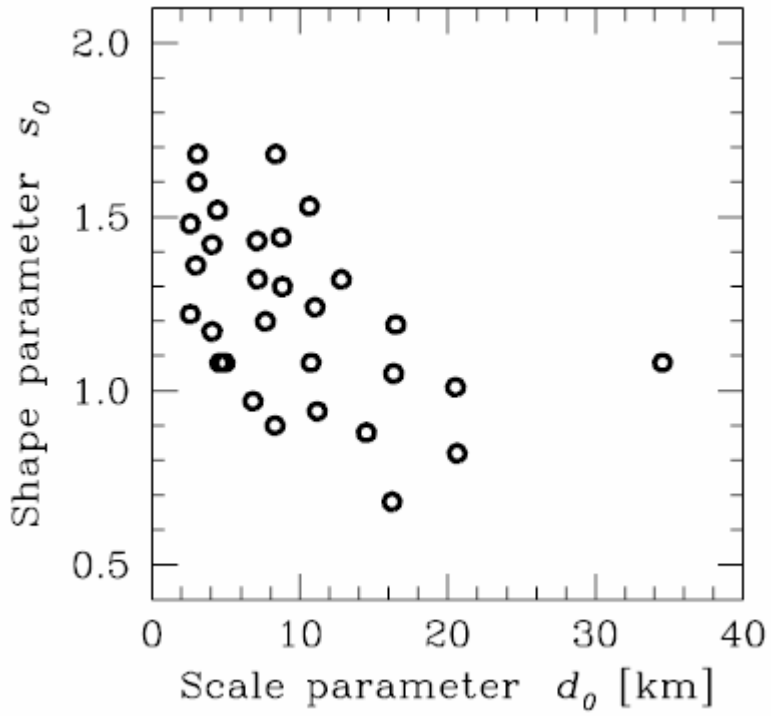

Figure B.5. The scatter of the scale and shape parameters in the spatial correlation functions estimated for 32 individual storm events in the PicoNet sample. These estimates are based on 3-minute rainrate values.

Some part of these spatial correlation differences between the 32 events might be due to the estimation uncertainties because the sample sizes for each storm are relatively small. Therefore, to obtain more stable estimates, we aggregated these events into two classes of spatial variability based on the 1 km correlation estimates, $\rho_r(1km)$, applying Eq. (B.3) to the 3-minute rainrates in each storm. We selected the threshold of $\rho_r(1km)$ of about 0.9 to divide the storm sample into the

higher variability and lower variability subsamples, each containing 16 events. The estimated correlograms of the 3-minute rainrates for these two spatial variability classes are presented in Figure B.6. As expected, the two spatial correlation functions are considerably different both in their shapes and decorrelation scales. What is more surprising is the relatively high value of the shape parameter, $s_0=1.47$, for the lower spatial variability class that corresponds to the strong flattening of its correlogram at the shortest distances. Note that the whole-sample analysis in the previous section indicated that, at the shortest time-scales, the spatial decorrelation in rainfall is approximately an exponential function that drops linearly at the distances close to zero (or much smaller than the correlation scale). Specifically, the shape parameter $s_0=1.25$, for the whole-sample estimate at the 3-minute time-scale. The upper correlogram in Figure B.6 indicates that this behavior does not apply to the rainfall intensity fields in all types of storms. Furthermore, it seems that the shape of the whole-sample correlogram for short rainfall averaging intervals can be dominated by the storms with the highest spatial variability. For the higher variability class, the estimated shape parameter $s_0=1.24$, which is practically the same as the whole-sample estimate. This domination effect is in qualitative agreement with the simulation study on the estimation of multiscaling characteristics by Harris et al. [17].

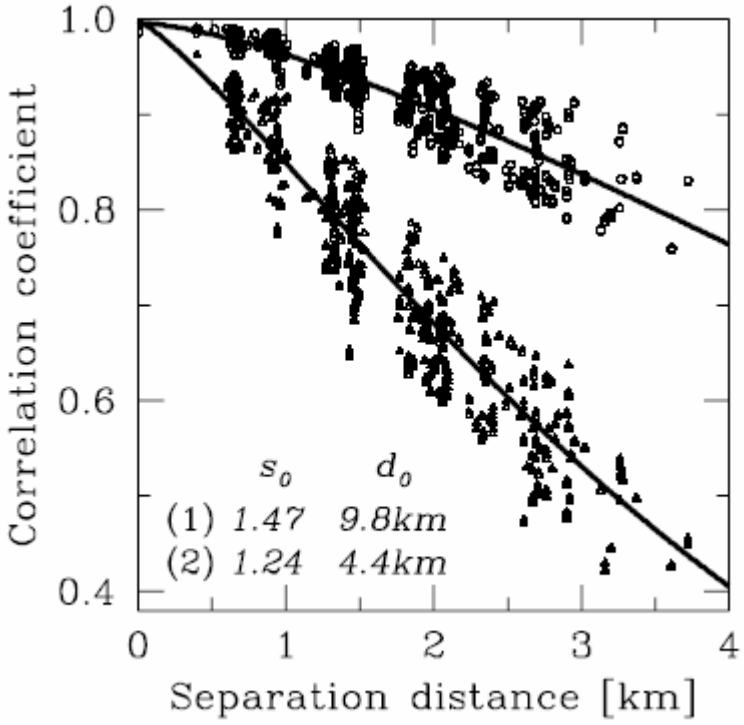

Figure B.6. Inter-gauge correlation coefficients and fitted parametric correlation functions for two classes of storms with low and high spatial variability. The estimated shape and scale parameter values of the two parametric correlograms are also shown.

In the class of storms with higher spatial variability defined above, the aggregated rainfall depth and duration are about 434 mm and 68 hours, respectively, and the peak 3-minute rainrate is about 86 mm/h. In the spatially smoother class, the total rainfall depth and duration are about 423 mm and 73 hour, and the peak rainrate is about 223 mm/h. Therefore, the two storm classes

constitute similar data samples in respect to their sizes and average rainfall intensities. However, the peak rainfall intensities in the two subsamples differ about three times in magnitude and, contrary to our expectations; they are stronger in the subsample with higher spatial correlations. This difference suggests that there might exist an interesting (and, perhaps, counterintuitive) relationship between two different characteristics of rainfall events. Namely, the storms with higher extremes in the rainfall intensities seem to be less variable is space. The results in Figure B.7 attempt to address this question in more detail. The figure shows the 1-km correlations, $\rho_r(1km)$, of the individual storms as functions of the peak 3-minute rainrates (left panel) and the storm-average rainrates (right panel). Although the scatter of points in the left panel is far from a strong functional relationship, it shows clearly that the rainfall events that have the highest peak rainrates are also the least variable in space. On the other hand, the right panel indicates that there is only a very weak, if any, dependence between spatial variability and average rainrate in the storms.

Comprehensive investigation of possible relationships between various characteristics of the individual storms that are measurable in the PicoNet is beyond the scope of this study. We will continue working on this interesting problem in the future. However, the general question of quantifying the dependences between rainfall intensity and its spatial correlation structure fits well with the leading topic of this paper and we elaborate on this subject in the next section.

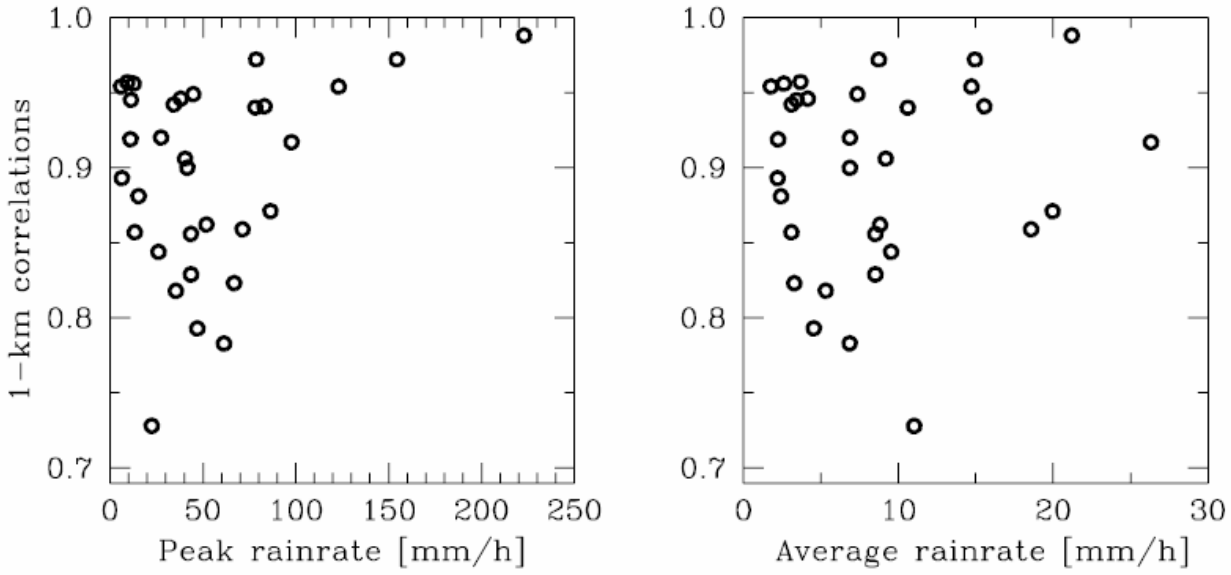

Figure B.7. Dependences of the correlations at 1 km separation distance on the peak and storm-averaged rainrates for 32 individual storm events in the PicoNet sample.

5. Conditioning on rainfall intensities

An apparently straightforward way to extract more detailed information about the spatial rainfall structure based on dense raingauge networks is through estimating the spatial correlation functions conditioned on rainfall intensities. Such conditional correlation functions are, for example, the necessary component of the conditional distribution transformation (CDT) method described and evaluated by Habib et al. [15]. They showed that the CDT method can effectively

filter-out the area-point errors from radar-raingauge verification statistics, provided the spatial correlograms of raingauge rainfall conditioned on radar rainfall values are known. In fact, the analysis described below was directly motivated by the practical implementation issues of the CDT method.

In practice, the conditioning has to specify intervals of rainfall intensity values that are broad enough to create reasonably large subsamples for the conditional correlation estimates. In this study, we condition the estimates on the gauge-averaged rainfall values and use variable conditioning intervals defined based on the following formula:

$$\frac{R_c}{k} < R_a < R_c k \,. \qquad \text{(B.4)}$$

where R_a is the gauge-averaged rainrate, R_c is the geometric center of a conditioning interval, and k is the parameter controlling the interval width. The interval width increases linearly with the rainfall intensity in order to partially compensate for the rapidly decreasing number of data points with increasing rainfall values (see Figure B.1). We applied this conditioning rule to all the 3-minute rainrates based on the PicoNet data sample used here.

For any subsample defined by the selected k and R_c values, we can estimate the parameters c_0, d_0, and s_0 of the spatial correlation function (B.2), and the resulting 1-km correlation coefficients, $\rho_r(1km)$. In Figure B.8, we present the conditional 1-km correlations as functions of the R_c values, for three choices of the width parameter, k. One striking feature of these results is a strong and systematic dependence of the conditional correlations on the width of the conditioning intervals. All three curves seem to confirm that the rainfall fields are smoother for higher rainrates ($\rho_r(1km)$ increases with R_c), which is in qualitative agreement with the storm-by-storm results in the previous section. However, for each fixed rainrate value, R_c, the 1-km correlation coefficient conditioned on R_c is a monotonically increasing function of the width of the conditioning interval determined by the k parameter in (B.4). Furthermore, the $\rho_r(1km)$ estimates seem to be more sensitive to the k parameter than to the rainfall intensities. The results in Figure B.8 demonstrate that the correlation functions conditioned on rainfall intensities are highly ambiguous characteristics of spatial rainfall structure because they can be completely different depending on a particular conditioning scheme used for their estimation. These ambiguities are caused by additional statistical dependences that are imposed on the data in the sub-samples by the conditioning. The conditioning is a constraining factor that binds the collective behavior of the data, including the pair-wise correlations. The simplest illustration of such conditioning effect can be obtained by generating a large sample from a bivariate standard normal distribution with the correlation coefficient between the two variables equal to 0.9, for example. If we consider a sub-sample of pairs bound by the condition that the average of the two values is between, say, 0.3 and 0.7, then we can easily check that the sub-sample correlation coefficient is much smaller than the 0.9 value of the parent population.

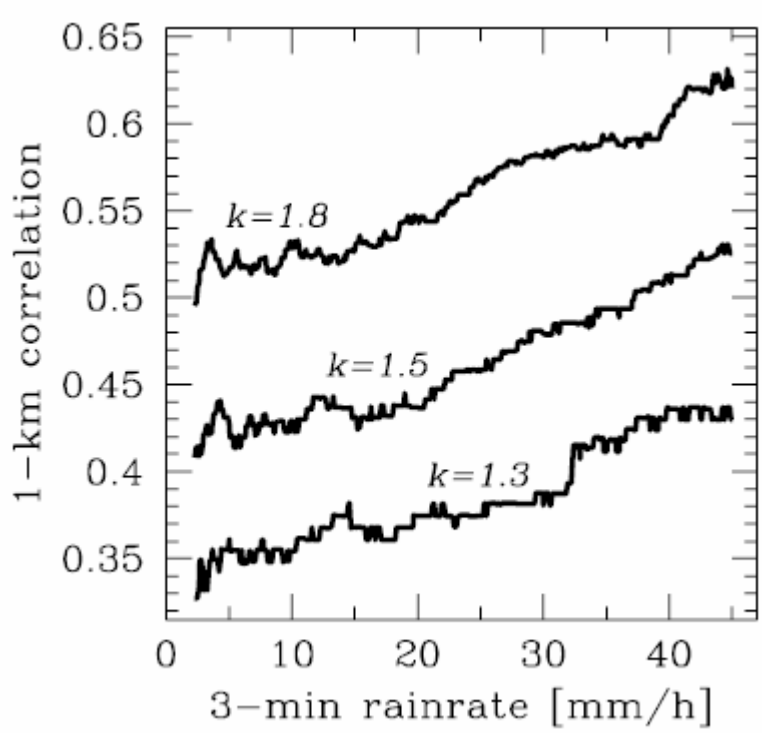

Figure B.8. Dependences of the correlations at 1 km separation distance on the 3-minute rainrates for three values of the window-width parameter. These estimates are based on the whole PicoNet sample.

Of course, for any rigorously defined conditioning rule, the conditional correlation functions can still be useful in many applications ([23], [24], [15]). However, while interpreting and applying the results of the spatial correlations conditioned on rainfall values, one has to be cautious and fully aware of their strong dependence on the conditioning intervals and of the possible consequences of this dependence. An example of the situation where this effect can lead to considerable errors is practical implementation of the abovementioned CDT method ([15]). The method requires estimating the conditional spatial correlation functions of raingauge measured rainfall conditioned on radar rainfall values. This can be done, if a dense local cluster of gauges is available under the radar umbrella. However, because radar rainfall uncertainties are strongly dependent on the distance from the radar, conditional correlations obtained at one distance might not be applicable at a different distance. Clearly, either a number of raingauge clusters located at different distances is necessary for correct application of the CDT procedure in its present formulation tested in [15], or one has to find new methods to account for the range effects on the conditioning results.

The statistical effects of the conditioning described above, if not recognized, can often lead to confusing conclusions about the actual properties of rainfall fields. For example, the estimates of conditional spatial correlation functions in rainfall can be found in Habib and Krajewski [14], and in Habib et al. [15]. In both cases, the conditional correlations indicate that the heavy rainfall (above 10 mm/h) is more variable in space than the weaker rainfall (below 10 mm/h). This is contrary to the results in the previous section of this study showing that storms with higher peak rainrates are also spatially smoother. The most likely explanation of this contradiction is the

strong statistical effect of the conditioning on such correlation estimates. To illustrate this effect more clearly, we divided our PicoNet sample into stronger and weaker rainfall using different thresholds applied to the area-averaged rainrates. The time-scale here was 15 minutes, the same as in [14], and in [15]. In Figure B.9, we present the estimated conditional correlograms for two threshold values of 3 and 10 mm/h. The plots show that the conclusion about which class in rainfall intensity is spatially smoother can be different depending on the strong/weak division threshold.

Note that our results in this section do not imply that the general question about possible relationships between rainfall intensity and its spatial variability is ill-posed. They only show that spatial correlation functions conditioned on rainfall values cannot unambiguously characterize such relationships.

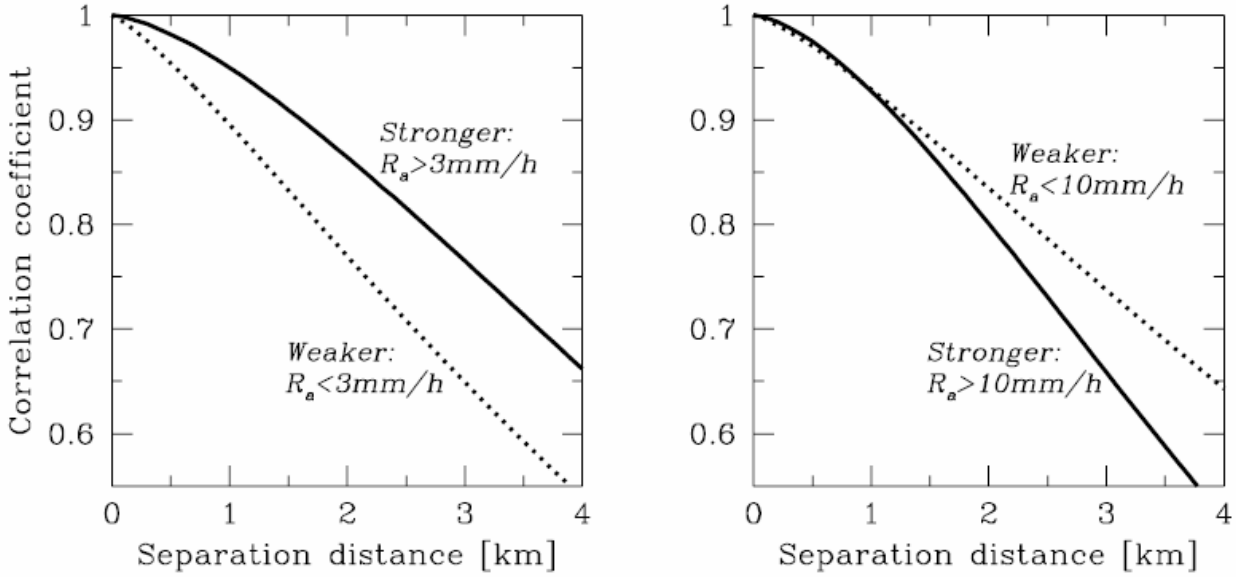

Figure B.9. Spatial correlograms in weaker and stronger rainfall for two values of 15-minute rainrate used as the classification thresholds. The conclusion about which class is spatially smoother depends on the threshold.

6. Conclusions

We presented empirical estimates of spatial correlations in small-scale rainfall based on a large sample from a super-dense raingauge network in Central Oklahoma. The dependency of the correlation function parameters on rainfall averaging interval shows that, at the time-scales below 10 minutes mainly the shape of the correlograms is affected by the temporal averaging, whereas at the time-scales above 1 hour the shape remains approximately constant and only the decorrelation distance changes. The individual rainfall events have vastly different values of their correlogram estimates and the storms with higher peak rainrates are spatially smoother. Conditioning spatial correlation estimates on rainfall intensity yields ambiguous results and can lead to misleading conclusions.

We realize that spatial correlograms, albeit useful in many practical applications, do not provide the most comprehensive quantitative description of the spatial dependences in rainfall.

From the perspective of the modern allometric multiscaling theories, the traditional geostatistical tools might even be viewed by some researchers as outdated. However, we limited this study to the classical spatial correlation functions for the obvious technical reason: they can be estimated based on the point rainfall measurements. The PicoNet cluster of 25 stations enables considering many inter-gauge distances, but is not enough to consider any relevant range of spatial averaging scales that is necessary in more sophisticated multiscaling analyses. Nevertheless, the spatial statistics that actually are observable with accurate raingauge measurements can also be quite informative and should be treated as valuable "reality checks" for different multiscaling spatial rainfall models.

The redundancy of the double-gauge design applied in the EVAC PicoNet is an extremely valuable feature of the network. It allows efficient quality control of the rainfall records and substantial improvement in the measurement accuracy (Ciach and Krajewski [6]; Ciach [5], Krajewski et al. [20], Steiner et al. [28]). A number of errors in the PicoNet measurements would be impossible to detect in the traditional system based on single raingauges. Broader application of the simple and relatively inexpensive multiple-gauge setups could result in a dramatic improvement of the quality of surface rainfall measurement.

References

[1]. Austin, P.M., 1987: Relation between measured radar reflectivity and surface rainfall. *Mon. Wea. Rev.*, 115, 1053-1070.

[2]. Bras, R.L., and I. Rodriguez-Iturbe, 1993: *Random Functions and Hydrology.* Dover, 559 pp.

[3]. Capsoni, C., F. Fedi, C. Magistroni, A. Paraboni, and A. Pawlina, 1987: Data and theory for a new model of the horizontal structure of rain cells for propagation applications, *Radio Science*, 22(3), 395-404.

[4]. Chumchean, S., A. Sharma, and A. Seed, 2003: Radar rainfall error variance and its impact on radar rainfall calibration. *J. Phys. Chem. Earth*, 28, 27-39.

[5]. Ciach G.J. 2003: Local random errors in tipping-bucket rain gauge measurements. *J. Atmos. Oceanic Technol.*, 20,752–759.

[6]. Ciach, G.J., and W.F. Krajewski, 1999: On the estimation of radar rainfall error variance. *Adv. Water Resour.*, 22, 585-595.

[7]. Ciach, G.J., M.L. Morrissey, and W.F. Krajewski, 2000: Conditional bias in radar rainfall estimation. *J. Appl. Meteor.*, 39(11), 1941-46.

[8]. Ciach, G.J., E. Habib, and W.F. Krajewski, 2003: Zero-covariance hypothesis in the Error Variance Separation method of radar rainfall verification. *Adv. Water Resour.*, 26(5), 673-680.

[9]. Crane, R.K., 1996: Electromagnetic Wave Propagation through Rain, Wiley Ser. Remote Sens., John Wiley, New York.

[10]. Cressie, N.A.C., 1993: *Statistics for Spatial Data.* John Wiley and Sons, 900 pp.

[11]. De Michele, C., N.T. Kottegoda, R. Rosso, 2001: The derivation of areal reduction factor of storm rainfall from its scaling properties. *Water Resour. Res.*, 37, 3247-3252.

[12]. Foufoula-Georgiou, E. and W.F. Krajewski, 1995: Recent advances in rainfall modeling, estimation, and forecasting, *Reviews of Geophysics*, U.S. National Report to *International Union of Geodesy and Geophysics* 1991-1994, 1125-1137.

[13]. Gebremichael, M., and W.F. Krajewski, 2004: Assessment of the statistical characterization of small-scale rainfall variability from radar: Analysis of TRMM GV data sets, *J. Appl. Meteor.*, 43(8), 1180-1199.

[14]. Habib, E., and W. F. Krajewski, 2002: Uncertainty analysis of the TRMM Ground Validation radar-rainfall products: Application to the TEFLUN-B field campaign. *J. Appl. Meteor.*, 41, 558-572.

[15]. Habib, E., Ciach, G.J., and W.F. Krajewski, 2004: A Method for Filtering out Raingauge Representativeness Errors from the Verification Distributions of Radar and Raingauge rainfall. *Adv. Water Resour.*, 27, 967-980.

[16]. Habib, E., W.F. Krajewski, and G.J. Ciach, 2001: Estimation of rainfall inter-station Correlation. *J. Hydrometeor.*, 2, 621-629.

[17]. Harris, D., A. Seed, Menabde, M., and G. Austin, 1997: Factors affecting multiscaling analysis of rainfall time series. *Nonlinear Process. Geophys.*, 4, 137-155.

[18]. Kitchen, M., and R.M. Blackall, 1992: Representativeness errors in comparisons between radar and gauge measurements of rainfall. *J. Hydrology*, 134, 13-33.

[19]. Krajewski, W.F., E.N. Anagnostou, and G.J. Ciach, 1996: Effects of the radar observation process on inferred rainfall statistics. *J. Geophys. Res.*, 101, 493-502.

[20]. Krajewski, W.F., G.J. Ciach, and E. Habib, 2003: An analysis of small-scale rainfall variability in different climatic regimes. *Hydrol. Sci. J.*, 48, 151-162.

[21]. Kundu, P.K., and T.L. Bell, 2003: A stochastic model of space-time variability of mesoscale rainfall: Statistics of spatial averages. *Water Resour. Res.*, 39, 1328, doi:10.1029/2002WR001802.

[22]. Lovejoy, S., and D. Schertzer, 1995: Multifractals and rain. In: *New uncertainty Concepts in Hydrology and Water Resources* (ed. by Z. Kundzewicz), 62-103. Cambridge University Press, Cambridge, UK.

[23]. Morrissey, M.L., 1991: Using sparse raingages to test satellite-based rainfall algorithms. *J. Geophys. Res.*, 96, 18561-18571.

[24]. Morrissey, M.L., and J.S. Greene, 1993: Comparison of two satellite-based rainfall algorithms using Pacific Atoll raingage data. *J. Appl. Meteor.*, 32, 411-425.

[25]. Paulson, K.S., 2002: The spatial temporal statistics of rain rate random fields, *Radio Science*, 37(5).

[26]. Seed, A.W., R. Srikanthan, and M. Menabde, 1999: A space and time model for design storm rainfall. *J. Geophys. Res.*, 104, 31623-31630.

[27]. Shimizu, K., 1993: A Bivariate mixed lognormal distribution with an analysis of rainfall data. *J. Appl. Meteor.*, 32, 161-171.

[28]. Steiner, M., J.A. Smith, S.J. Burges, C.V. Alonso and R.W. Darden, 1999: Effect of bias adjustment and rain gage data quality control on radar rainfall estimates. *Water Resources Research*, 35, 2487-2503.

Appendix C

Temporal Scale: Three Hours

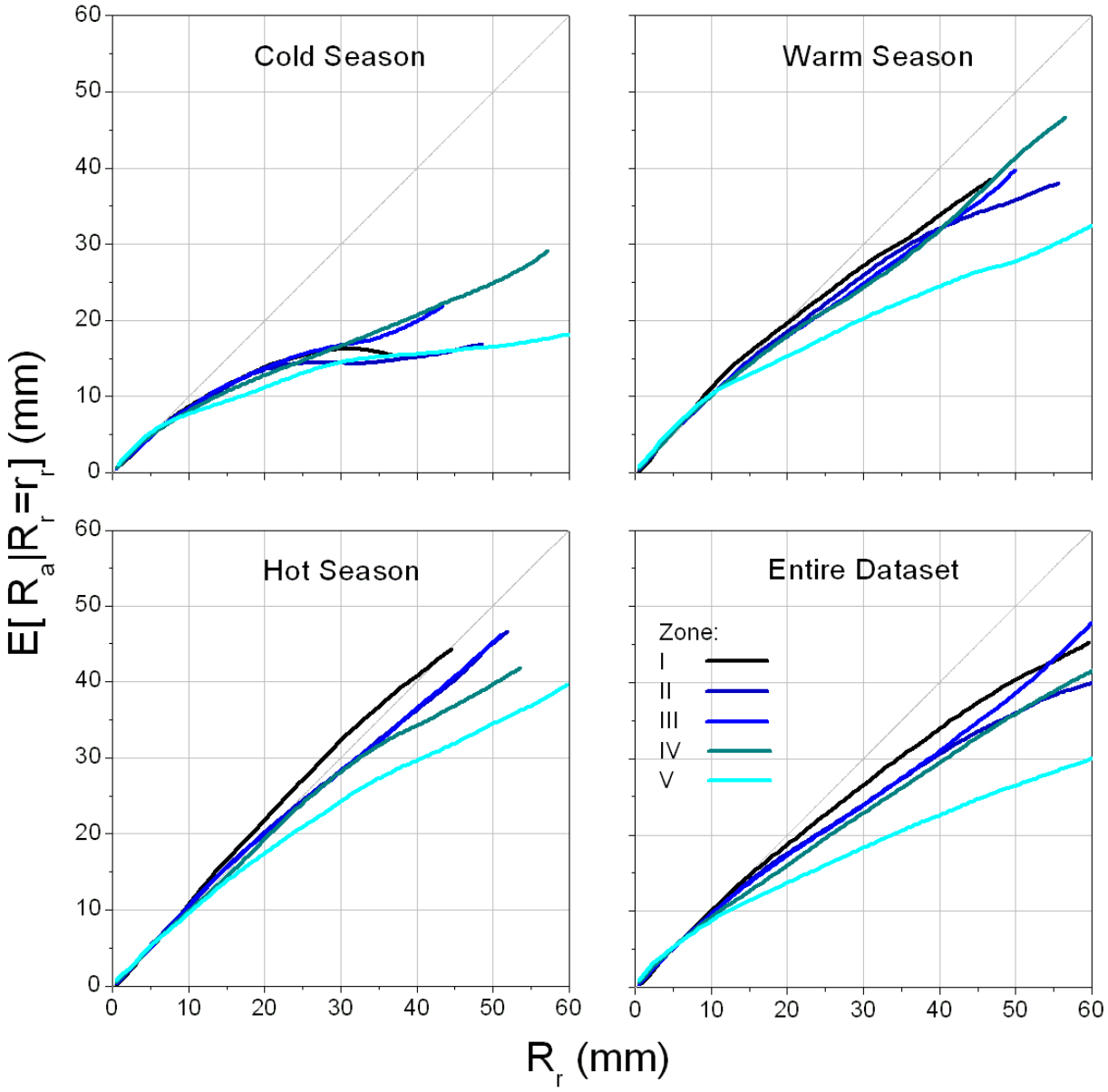

Figure C.1. Rain gauge averages, conditional on radar-rainfall values, after removing the overall bias for the three seasons and entire dataset for the 5 zones. The minimum weighted sample size is 100.

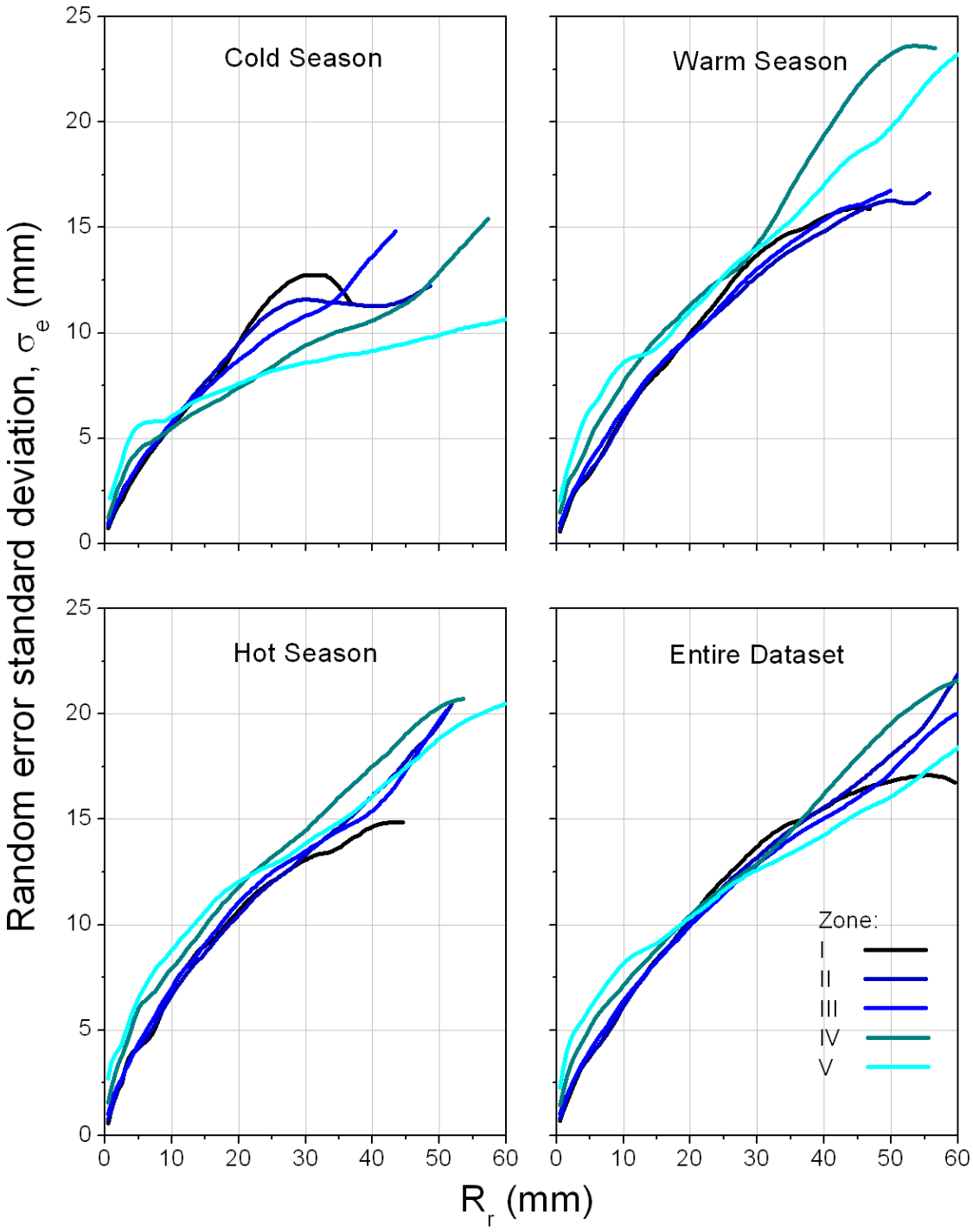

Figure C.2. Standard deviations of the random component in the additive form (mm) for the three seasons and entire dataset for the 5 zones. The minimum weighted sample size is 100.

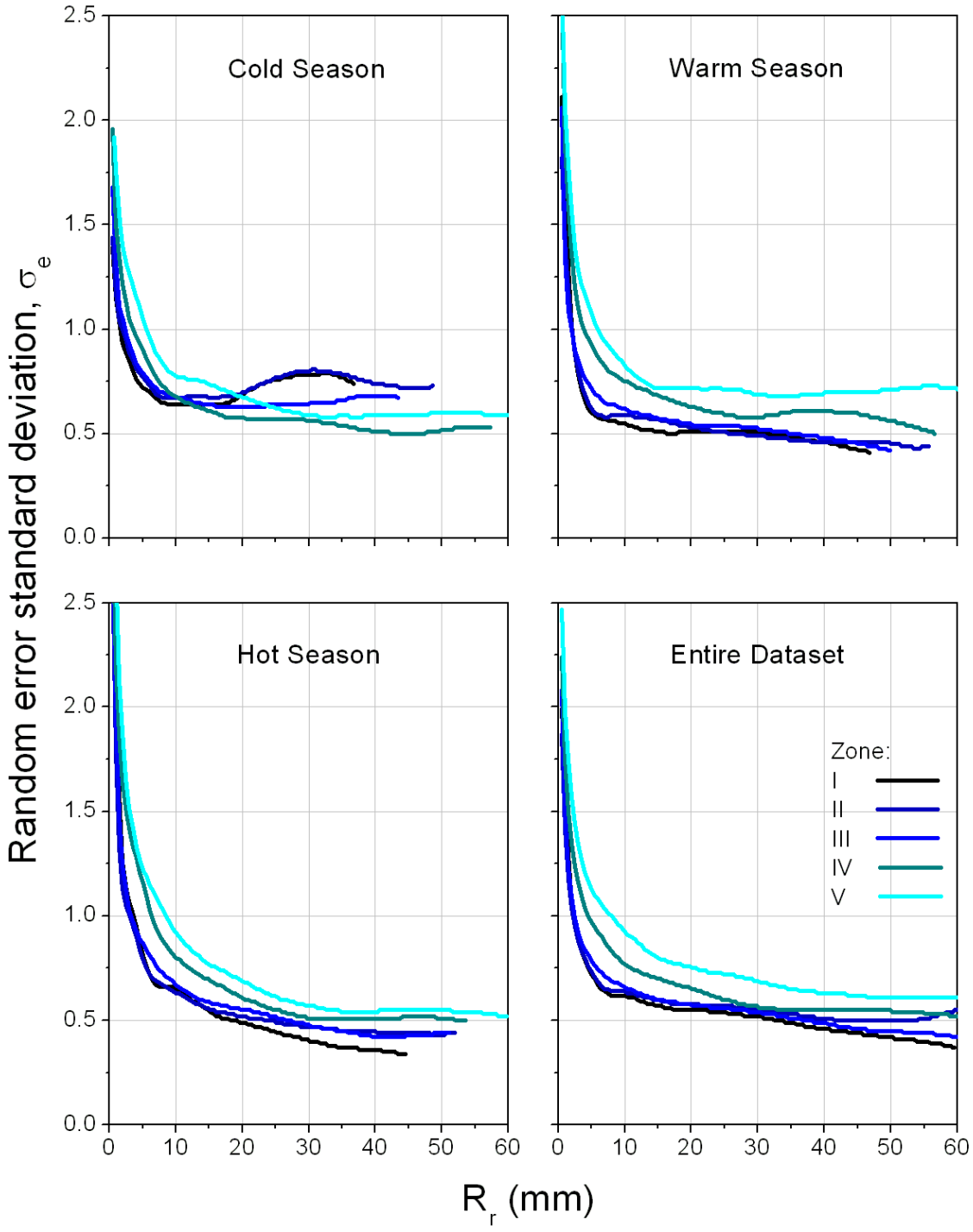

Figure C.3. Standard deviations of the random component in the multiplicative form for the three seasons and entire dataset for the 5 zones (1-h resolution). The minimum weighted sample size is 100.

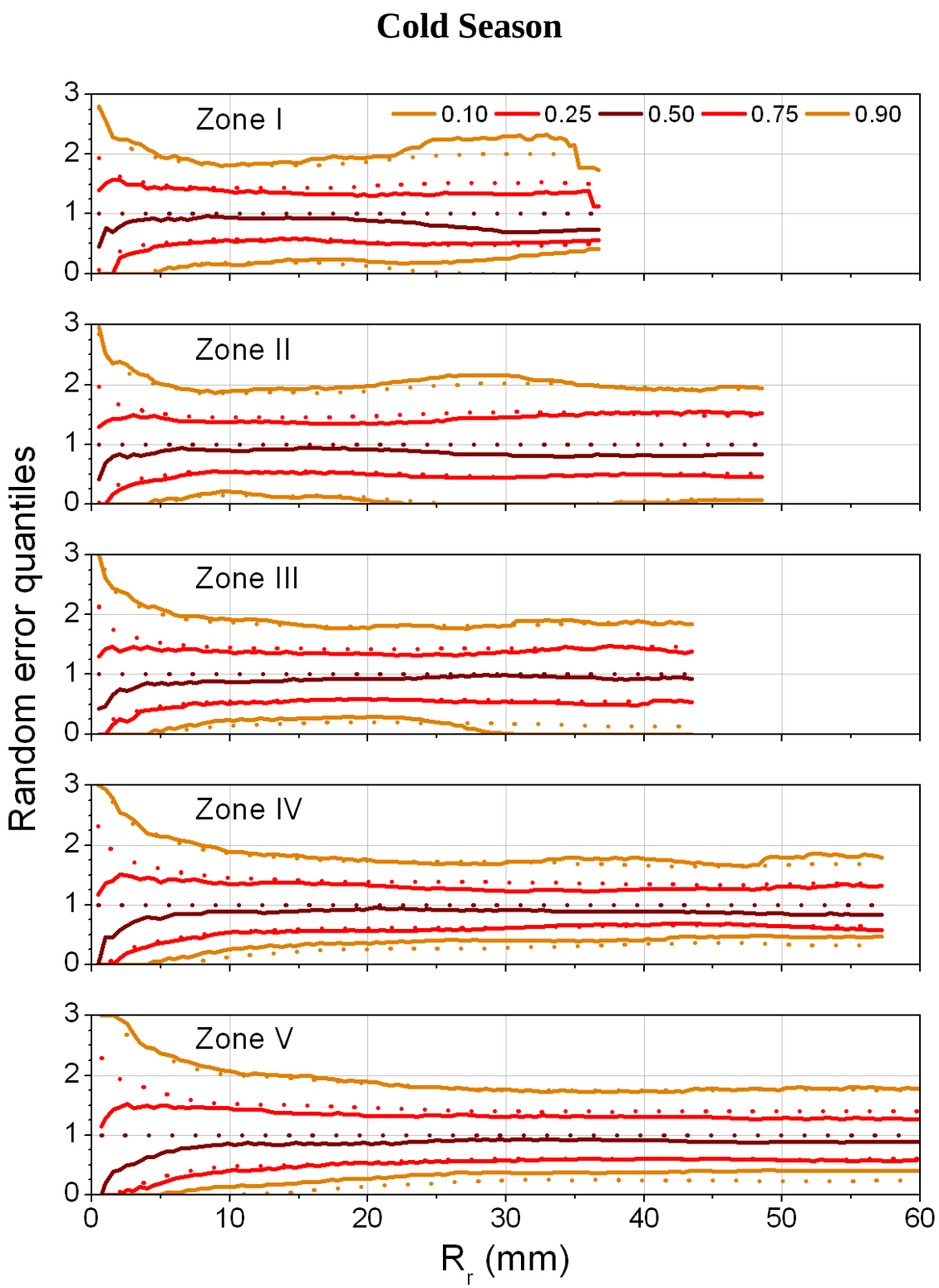

Figure C.4. Comparison of the empirical and Gaussian quantiles (p=0.1, 0.25, 0.5, 0.75, 0.9) for the five zones (cold season). The mean of the theoretical distribution is equal to 1 and the standard deviation is the standard deviation of the random component in the multiplicative form. The minimum weighted sample size is 100.

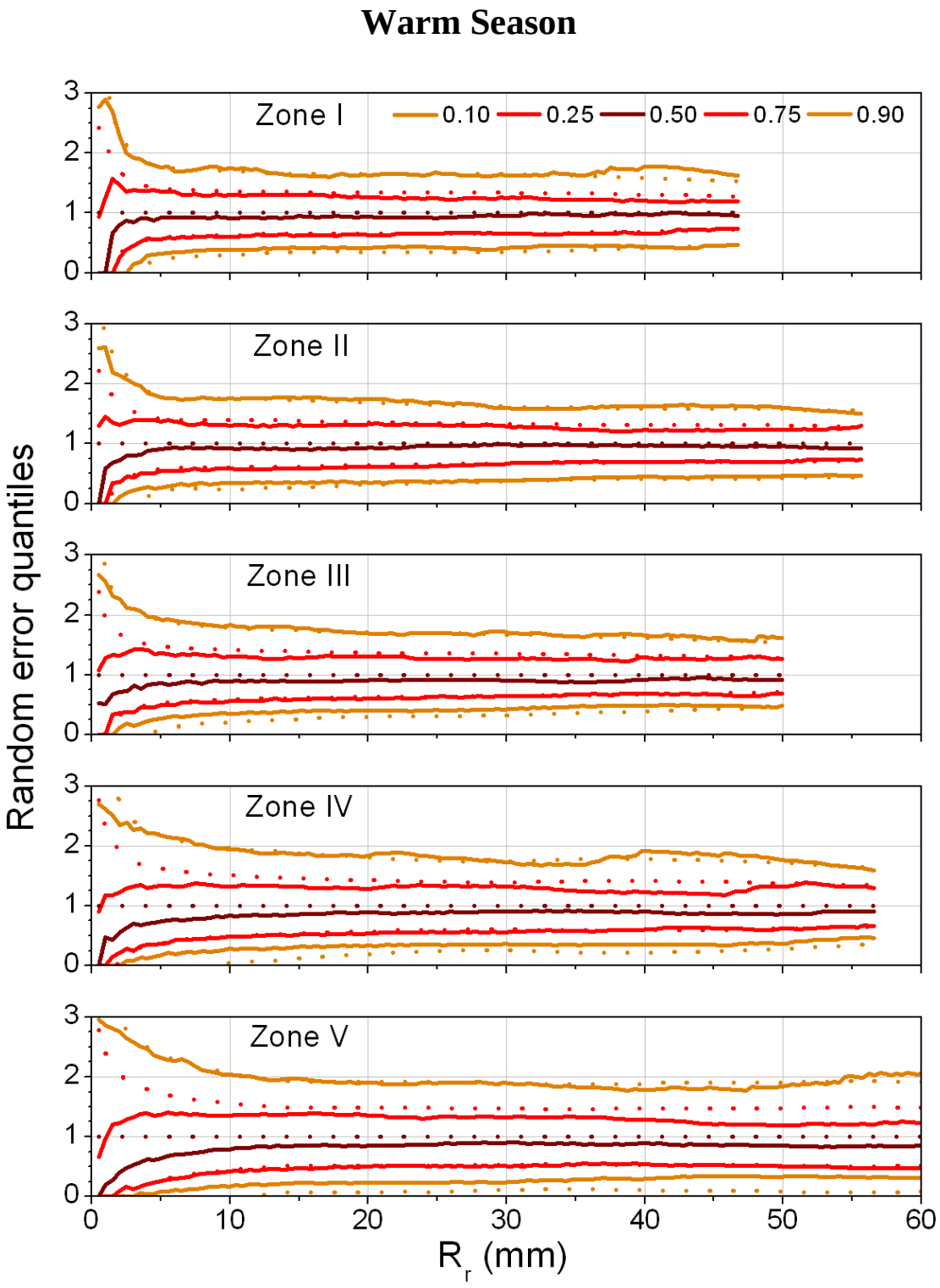

Figure C.5. Comparison of the empirical and Gaussian quantiles (p=0.1, 0.25, 0.5, 0.75, 0.9) for the five zones (warm season). The mean of the theoretical distribution is equal to 1 and the standard deviation is the standard deviation of the random component in the multiplicative form. The minimum weighted sample size is 100.

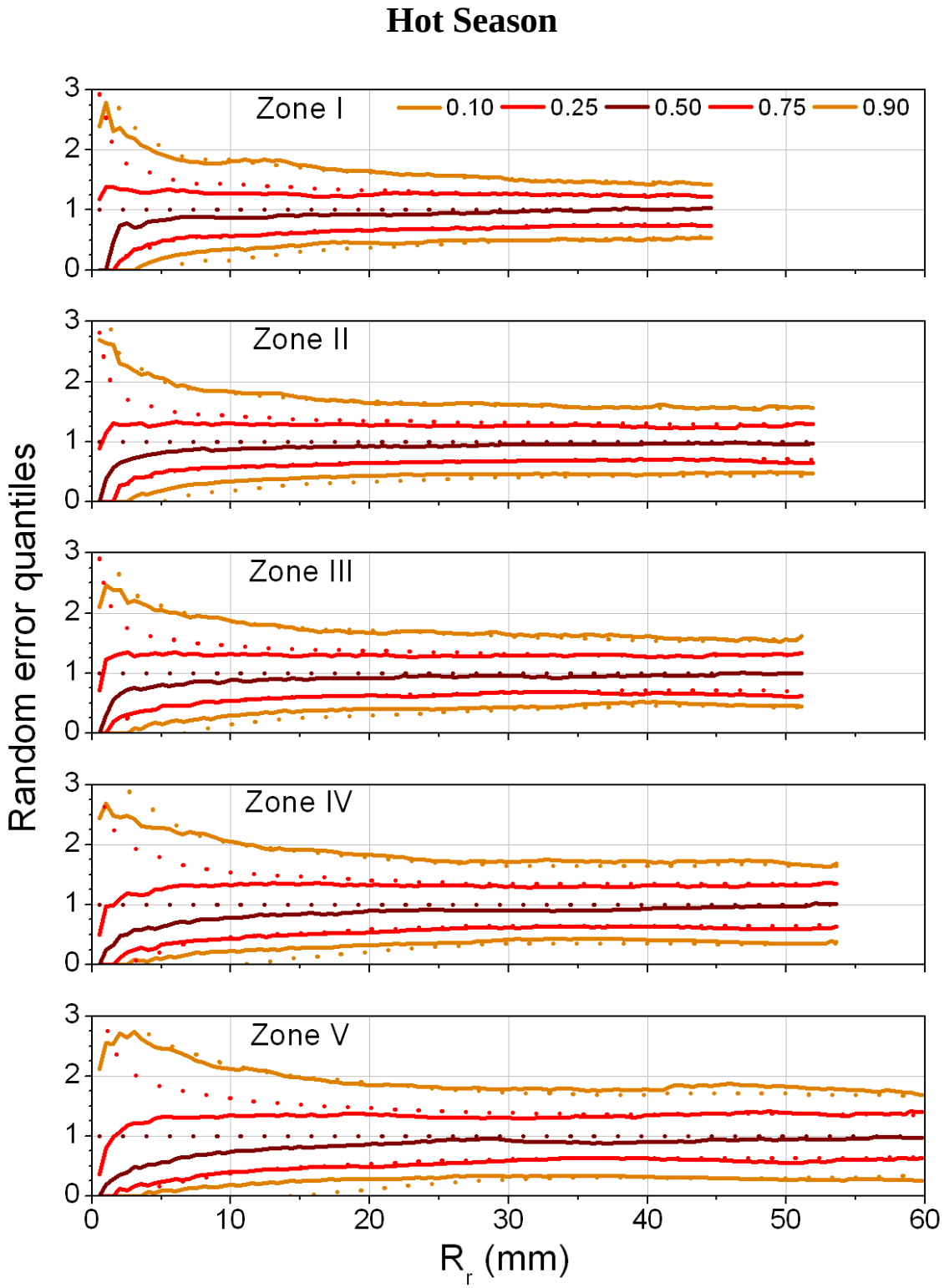

Figure C.6. Comparison of the empirical and Gaussian quantiles (p=0.1, 0.25, 0.5, 0.75, 0.9) for the five zones (hot season). The mean of the theoretical distribution is equal to 1 and the standard deviation is the standard deviation of the random component in the multiplicative form. The minimum weighted sample size is 100.

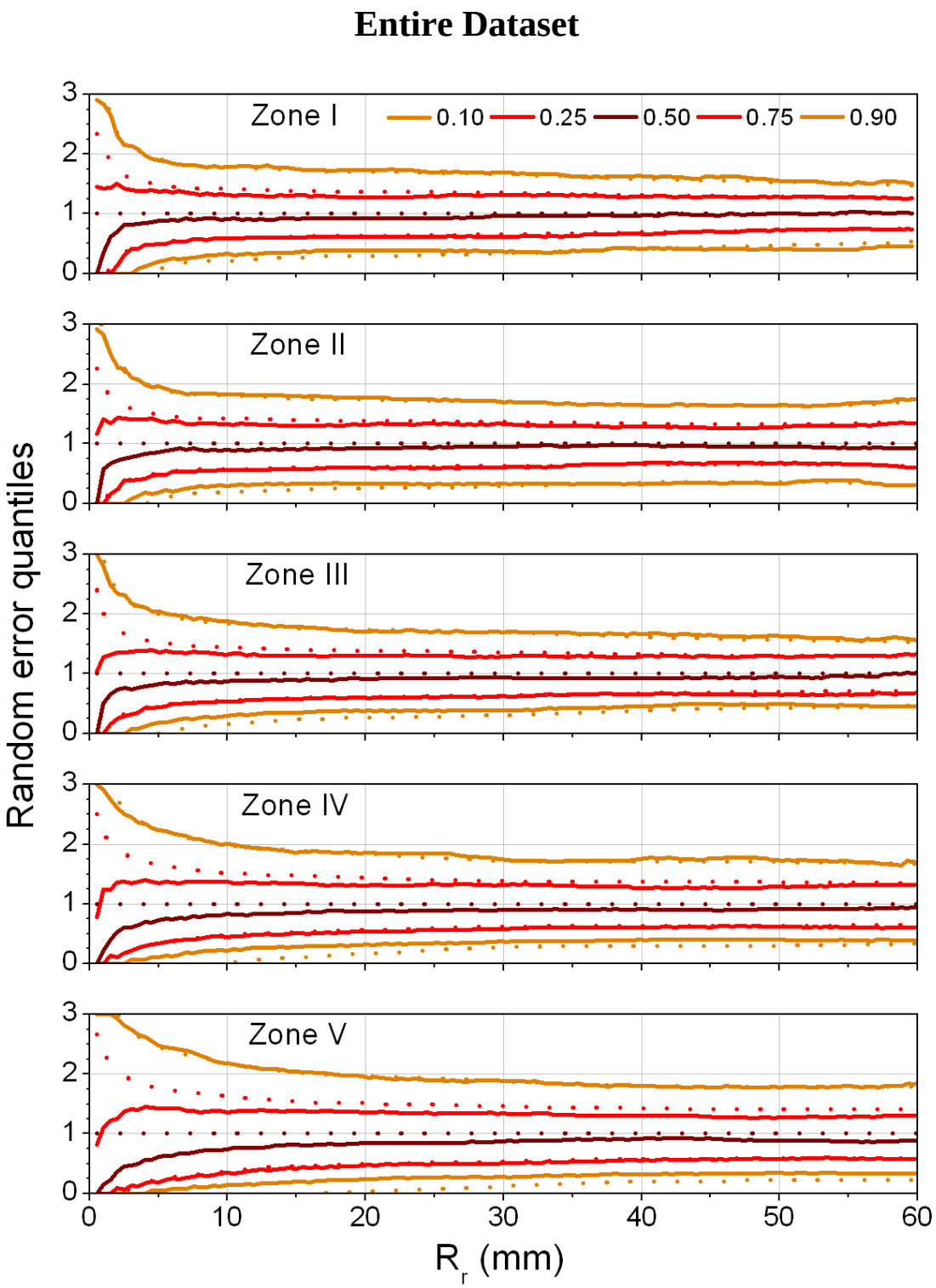

Figure C.7. Comparison of the empirical and Gaussian quantiles (p=0.1, 0.25, 0.5, 0.75, 0.9) for the five zones (all seasons). The mean of the theoretical distribution is equal to 1 and the standard deviation is the standard deviation of the random component in the multiplicative form. The minimum weighted sample size is 100.

Zone I

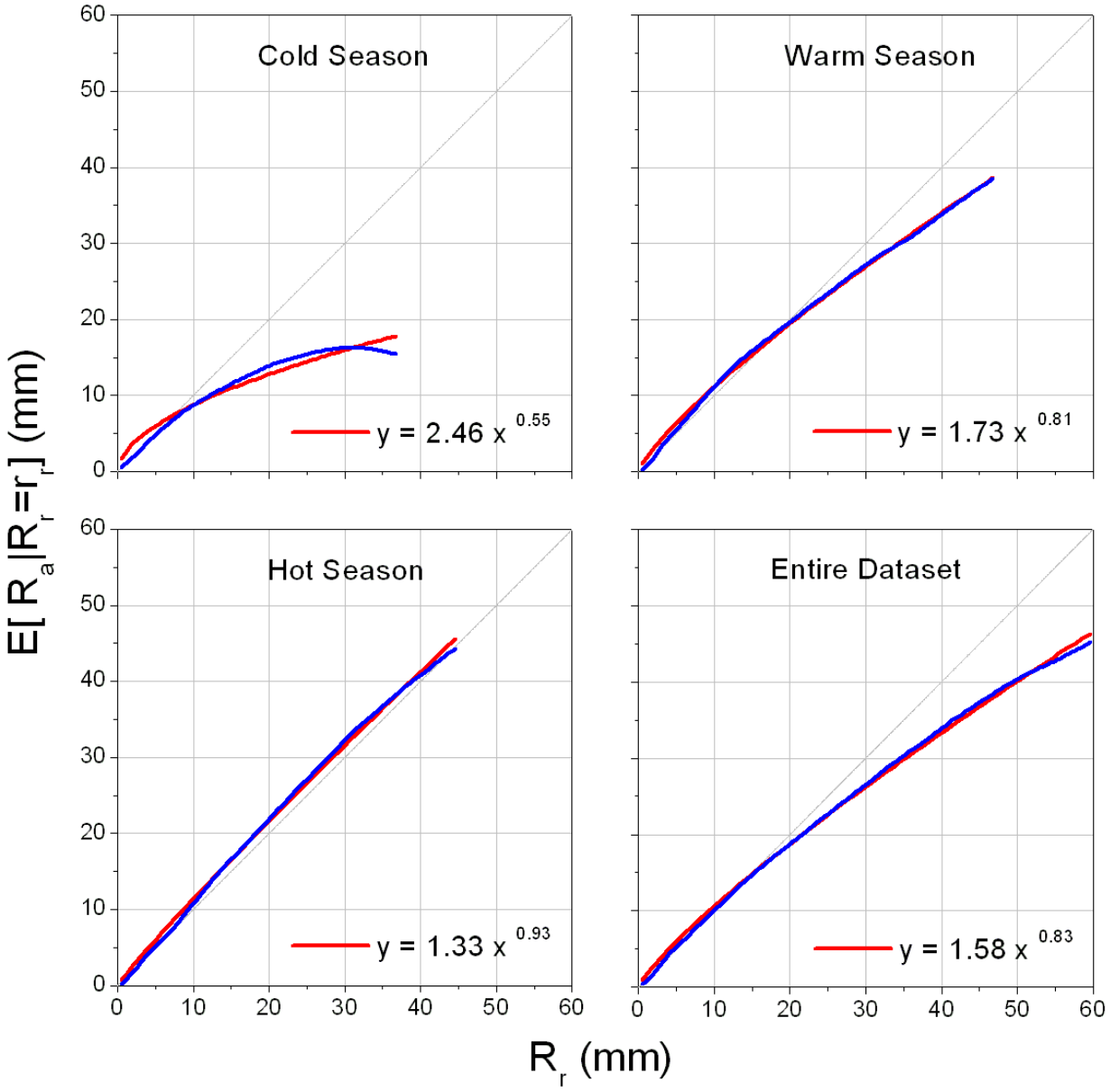

Figure C.8. Power law model approximation of the rain gauge conditional averages for the three seasons and the entire dataset for Zone I.

Zone II

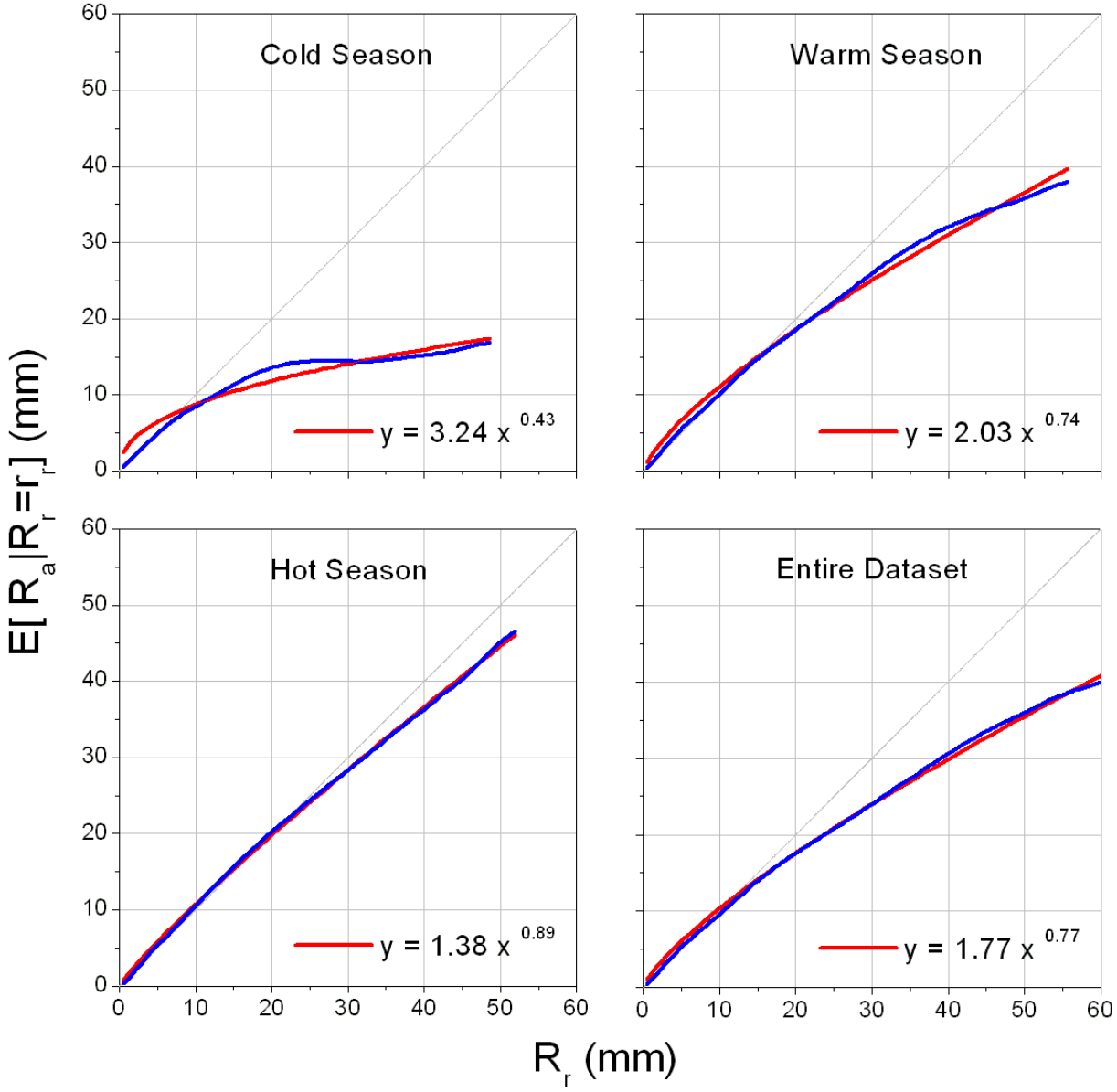

Figure C.9. Power law model approximation of the rain gauge conditional averages for the three seasons and the entire dataset for Zone II.

Zone III

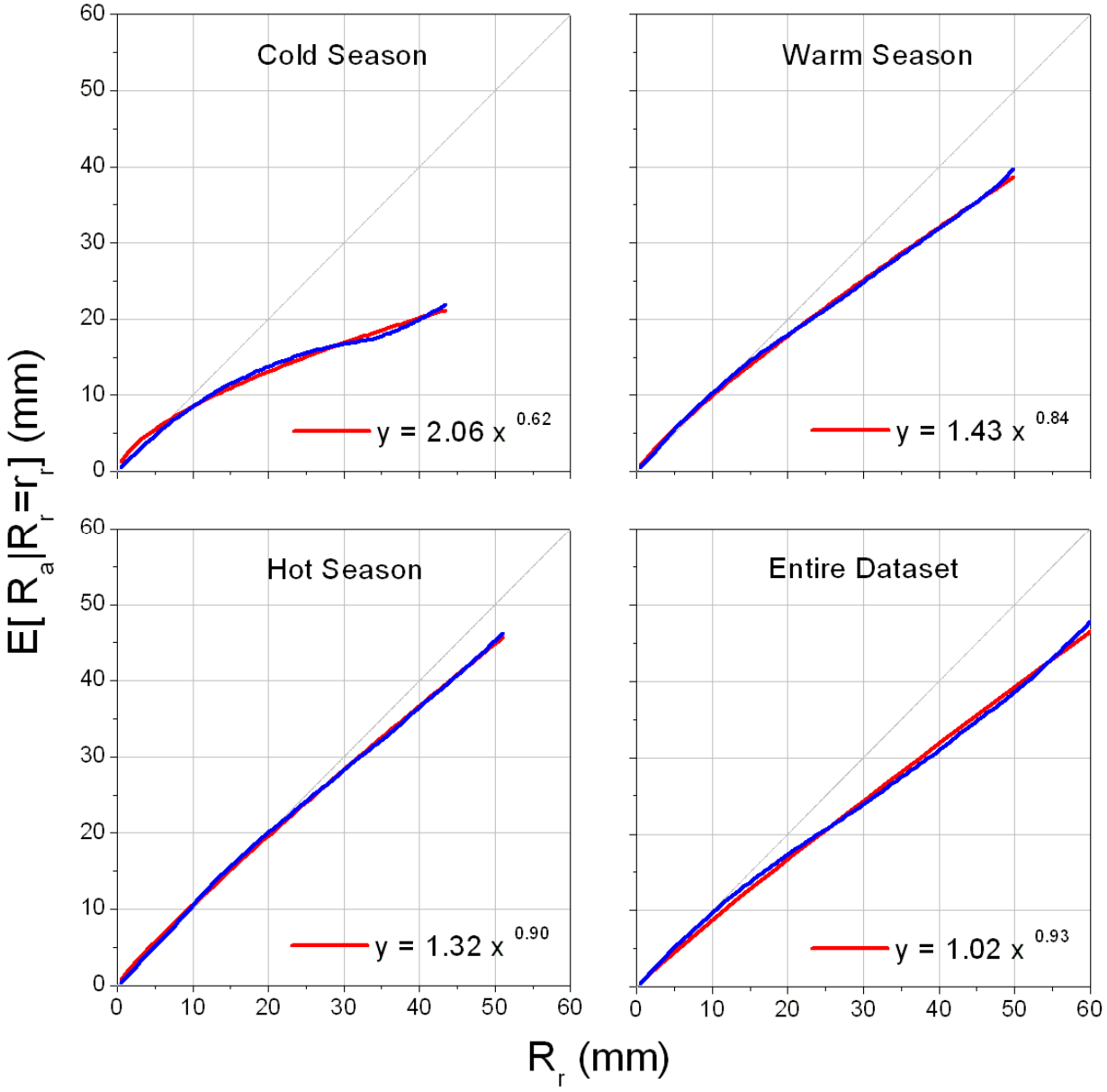

Figure C.10. Power law model approximation of the rain gauge conditional averages for the three seasons and the entire dataset for Zone III.

Zone IV

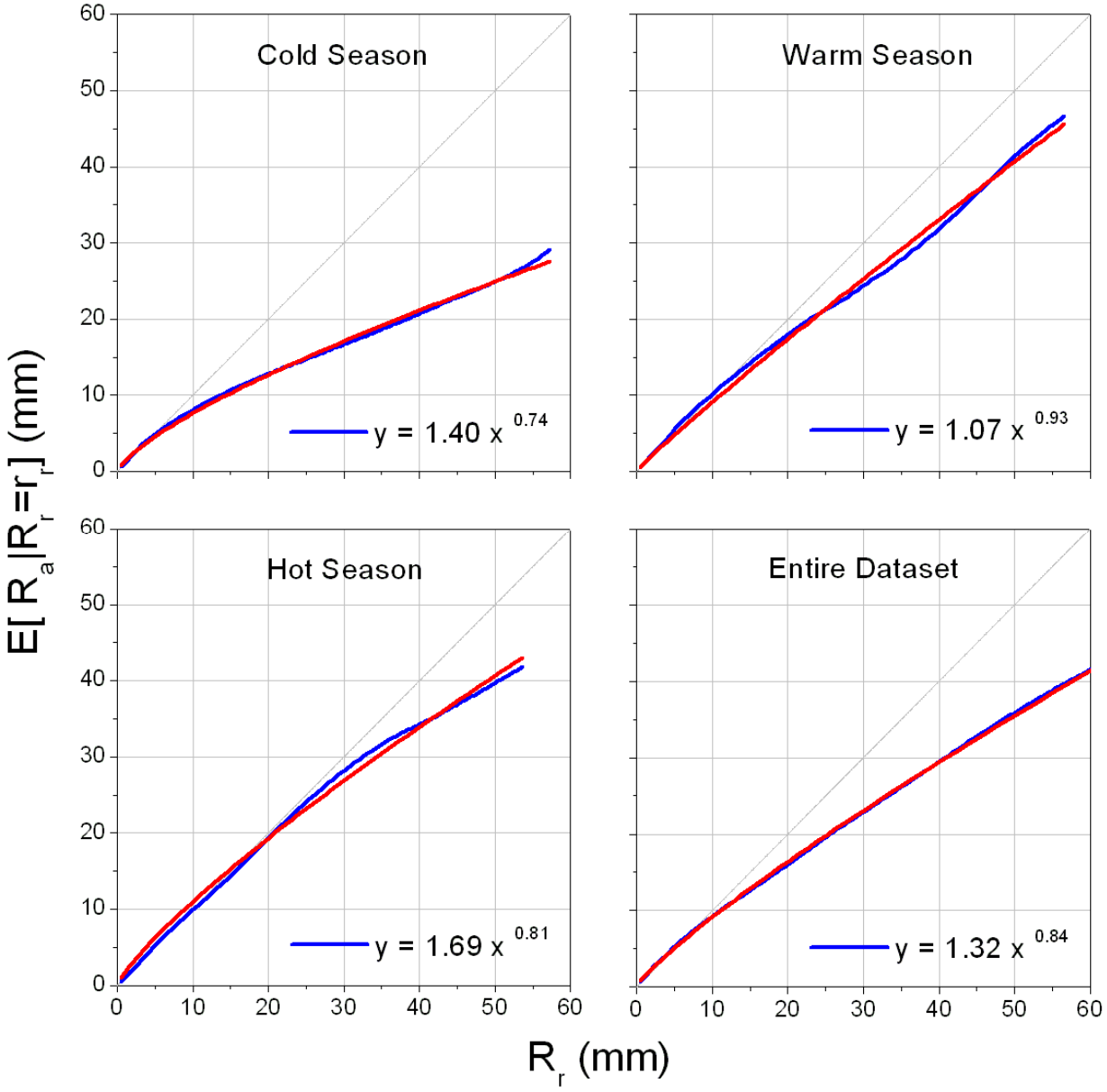

Figure C.11. Power law model approximation of the rain gauge conditional averages for the three seasons and the entire dataset for Zone IV.

Zone V

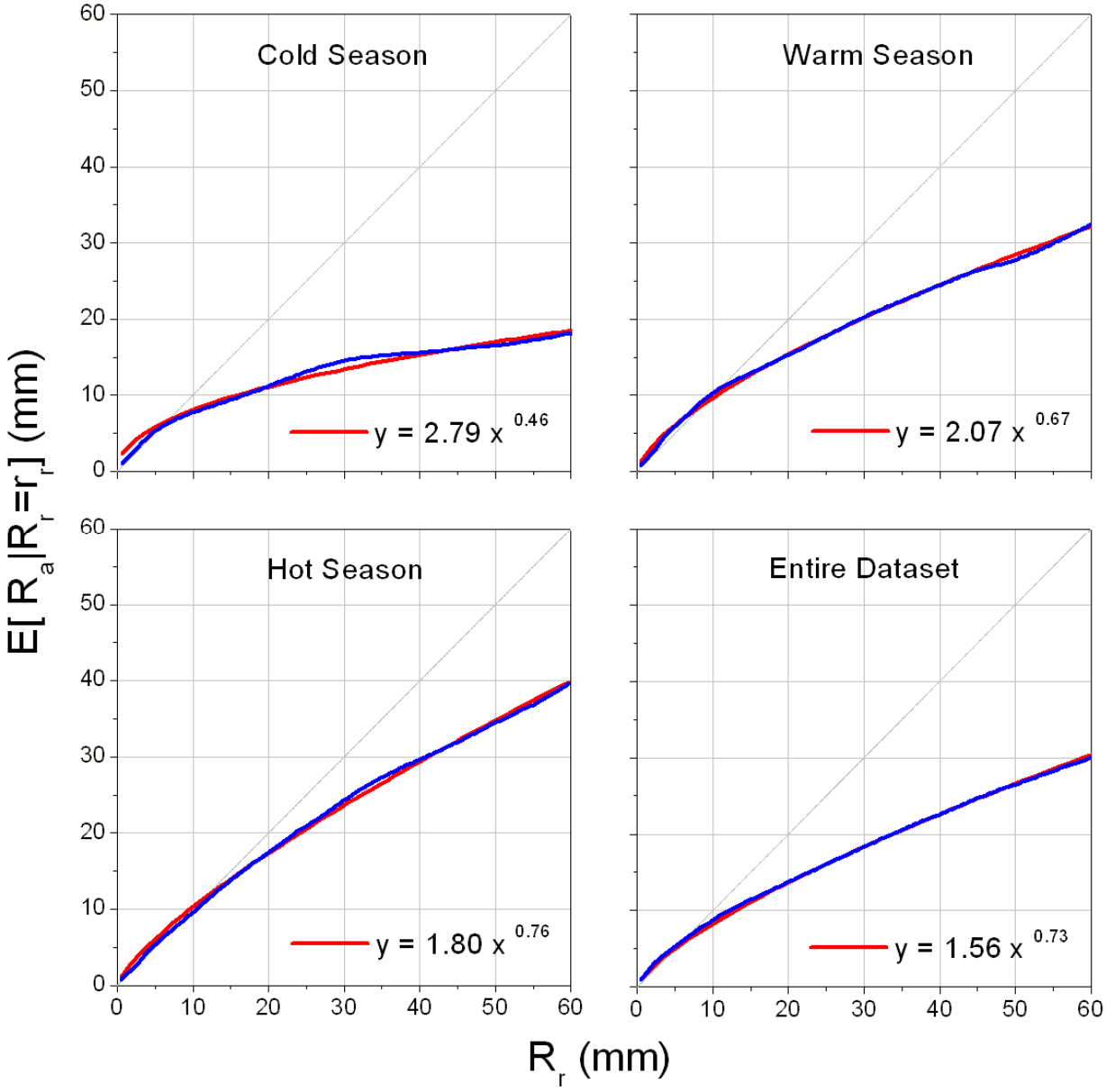

Figure C.12. Power law model approximation of the rain gauge conditional averages for the three seasons and the entire dataset for Zone V.

Zone I

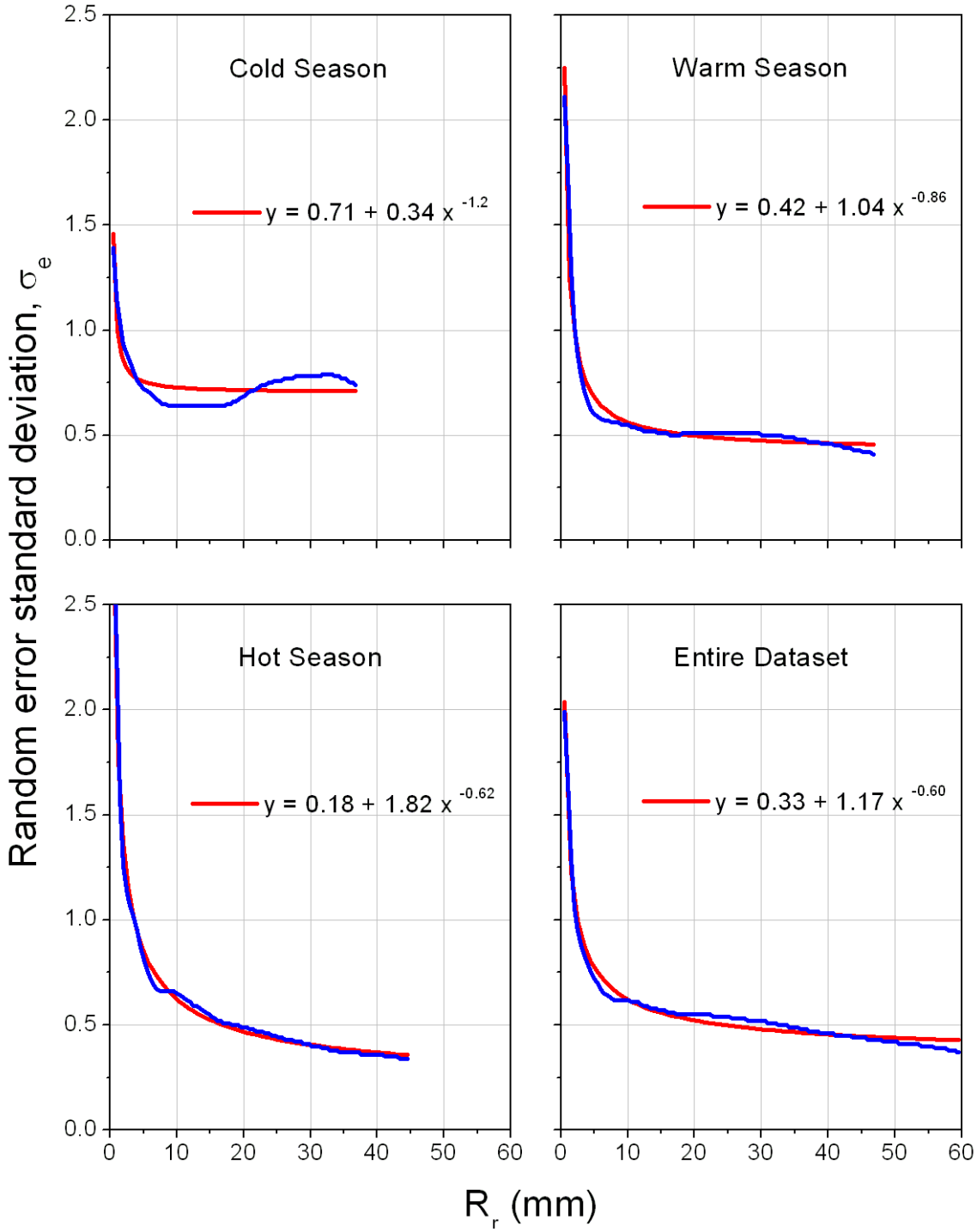

Figure C.13. Model approximation of the conditional multiplicative standard deviation for the three seasons and the entire dataset for Zone I.

Zone II

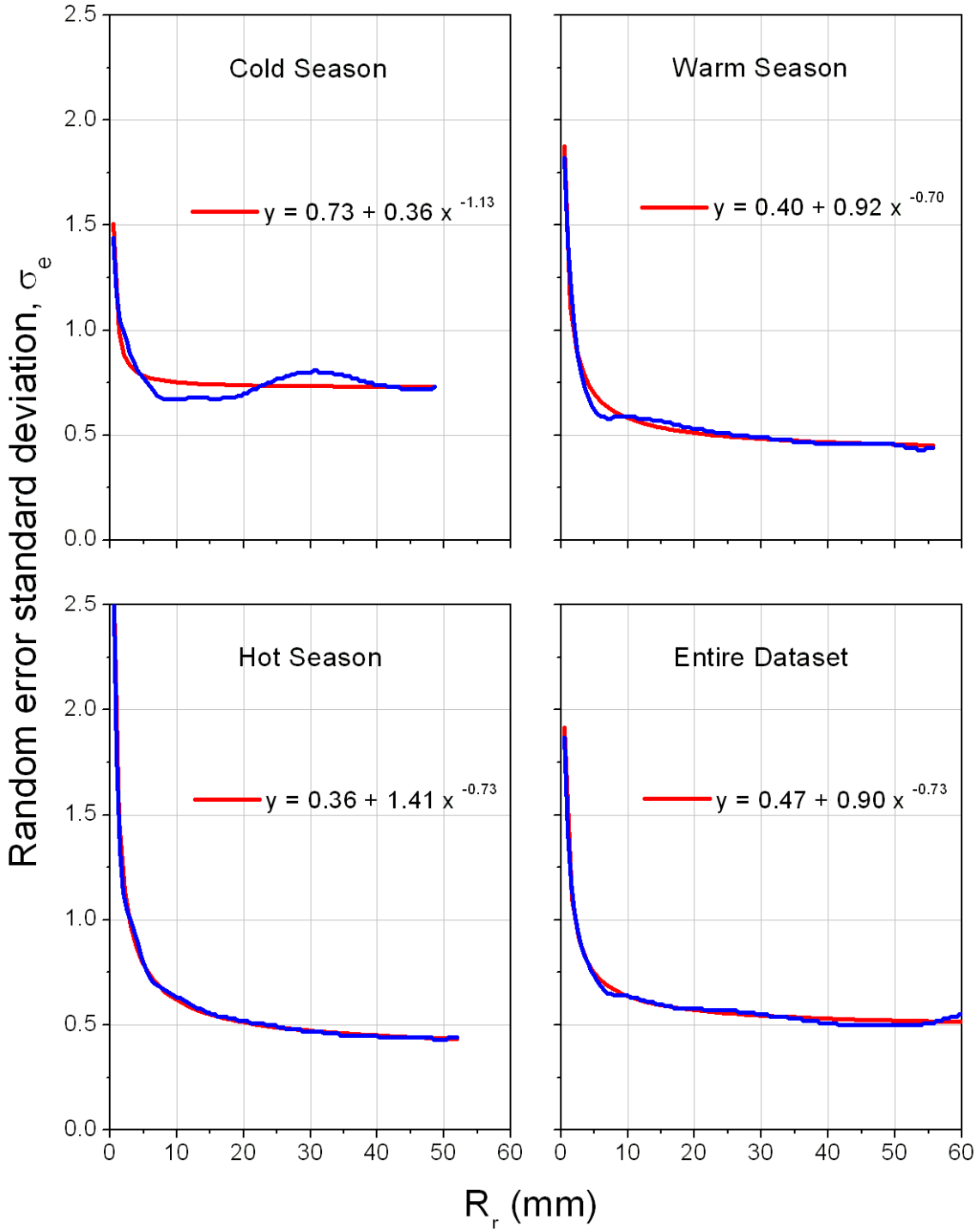

Figure C.14. Model approximation of the conditional multiplicative standard deviation for the three seasons and the entire dataset for Zone II.

Zone III

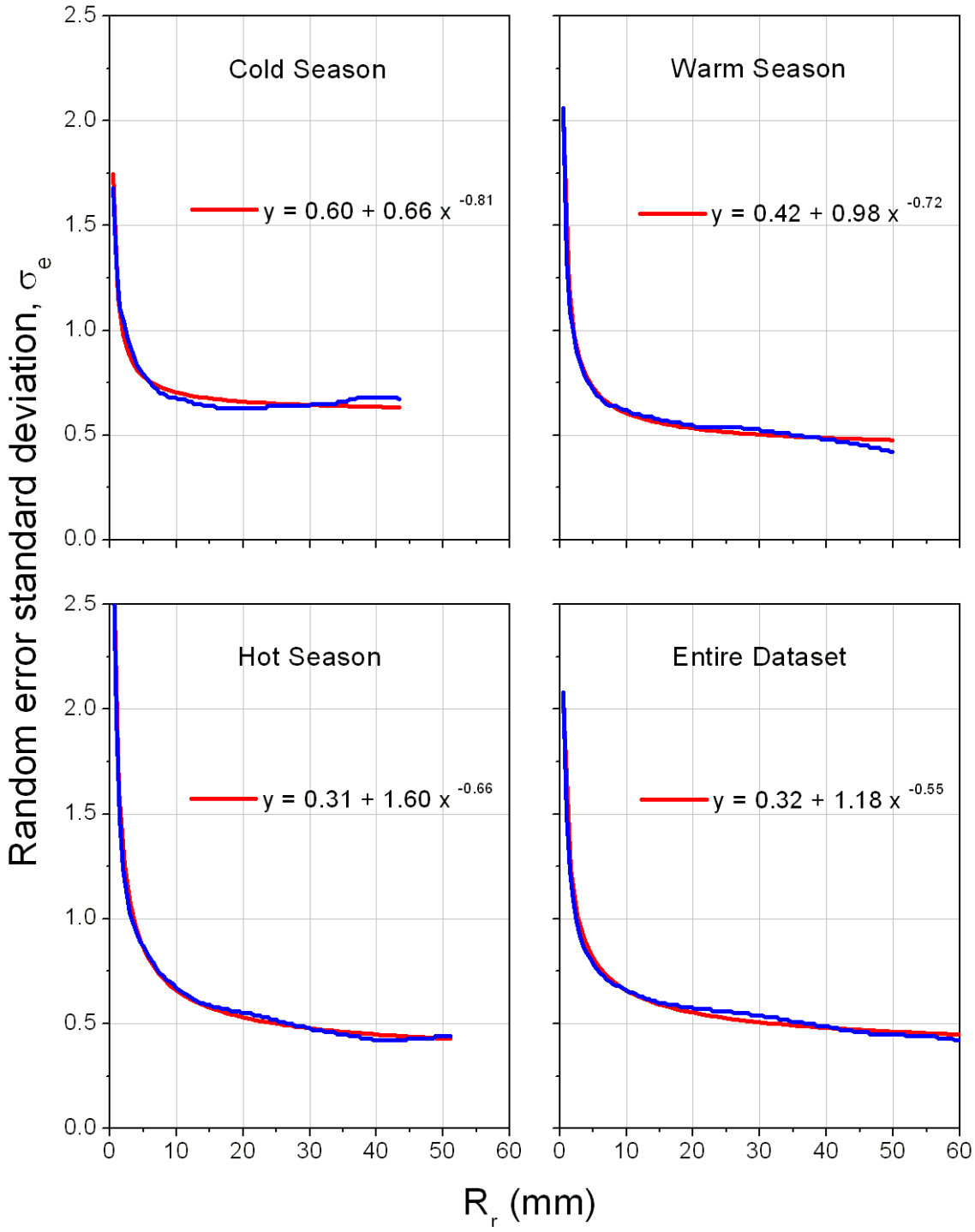

Figure C.15. Model approximation of the conditional multiplicative standard deviation for the three seasons and the entire dataset for Zone III.

Zone IV

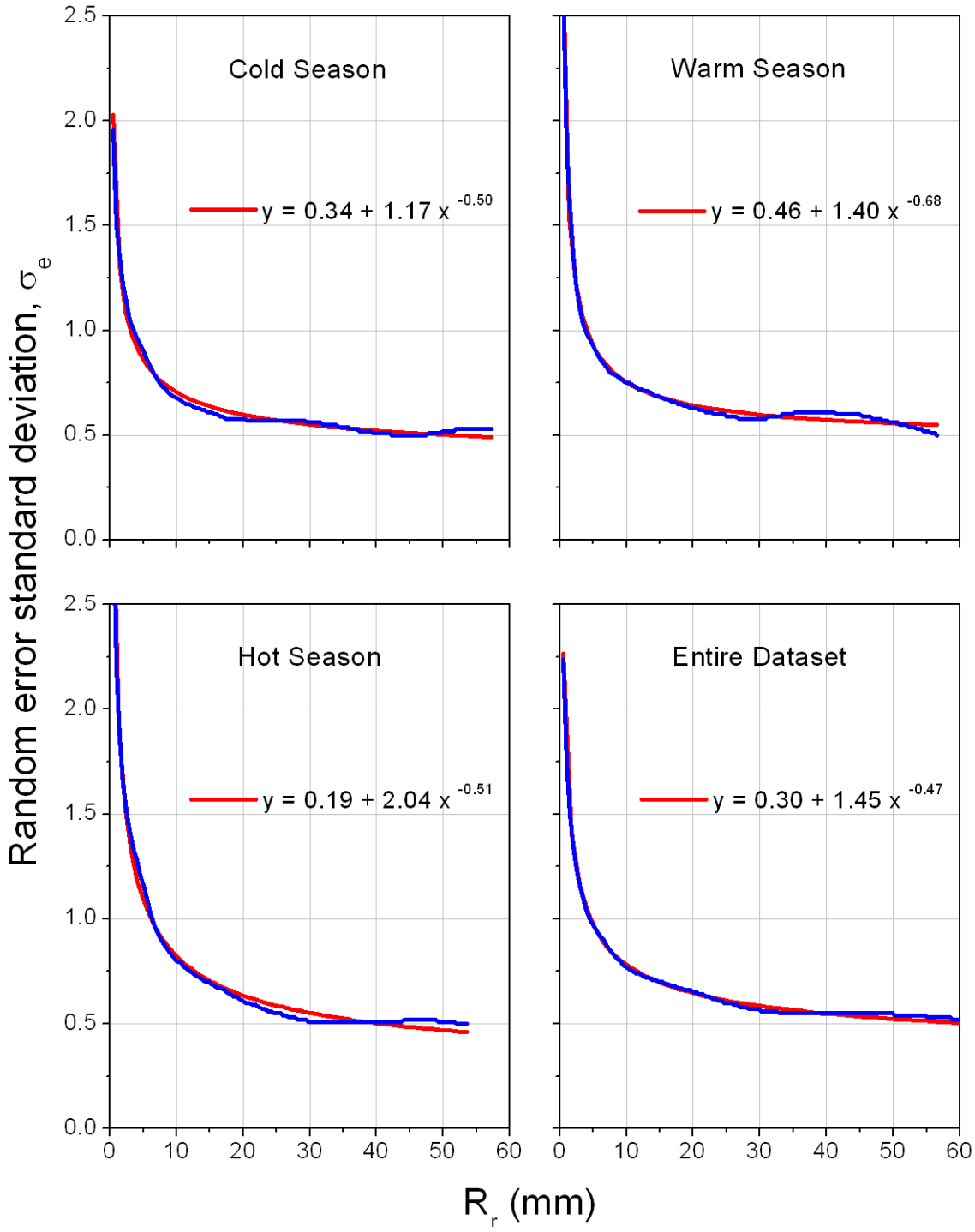

Figure C.16. Model approximation of the conditional multiplicative standard deviation for the three seasons and the entire dataset for Zone IV.

Zone V

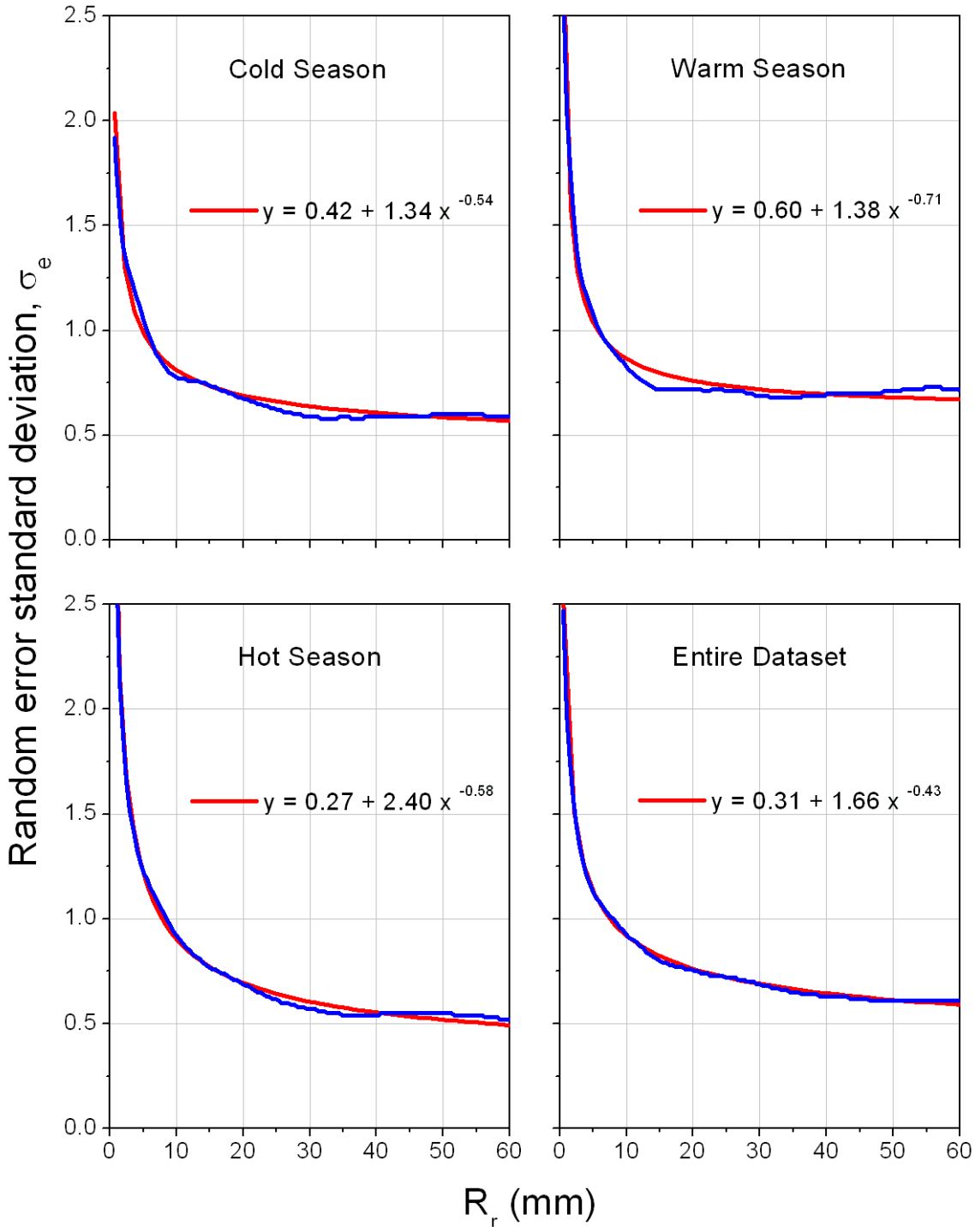

Figure C.17. Model approximation of the conditional multiplicative standard deviation for the three seasons and the entire dataset for Zone V.

Spatial and Temporal Correlation Structure

Winter Season

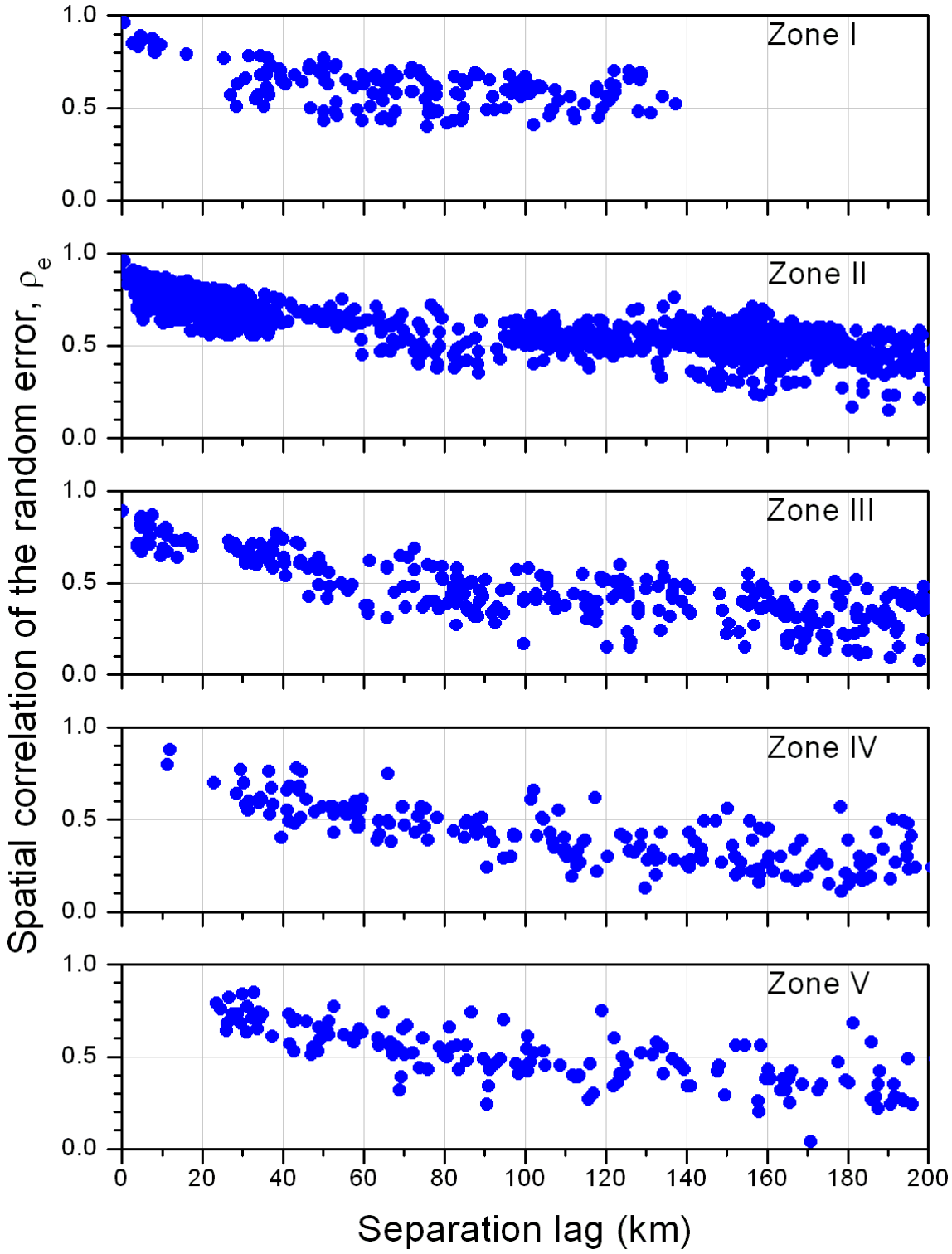

Figure C.18. Intergauge spatial Pearson correlation of the random component for the winter season.

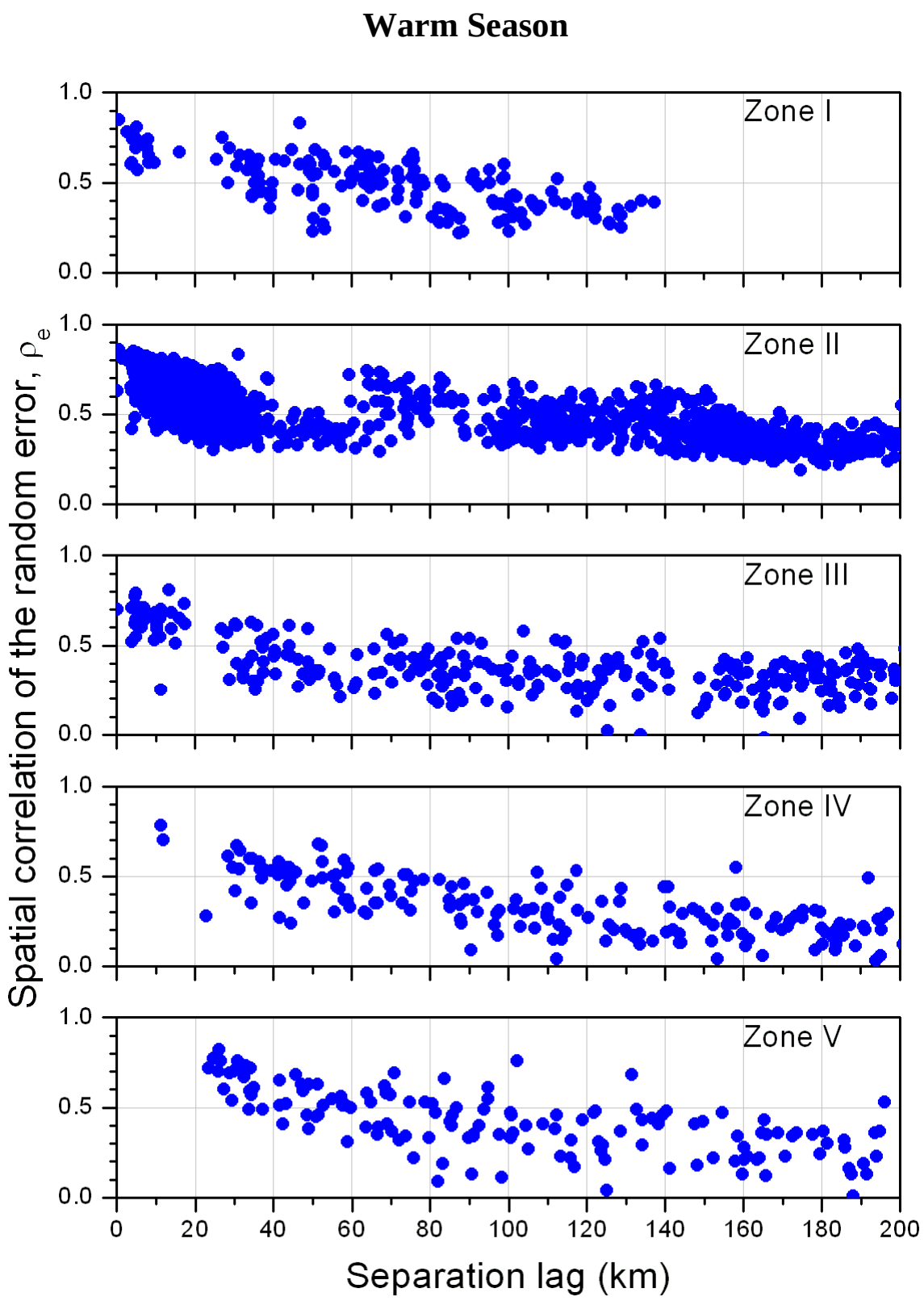

Figure C.19. Intergauge spatial Pearson correlation of the random component for the warm season.

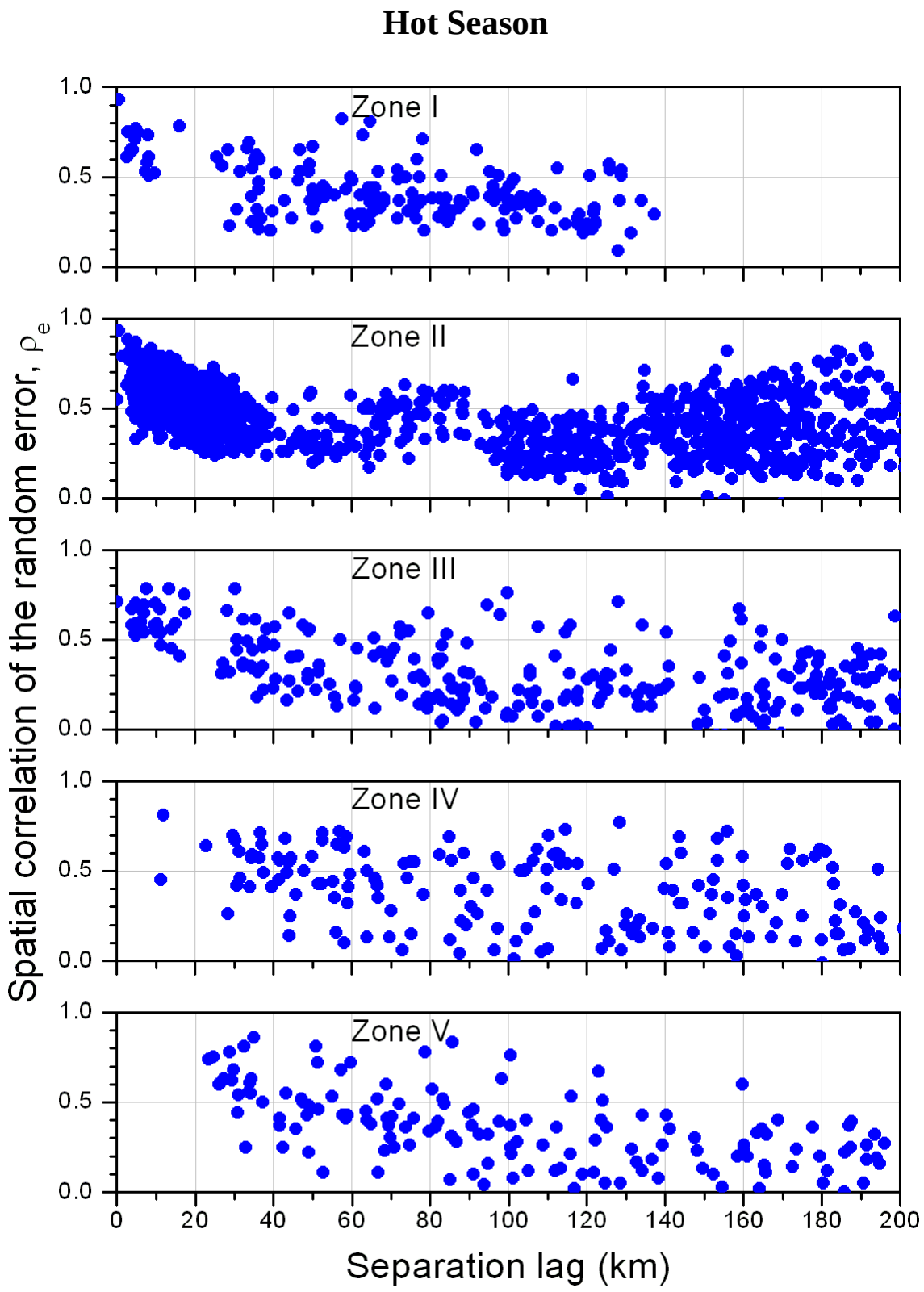

Figure C.20. Intergauge spatial Pearson correlation of the random component for the hot season.

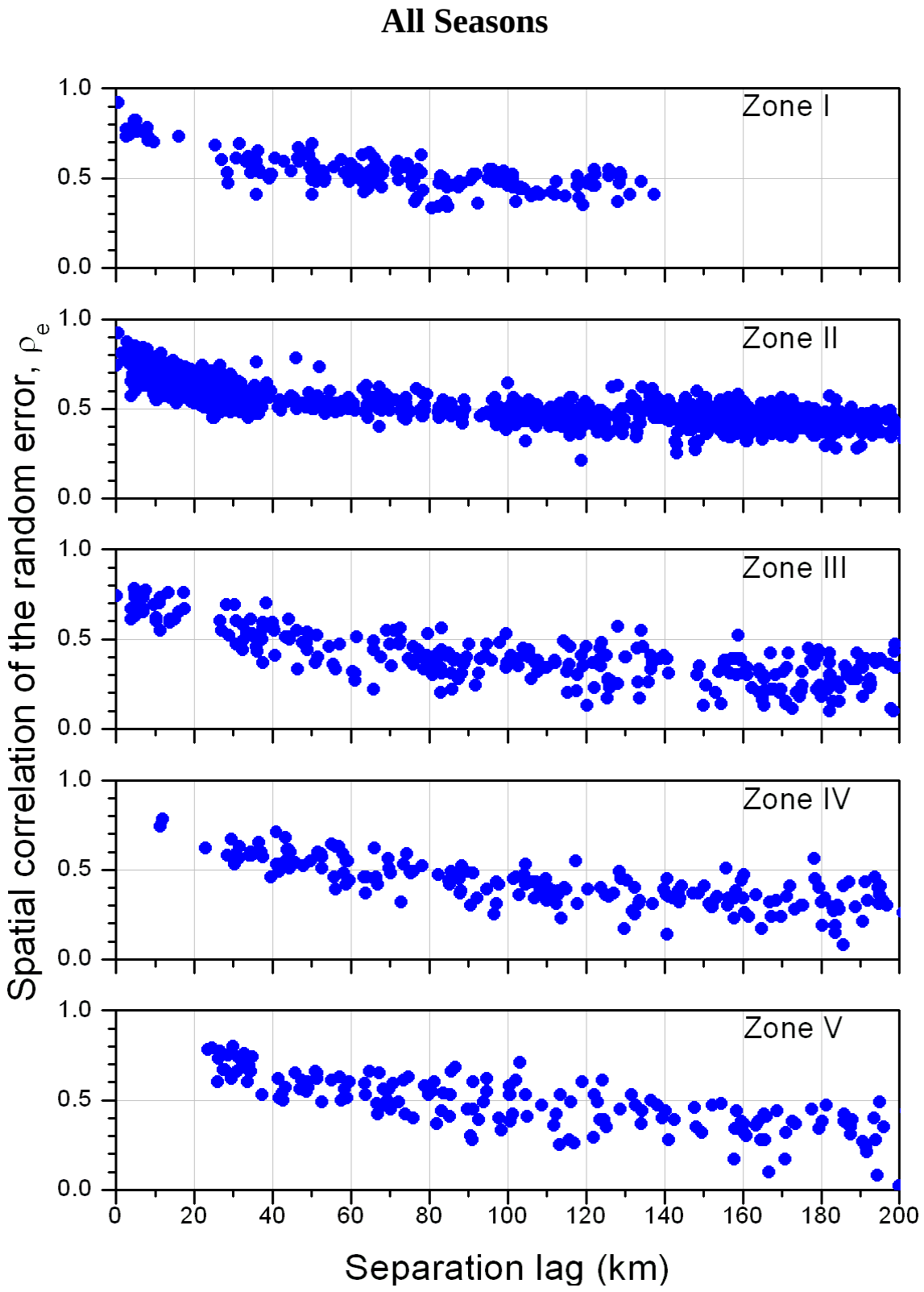

Figure C.21. Intergauge spatial Pearson correlation of the random component for all seasons.

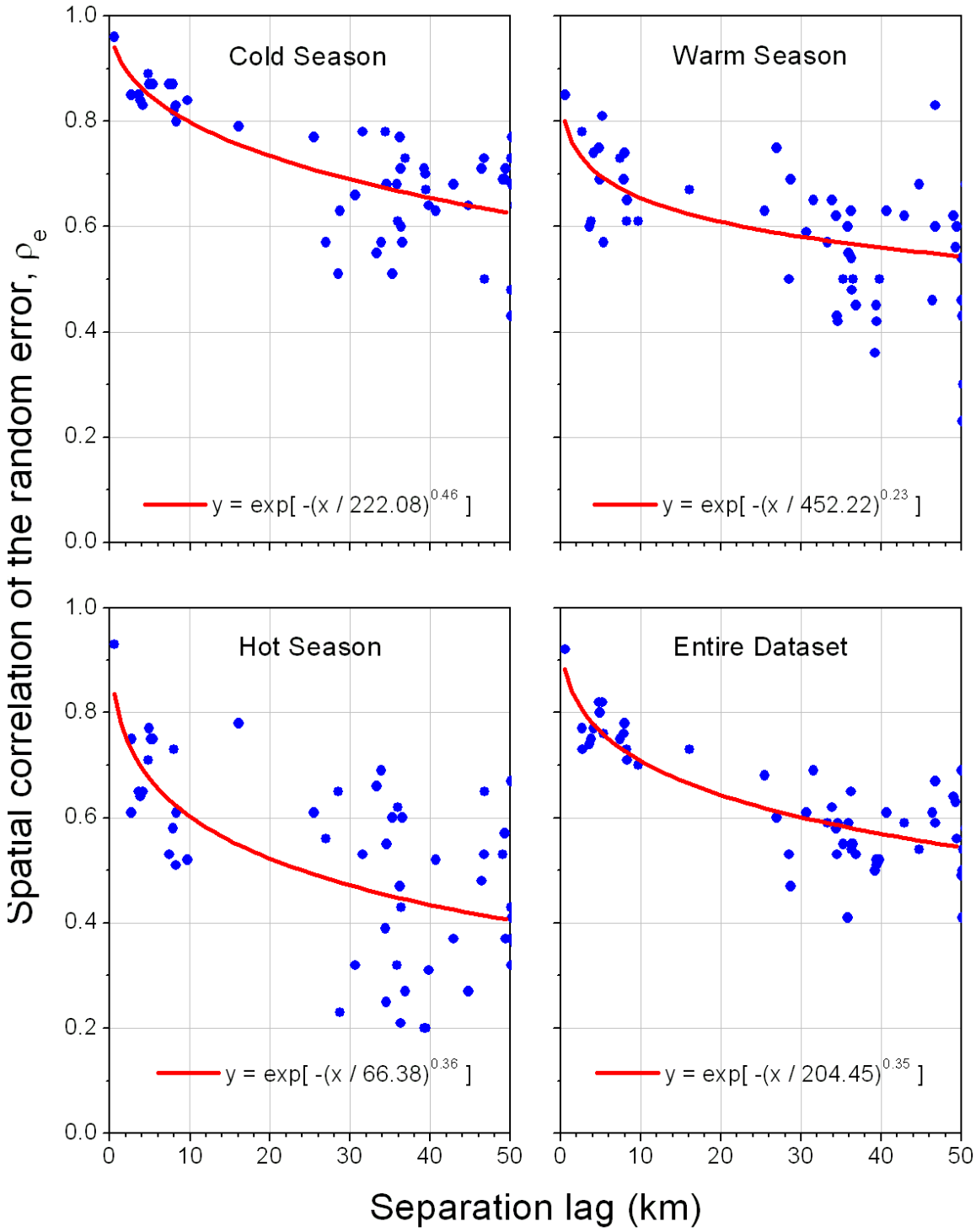

Figure C.22. Empirical intergauge spatial correlation over a limited range with a three-parameter exponential model approximation for Zone I.

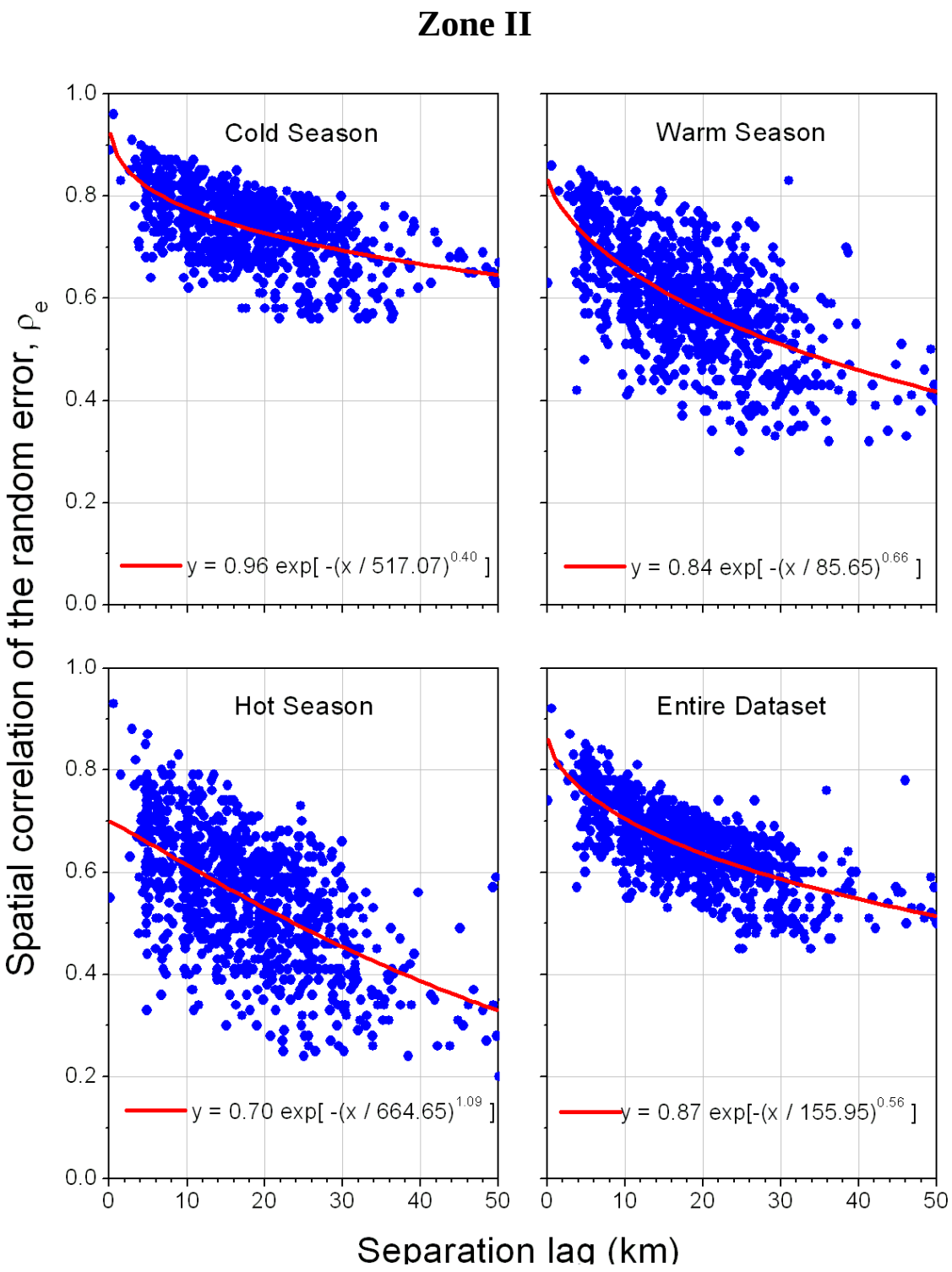

Figure C.23. Empirical intergauge spatial correlation over a limited range with a three-parameter exponential model approximation for Zone II.

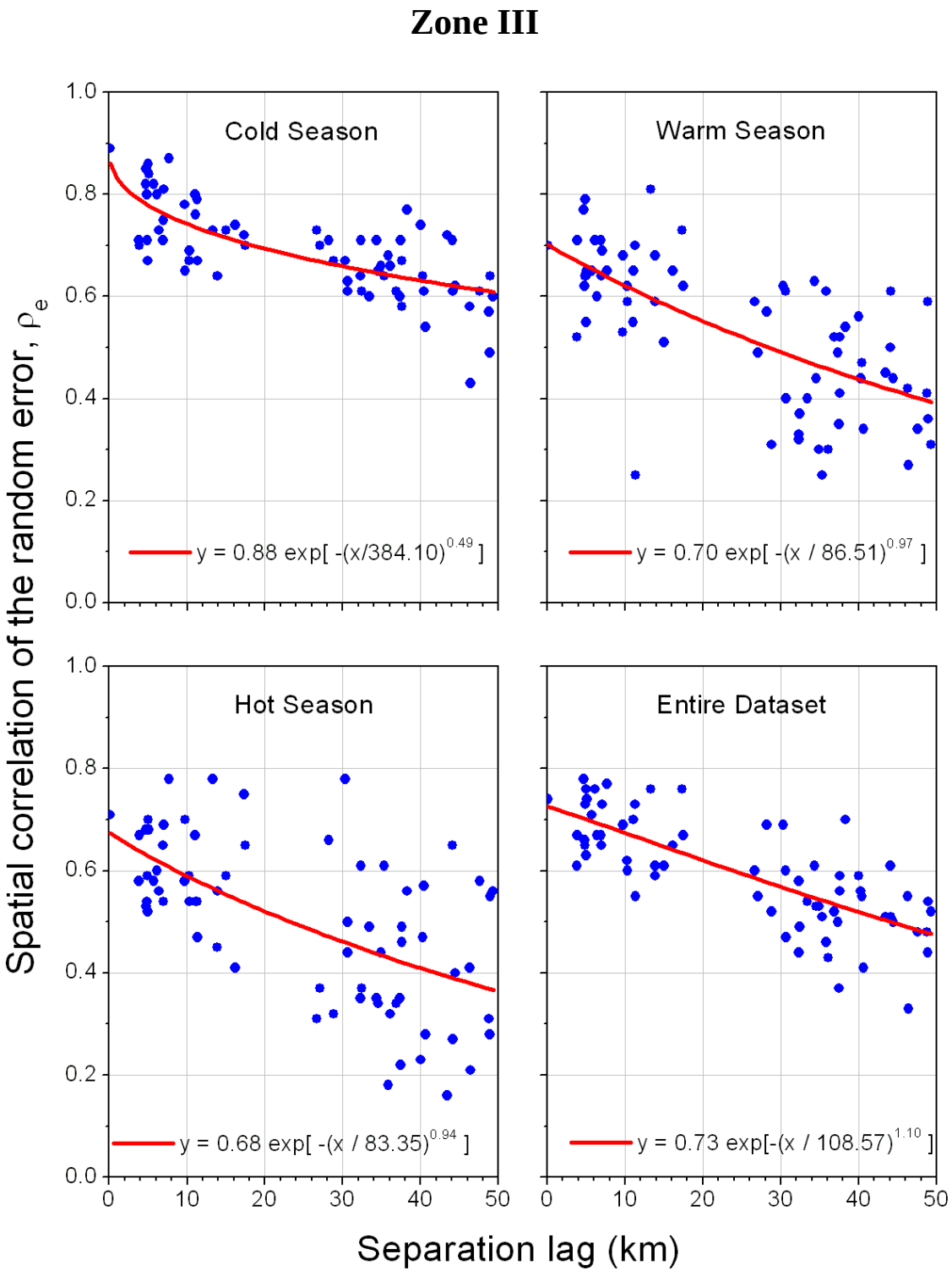

Figure C.24. Empirical intergauge spatial correlation over a limited range with a three-parameter exponential model approximation for Zone III.

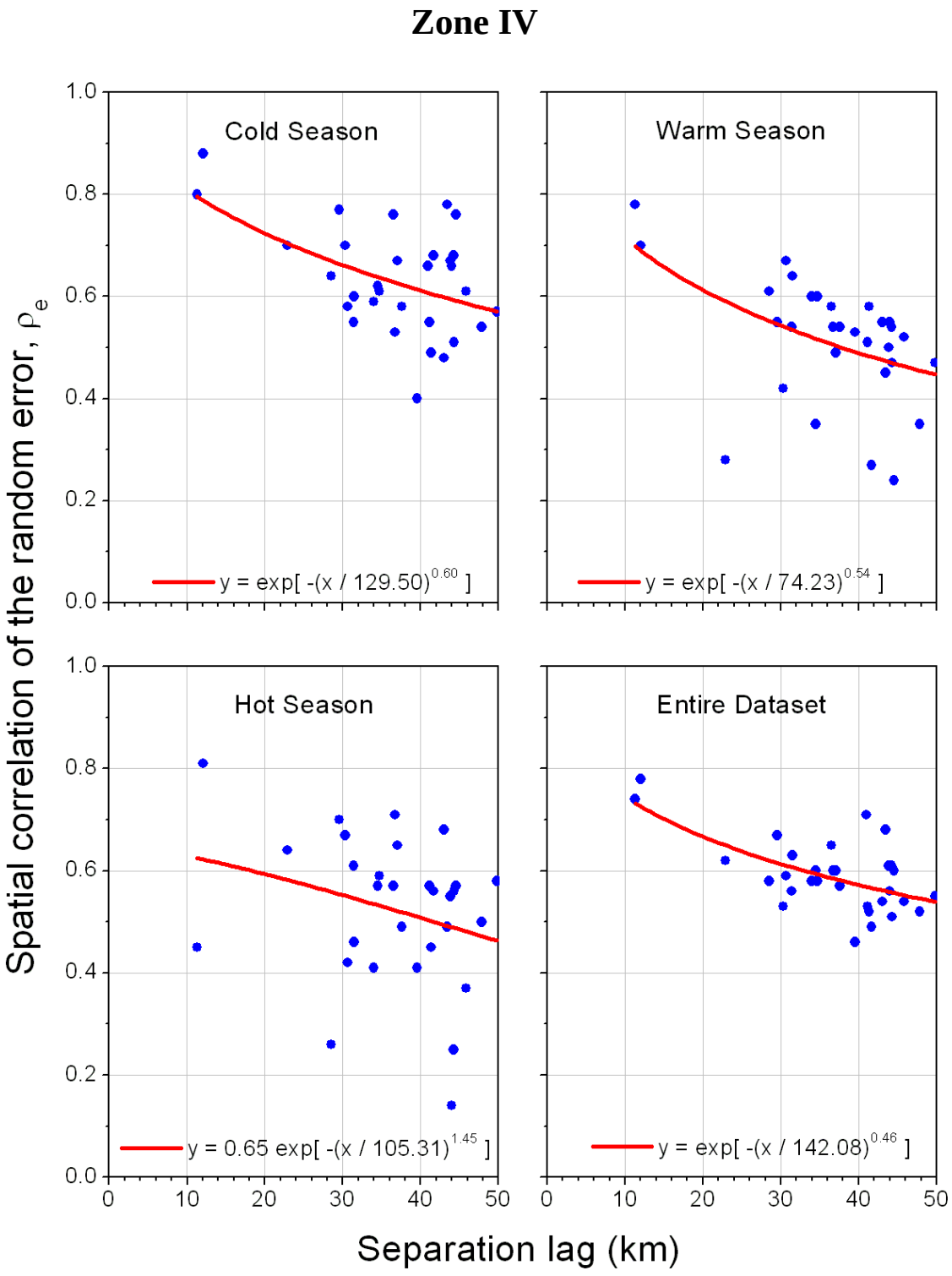

Figure C.25. Empirical intergauge spatial correlation over a limited range with a three-parameter exponential model approximation for Zone IV.

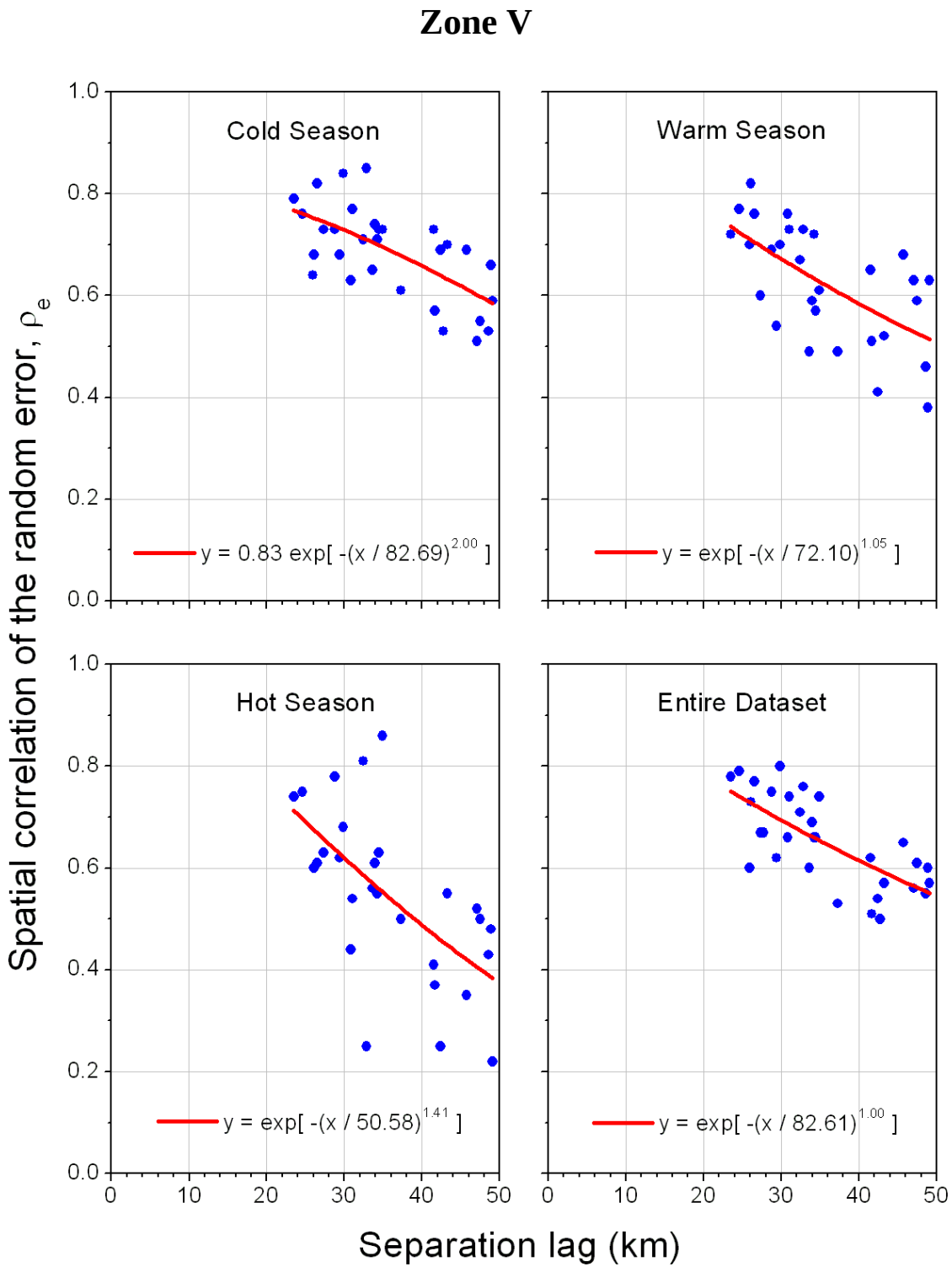

Figure C.26. Empirical intergauge spatial correlation over a limited range with a three-parameter exponential model approximation for Zone V.

Zone I

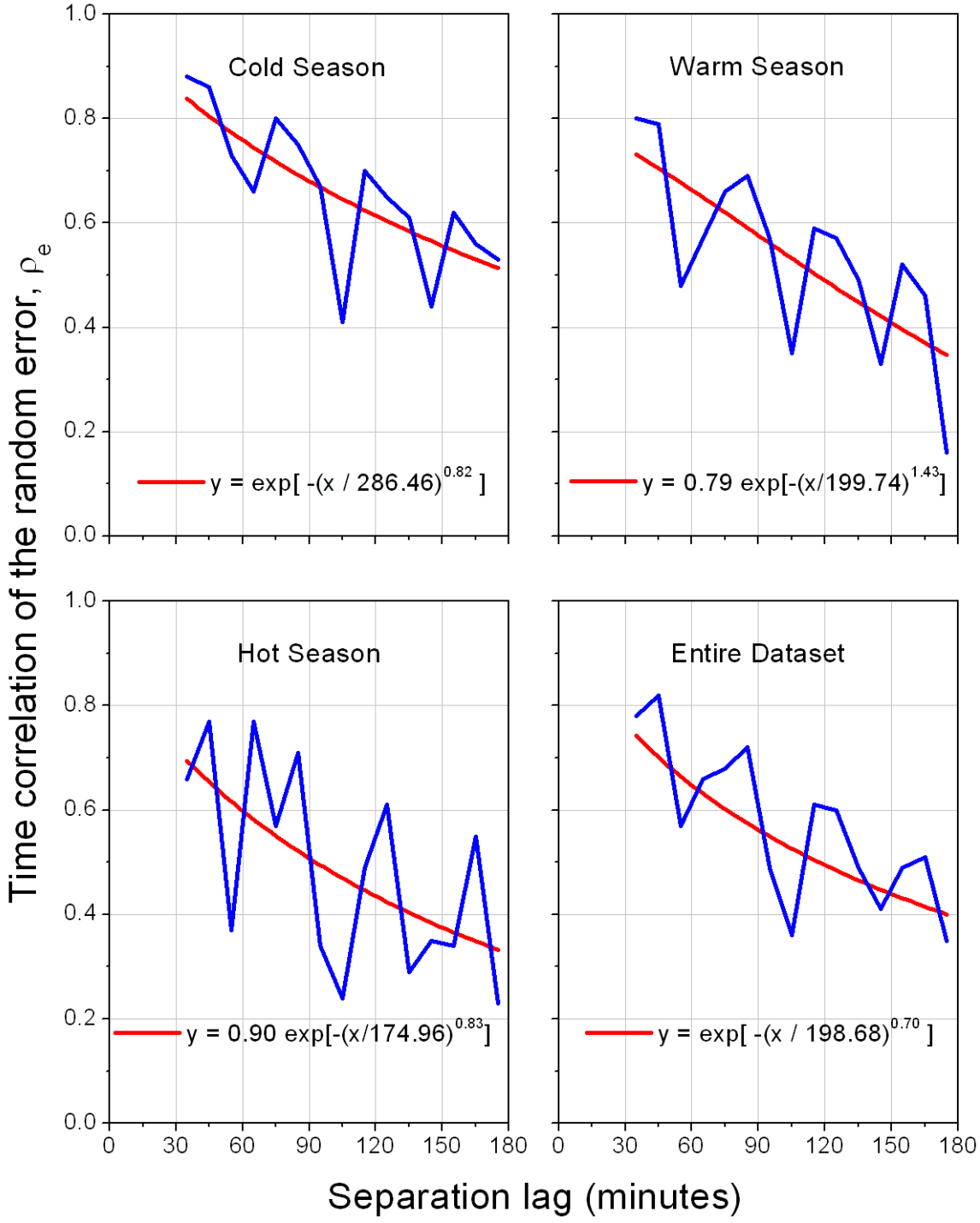

Figure C.27. Empirical and model approximated temporal correlation of the random component for Zone I.

Zone II

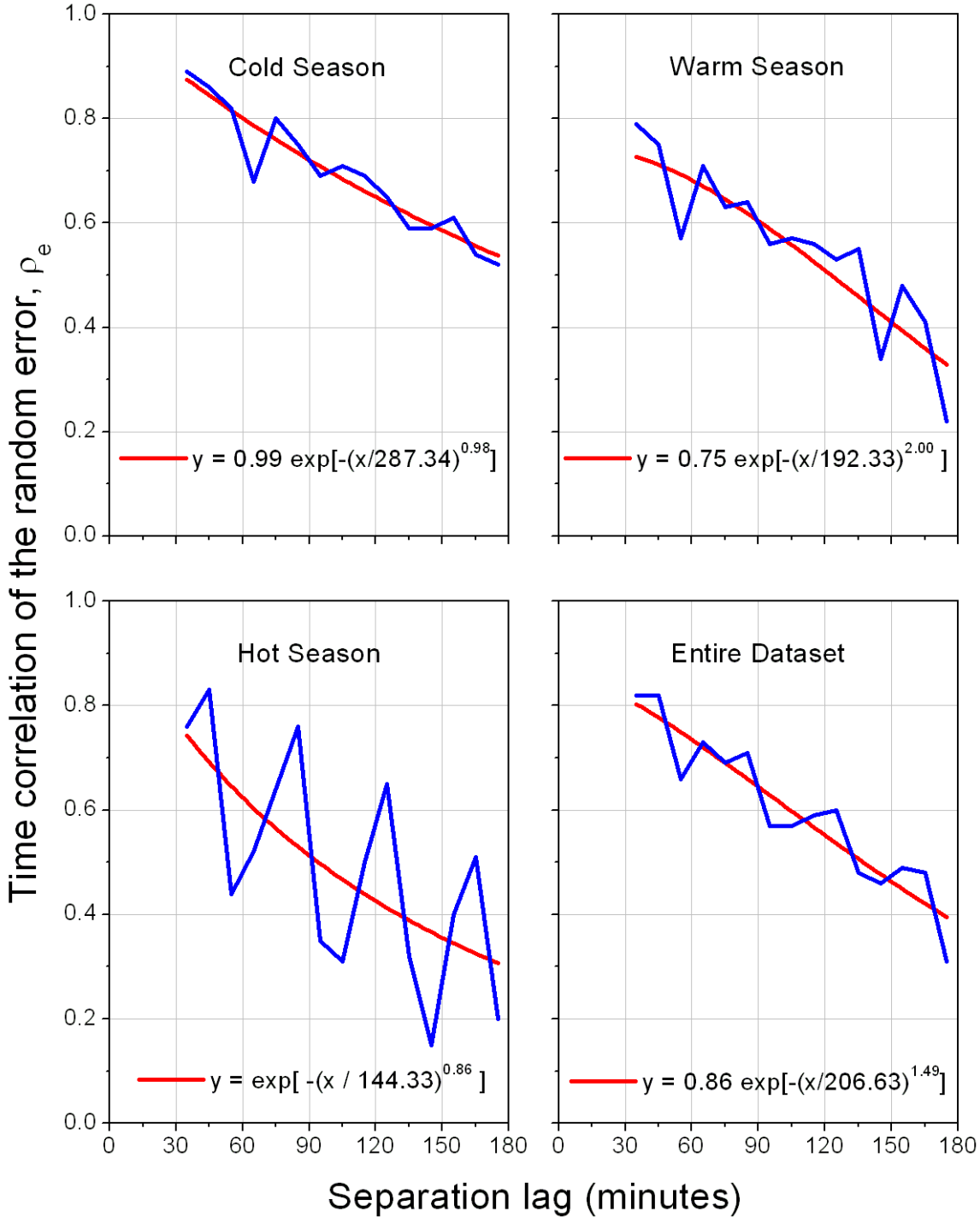

Figure C.28. Empirical and model approximated temporal correlation of the random component for Zone II.

Zone III

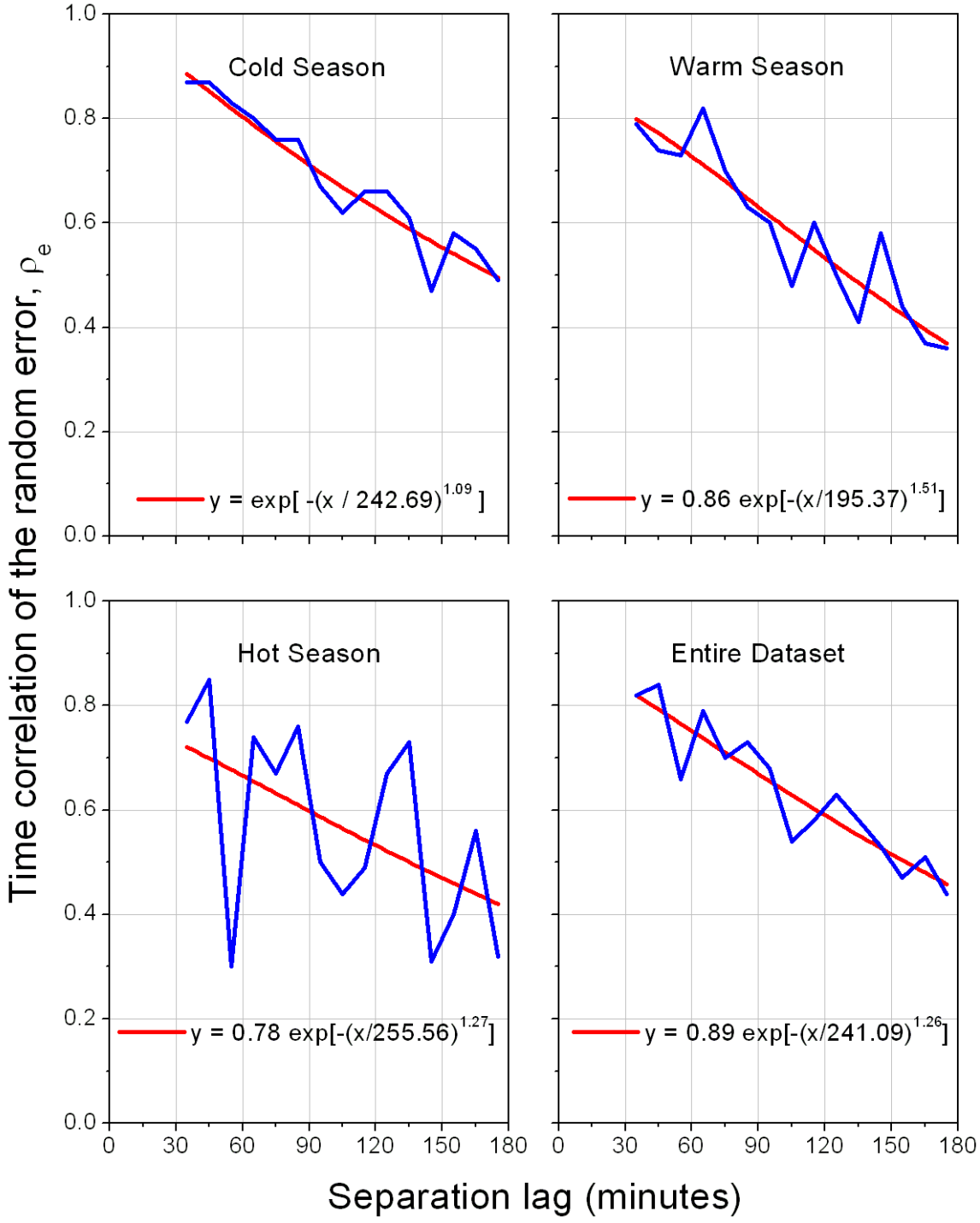

Figure C.29. Empirical and model approximated temporal correlation of the random component for Zone III.

Zone IV

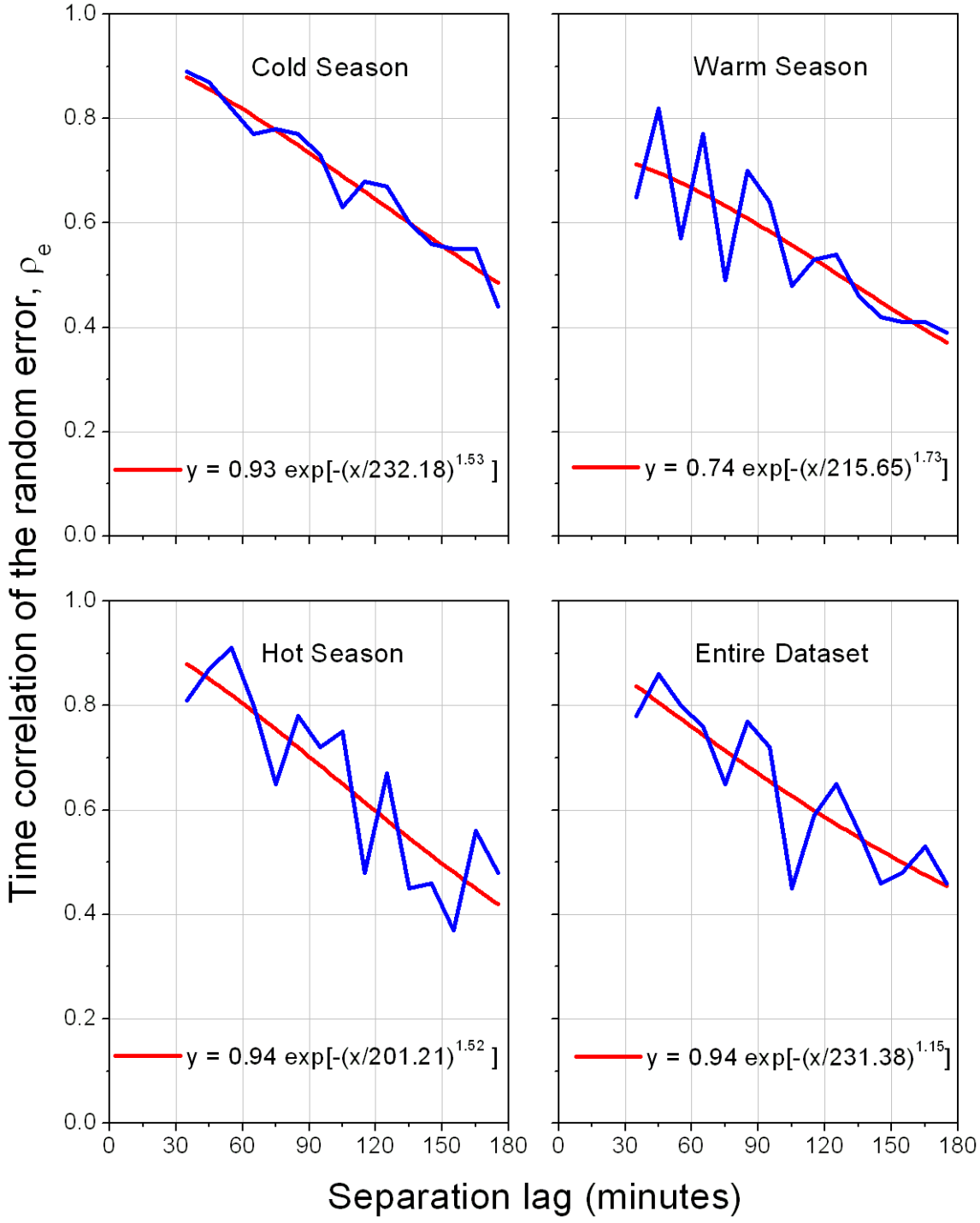

Figure C.30. Empirical and model approximated temporal correlation of the random component for Zone IV.

Zone V

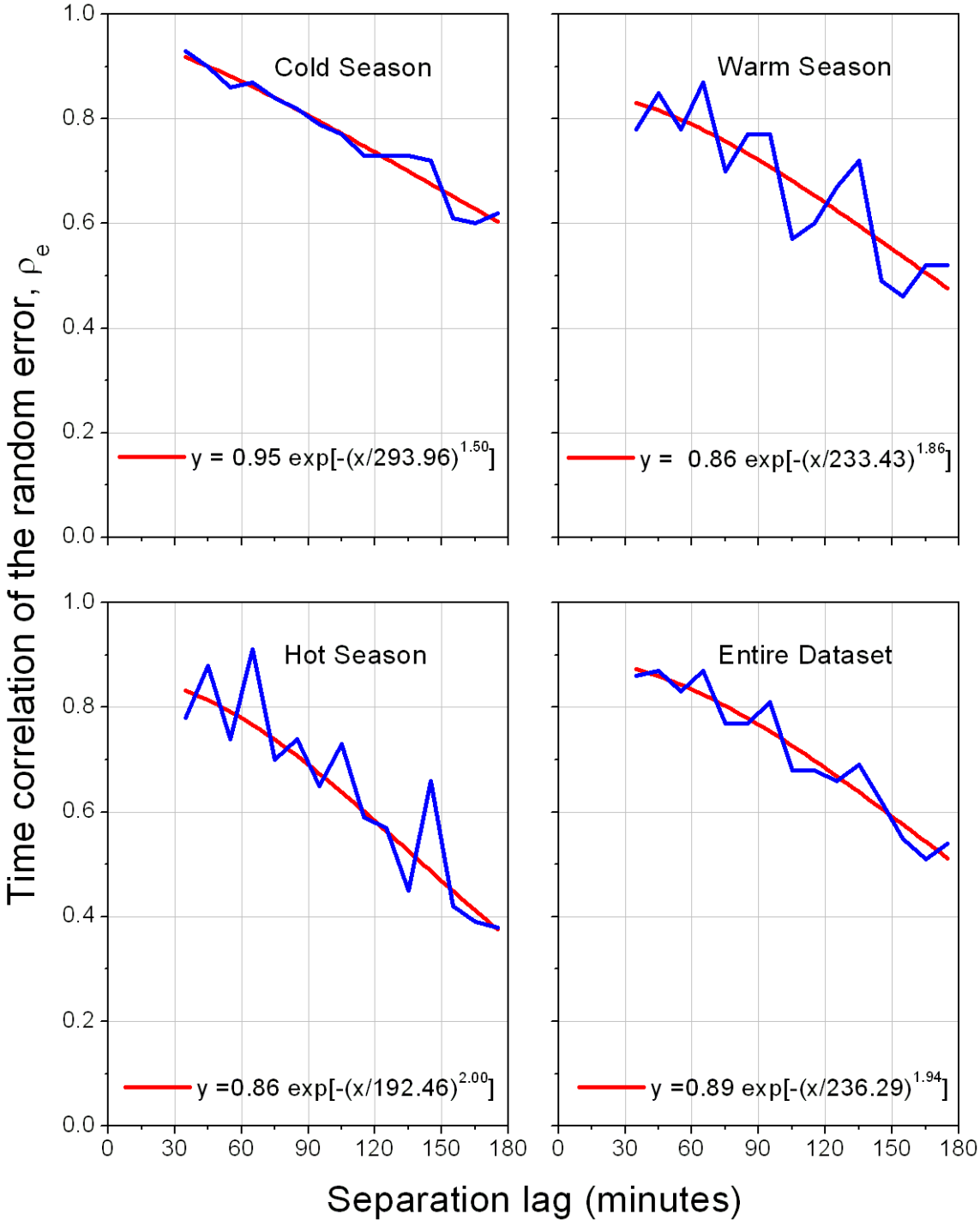

Figure C.31. Empirical and model approximated temporal correlation of the random component for Zone V.

Appendix D

Temporal Scale:
Six Hours

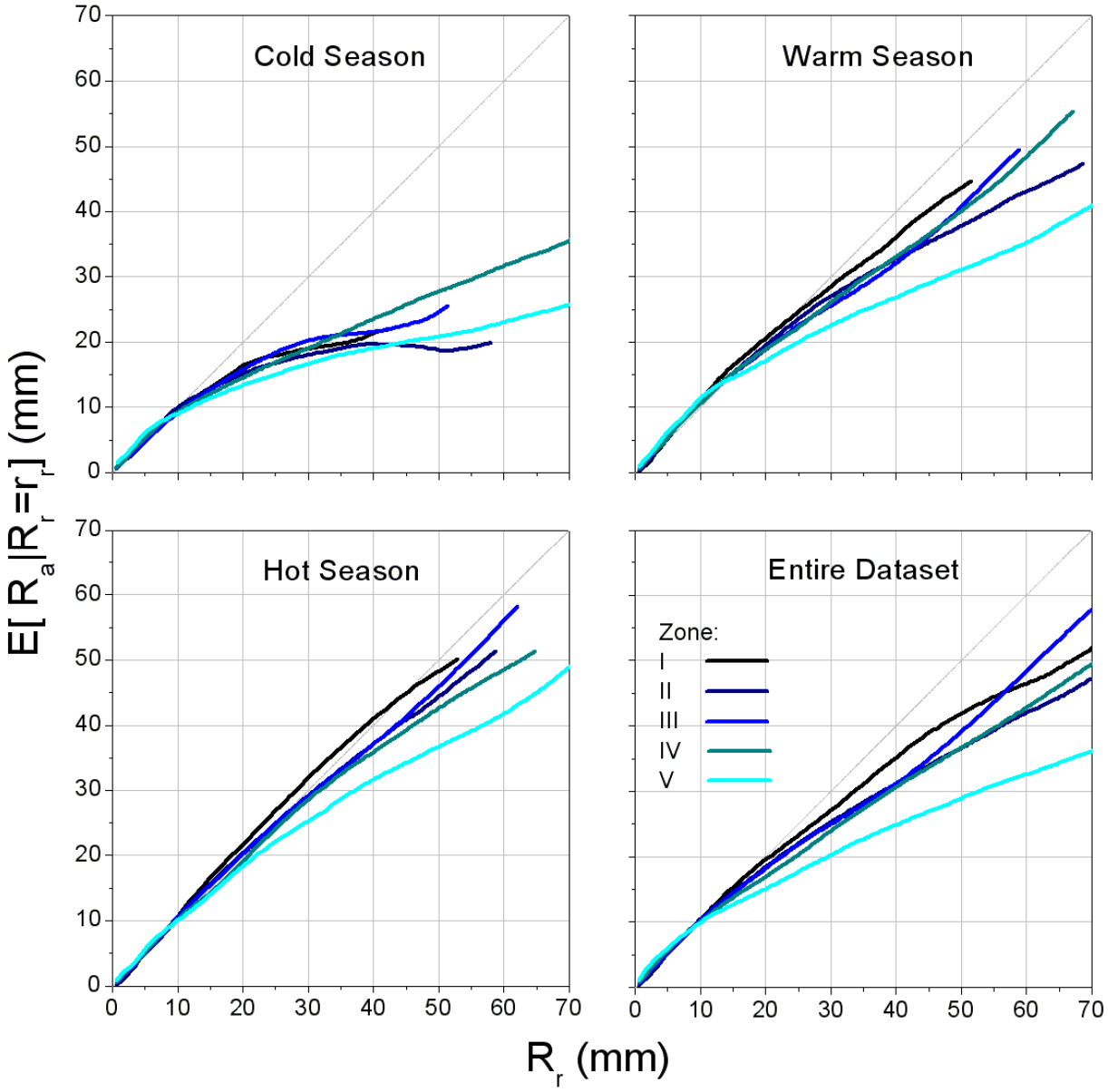

Figure D.1. Rain gauge averages, conditional on radar-rainfall values, after removing the overall bias for the three seasons and entire dataset for the 5 zones. The minimum weighted sample size is 100.

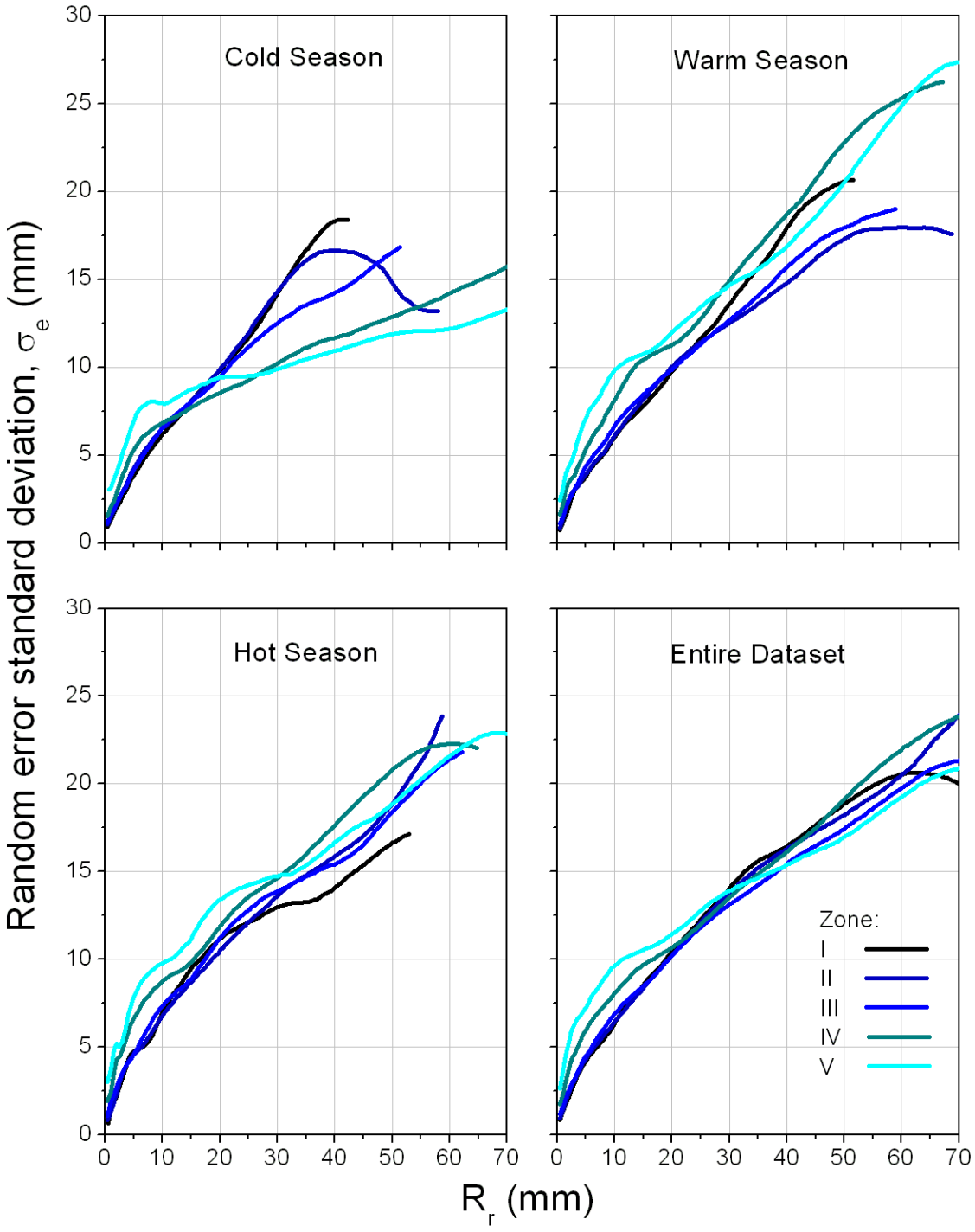

Figure D.2. Standard deviations of the random component in the additive form (mm) for the three seasons and entire dataset for the 5 zones. The minimum weighted sample size is 100.

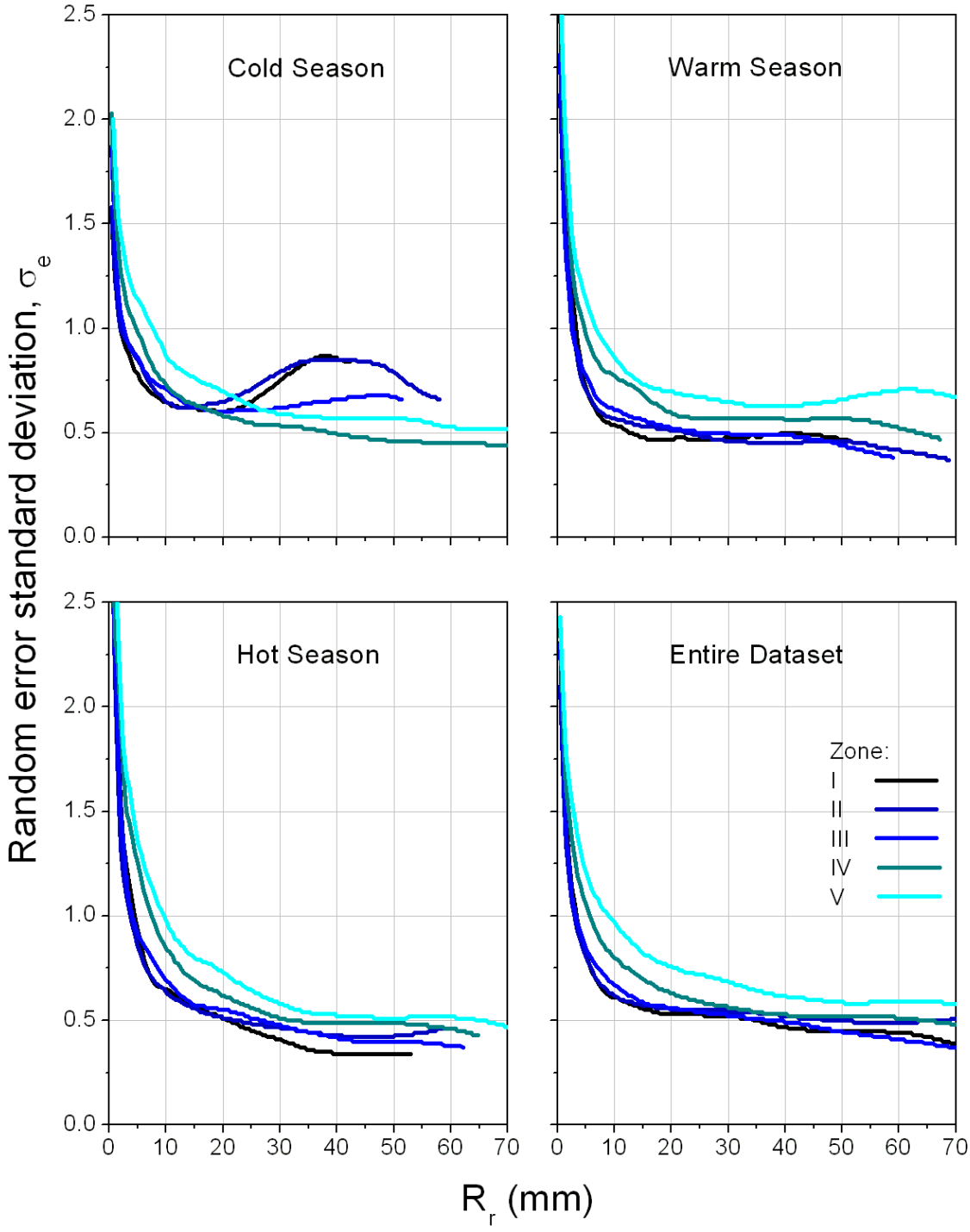

Figure D.3. Standard deviations of the random component in the multiplicative form for the three seasons and entire dataset for the 5 zones. The minimum weighted sample size is 100.

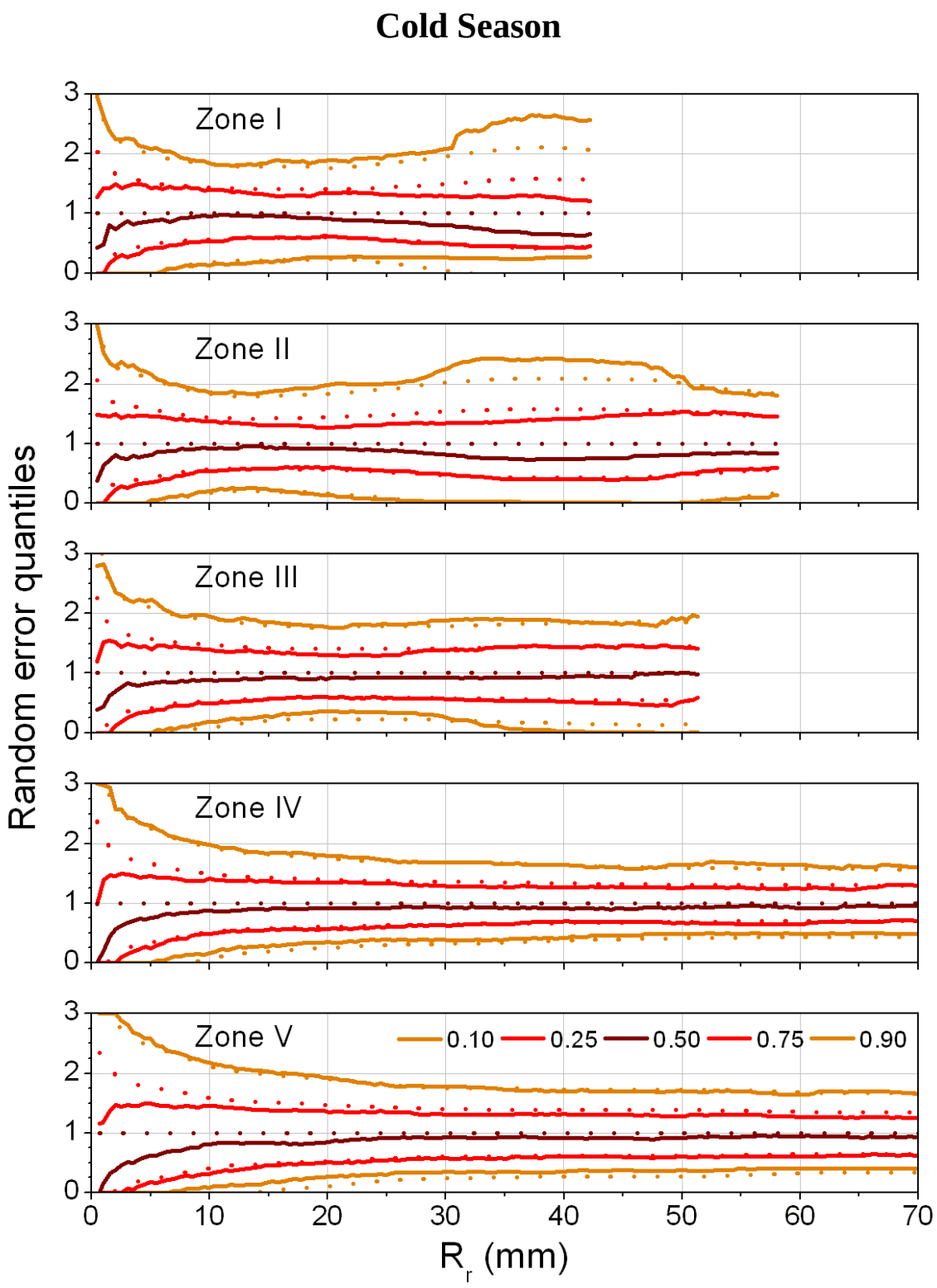

Figure D.4. Comparison of the empirical and Gaussian quantiles (p=0.1, 0.25, 0.5, 0.75, 0.9) for the five zones (cold season). The mean of the theoretical distribution is equal to 1 and the standard deviation is the standard deviation of the random component in the multiplicative form. The minimum weighted sample size is 100.

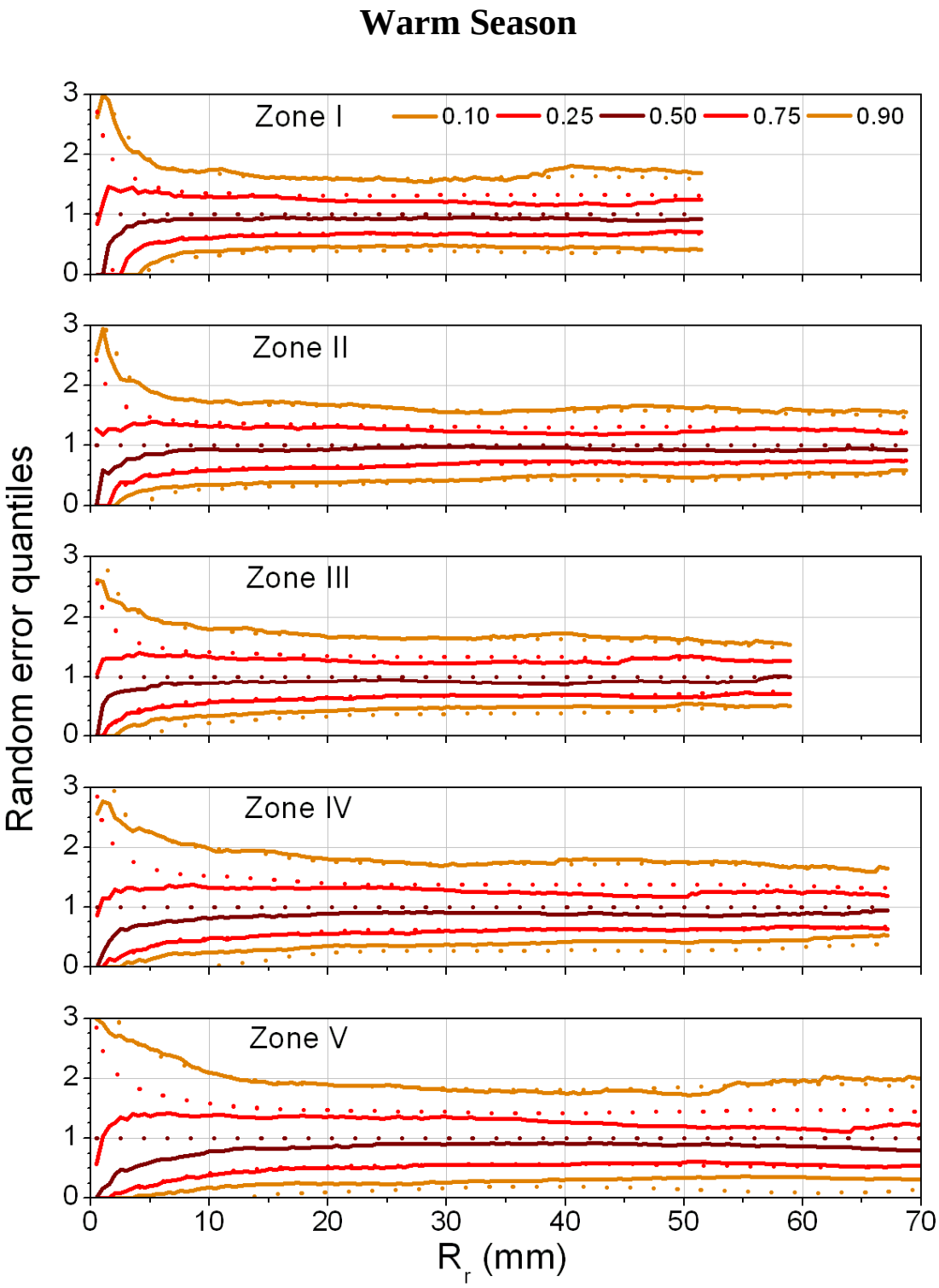

Figure D.5. Comparison of the empirical and Gaussian quantiles (p=0.1, 0.25, 0.5, 0.75, 0.9) for the five zones (warm season). The mean of the theoretical distribution is equal to 1 and the standard deviation is the standard deviation of the random component in the multiplicative form. The minimum weighted sample size is 100.

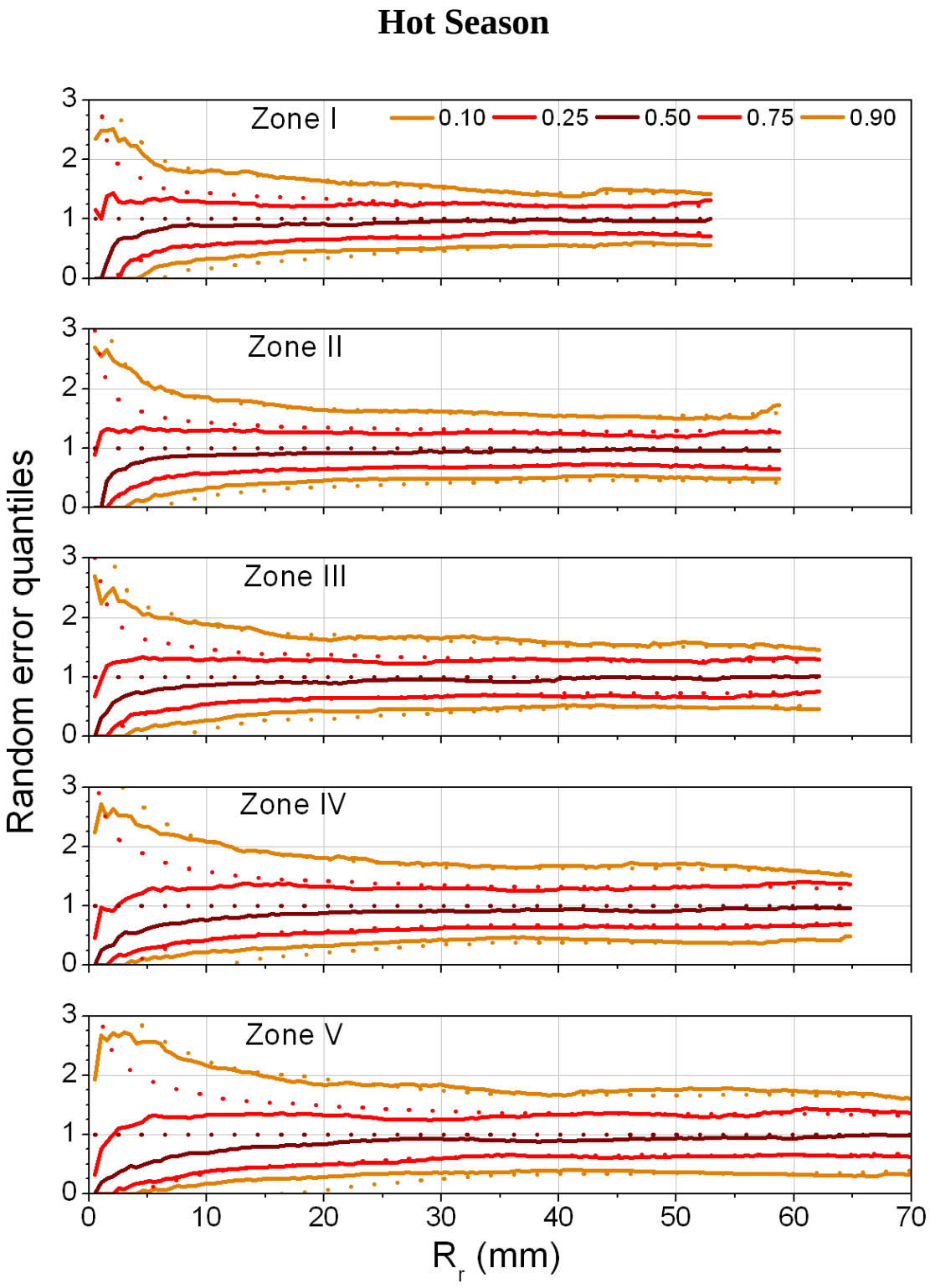

Figure D.6. Comparison of the empirical and Gaussian quantiles (p=0.1, 0.25, 0.5, 0.75, 0.9) for the five zones (hot season). The mean of the theoretical distribution is equal to 1 and the standard deviation is the standard deviation of the random component in the multiplicative form. The minimum weighted sample size is 100.

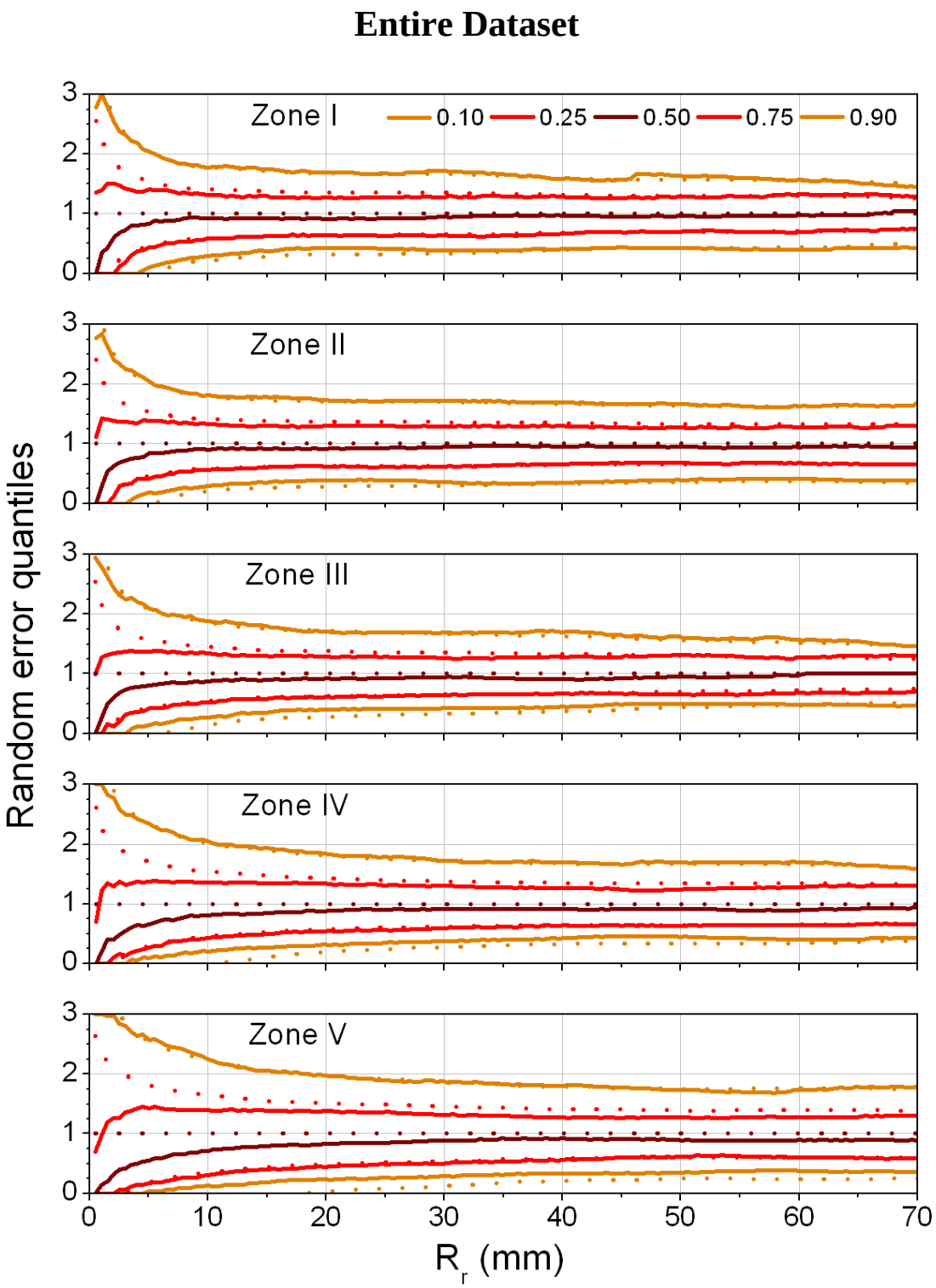

Figure D.7. Comparison of the empirical and Gaussian quantiles (p=0.1, 0.25, 0.5, 0.75, 0.9) for the five zones (all seasons). The mean of the theoretical distribution is equal to 1 and the standard deviation is the standard deviation of the random component in the multiplicative form. The minimum weighted sample size is 100.

Zone I

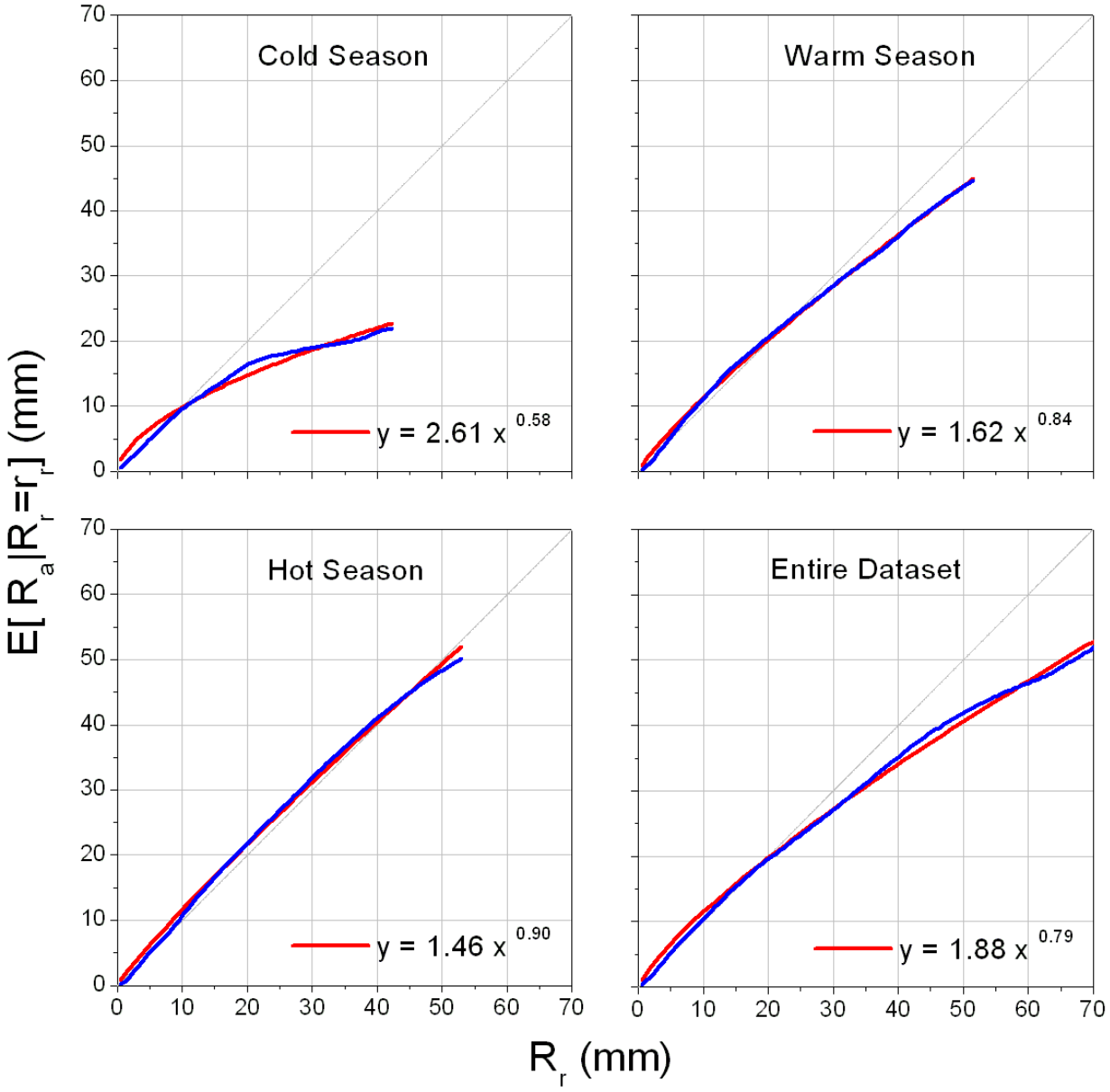

Figure D.8. Power law model approximation of the rain gauge conditional averages for the three seasons and the entire dataset for Zone I.

Zone II

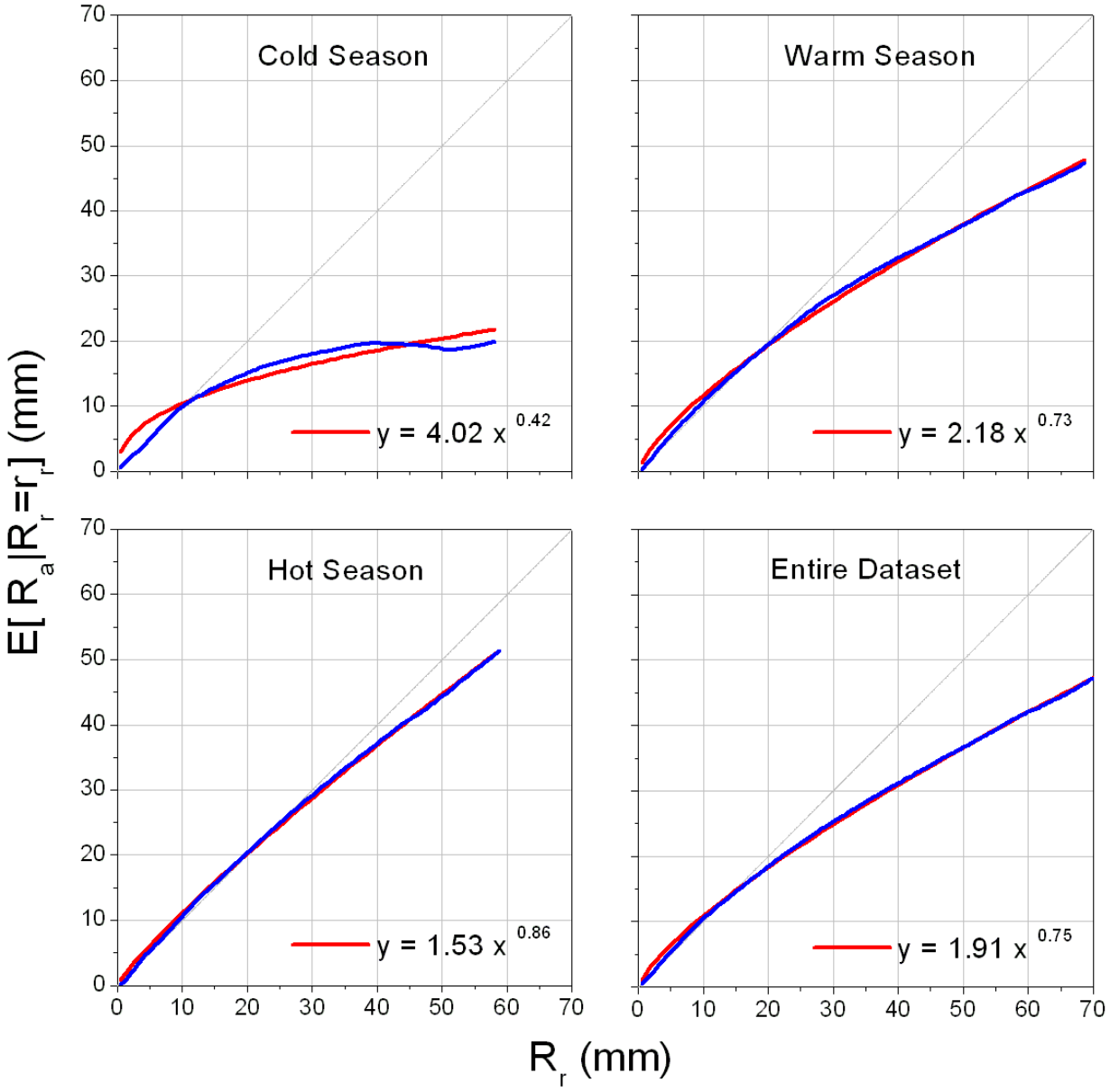

Figure D.9. Power law model approximation of the rain gauge conditional averages for the three seasons and the entire dataset for Zone II.

Zone III

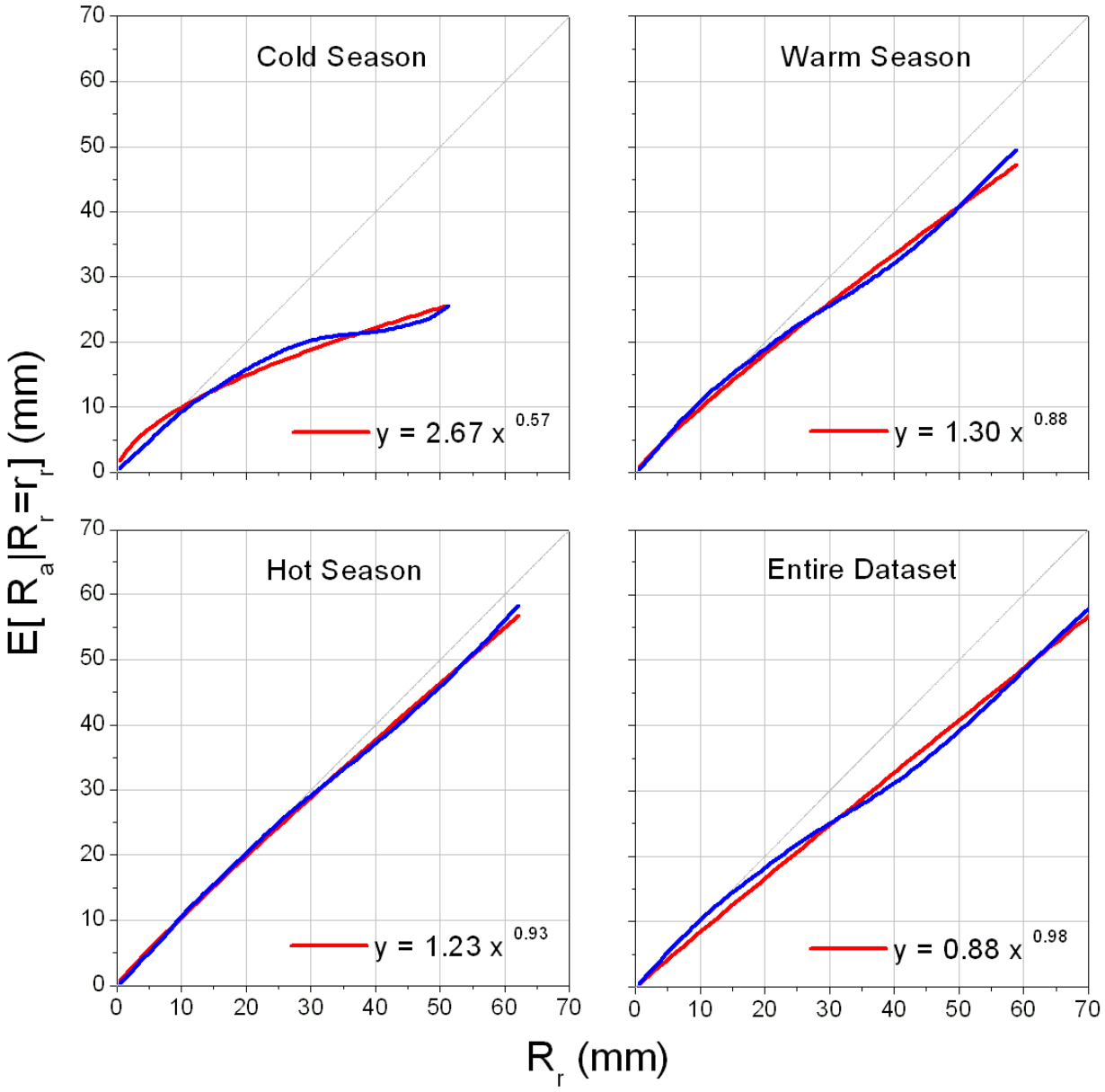

Figure D.10. Power law model approximation of the rain gauge conditional averages for the three seasons and the entire dataset for Zone III.

Zone IV

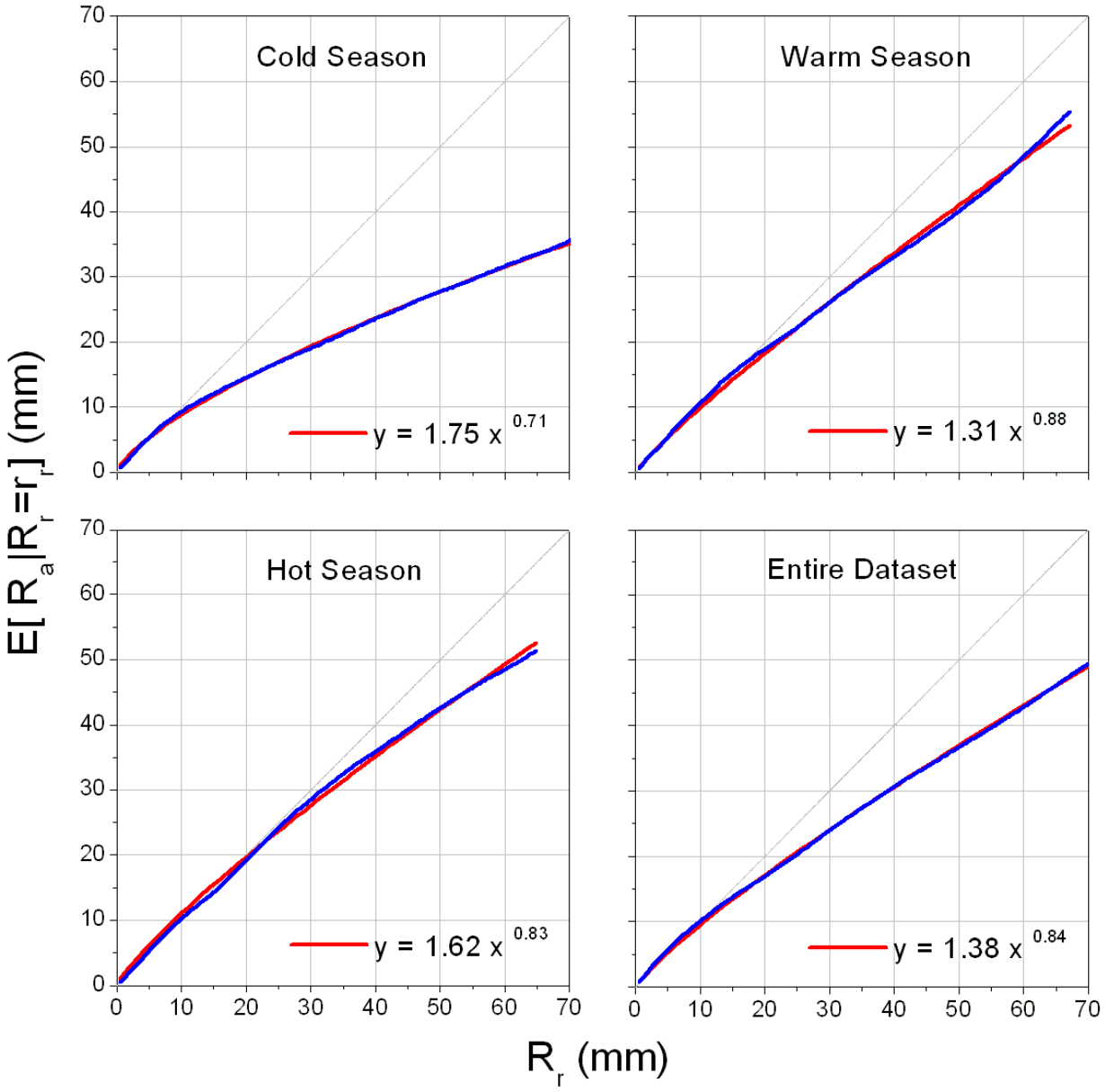

Figure D.11. Power law model approximation of the rain gauge conditional averages for the three seasons and the entire dataset for Zone IV.

Zone V

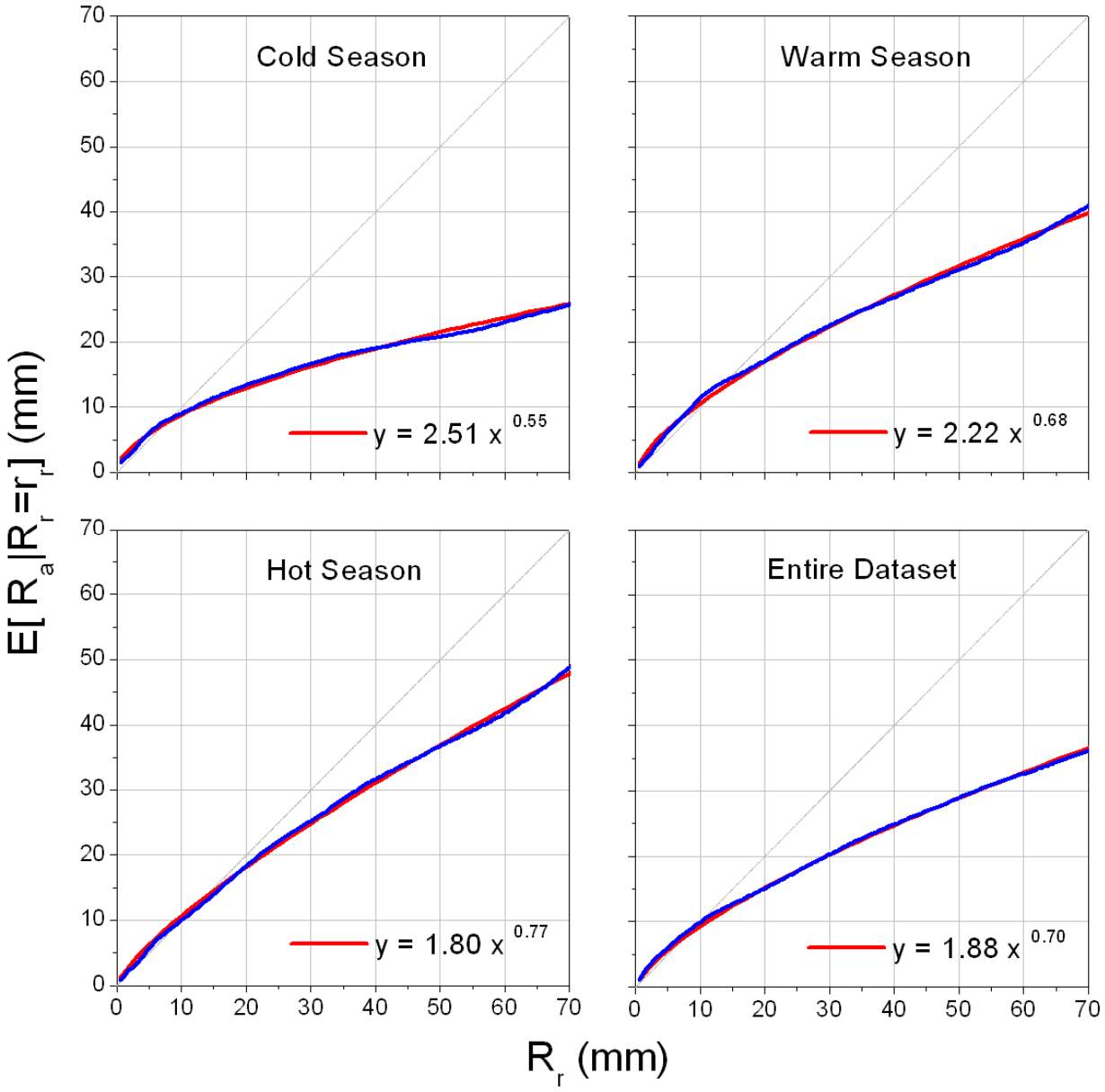

Figure D.12. Power law model approximation of the rain gauge conditional averages for the three seasons and the entire dataset for Zone V.

Zone I

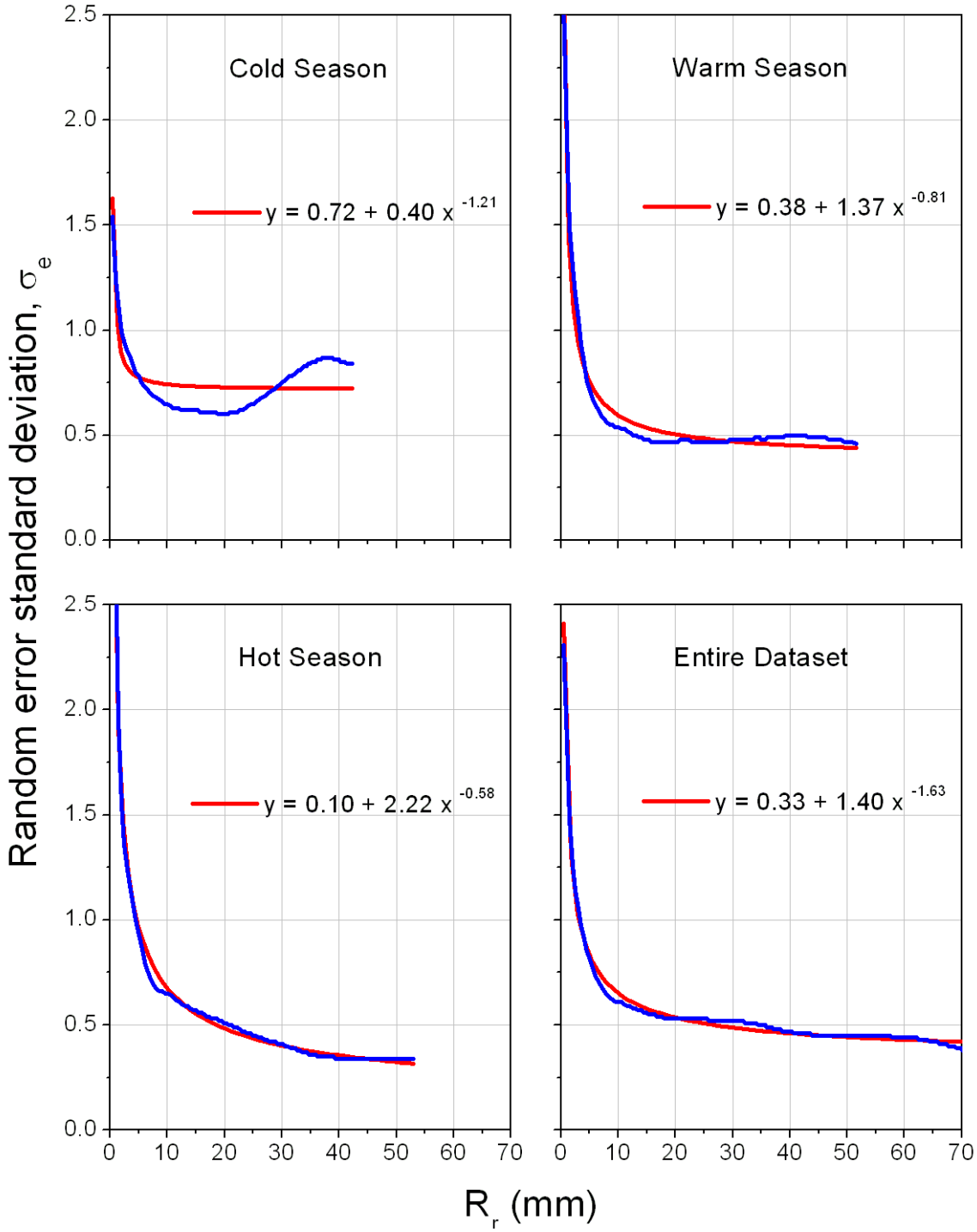

Figure D.13. Model approximation of the conditional multiplicative standard deviation for the three seasons and the entire dataset for Zone I.

Zone II

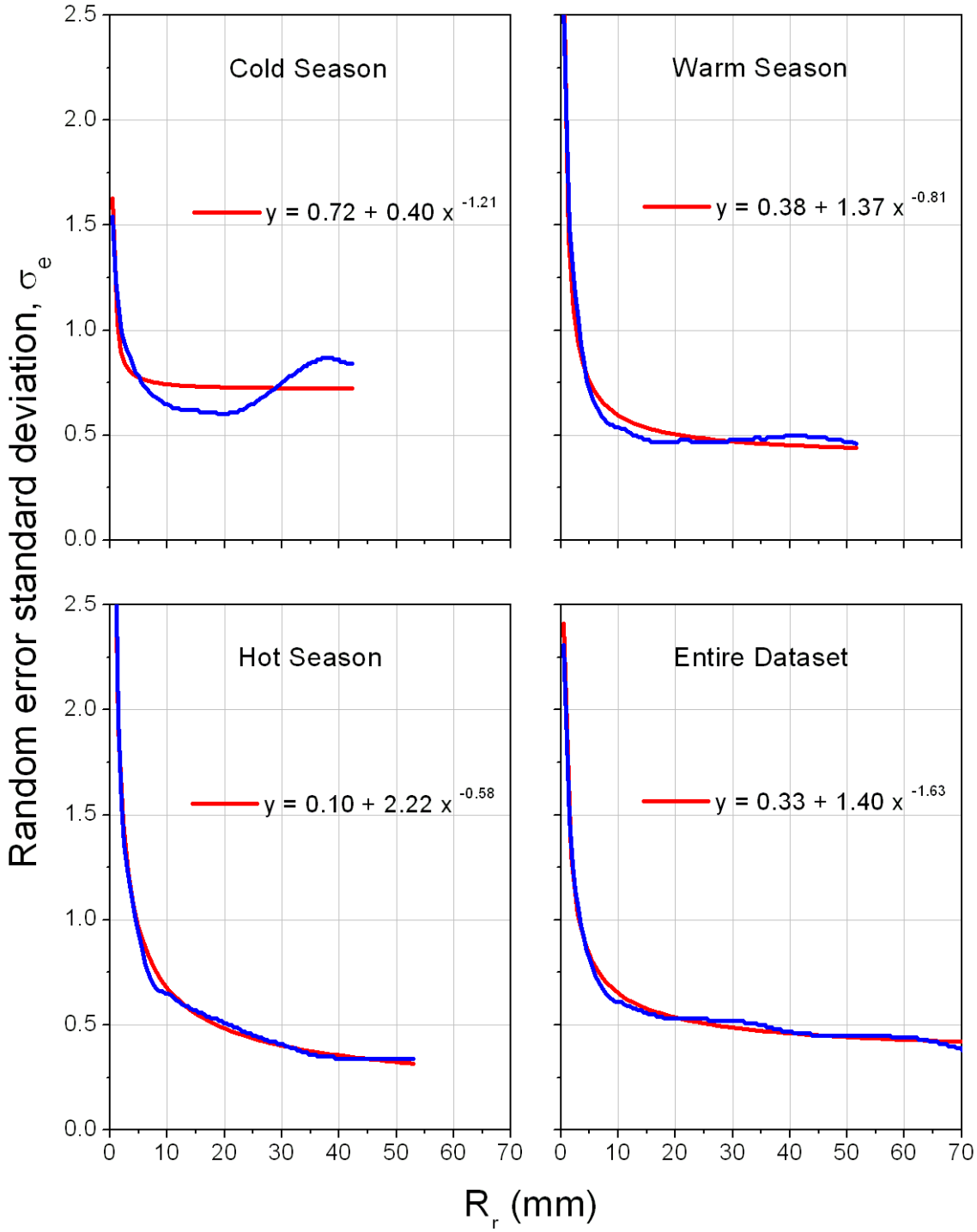

Figure D.14. Model approximation of the conditional multiplicative standard deviation for the three seasons and the entire dataset for Zone II.

Zone III

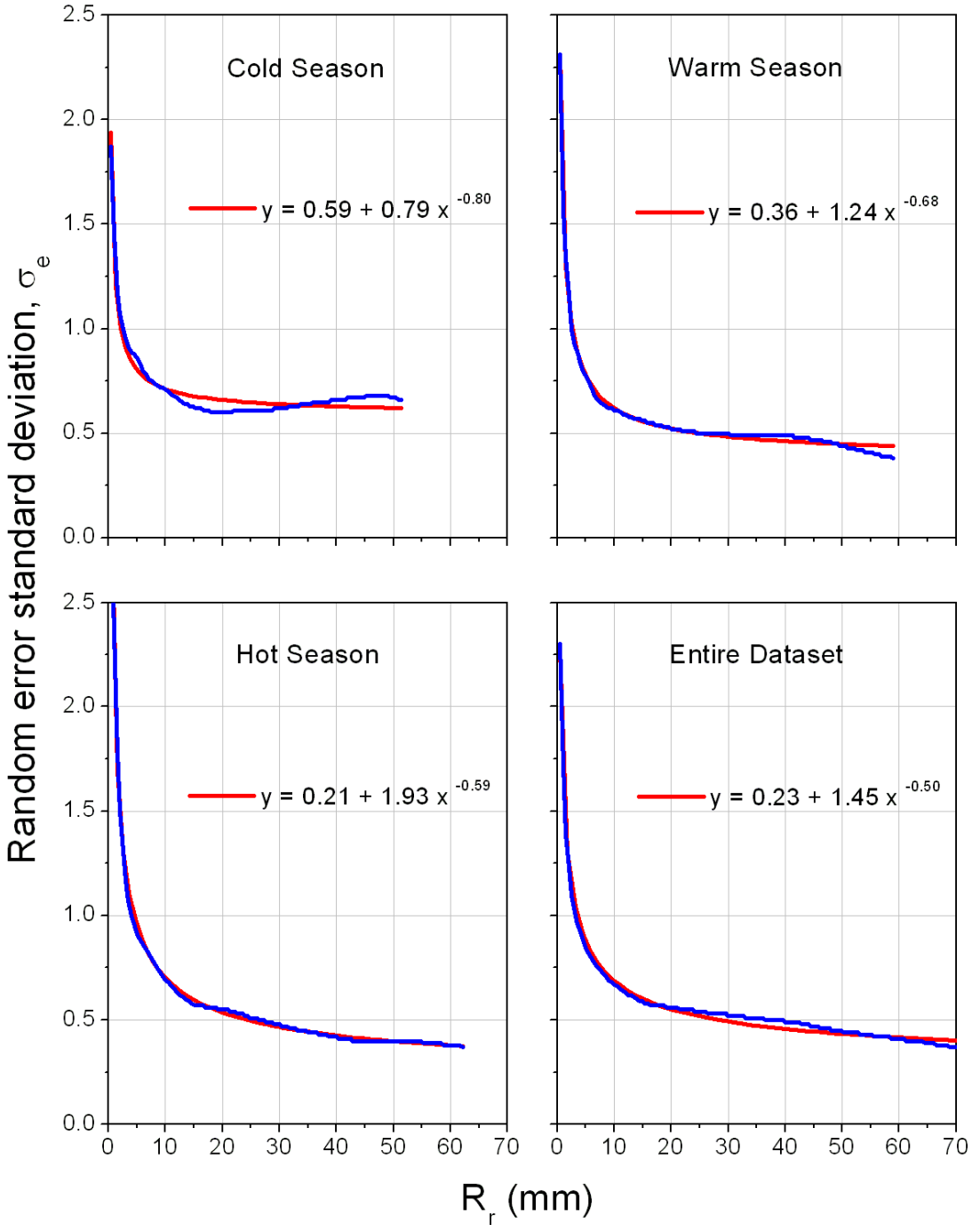

Figure D.15. Model approximation of the conditional multiplicative standard deviation for the three seasons and the entire dataset for Zone III.

Zone IV

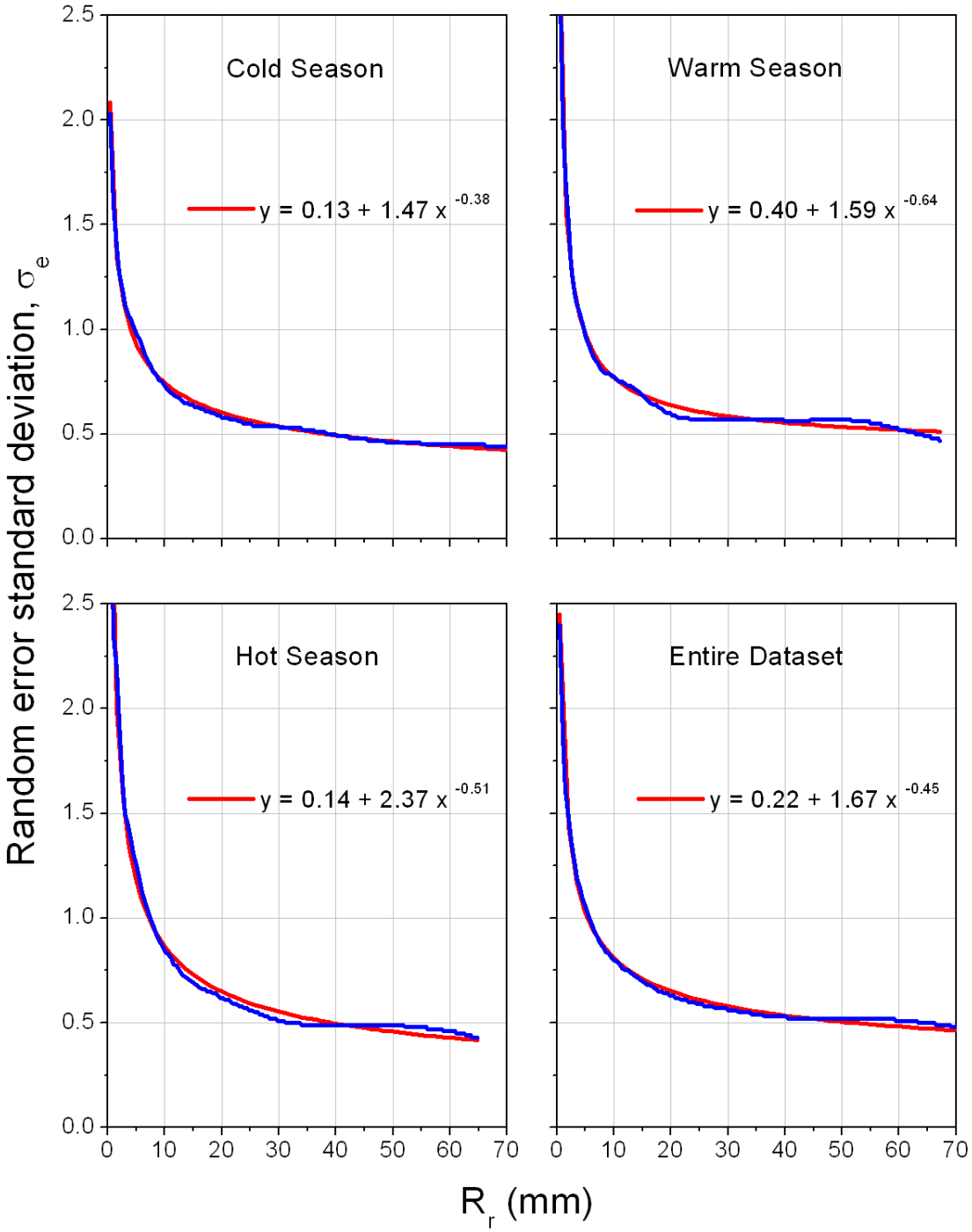

Figure D.16. Model approximation of the conditional multiplicative standard deviation for the three seasons and the entire dataset for Zone IV.

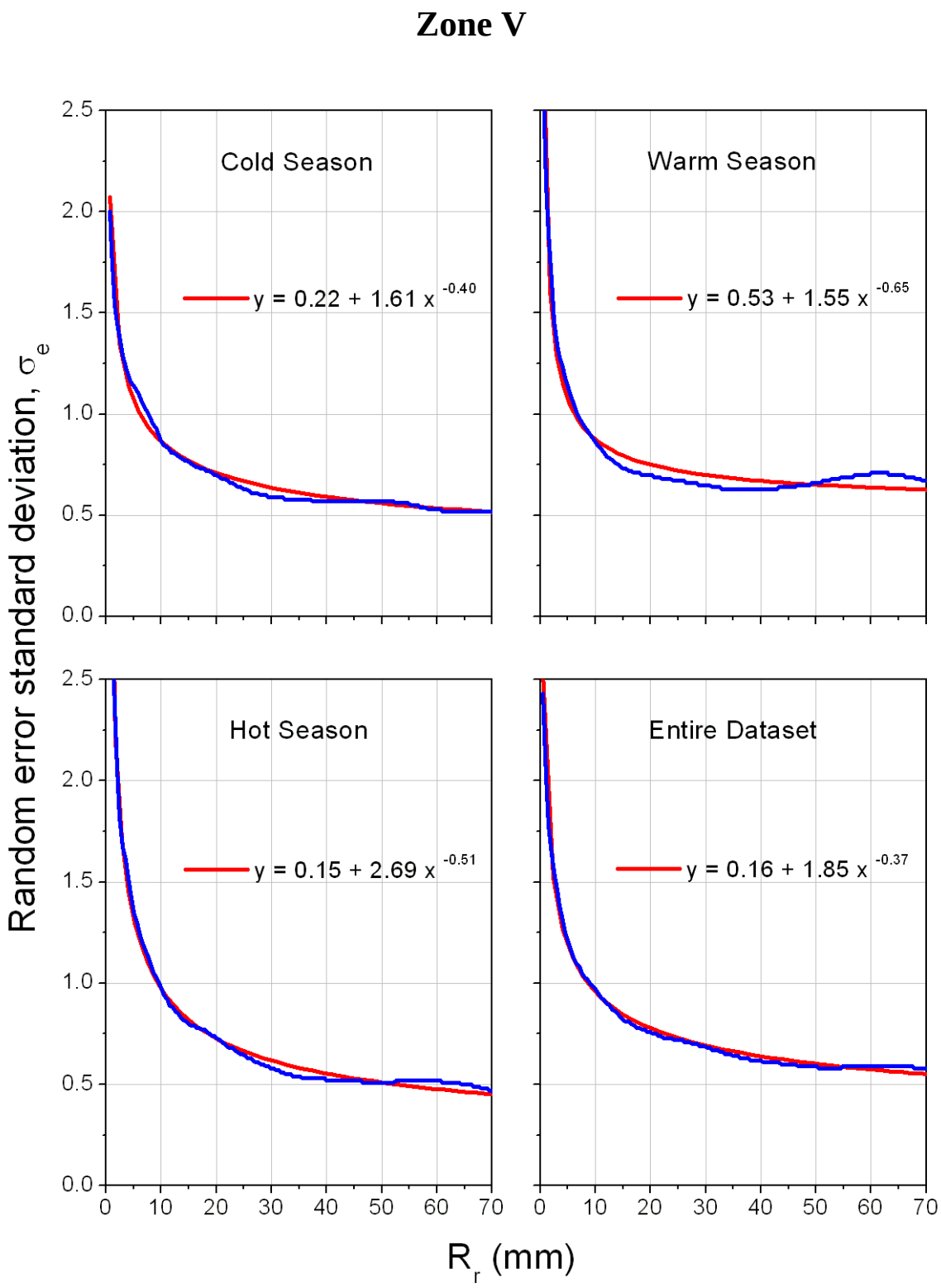

Figure D.17. Model approximation of the conditional multiplicative standard deviation for the three seasons and the entire dataset for Zone V.

Spatial and Temporal Correlation Structure

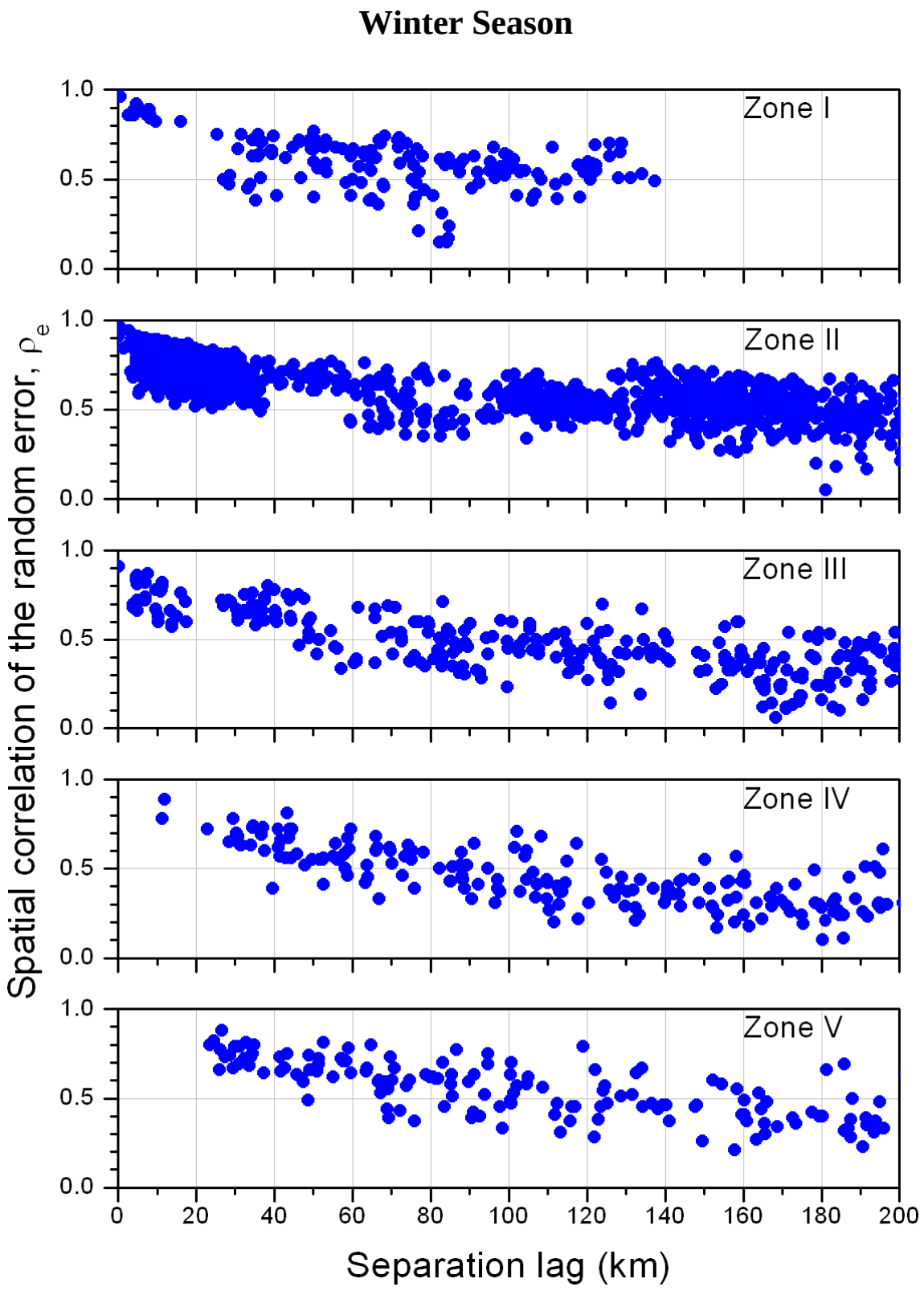

Figure D.18. Intergauge spatial Pearson correlation of the random component for the winter season.

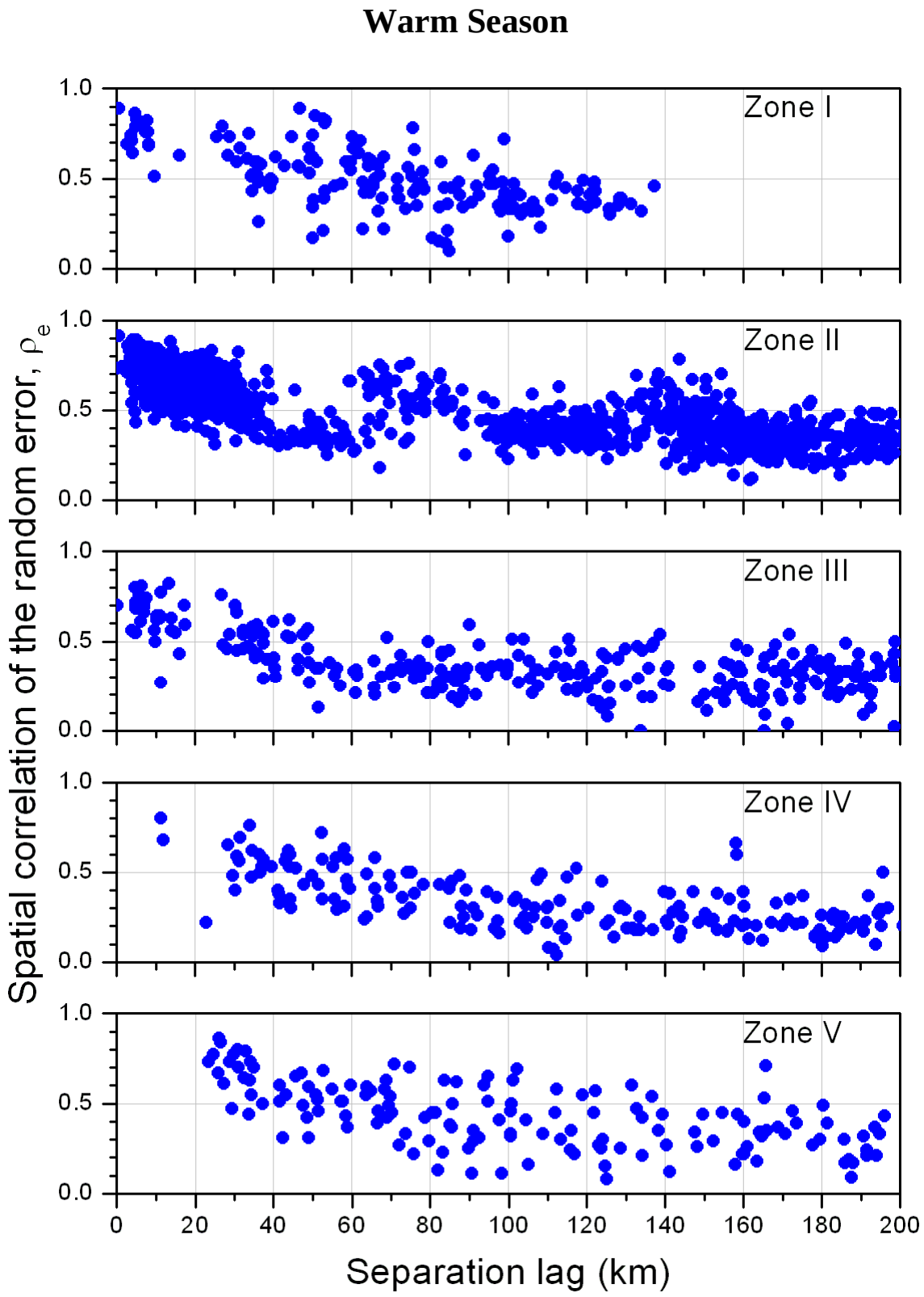

Figure D.19. Intergauge spatial Pearson correlation of the random component for the warm season.

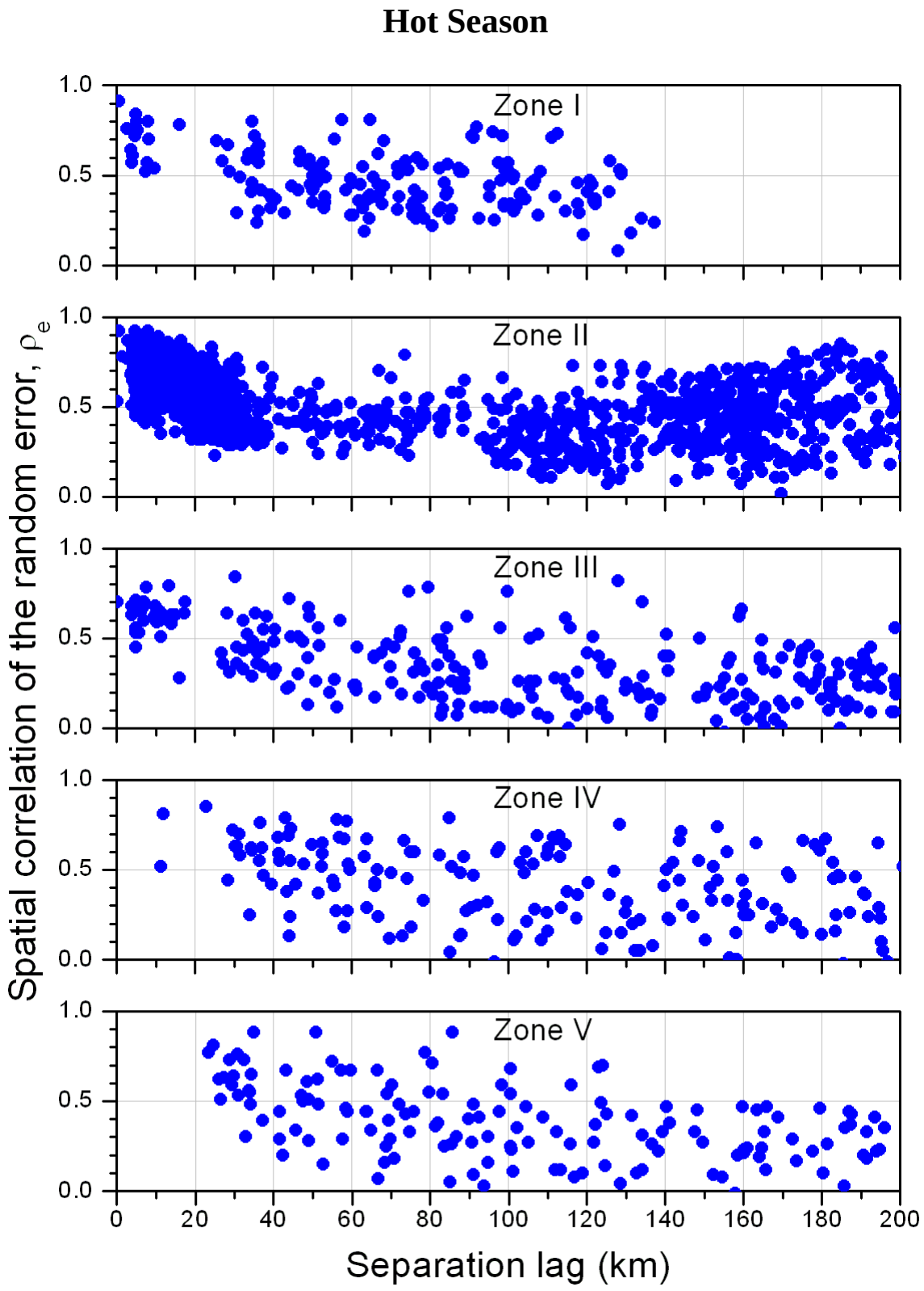

Figure D.20. Intergauge spatial Pearson correlation of the random component for the hot season.

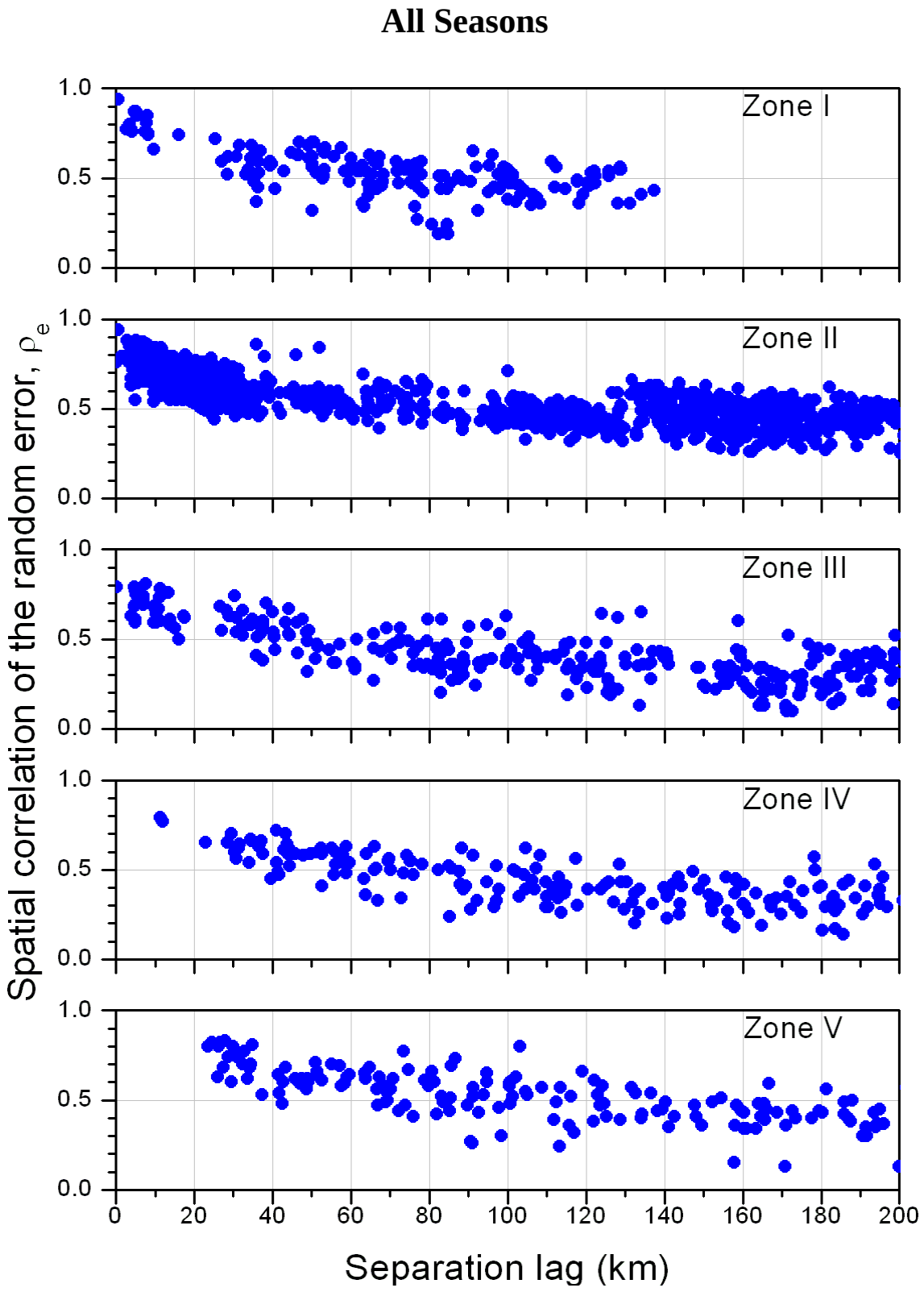

Figure D.21. Intergauge spatial Pearson correlation of the random component for all seasons.

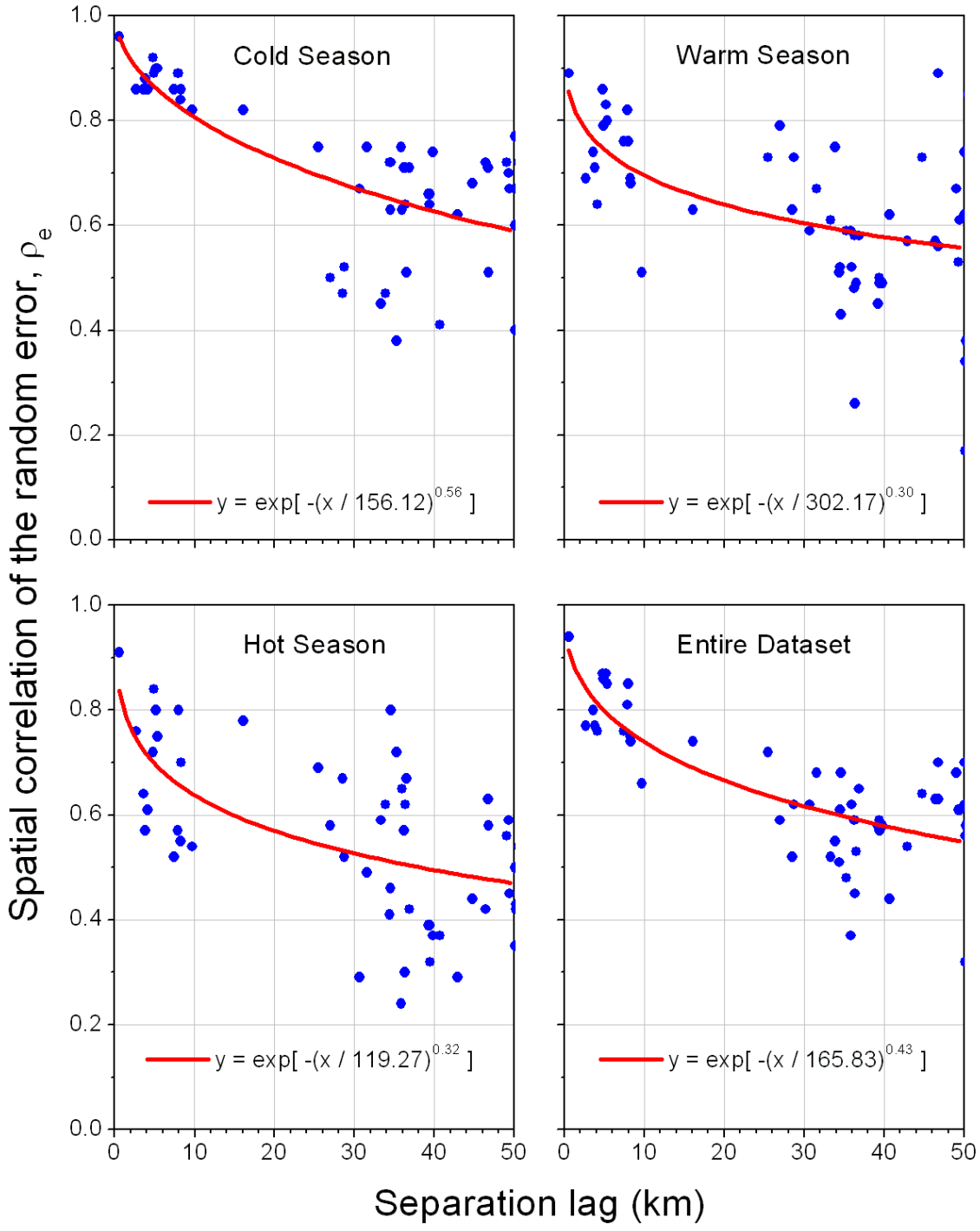

Figure D.22. Empirical intergauge spatial correlation over a limited range with a three-parameter exponential model approximation for Zone I.

Zone II

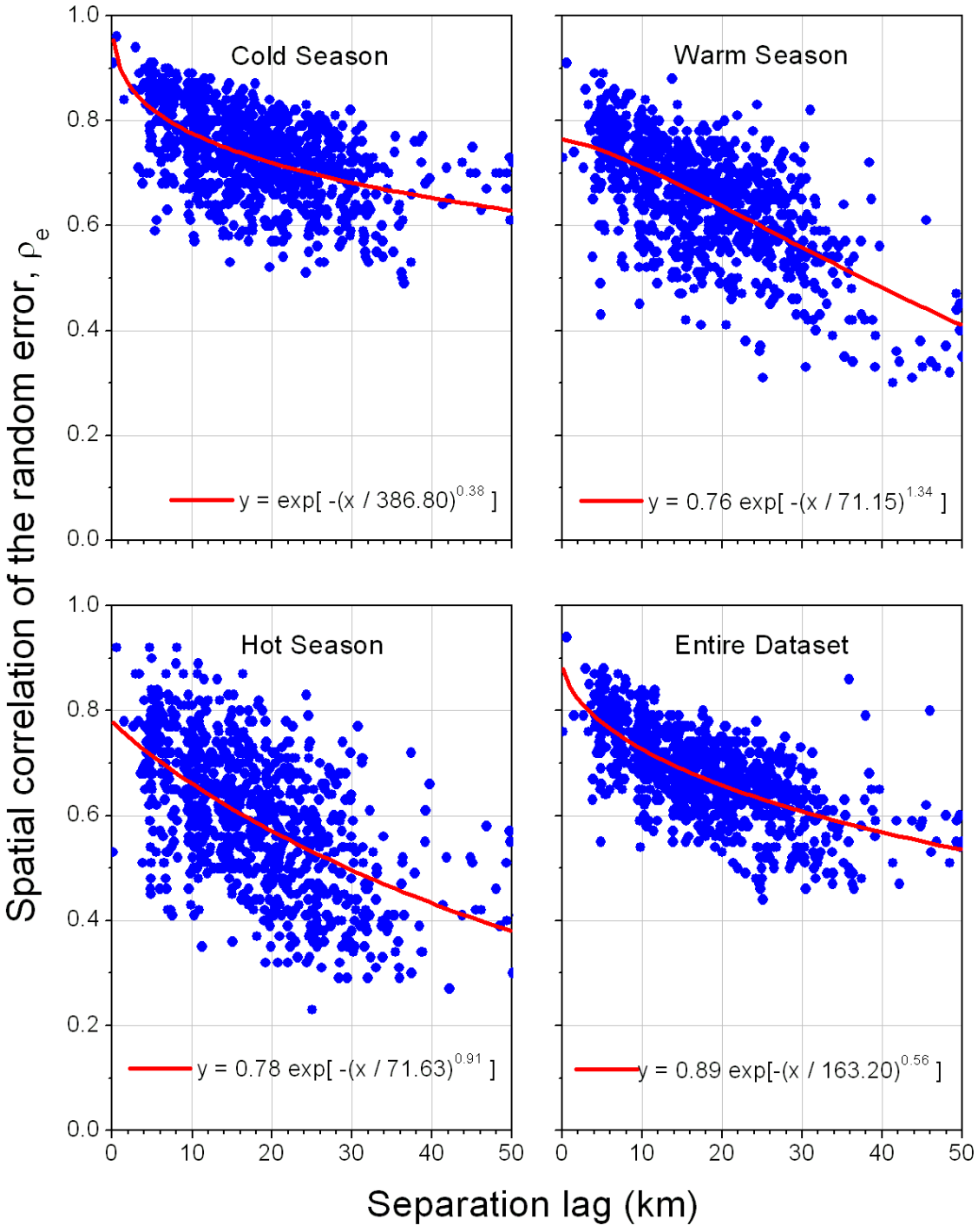

Figure D.23. Empirical intergauge spatial correlation over a limited range with a three-parameter exponential model approximation for Zone II.

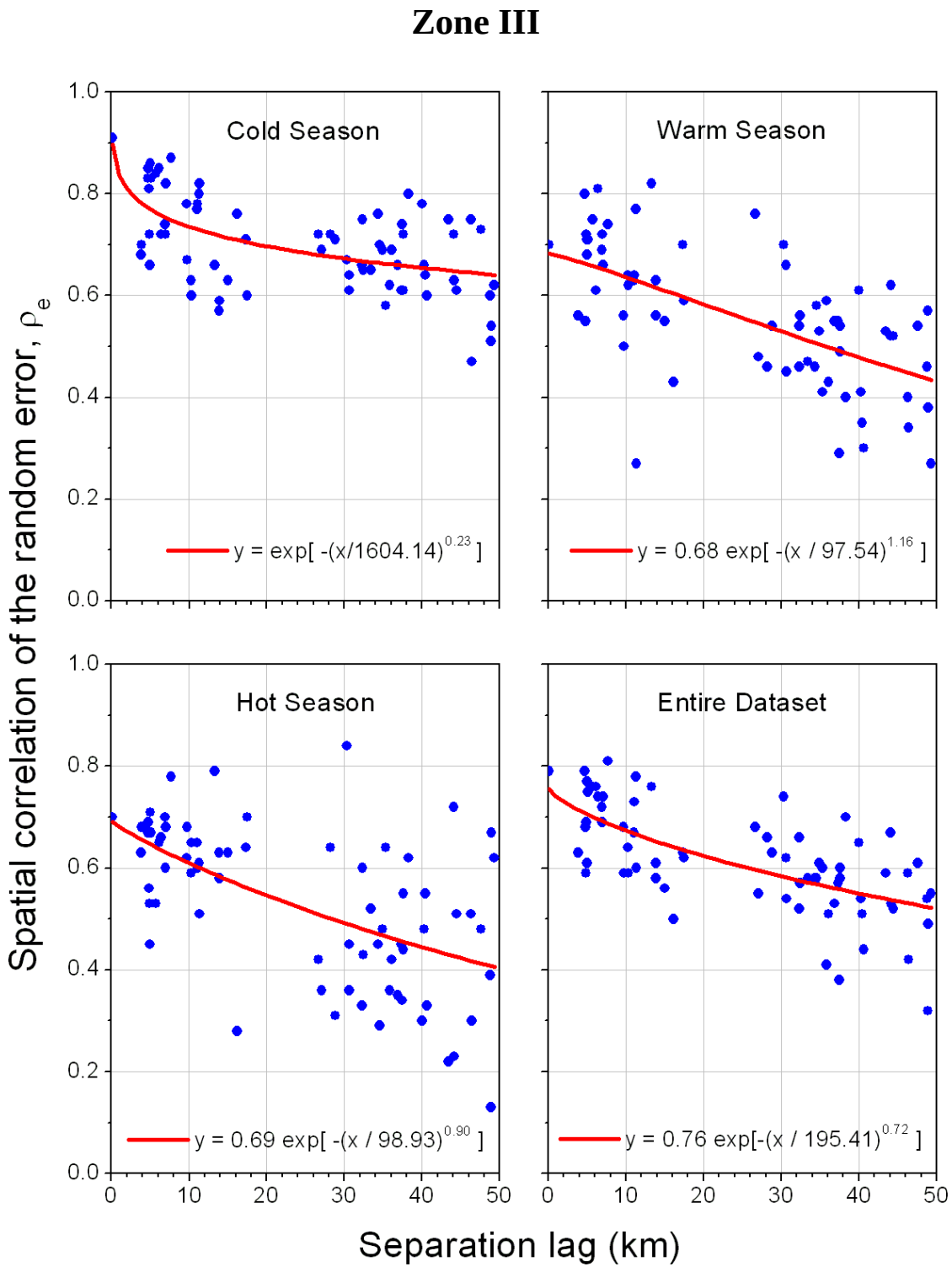

Figure D.24. Empirical intergauge spatial correlation over a limited range with a three-parameter exponential model approximation for Zone III.

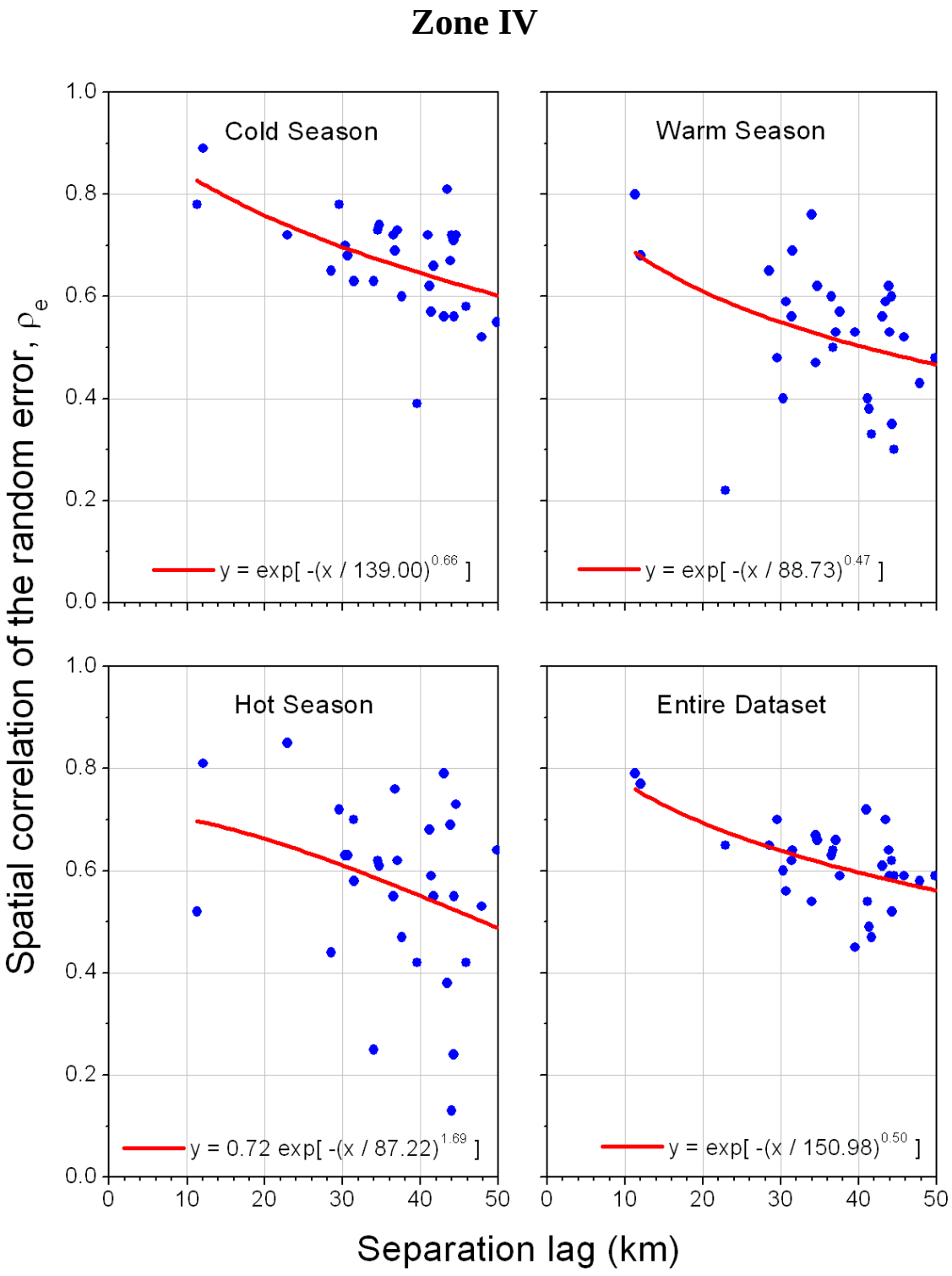

Figure D.25. Empirical intergauge spatial correlation over a limited range with a three-parameter exponential model approximation for Zone IV.

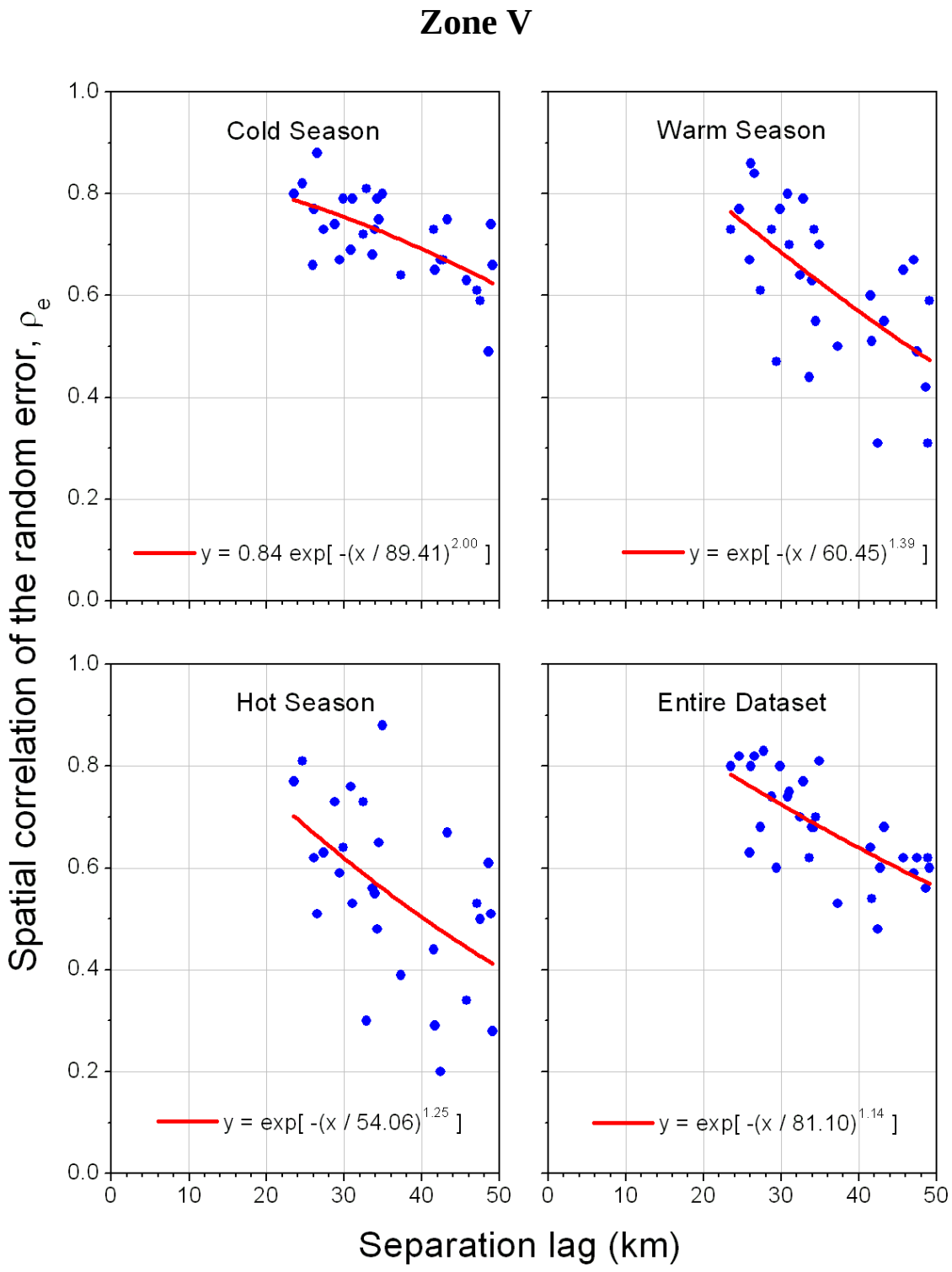

Figure D.26. Empirical intergauge spatial correlation over a limited range with a three-parameter exponential model approximation for Zone V.

Zone I

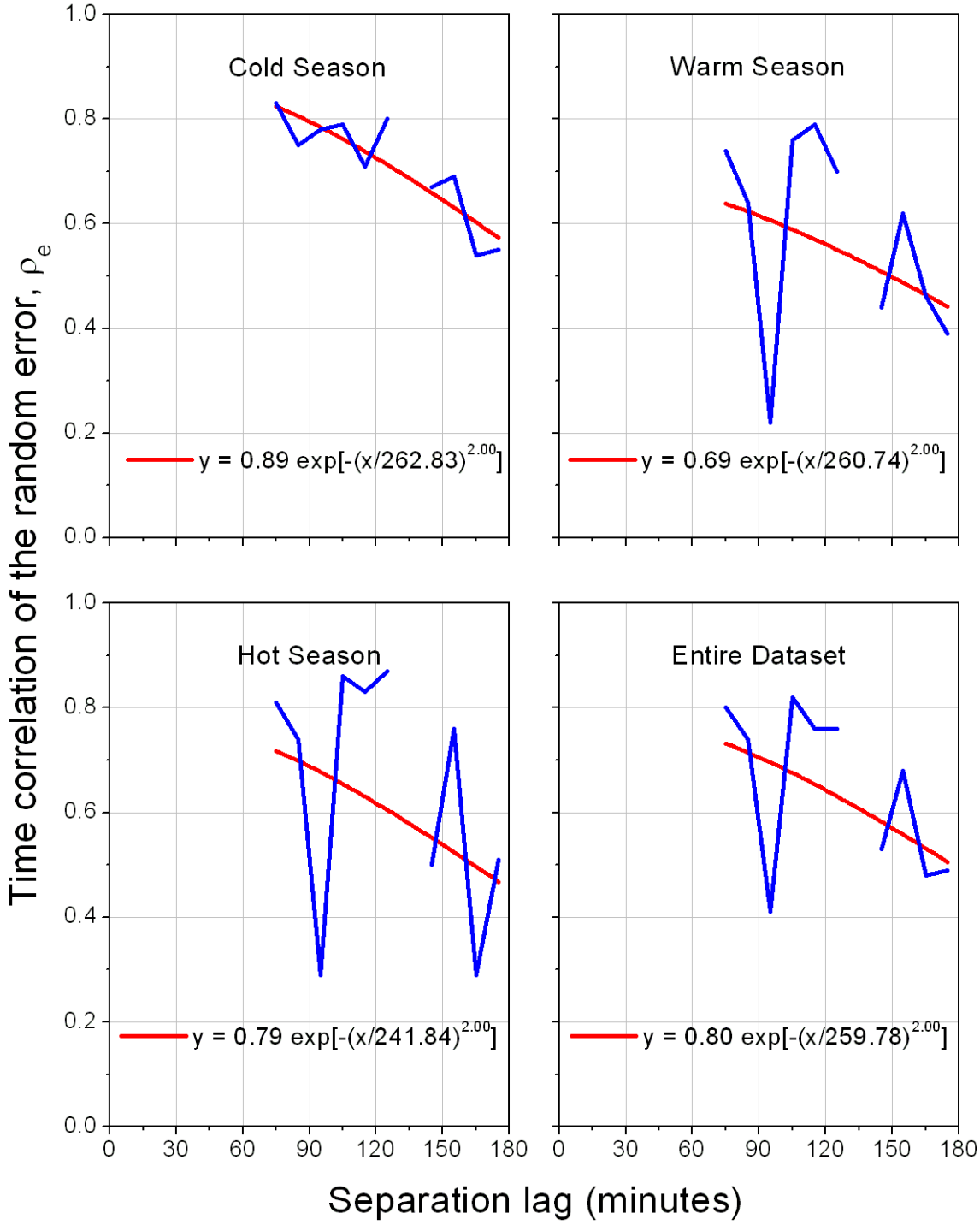

Figure D.27. Empirical and model approximated temporal correlation of the random component for Zone I.

Zone II

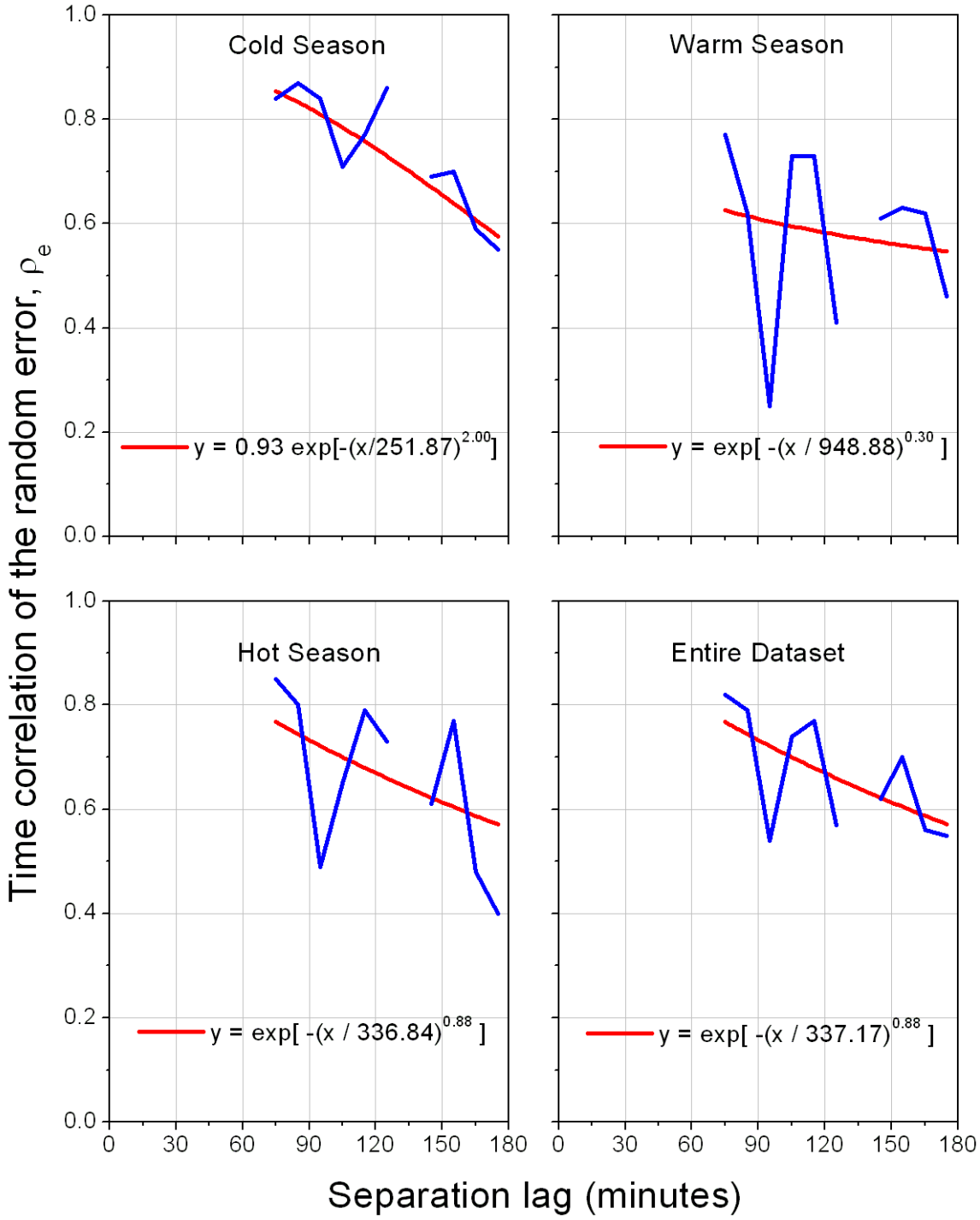

Figure D.28. Empirical and model approximated temporal correlation of the random component for Zone II.

Zone III

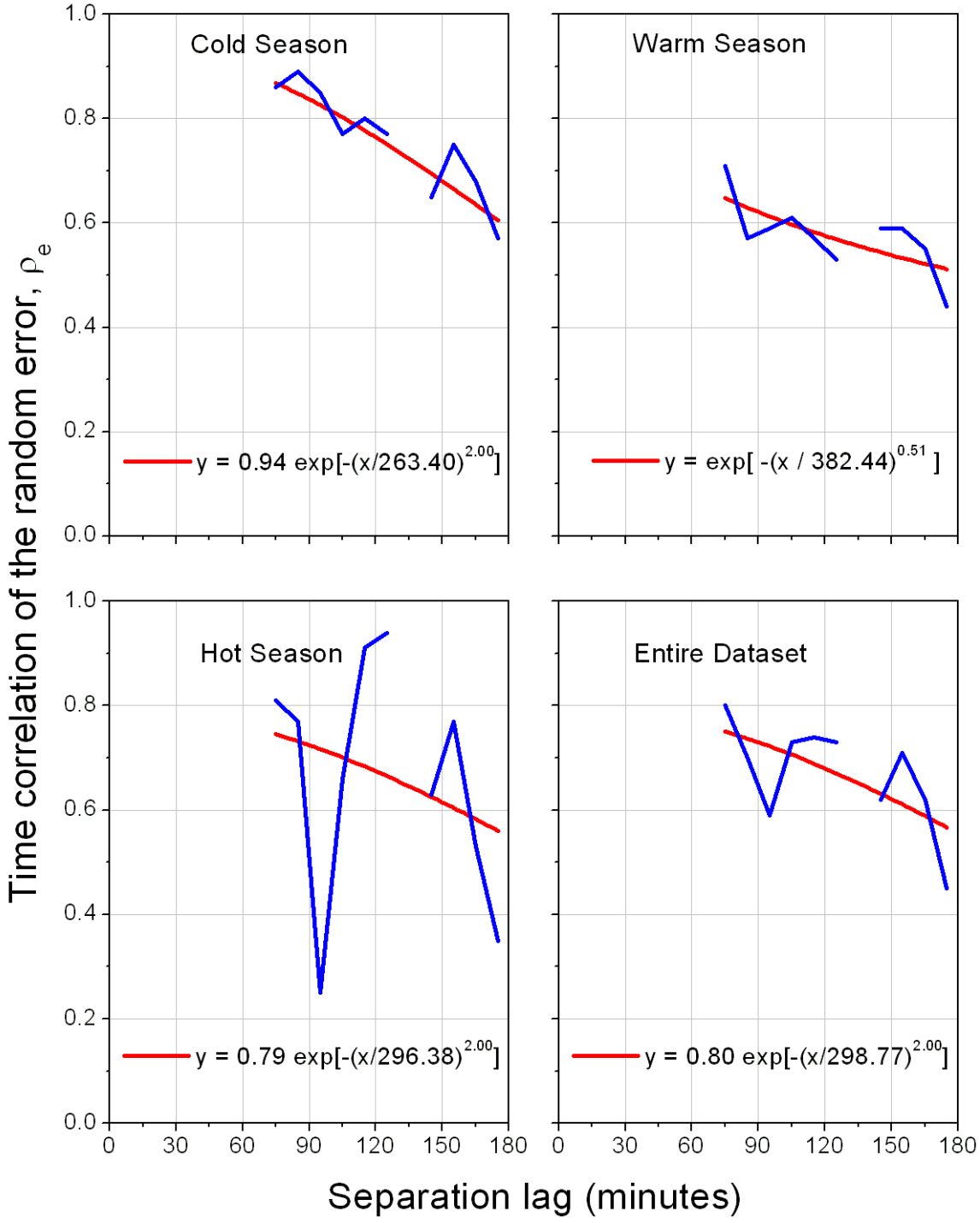

Figure D.29. Empirical and model approximated temporal correlation of the random component for Zone III.

Zone IV

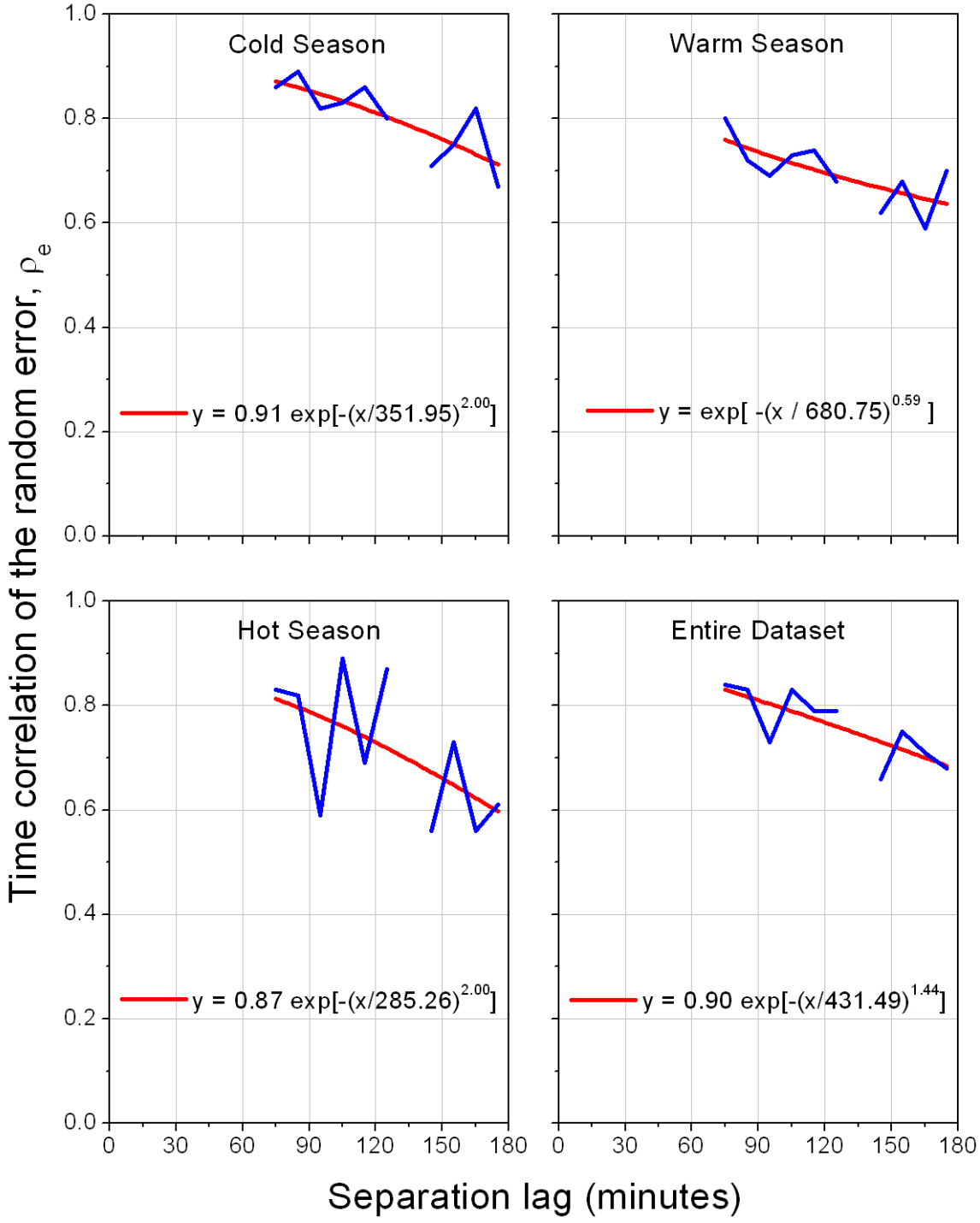

Figure D.30. Empirical and model approximated temporal correlation of the random component for Zone IV.

Zone V

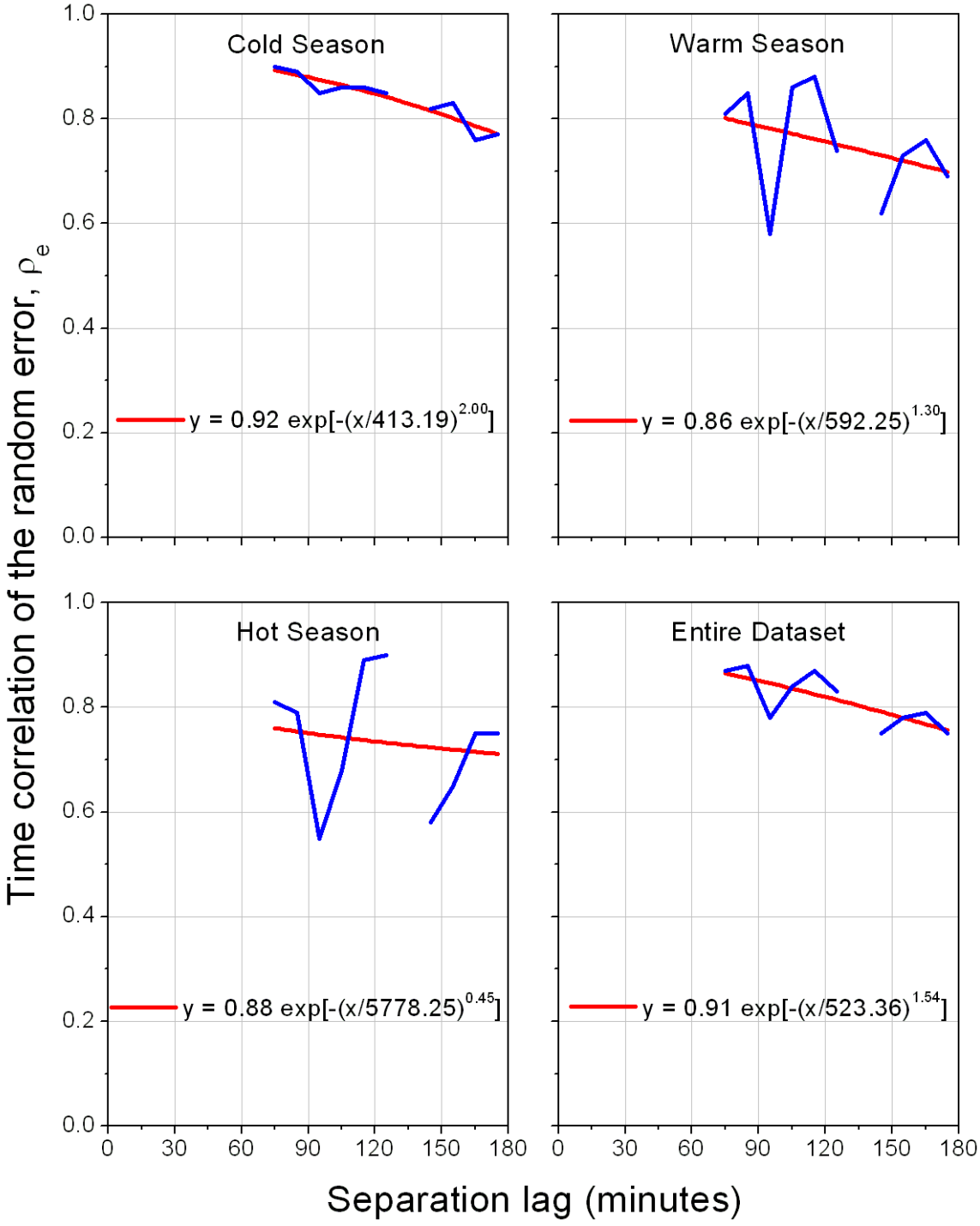

Figure D.31. Empirical and model approximated temporal correlation of the random component for Zone V.

Appendix E

Temporal Scale: Daily

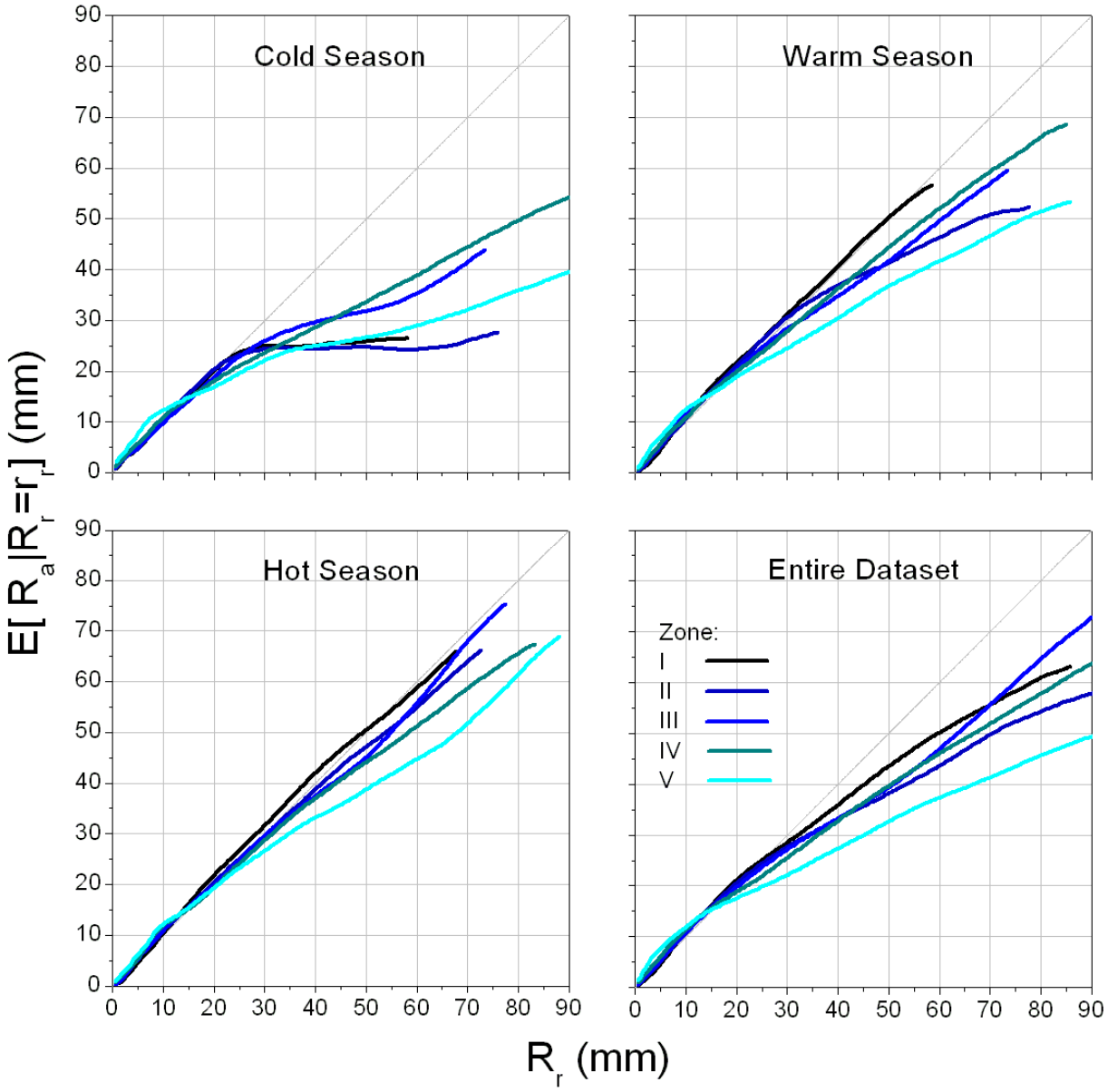

Figure E.1. Rain gauge averages, conditional on radar-rainfall values, after removing the overall bias for the three seasons and entire dataset for the 5 zones. The minimum weighted sample size is 100.

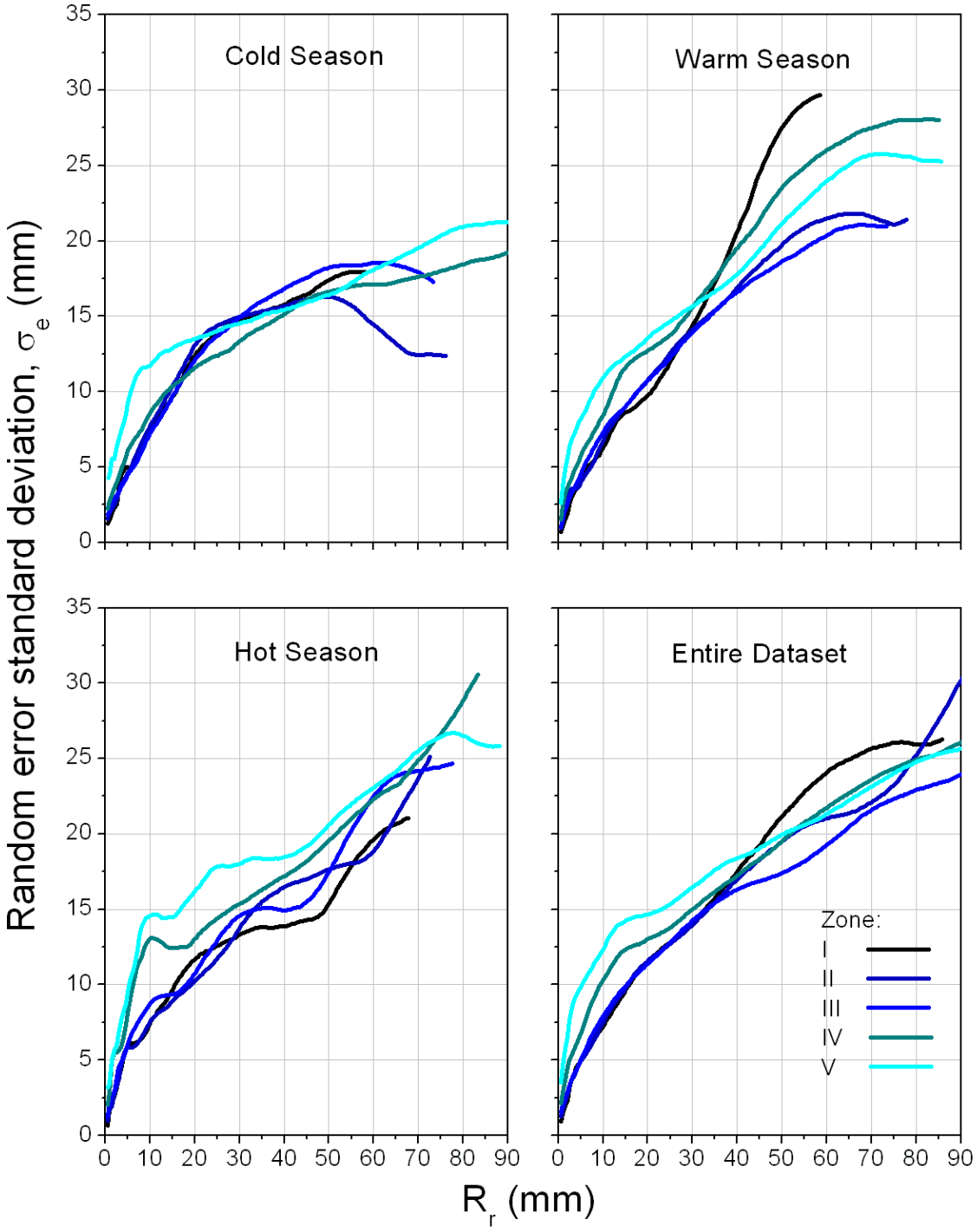

Figure E.2. Standard deviations of the random component in the additive form (mm) for the three seasons and entire dataset for the 5 zones. The minimum weighted sample size is 100.

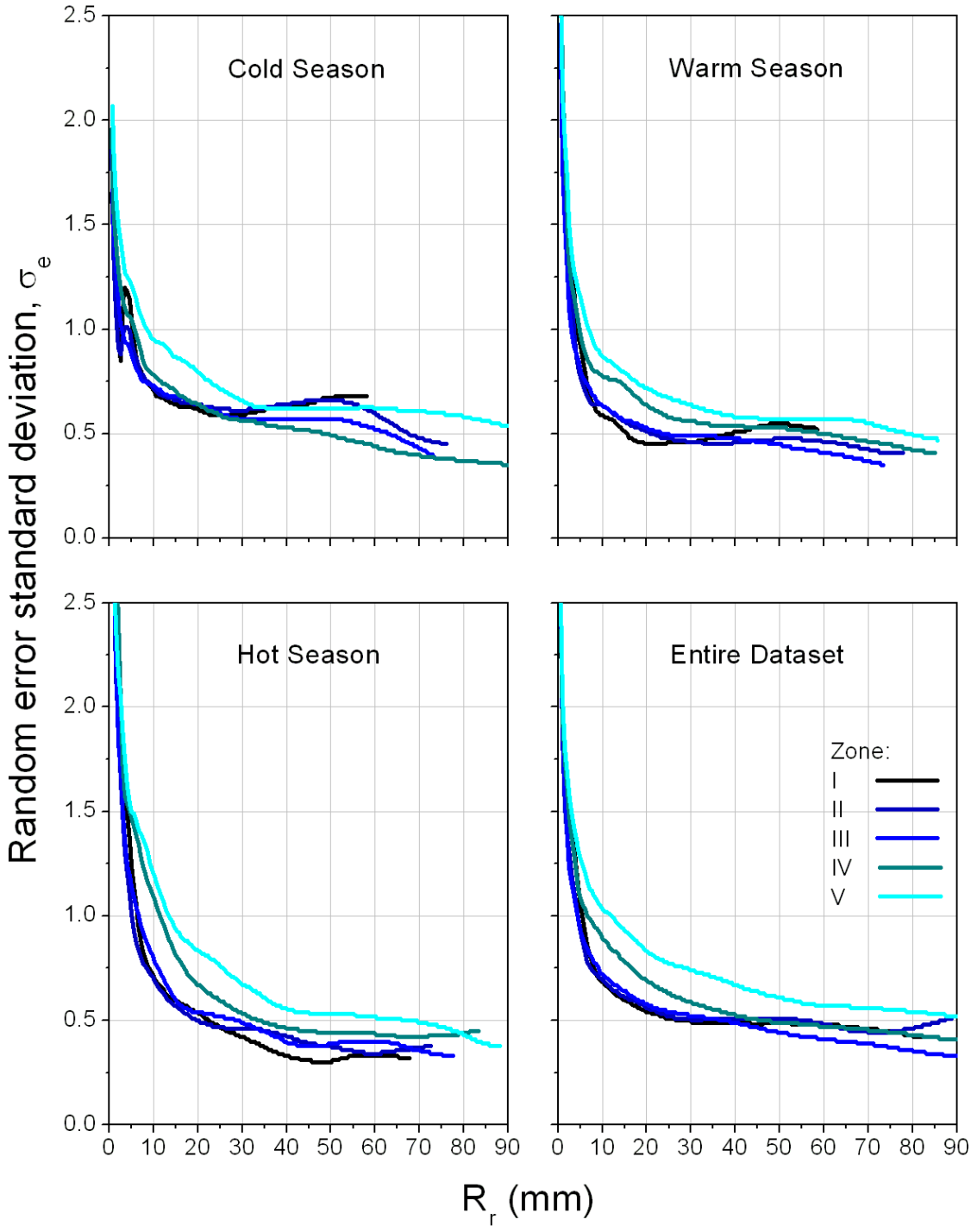

Figure E.3. Standard deviations of the random component in the multiplicative form for the three seasons and entire dataset for the 5 zones (1-h resolution). The minimum weighted sample size is 100.

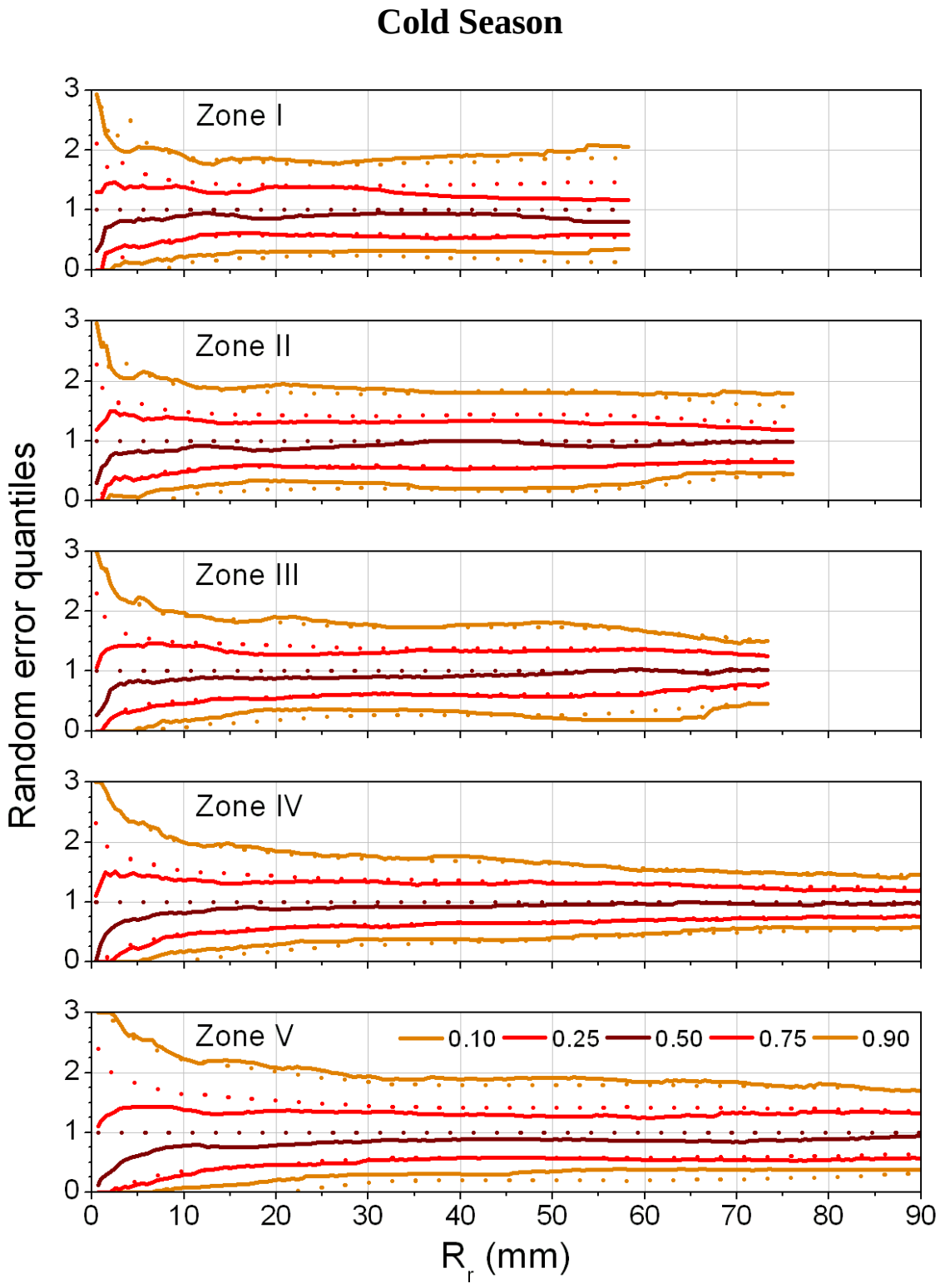

Figure E.4. Comparison of the empirical and Gaussian quantiles (p=0.1, 0.25, 0.5, 0.75, 0.9) for the five zones (cold season). The mean of the theoretical distribution is equal to 1 and the standard deviation is the standard deviation of the random component in the multiplicative form. The minimum weighted sample size is 100.

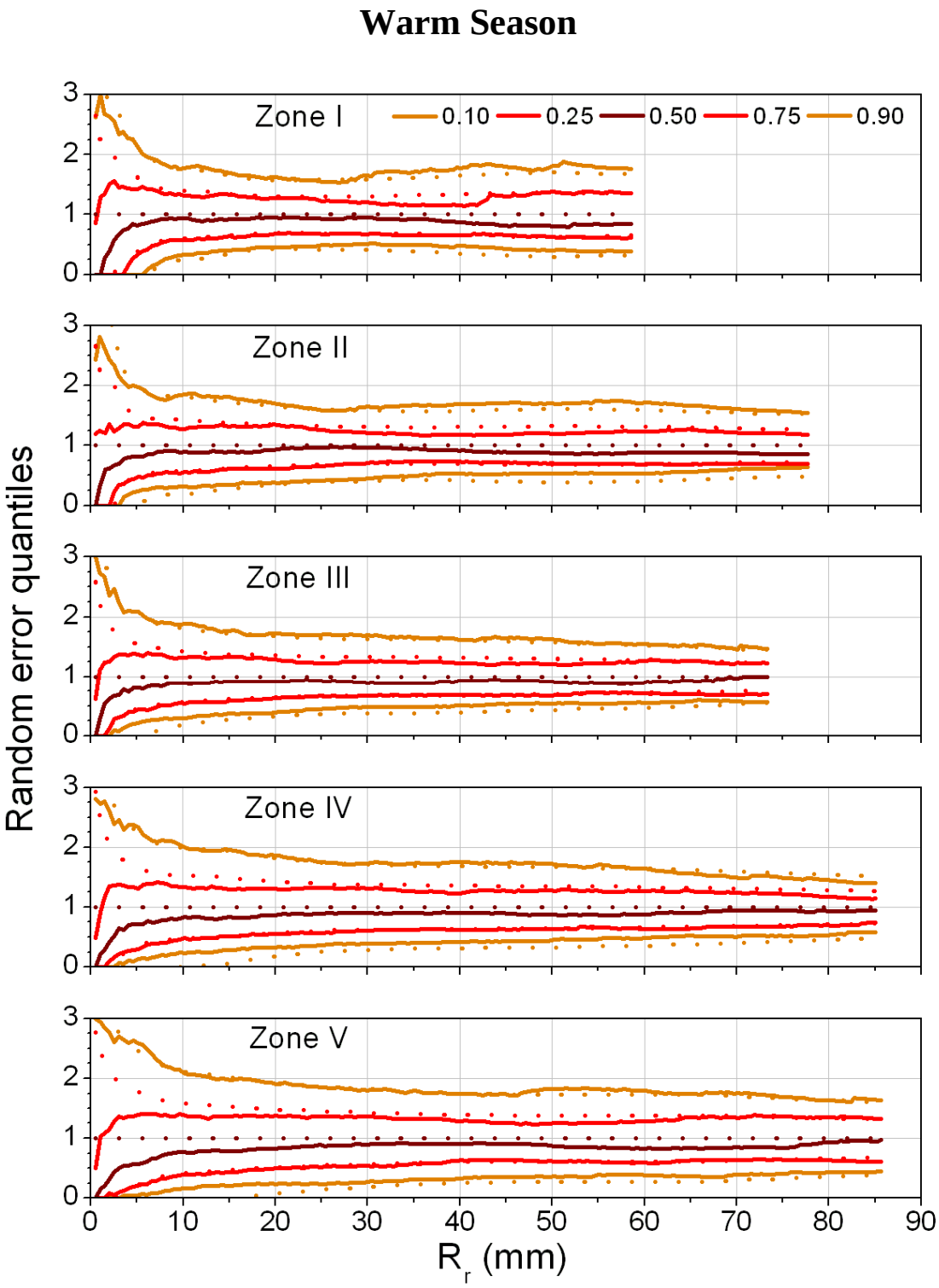

Figure E.5. Comparison of the empirical and Gaussian quantiles (p=0.1, 0.25, 0.5, 0.75, 0.9) for the five zones (warm season). The mean of the theoretical distribution is equal to 1 and the standard deviation is the standard deviation of the random component in the multiplicative form. The minimum weighted sample size is 100.

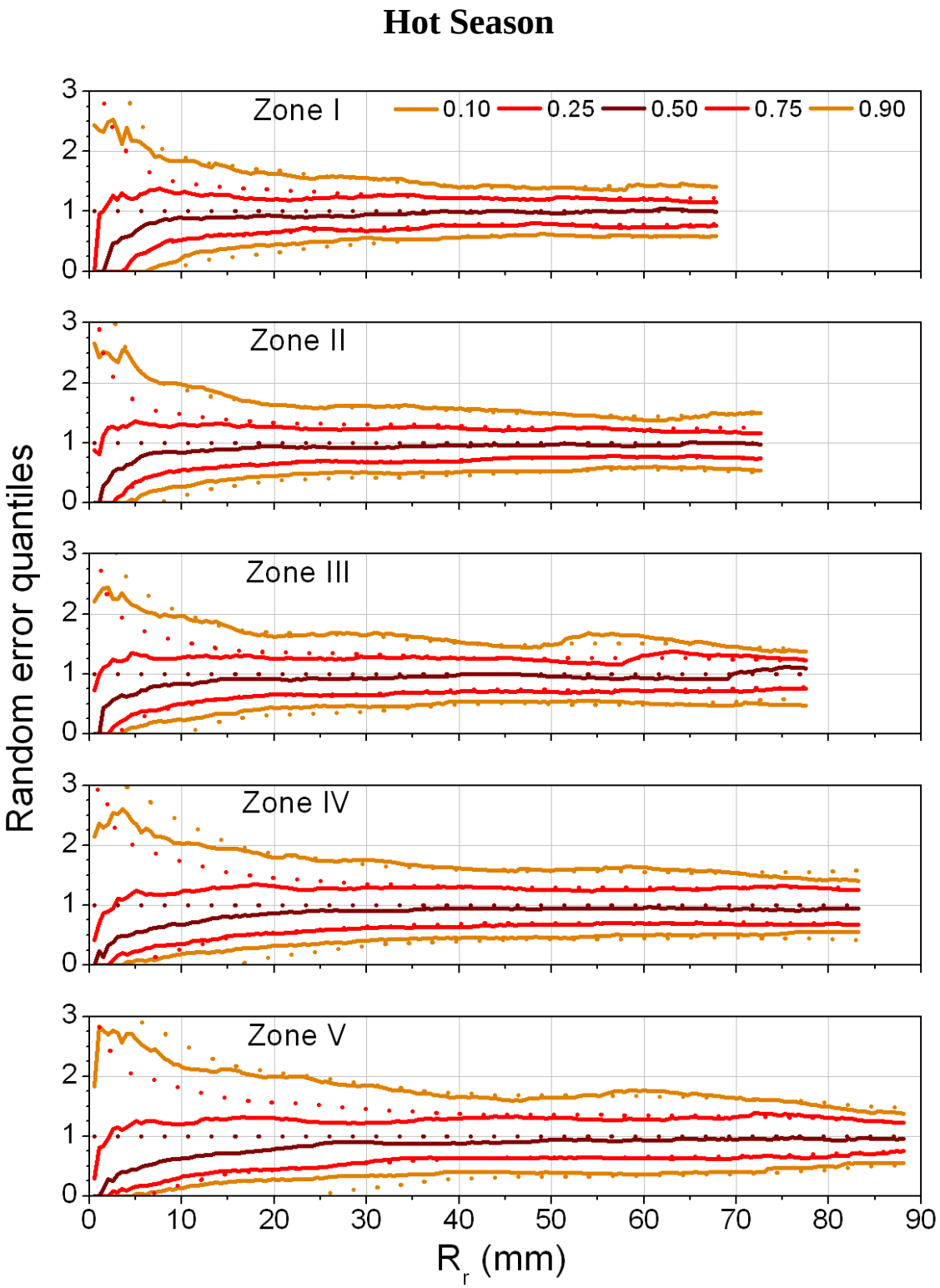

Figure E.6. Comparison of the empirical and Gaussian quantiles (p=0.1, 0.25, 0.5, 0.75, 0.9) for the five zones (hot season). The mean of the theoretical distribution is equal to 1 and the standard deviation is the standard deviation of the random component in the multiplicative form. The minimum weighted sample size is 100.

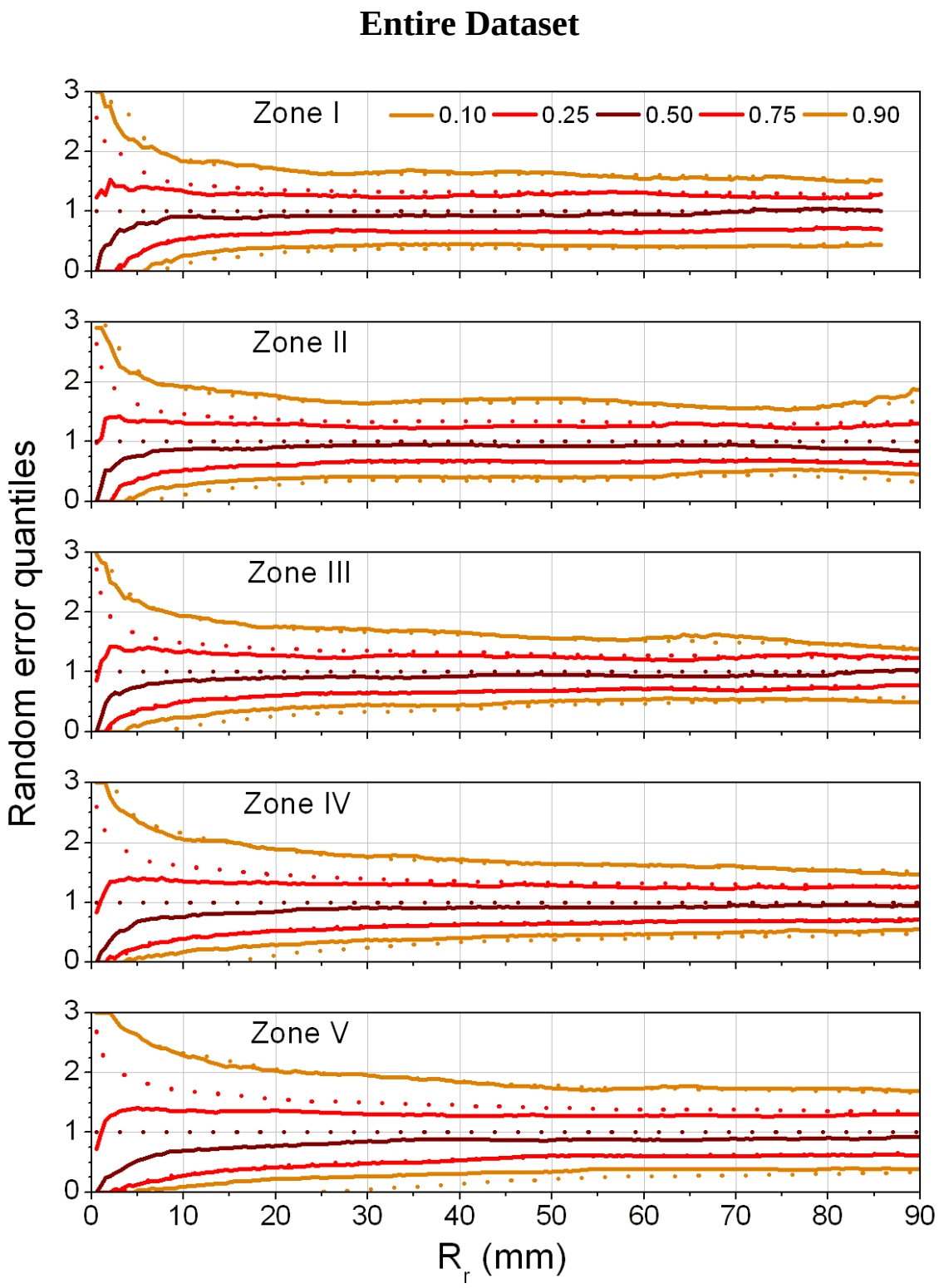

Figure E.7. Comparison of the empirical and Gaussian quantiles (p=0.1, 0.25, 0.5, 0.75, 0.9) for the five zones (all seasons). The mean of the theoretical distribution is equal to 1 and the standard deviation is the standard deviation of the random component in the multiplicative form. The minimum weighted sample size is 100.

Zone I

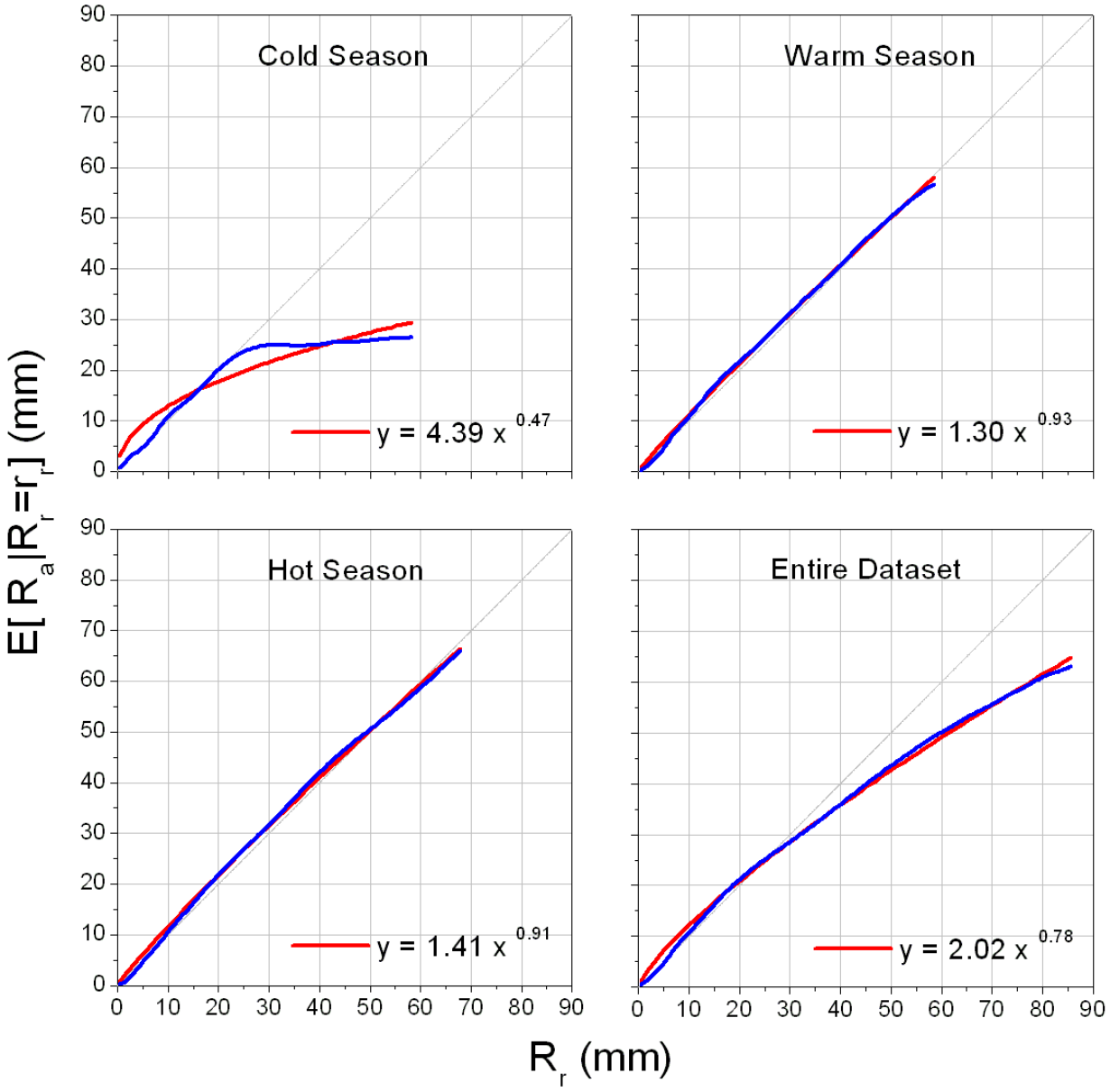

Figure E.8. Power law model approximation of the rain gauge conditional averages for the three seasons and the entire dataset for Zone I.

Zone II

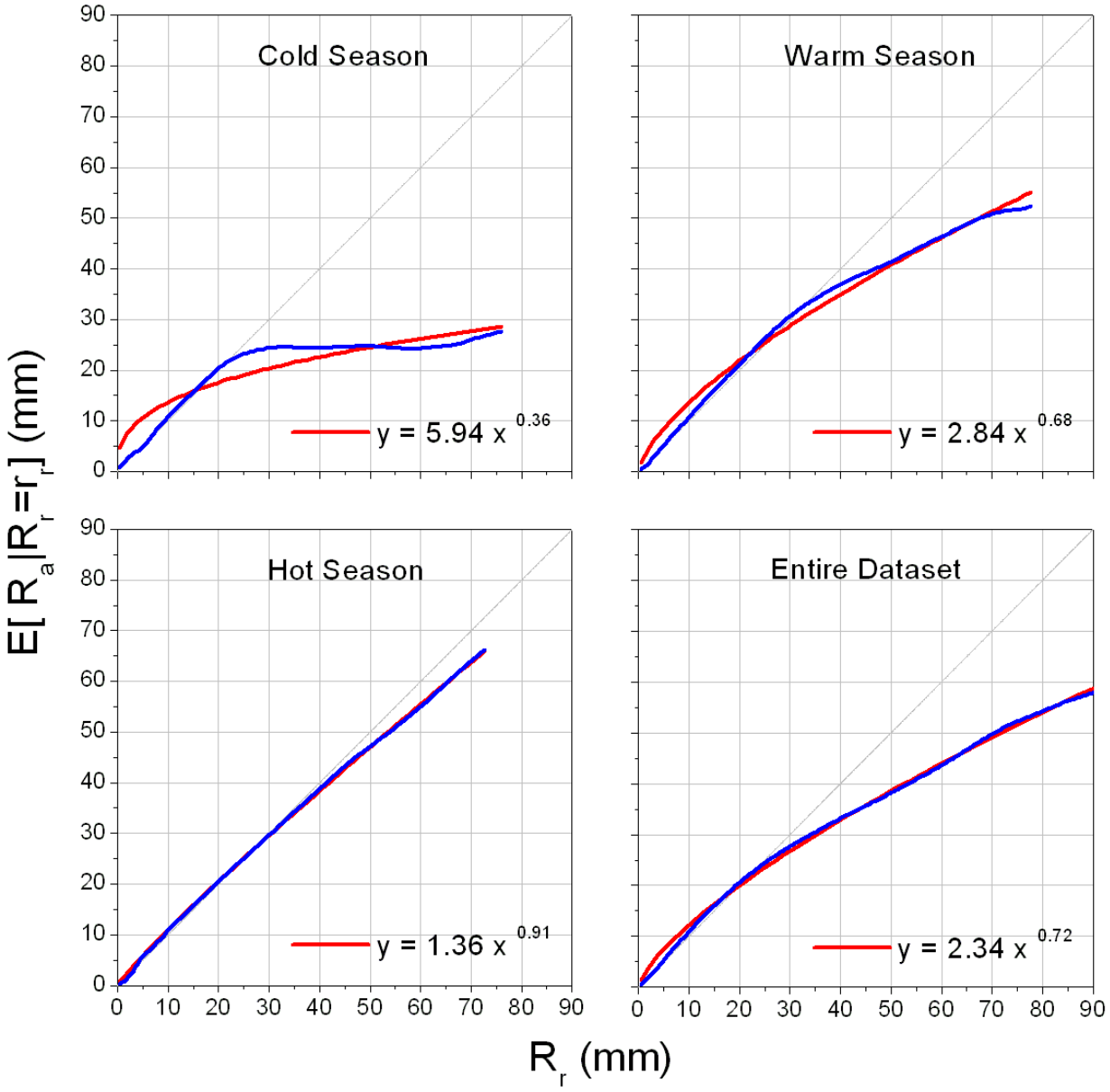

Figure E.9. Power law model approximation of the rain gauge conditional averages for the three seasons and the entire dataset for Zone II.

Zone III

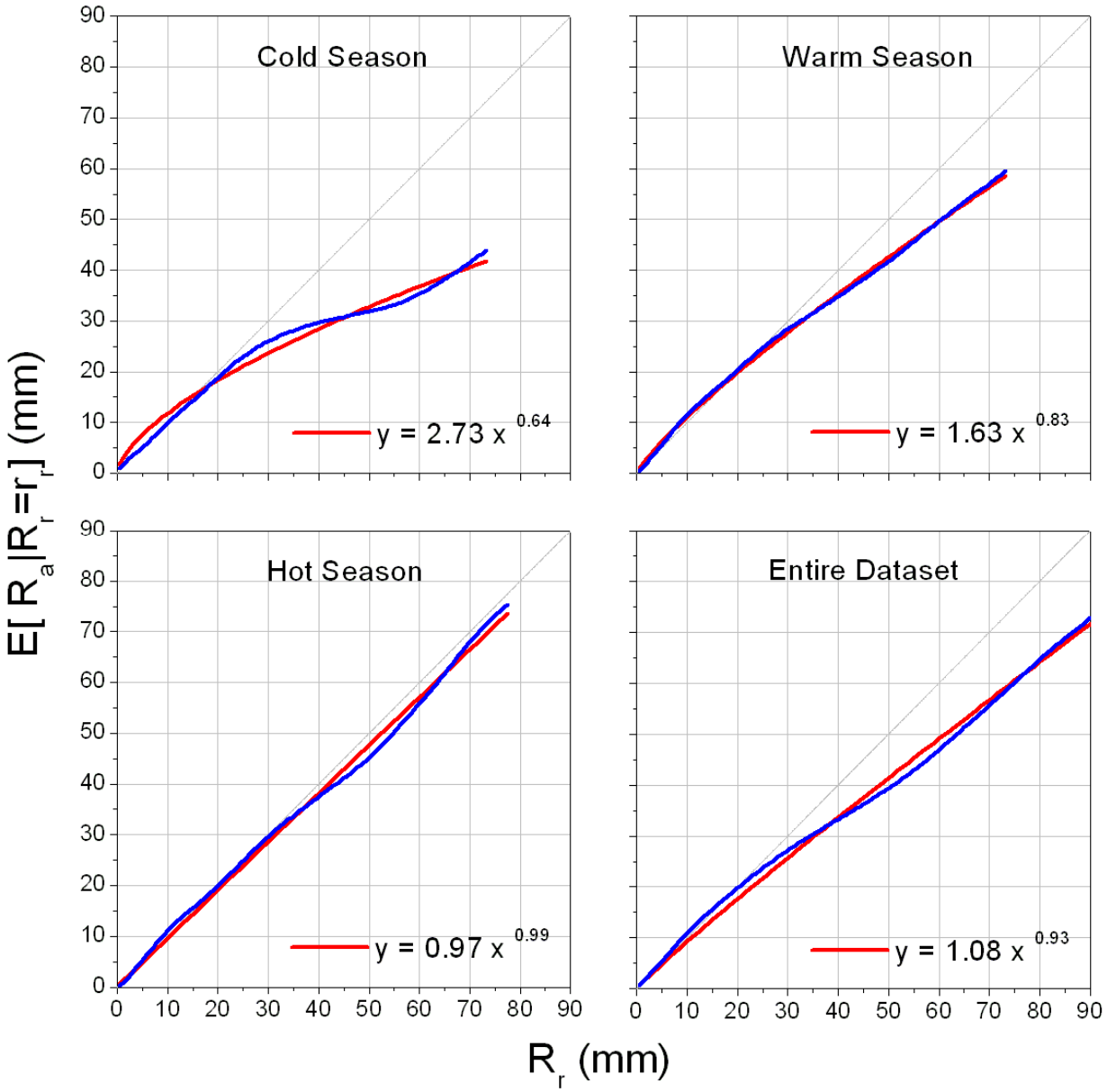

Figure E.10. Power law model approximation of the rain gauge conditional averages for the three seasons and the entire dataset for Zone III.

Zone IV

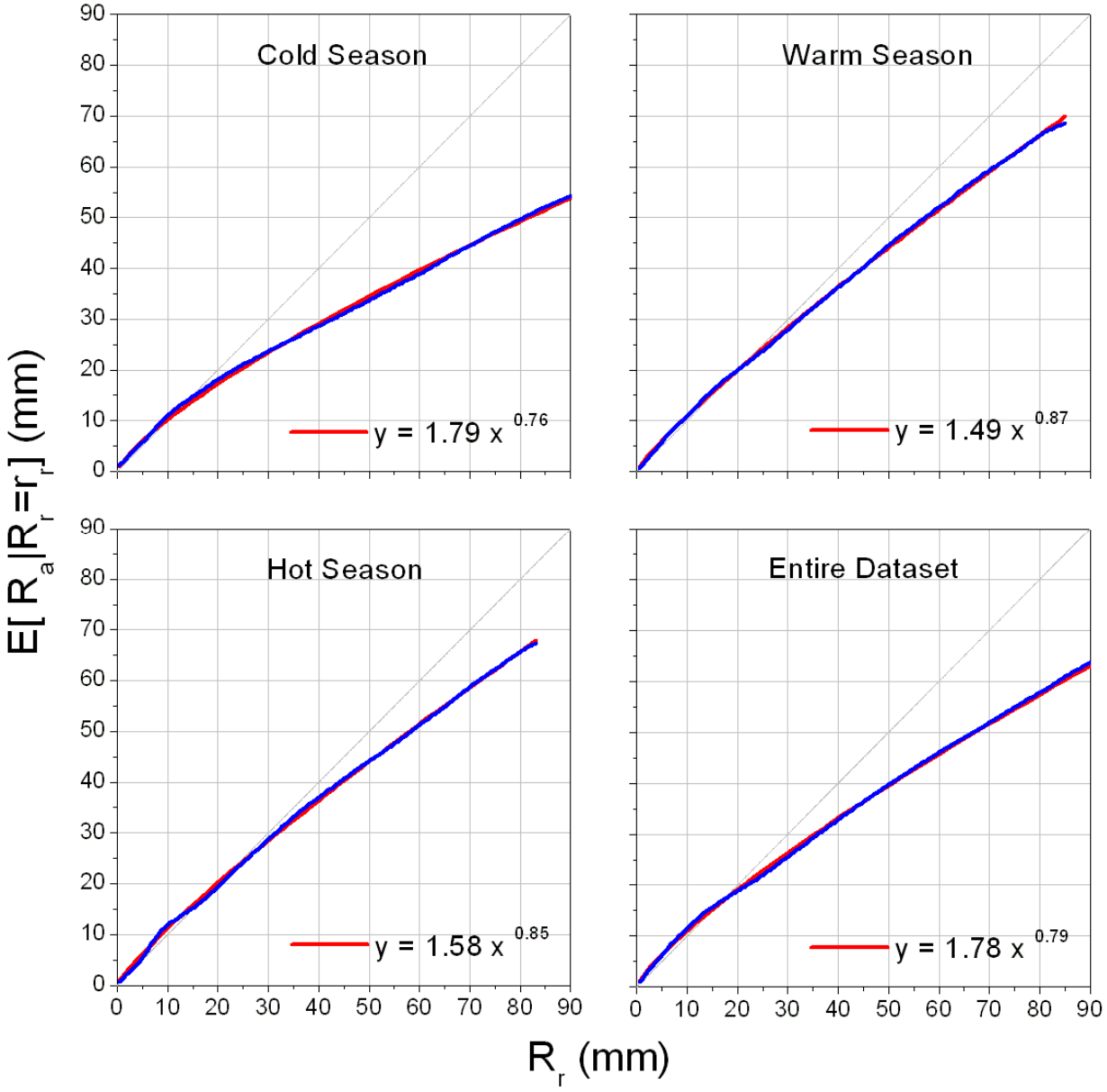

Figure E.11. Power law model approximation of the rain gauge conditional averages for the three seasons and the entire dataset for Zone IV.

Zone V

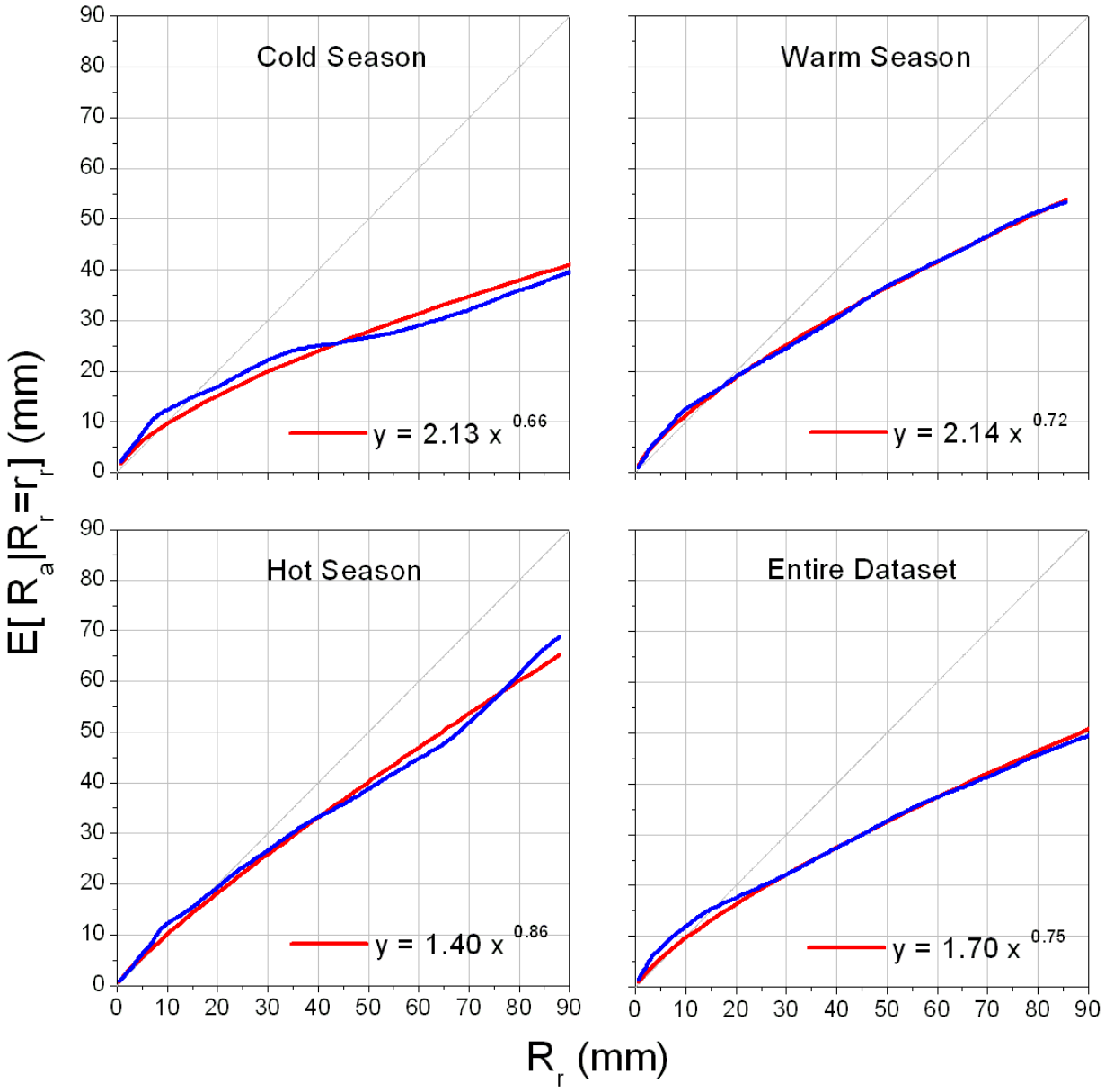

Figure E.12. Power law model approximation of the rain gauge conditional averages for the three seasons and the entire dataset for Zone V.

Zone I

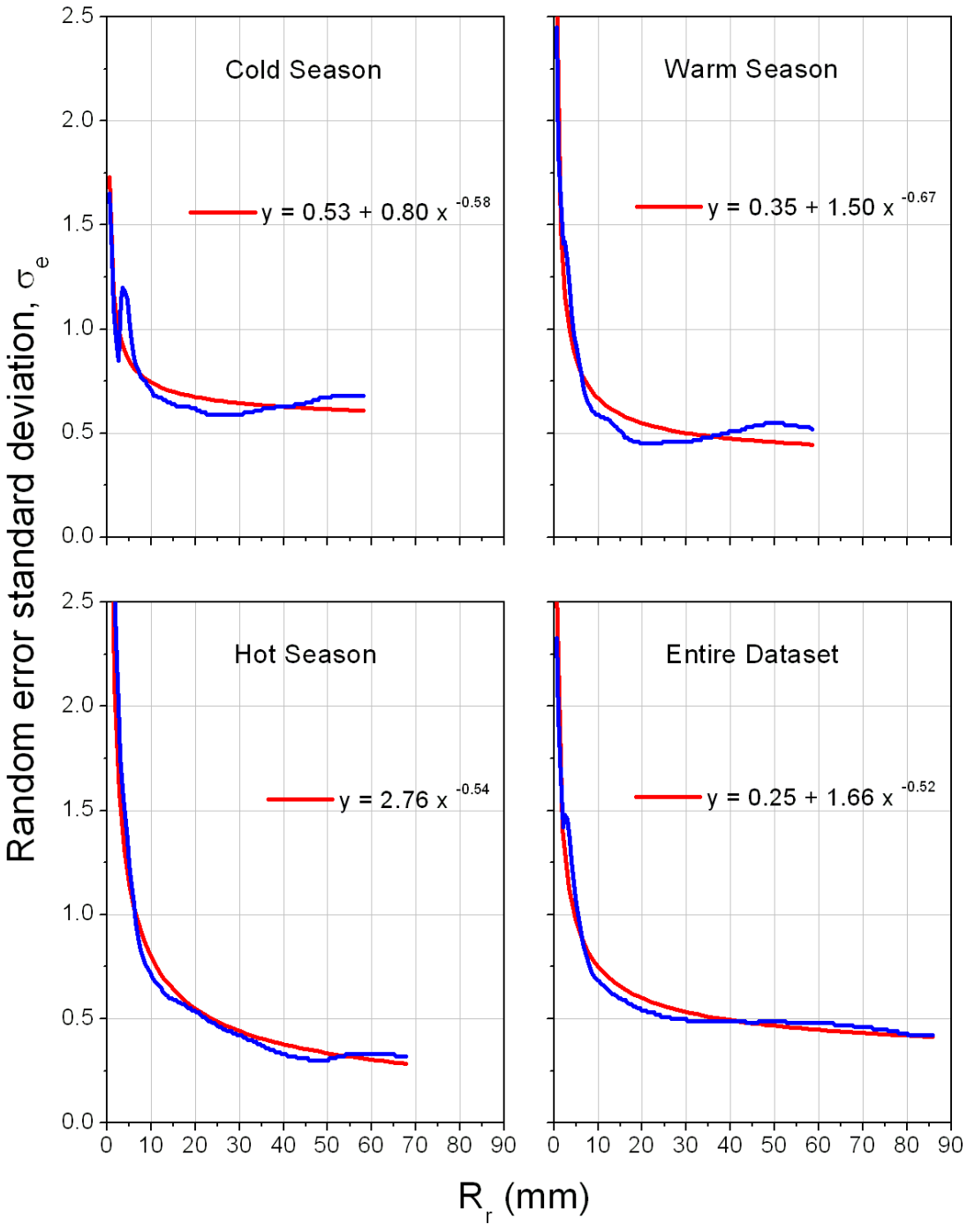

Figure E.13. Model approximation of the conditional multiplicative standard deviation for the three seasons and the entire dataset for Zone I.

Zone II

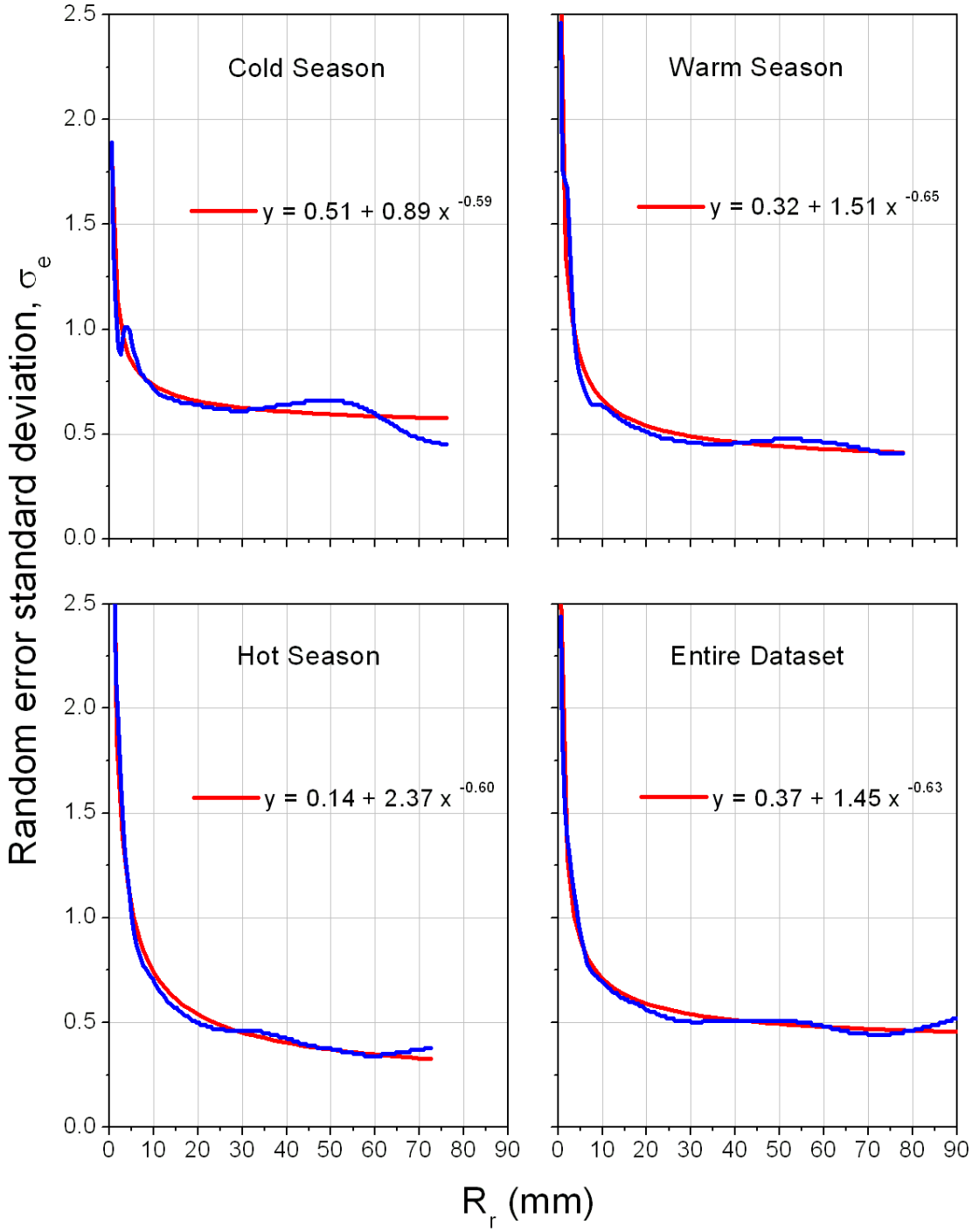

Figure E.14. Model approximation of the conditional multiplicative standard deviation for the three seasons and the entire dataset for Zone II.

Zone III

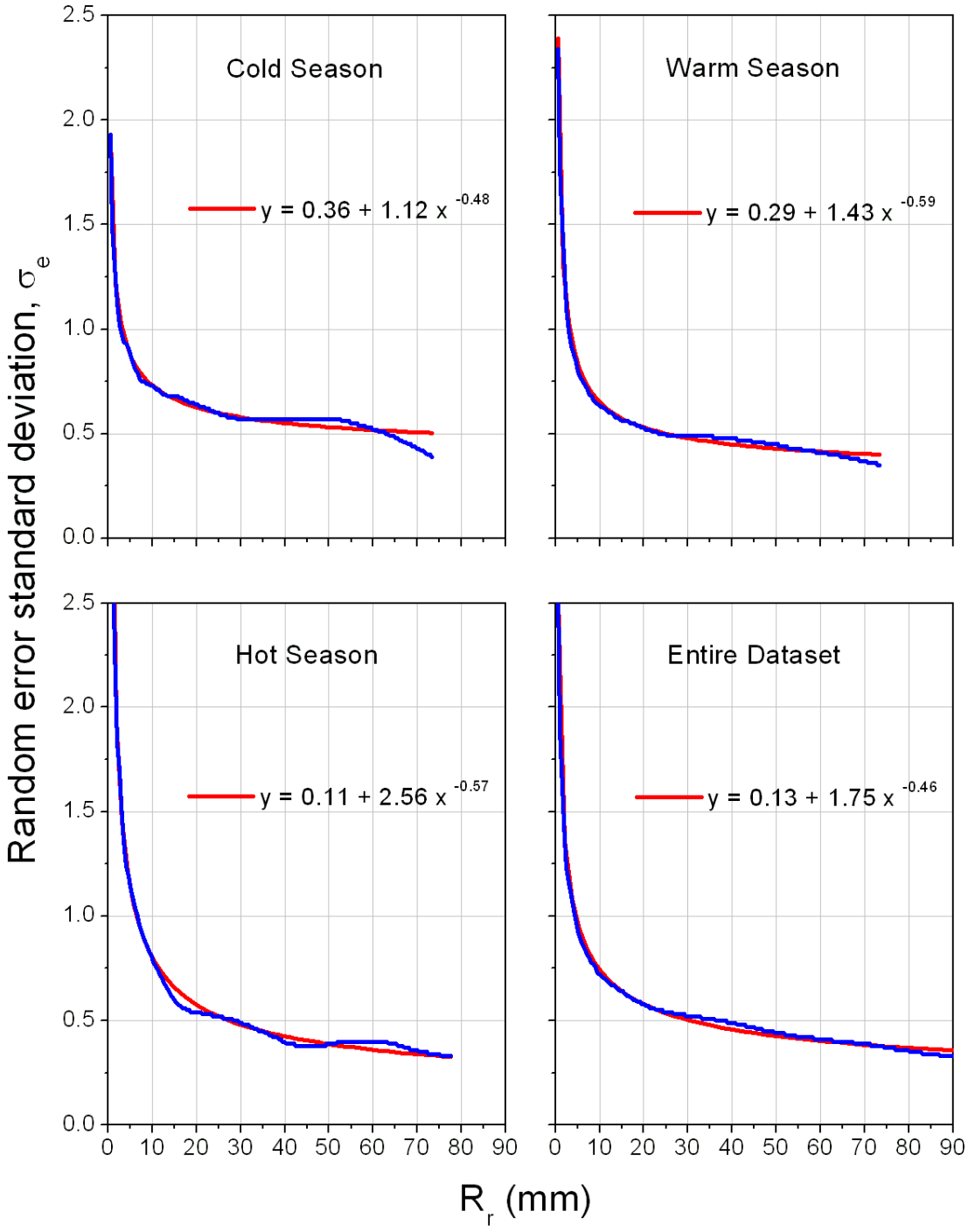

Figure E.15. Model approximation of the conditional multiplicative standard deviation for the three seasons and the entire dataset for Zone III.

Zone IV

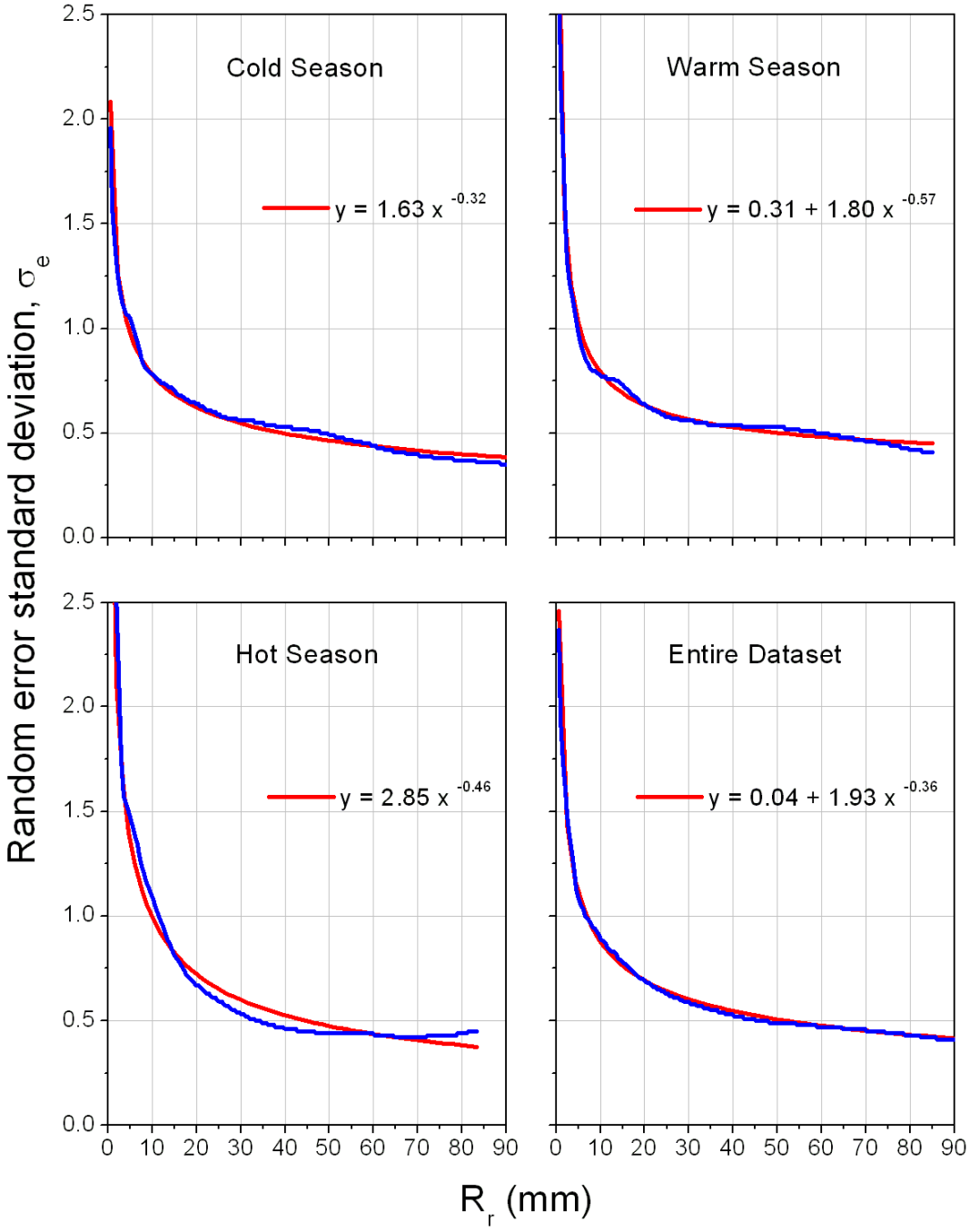

Figure E.16. Model approximation of the conditional multiplicative standard deviation for the three seasons and the entire dataset for Zone IV.

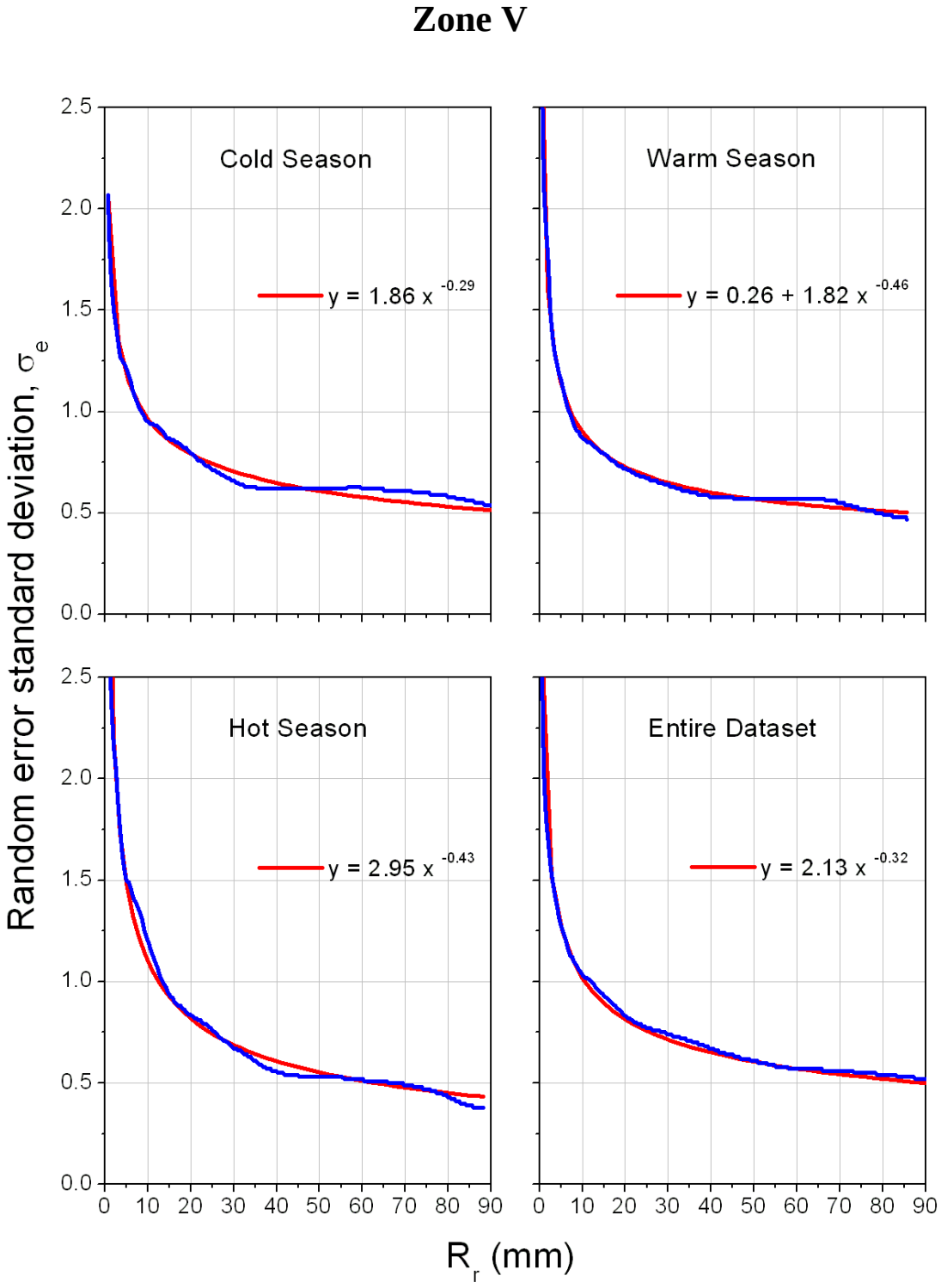

Figure E.17. Model approximation of the conditional multiplicative standard deviation for the three seasons and the entire dataset for Zone V.

Spatial and Temporal Correlation Structure

Winter Season

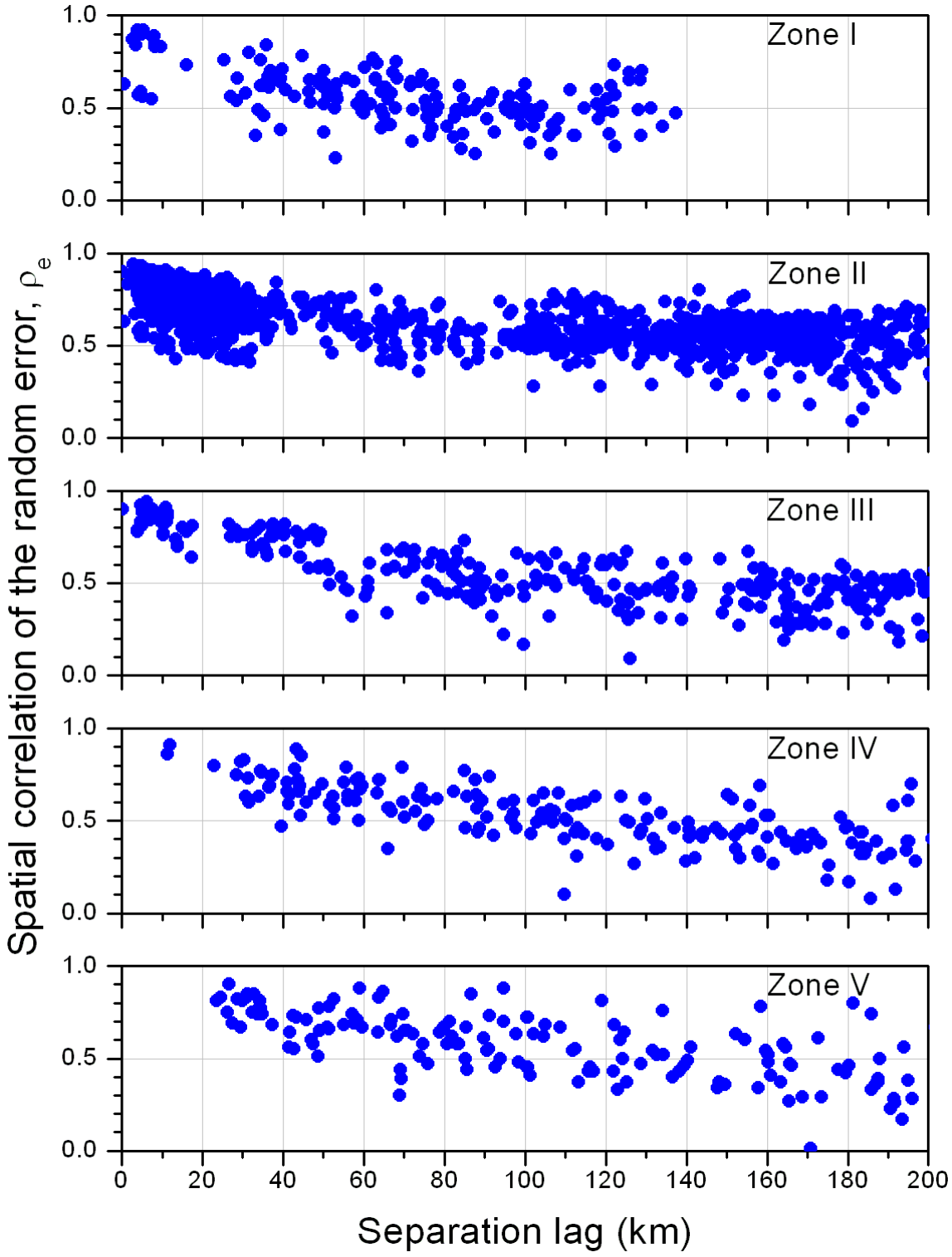

Figure E.18. Intergauge spatial Pearson correlation of the random component for the winter season.

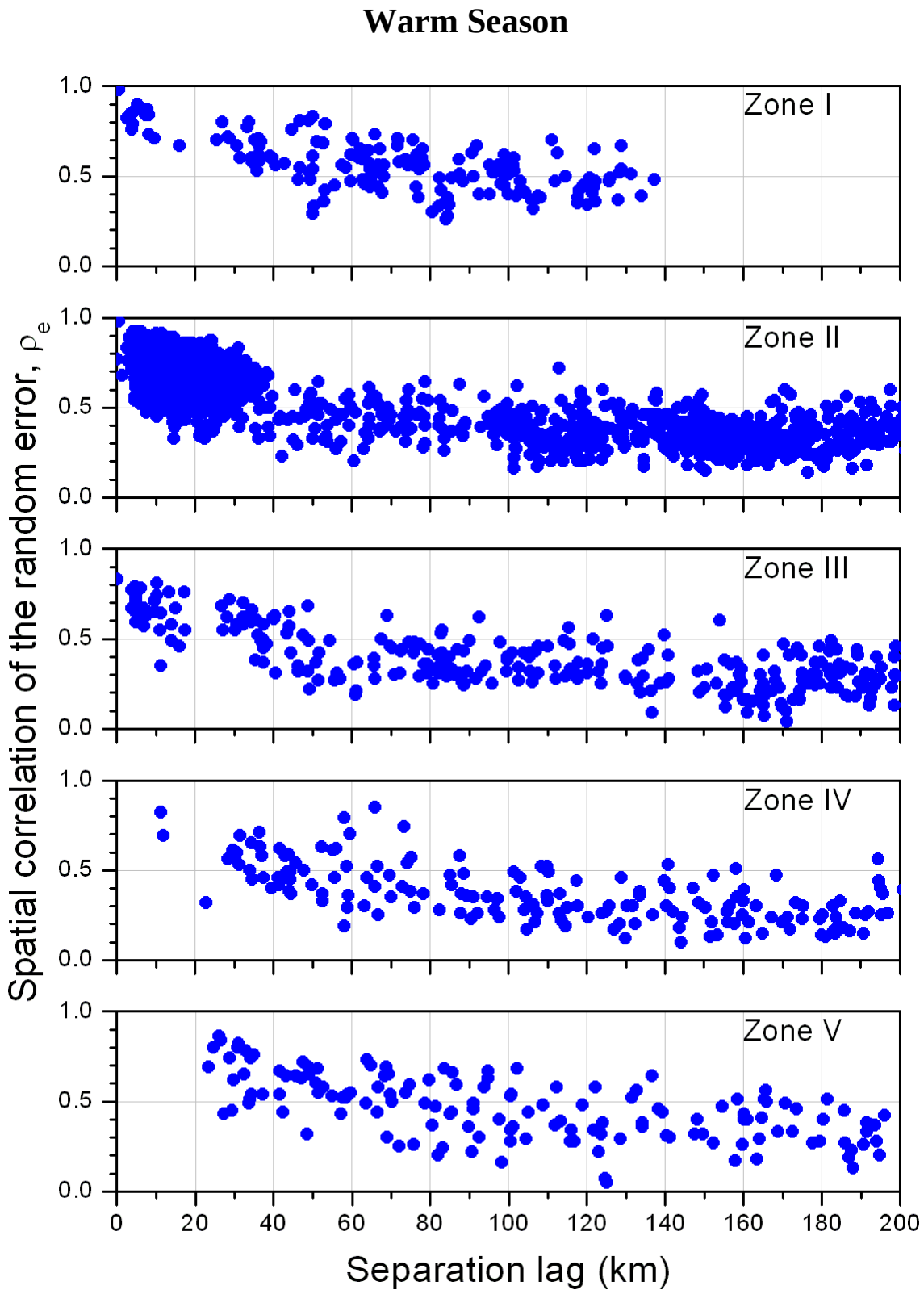

Figure E.19. Intergauge spatial Pearson correlation of the random component for the warm season.

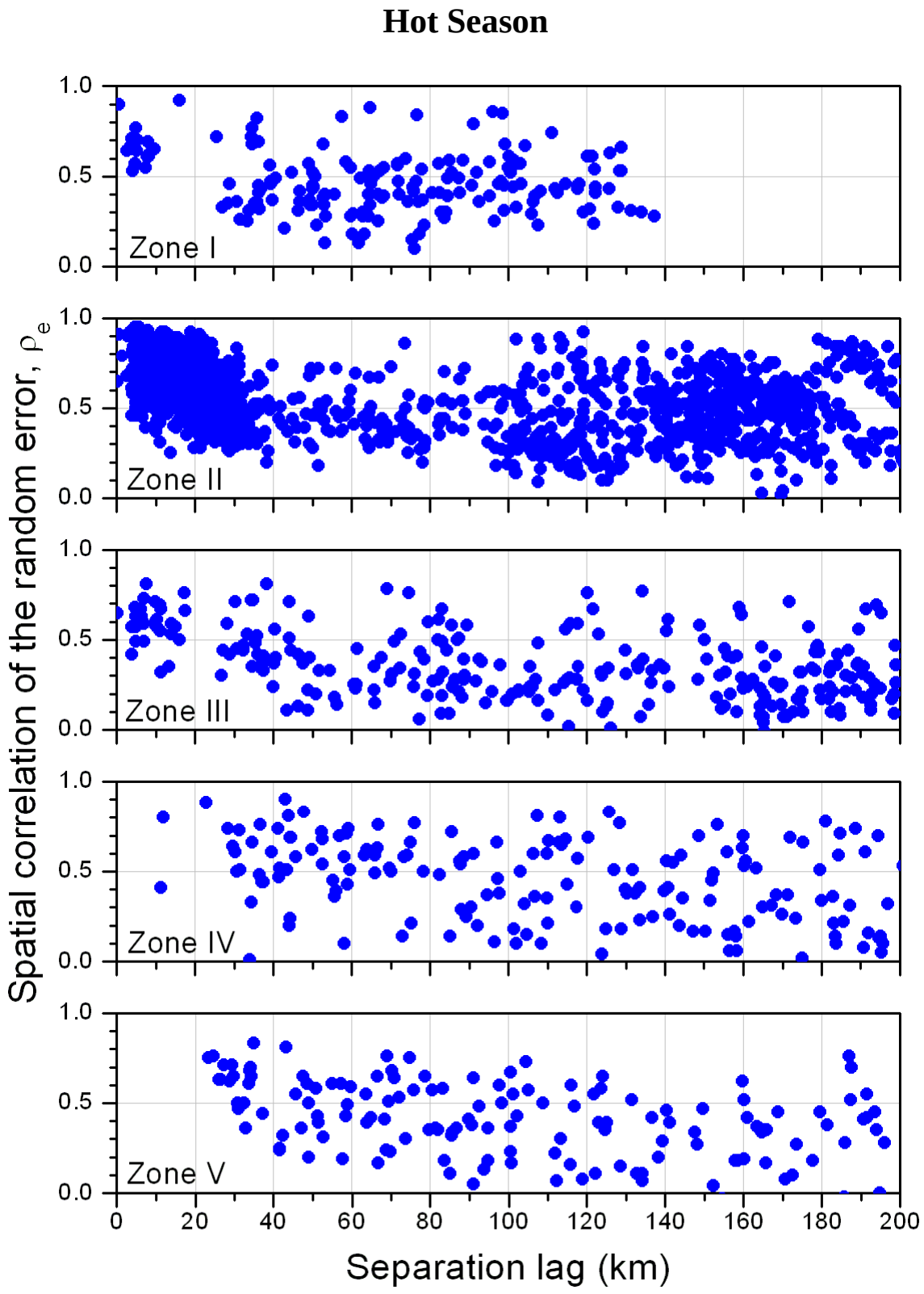

Figure E.20. Intergauge spatial Pearson correlation of the random component for the hot season.

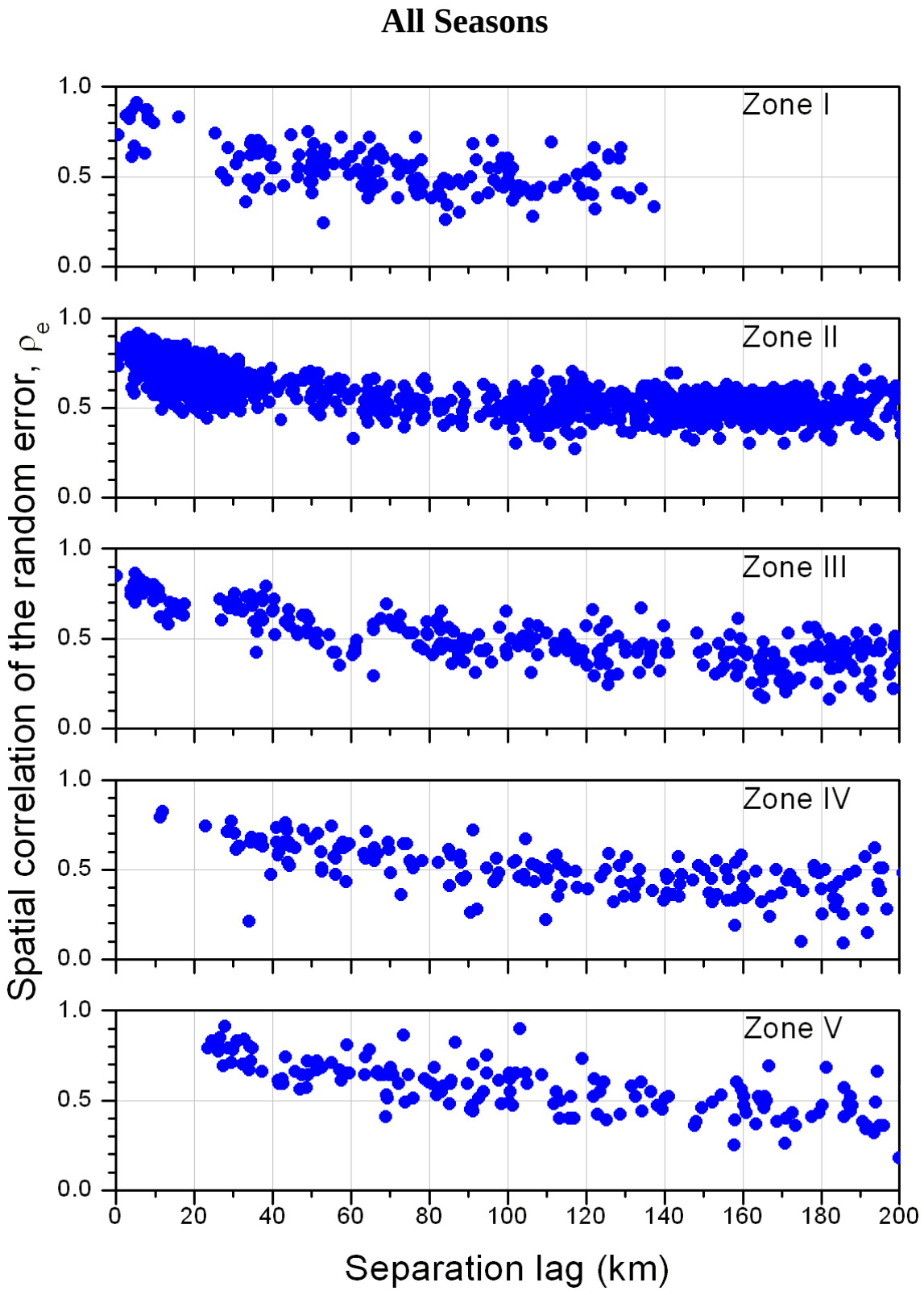

Figure E.21. Intergauge spatial Pearson correlation of the random component for all seasons.

Zone I

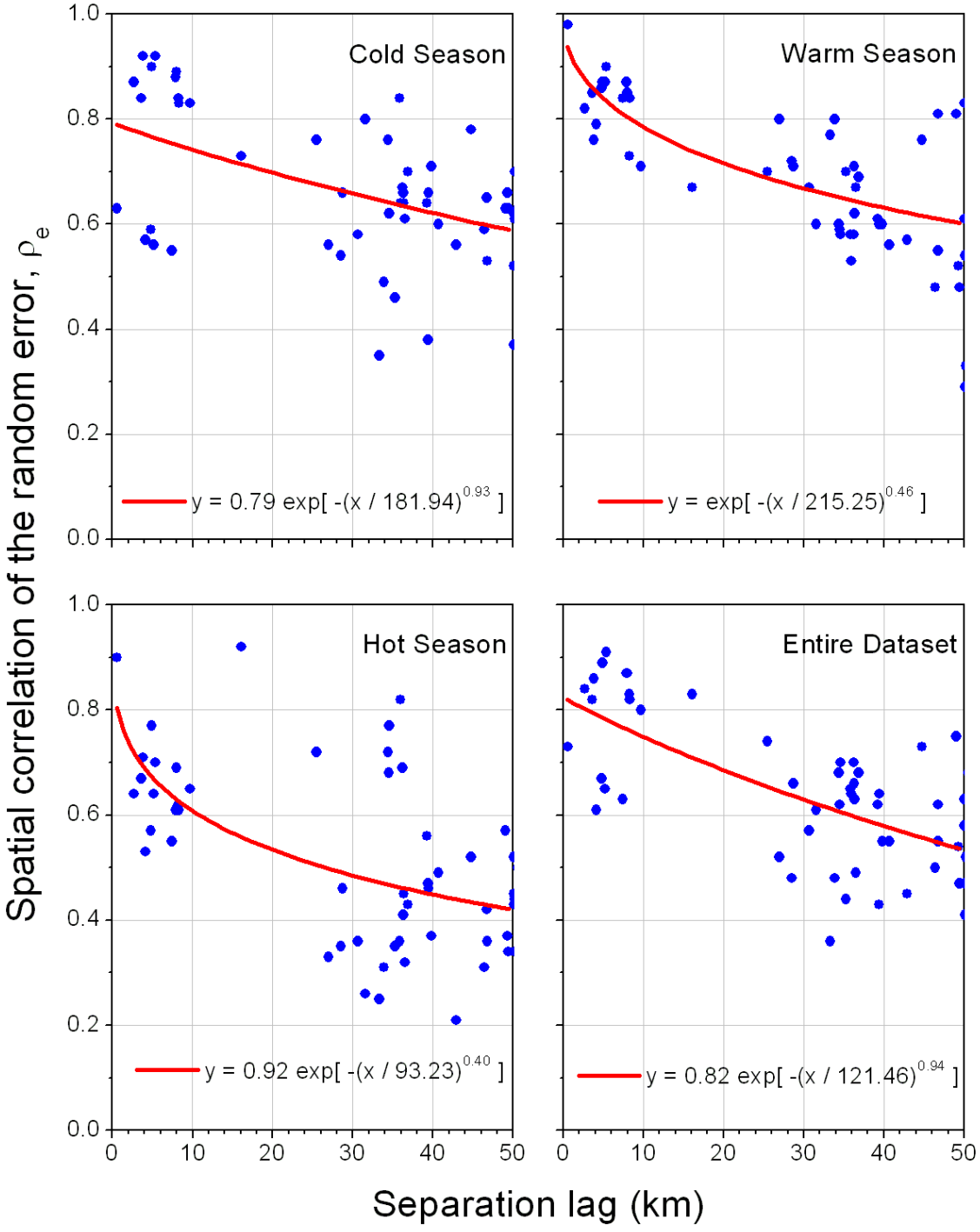

Figure E.22. Empirical intergauge spatial correlation over a limited range with a three-parameter exponential model approximation for Zone I.

Zone II

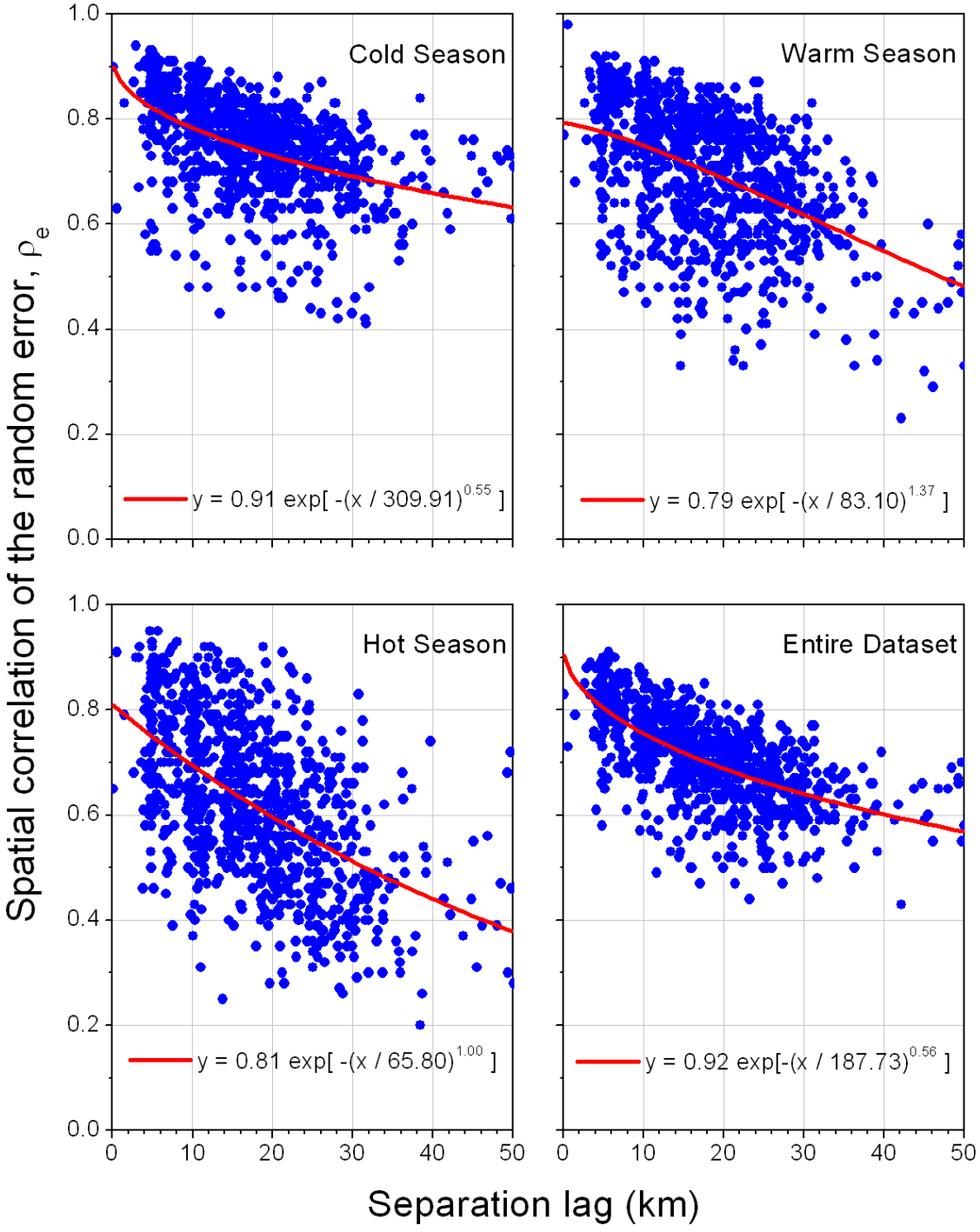

Figure E.23. Empirical intergauge spatial correlation over a limited range with a three-parameter exponential model approximation for Zone II.

Zone III

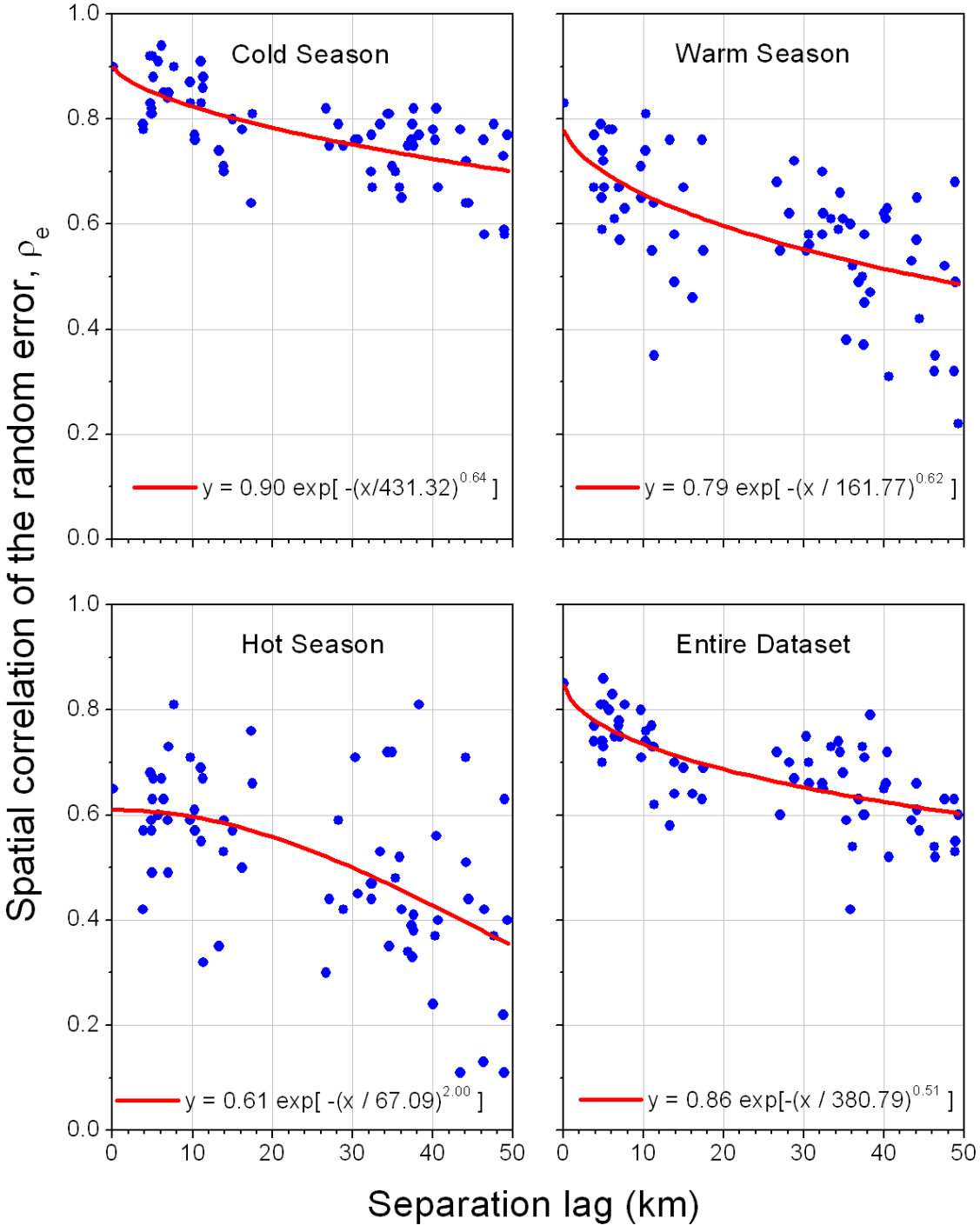

Figure E.24. Empirical intergauge spatial correlation over a limited range with a three-parameter exponential model approximation for Zone III.

Zone IV

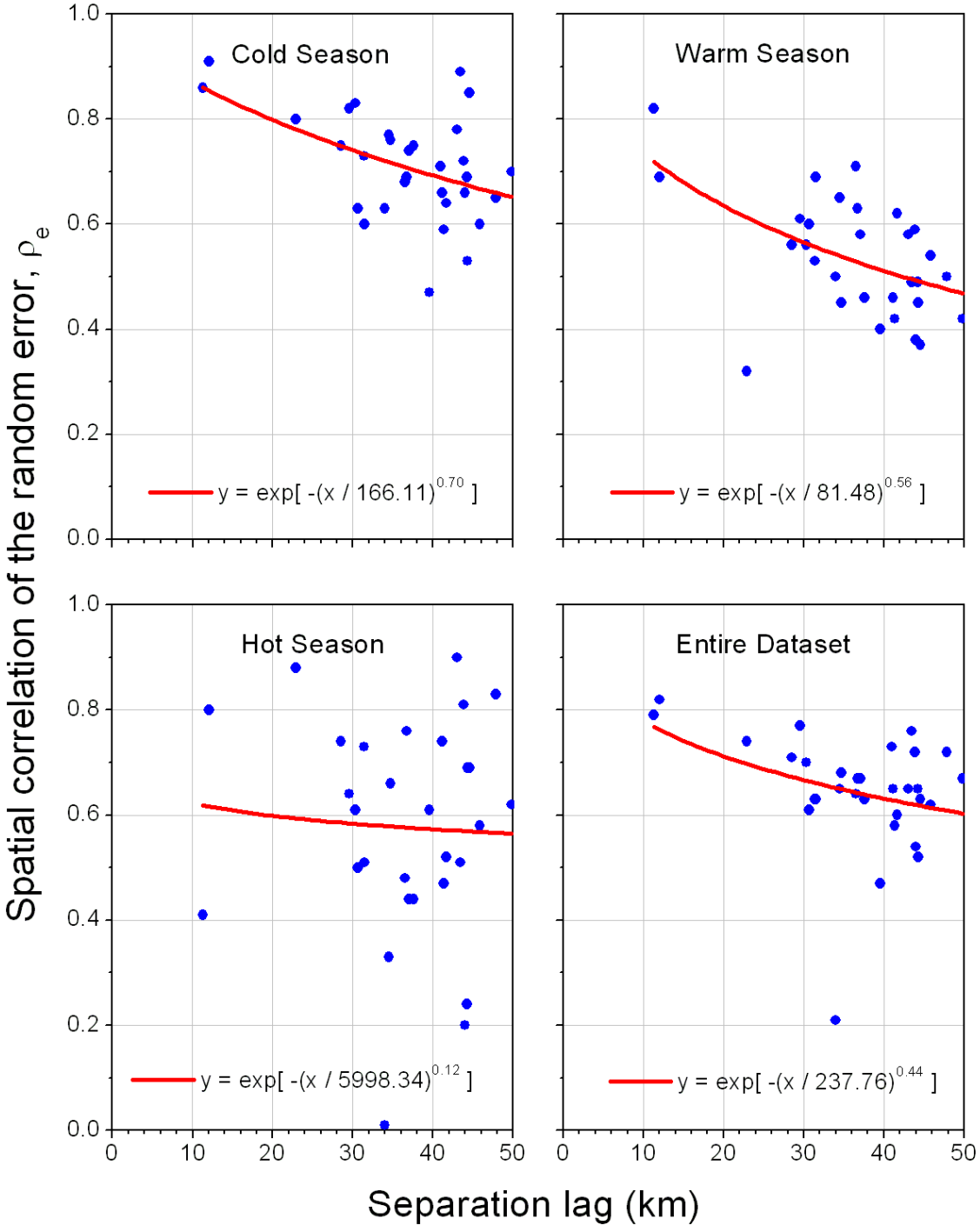

Figure E.25. Empirical intergauge spatial correlation over a limited range with a three-parameter exponential model approximation for Zone IV.

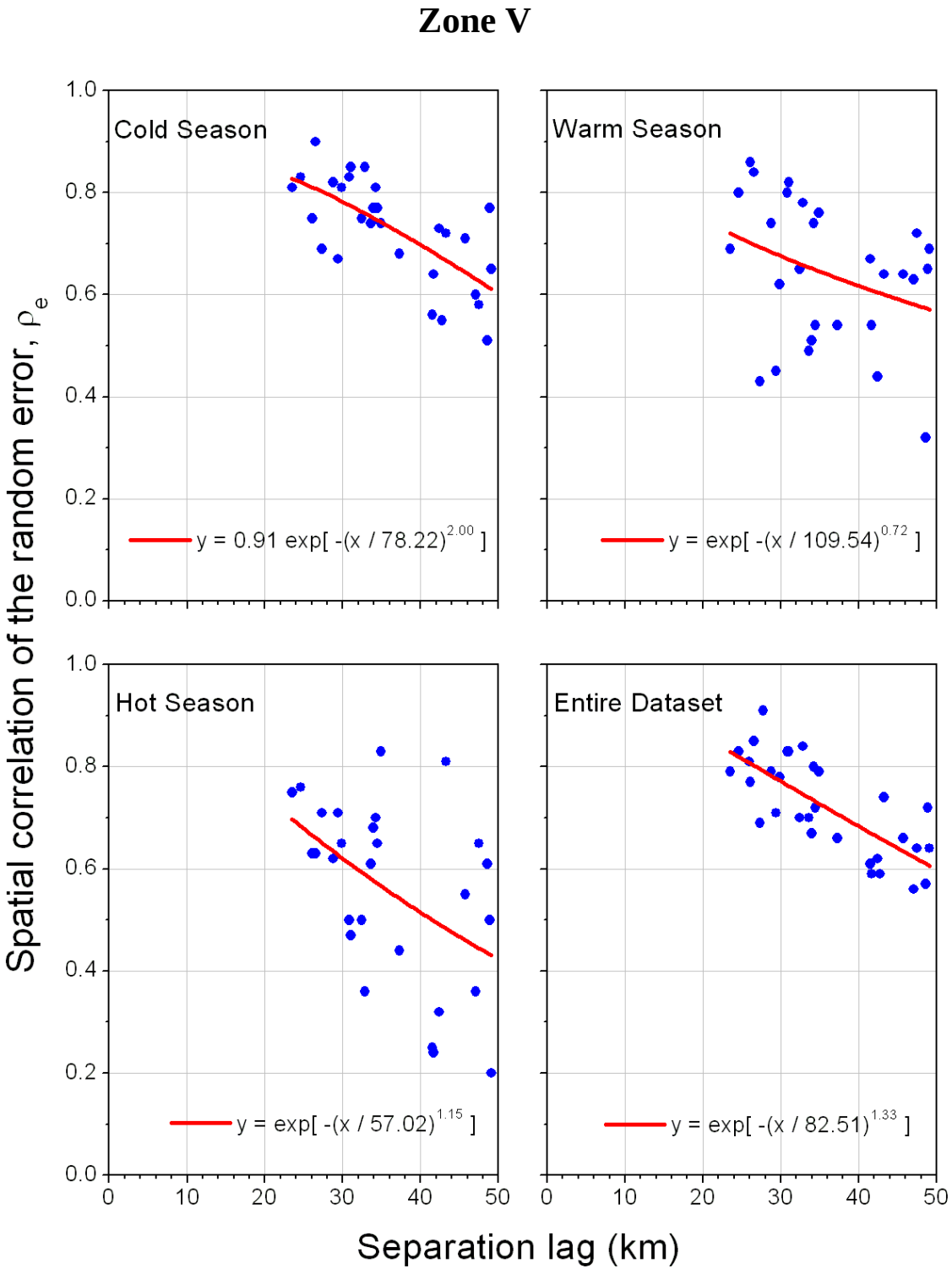

Figure E.26. Empirical intergauge spatial correlation over a limited range with a three-parameter exponential model approximation for Zone V.